UiT
THE ARCTIC
UNIVERSITY
OF NORWAY

Faculty of Science and Technology
Department of Physics and Technology

In-situ Measurements of Mesospheric Aerosols

On the observable characteristics of nanoscale ice and meteoric smoke particles

—

Tarjei Antonsen

A dissertation for the degree of Philosophiae Doctor – October 2018

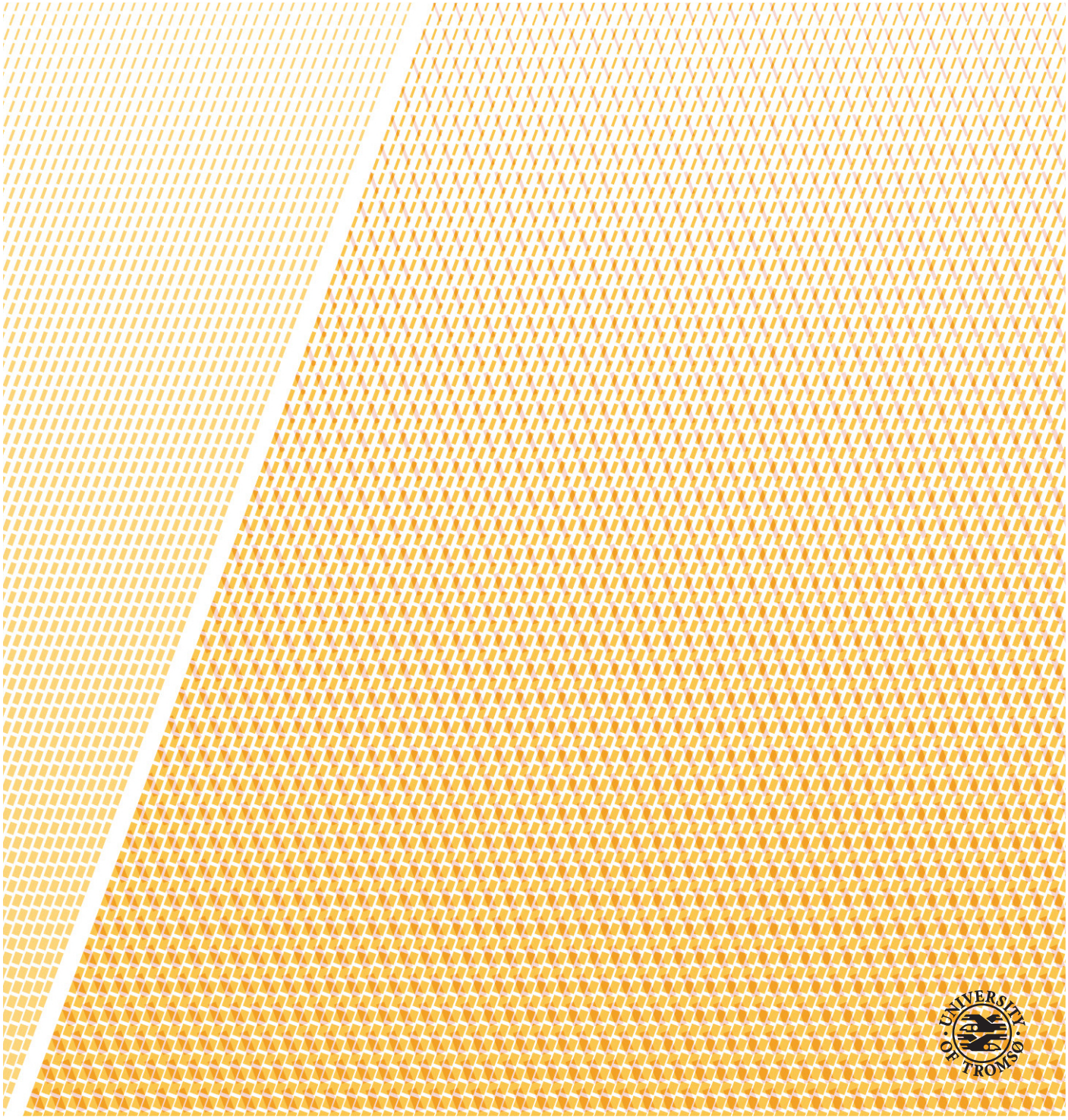

Abstract

Two sounding rocket payloads were launched from Andøya Space Centre (69.29°N, 16.02°E) during the summer of 2016 within the MAXIDUSTY campaign. Their payloads contained instrumentation aimed at investigating the characteristics of nanoscale aerosols in the upper summer mesosphere, and the role of these particles in phenomena like noctilucent clouds and polar mesospheric summer echoes (PMSE). The mesopause region, situated between $\sim$ 80 and 90 km, contain a variety of different particle types such as ice particles, meteoric smoke particles (MSPs) and hybrids of these. The role of such particles in a number of processes in the mesopause and further down in the atmosphere is not well understood. This work aims to close some of the gaps in our current understanding mainly by using aerosol detectors of the Faraday cup type. For this purpose, we have developed new observational techniques using such probes, which makes it possible to obtain information on intrinsic particle properties such as charge state, size and number density of both ice and MSPs. The configuration and technical capabilities of the probes on MAXIDUSTY also allows for observation of spatial structures in the dusty plasma down to scales of $\sim$ 10 cm. Notably, we are able to calculate the size distribution and charge state of ice particles on scales well below 1 metre. With the impact probe MUDD, we are able to infer the size distribution and volume content of MSPs embedded in larger ice particles. We moreover present the first observations of mesospheric clouds situated well below the summer mesopause, at altitudes between 66 and 78 km, which implies a significant updraft in this region. From a thorough investigation into spatial fluctuations on different length scales, we find that the aerosol-electron coupling is changing throughout a cloud system and not strictly anti-correlated. We also find that a simple relationship between PMSE and dusty plasma parameters is not possible to obtain from MAXIDUSTY measurements.

Sammendrag

To sonderaketter ble skutt opp fra Andøya Space Center (69.29˚N, 16.02˚E) under MAXIDUSTY-kampanjen sommeren 2016. Deres nyttelaster inneholdt instrumentering med mål om å undersøke karakteristika av nanoskala aerosoler i den øvre mesosfære, og rollen til disse partiklene i fenomener som nattlysende skyer og polare sommer-mesosfæriske ekko (PMSE). Mesopausen, lokalisert i høydeområdet $\sim$ 80 til 90 km, inneholder mange forskjellige partikkeltyper som ispartikler, meteoriske røykpartikler (MSP) og hybrider av disse. Rollen til slike partikler i mange prosesser i den øvre atmosfære er ikke godt forstått. Dette arbeidet sikter på å besvare noen av de ubesvarte spørsmål om mesosfæriske aerosoler ved å hovedsaklig bruke såkalte Faraday-bøtter. Vi har utviklet nye observasjonsteknikker for slike prober som gjør det mulig å få informasjon om egenskaper som ladning, størrelse og nummertetthet til både is og MSP. Konfigurasjonen og de tekniske egenskapene til probene på MAXIDUSTY-nyttelastene gjør det også mulig å måle romlige fluktuasjoner i støvplasmaet på skalaer ned til $\sim$ 10 cm. Spesielt nevnes at vi har målt størrelsesfordelingen og ladningstilstanden til ispartikler på skalaer vel under 1 meter. Med proben MUDD kan vi estimere strørrelsesfordelingen til MSPer som er innevokst i større ispartikler. Vi presenterer den første observasjonen av mesosfæriske skyer vel under mesopausehøyder i sommermesosfæren – mellom 66 og 78 km. Dette implisererer en signifikant oppdrift i denne regionen. Fra en undersøkelse av fluktuasjoner på forskjellige lengdeskalaer, finner vi at aerosol-elektron-koplingen endrer seg gjennom et skylag og ikke strengt anti-korrelert. Vi finner også at et enkelt forhold mellom PMSE og støvplasmaparametere ikke er mulig å finne fra målingene gjort under MAXIDUSTY.

Contents

Preface

It was during the time I wandered about and starved in Tromsø: Tromsø, this singular city, from which no man departs without carrying away the traces of his sojourn there.

As a fresh physics student in Paris of the North[1], my impression of the space related research conducted at the Univeristy was that radars were the big thing; Auroras, ionospheric processes and all that jazz. I remember reading about rocket experiments in an old brochure about UiT while I was in high school, and it was perhaps the main reason I chose to study space physics there. In spite of this, I knew little about the rocket related activities at UiT during my first three years in Tromsø.

In conjunction with a course in remote sensing on Andøya Rocket Range, I came in contact with Dr. Alexander Biebricher at NAROM. He was a former PhD fellow under Prof. Ove Havnes, working mainly with radar phenomena in the mesosphere. I told him about my fascination with rockets, and he brought me into contact with Prof. Havnes. At that time and as is still the case, the rocket group in Tromsø was small, with two engineers doing the work of ten men. The MAXIDUSTY project had started some time before, but a reasonable deal of work still remained: for example regarding the testing of instruments in vacuum. I was warmly welcomed into the group, and worked with vacuum testing under Prof. Åshild Fredriksen. I was lucky enough to continue some of the work I had started on during my Master's work in a PhD fellowship. The culmination was the MAXIDUSTY launch during the summer of 2016.

During the last four years I have been working with many different aspects of the MAXIDUSTY rocket campaign. This involvement, together with excellent follow-up and a good relationship with my supervisors, I feel have given me a wider set of skills than I could have hoped for going into the project; I now feel in some ways like a scientific mongrel, which is a good thing.

[1] As I am not a local, I agree this is an absurd name for Tromsø.

I do not really know what a good preface is, in fact, I just learned from my British colleague that I have been pronouncing it wrong for years. I would imagine such a text should have an underlying message or a good advice. I don't know if I can live up to that anticipation, but while I have your attention;

To the person who has stolen all my good pens the last three years: Please return them, those are expensive pens. I hope you have enjoyed pen heaven.

Overview of this thesis

Chapter 1 provides a brief history of sounding rockets, and how mesospheric rocket soundings have developed into how we currently carry out in-situ measurements of the upper mesosphere. It also describes the scientific motivation for the MAXIDUSTY project. Chapter 2 presents an introduction into the general characteristics of the mesosphere and nanoscale ice and meteoric smoke particles residing in the upper mesosphere. In Chapter 3 we introduce the theory behind modelling the movement of nanoparticles around rocket probes, and discuss the interaction of aerosols with rocket probes. Concepts such as secondary charging and adverse effects for detection are introduced. The MAXIDUSTY campaign and payloads are introduced in Chapter 4. Special emphasis is put on the probes built at UiT, which the author has worked with. The Faraday cups introduced there constitute the main framework for the included publications in the thesis. Chapter 5 presents the topic of sizes of mesospheric ice and meteoric smoke, as this is the main focus in Papers II and IV. In Chapter 6 we present the concept of multi-scale measurements of dusty plasma, and how it can be used to resolve certain open questions regarding mesospheric aerosols. A list of abbreviations is included as an appendix.

The thesis includes five papers, of which three are published in peer-reviewed journals and two are currently under revision in a peer-reviewed journal. The papers are shortly summarized in the following.

The developmental work and testing done during MAXIDUSTY constitutes a large part of the PhD work, which is not elaborated on in the thesis introduction. Chapter 6 includes a description of the ICON instrument, which represents a large part of the developmental efforts by the author.

Tarjei Antonsen, Tromsø, 2018

List of papers

This thesis consists of a subject introduction, an overview of the MAXIDUSTY campaign and the UiT instruments on the MAXIDUSTY payloads and the following peer-reviewed papers:

I Antonsen, T. and Havnes, O. (2015) *On the detection of mesospheric meteoric smoke particles embedded in noctilucent cloud particles with rocket-borne dust probes*, Review of Scientific Instruments, **86**(3), 033305, 1–12, March 2015.
doi: 10.1063/1.491439.

II Antonsen, T., Havnes, O. and Mann, I. (2017), *Estimates of the Size Distribution of Meteoric Smoke Particles From Rocket-Borne Impact Probes*, Journal of Geophysical Research: Atmospheres, **122**, 12353–12365, November 2017.
doi:10.1002/2017JD027220.

III Antonsen, T., Havnes, O. and Spicher, A. (2018), *Multi-scale Measurements of Mesospheric Aerosols and Electrons During the MAXIDUSTY Campaign*, Atmospheric Measurement Techniques, **In Review**, 1–12, June 2018.
doi:–.

IV Havnes, O., Antonsen, T., Baumgarten, G., Hartquist, T., Biebricher, A., Fredriksen, Å., Friedrich, M., and Hedin, J. (2018), *A new method to inference the size, number density, and charge of mesospheric dust from its in situ collection by the DUSTY probe*, Atmospheric Measurement Techniques, **In Review**, 1–12, June 2018.
doi:–.

V Havnes., O., Latteck, R., Hartquist, T., and Antonsen, T., (2018), *First simultaneous rocket and radar detections of rare low summer mesospheric clouds*, Geophysical Research Letters, **45**(11), 5727–5734, May 2018.
doi:10.1029/2018GL078218.

Short Summaries and Author Contributions

Paper I The paper presents the MUDD probe as it was launched on the PHOCUS payload (see also Havnes et al. (2014)), and finds that meteoric smoke particles (MSPs) which are embedded in mesospheric ice particles can be detected, and their size distribution inferred, with modified Faraday Cups. The paper, containing extensions and improvements of initial simulations done during work presented in Antonsens Master's Thesis "*On the internal physical conditions in dust probes: transport, heating and evaporation of fragmented dust particles*" (2013), was decisive in the process of the implementation of MUDD on MAXIDUSTY. Furthermore, the paper introduces a method to determine the dynamics of nanoscale particles in the vicinity of rocket probes which can be generalized to a number of different geometries, particle types and ambient conditions. A key result is that the current of fragments of large $\gtrsim$ 10 nm ice particles is probably dominated by pure MSPs, which implies that Faraday cups can measure the size distribution of these embedded particles. The theory was extended for use in mesospheric rocket studies by Antonsen and Havnes and the original MUDD design is by Havnes. All simulations were run by Antonsen, who also wrote the dust transport code. The manuscript was in its entirety prepared by Antonsen with contributions from Havnes.

Paper II This work presents an analysis of the measurements carried out by two triplets of MUDD probes on the MXD-1 and MXD-1B payloads launched in June and July of 2016, respectively. The data is analysed on the basis of the theoretical findings from Paper I and consists of MUDD data from 10 unique biased channels – from which one is able to infer 10-point energy distributions of dust fragments/MSPs. The main finding is that fragments of large ice particles, whos currents are presumably dominated by pure MSPs, follow an inverse power law which is slightly steeper than theoretical distributions (see e.g. Megner et al. (2006); Bardeen et al. (2008); Hunten et al. (1980)). Moreover, it is found that the meteoric content inside the ice is of the order of up to a few percent by volume, confirming earlier results (Hervig et al., 2012; Havnes et al., 2014). The manuscript was prepared in its entirety by Antonsen with contributions from co-authors.

Paper III In this work, we have analysed in-situ measurements of mesospheric aerosols and electrons during the MAXIDUSTY campaign, with special emphasis on the second flight, MXD-1B, where highly interesting features

were encountered. The in-situ data comes from the DUSTY and MUDD Faraday cups and the multi-Needle Langmuir Probe built by the University of Oslo. One key result is that two mechanically and electronically identical DUSTY probes with an interspacing of $\sim$ 10 cm detected very different currents through parts of a cloud system, which we attribute to aerodynamic modulation of small aerosols. We also conduct a spectral analysis, and discuss shortly the relationship between the frequency spectra of aerosol fluctuations and PMSE. From this discussion, we find it difficult to conclude with a simple relationship, and moreover find that a simple proxy from a linear combination of dusty plasma parameters is hard to obtain. The manuscript was prepared in its entirety by Antonsen with contributions from co-authors.

Paper IV In this study we present a new extended method of analyzing measurements of mesospheric dust made with DUSTY Faraday cup probes. With this method, the variation of fundamental dust parameters through a mesospheric cloud – such as size, charge state and number density – with an altitude resolution down to 10 cm or less can be obtained. We extend the analysis of DUSTY data by using the impact currents on its main grid and the bottom plate as in earlier works, in combination with a dust charging model and a secondary charge production model. The method is furthermore used on the MAXIDUSTY Faraday cup measurements and compared to remote (lidar) and in-situ (photometer) data. The conclusion is that the introduced method can be utilized as a powerful tool to determinine the size and charge state of dust particles, with good accuracy and high resolution. Havnes, Biebricher, Antonsen and Hartquist extended the theory for analyzing the rocket data. Havnes and Antonsen analyzed the rocket data. Baumgarten and Hedin collected and analyzed the optical data. Antonsen and Fredriksen tested the rocket instruments. Friedrich analyzed the Faraday data and provided the electron density data. Havnes prepared the manuscript with contributions from all co-authors.

Paper V This paper confirms that weak dust clouds at altitudes lower than the mesopause altitudes can occur and be sustained for longer times in the polar summer. Due to lack of observational evidence and holes in the theoretical understanding, such clouds were difficult to justify earlier. However, with more powerful radars (i.e. MAARSY close to the Andøya rocket range) and sensitive in-situ probes, the detection of very tenuous and low dust clouds is now confirmed to be possible. Paper V presents the first si-

multaneous rocket and radar observation of such low altitude dust clouds – observed between 66 and 78 km during the MAXIDUSTY campaign – which we have termed *Rare Low Summer Echoes*. The features were encountered during the MXD-1 flight, and we find that the presence of relatively large dust at low altitudes is consistent with smaller MSPs being swept out of the low mesospheric cloud region during the summer, while larger MSPs remain where their fall velocities equals the circulation updraught velocities. The rocket data was obtained and analysed by Havnes and Antonsen. Remote measurements were analysed by Latteck. The preparation of the manuscript was prepared by Havnes and Hartquist with contribution from the other authors.

In the text, these papers will be referred to by their Roman numerals.

Acknowledgements

This thesis was completed at UiT - The Arctic University of Norway under the supervision of Åshild Fredriksen (main supervisor), Ove Havnes and Björn Gustavsson. I am very grateful for their support, which have been impeccably great. I must also direct a sincere thank you to group leader Ingrid Mann, who have reviewed much of my work related to this thesis and its papers and moreover helped me through good discussions.

Ove Havnes deserves a special thank you for including me so selflessly and deeply into his work, even as a helpless Master's student. Thank you for the good conversations about physics and all other miscellaneous topics.

The MAXIDUSTY rocket campaign and the construction of the rocket instrumentation was supported by grants from the Norwegian Space Centre (VIT.04.14.7, VIT.02.14.1, VIT.03.15.7, VIT.03.16.7) and the Research Council of Norway (Grant no. 240065). I acknowledge the support of the people at Andøya Space Center during the integration and campaign work.

The engineers of the project, Sveinung Olsen and Yngve Eilertsen (alphabetic order by first name, no preference) deserves tremendous acknowledgement for their work. I want to personally thank them for the trips to Andøya Space Center and all the ferry rides we have shared.

Throughout the work with MAXIDUSTY I have met and cooperated with a large group of people. Amongst them I wish to thank Ralph Latteck, Gerd Baumgarten, Jan Ove Karlberg, Martin Friedrich, Tom Hartquist, John Plane, Jøran Moen and Espen Trondsen. All co-authors of papers are also thanked in their respective works. In addition, I direct a special thank you to Zoltan Sternovsky for helping with grant application and nice discussions during work with the MXD observations.

I have been fortunate enough to get to work with the student rocket G-Chaser as both a participant and supervisor. I want to thank all the participants on the

SPID team. I acknowledge intern Adrien Pineau for running simulations of dust movement in the SPID probe, some of which have been reproduced in this thesis.

To my fellow office confederates/comrades/accomplices in cahoots; Derek, Theresa and Andreas: Do not fear, we shall rise again. Also, thank you to my previous office partners Lindis, Njål, Jonas and Henry.

I wish to thank my friends and my family. I also wish I had the time to mention you all by name, but alas. Most of all I thank my closest friend Rikard and my partner Tove for their ever loving support.

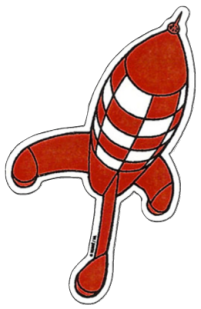

Hooray! Hooray! The end of the world has been postponed!

Hergé
The Shooting Star

Chapter 1

Introduction

This work describes the employment of different sounding rocket probes during the two launches comprising the MAXIDUSTY campaign in the summer of 2016. A main scientific goal of the project is to obtain a greater knowledge about the instrinsic properties of nanoscale aerosols in the upper mesosphere. The multi-scale dynamics of these particles and their interplay with electrons in the dusty plasma is another subject that is given particular attention. The thesis describes the theoretical background of ice particles and particles of meteoric origin in the upper mesosphere, and how these interact with and are detected in rocket probes. Special emphasis is put on the utilization of Faraday cups in determining the sizes, charge state and number density of ice particles and meteoric smoke particles (MSPs) presumed to reside inside them. This volume presents a general overview of the MAXIDUSTY projects and the instruments and a number of key questions connected to the physics of aerosols in mesospheric cloud layers.

A Brief History of Mesospheric Rockets

The *mesosphere* is the atmospheric layer situated between $\sim$ 50 km to $\sim$ 100 km. A thorough introduction is given in chapter 2. As mentioned later on, the first phenomena which where studied in this height region were the optical phenomena; noctilucent clouds were first reported on in the 1880s. In the first half of the 20^{th} century, remote measurements were the only means of investigating the near-Earth space. In 1923, Hermann Oberth introduced the concept of orbital launchers in his book *Rakete zu den Planetenräumen*. In the years around this publication, enthusiasts and military funded scientists set up societies with mission studies and carried out experimental tests of launch vehicles. The first spaceflight society was arguably the German *Verein für Raumschiffahrt*, estab-

lished in 1927.

Along with the second world war came rocket technology and launch vehicles capable of carrying payloads to the boarder of outer space. The V2-rocket desgined by von Braun was arguably the first rocket to be used as a sounding rocket, when it was launched on several occasions from March 1944 and onwards to carry out atmospheric measurements. The first instrumentation included UV spectrometers and barometers (Seibert and Battrick, 2006). The first purely scientific launches thus happened approximately 30 years after Oberth's first conception. After the first sounding rocket launches during WWII, the further development of launchers and rocket boosters gained considerable momentum due to the cold war technology race. After the peak of the cold war armament, large surplusses of solid rocket boosters gave scientists the opportunity to launch payloads to into near-Earth space relativly inexpensively.

The earliest studies of the upper mesosphere were meteorological inquiries. One early investigation technique was to use grenade launches to trace wind (Stroud et al., 1960). Temperature measurements were also among the parameters measured by the first sounding rockets, revealing perplexingly low temperaturs in the summer polar mesopause regions. Rocket observation of this height region soon shifted towards measurements of electrons and ionized species. Pedersen et al. (1970) first reported on the electron bite-out and Anderson (1971) used rockets to measure mesospheric OH. In the following years, electron measurements by Faraday rotation became a standard experiment on typical mesosphere rockets and bite-outs were commonly measured (see e.g Jacobsen and Friedrich (1979)). The mechanism behind the electron depletions and electron density gradients, which were thought to be involved in PMSE, was not known. Havnes et al. (1996) presented a confirmation of the presence of charged particles in the Earth's mesosphere, and confirmed the hypothesis that aerosols could remove electrons by attachment. These measurements were done by the DUSTY instrument – the same design was flown on the MAXIDUSTY payloads. Shortly after the first DUSTY launches, Gelinas et al. (1998) reported on the measurement of $\mathcal{O}(1)$ nanometre particles in the tropical mesosphere; also with a Faraday cup type probe. Since then, Faraday cups have become a common instrument on mesosheric rocket payloads.

Throughout the last decades, the diversity of mesospheric rocket experiments have become greater and instruments have become more capable; among several feats, the unambiguous detection of particles smaller than a few nanometers have become possible. We now have exellent profiles of temperature and neutral

densities in the mesosphere due to a series of falling sphere experiments done in the 1990s (Lübken et al., 1994; Lübken, 1999). Around the same time, several sounding rocket projects had shared interests in the aerosol distribution, charge state and turbulence and wave activity in mesopause cloud systems – with special focus on the summer mesosphere. Collaborating projects such as DROPPS, mini-DUSTY and MIDAS/MaCWAVE gave important insights into such subjects (Goldberg et al., 2001).

In more recent years, a considerable portion of the attention of in-situ studies of the mesosphere have been directed towards the elusive meteoric smoke particles. These coagulates of ablation vapours have sizes up to a few nanometres and are notoriously difficult to probe, due to aerodynamic effects in a payload shock front (Horányi et al., 1999; Hedin et al., 2007; Antonsen and Havnes, 2015; Asmus et al., 2017). Schulte and Arnold (1992) launched an ion quadrupole spectrometre with the capability of characterizing the chemistry of particles related to meteoric ablation and remained the only publication on the topic for some time, before other authors followed (see e.g. Rapp et al. (2007a) for an overview). It has since been found that products of meteoric ablation probably have important roles in the upper atmosphere chemistry. Processes involving sulphur-compounds in the stratosphere and even fertilization of the oceans have been reported on; these are only a couple of interesting processes meteoric smoke are thought to be involved in – see e.g. Bardeen et al. (2008); Megner et al. (2008); Hervig et al. (2017); Plane (2012) and references therein. Due to this, most of the recent mesosperic sounding rocket campaigns have included instrumentation aiming for a better understanding of MSPs. Among others, we mention the ECOMA project (Rapp et al., 2011), the PHOCUS sounding rocket (Hedin et al., 2014) and MAXIDUSTY as some of the more recent endevours looking into meteoric smoke to a certain degree. At the time of writing, measurements from the PMWE-payloads built by IAP and DLR are being processed; the payloads carried several instruments which are aimed towards studying MSPs.

Chapter 2

Nanoparticles In The Terrestrial Mesosphere

The current thesis has its main focus on observations of nanoscale aerosols in the mesosphere during the MAXIDUSTY campaign. The campaign, with principal investigator Ove Havnes of the University of Tromsø, was run with simultaneous support of PMSE and NLC measurements by the MAARSY radar and ALOMAR RMR lidar. In addition to observing large scale structures of mesospheric ice, the two launched payloads had instrumentation aimed towards characterizing intrinsic properties such as size, charge state and chemical content of both ice and meteoric particle species in the upper summer mesosphere. In this chapter, we thus present a thorough introduction to the general characteristics of the region of interest for this project. We discuss the two basic types of particles encountered in mesospheric rocket soundings: ice particles and meteoric smoke particles. We also give a brief introduction to radar measurements of the mesosphere and radar operation during MAXIDUSTY.

2.1 Introduction

The Earth's mesosphere ranges from an altitude of $\sim$ 50 km to $\sim$ 100 km, where it culminates in a region of minimum temperature between 80 and 90 km, called the mesopause. The mesosphere can be considered the uppermost part of the *conventional* atmosphere, as the degree of ionization is low, and turbulence keeps the mixing ratios of the major constituents constant up to altitudes of around 100 km. This latter altitude is also the Kármán definition of outer space. The upper part of the mesosphere is the ambient framework for a number of physical and chemical processes connecting Earth to space.

The meteoric influx to this region and inherent water vapour provides the necessary prerequisites to house a plethora of nanoscale particles. These particles can get ionized by photons from the sun and free electrons and ions, and they subsequently become a part of the *dusty* or *complex* plasma in the upper mesosphere. As table 2.1 shows, in the region immediately below and above the mesopause, the mean free path of neutral gas particles changes from millimetre to centrimetre-scale. For the experimentalist designing instruments for in-situ measurements, this means that ordering parameters such as mean free path, the plasma Debye-length and probe dimensions must be carefully taken into account to make sure an efficient detection of a certain species is made.

Table 2.1: Selected absolute neutral densities obtained by a series of in-situ measurements in the upper mesosphere for winter and summer conditions, as presented in Rapp et al. (2001). The units of densities are m^{-3}.

Altitude (km)	January - March	July - August	Mean Free Path (mm)
71	$9.88 \cdot 10^{20}$	$2.10 \cdot 10^{21}$	2.3/1.1
75	$6.03 \cdot 10^{20}$	$1.27 \cdot 10^{21}$	3.8/1.8
80	$2.82 \cdot 10^{20}$	$5.85 \cdot 10^{20}$	8.2/4.0
85	$1.33 \cdot 10^{20}$	$2.19 \cdot 10^{20}$	17.5/10.6
90	$6.11 \cdot 10^{19}$	$5.86 \cdot 10^{19}$	38.0/39.7

2.2 Thermal Structure and General Characteristics of the Mesosphere

The thermal structure of the upper mesoshere is highly complex with variations on the short time scales as those of gravity waves, to diurnal variations, to the timescales of the long-term trends which are also observed in lower parts of the atmosphere. The temperature is dependent on latitude, and the arctic summer mesopause with a mean temperature of $\lesssim$ 150 K is the coldest part of the entire atmosphere (Lübken, 1999). Due to the relatively high neutral density, the electrons and ions thermalize with the neutrals during undisturbed conditions; $T = T_e = T_i$. With forcing from gravity waves breaking in the mesopause, the temperature can in some rare cases approach 100 K. The winter mesosphere is, somewhat counter intuitive, warmer than the summer mesosphere, and the arctic mesopause region generally have a temperature of above 200 K (Lübken et al., 2006). The reason for the difference in temperature between the summer and winter mesopause must be expained in the framework of large scale

transport and fluid mechanics; Upward propagating gravity waves grow in amplitude as they move to higher altitudes due to decreasing ambient density – i.e. energy conservation. As they reach the mesopause region they can break and deposit momentum which counteracts the radiatively driven winds and reverse the global circulation at 80-90 km. The net effect is a pole to pole circulation, which due to continuity implies a compression of the winter mesopause and expansion of the summer mesosphere. Consequently the summer mesopause is $\sim$ 70 K colder than it would be if only a radiative equilibrium is considered. The winter mesopause is conversely $\sim$ 20 K warmer than this equilibrium (see e.g. Meriwether and Gerrard (2004) and references therein). Figure 2.1, from Lübken et al. (2009), gives a description of the temperature of the upper mesosphere throughout the year, based on lidar measurements. The summer-winter difference is clearly apparent here.

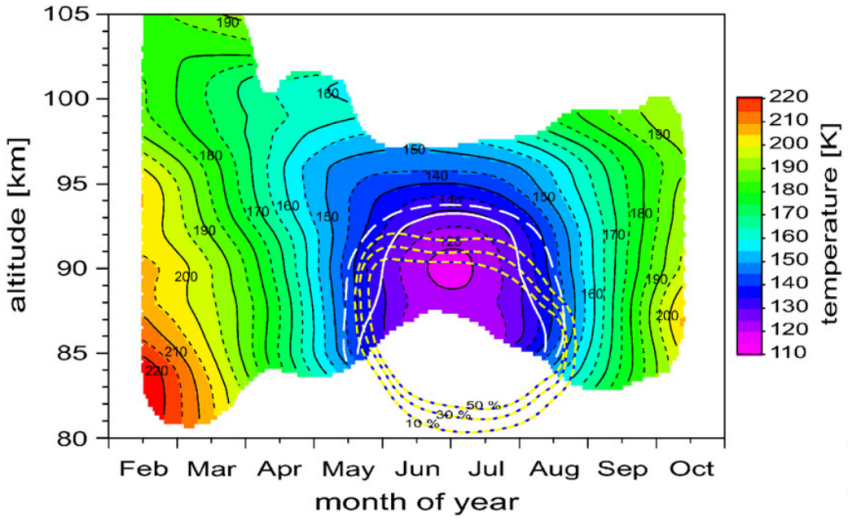

Figure 2.1: Monthly mean temperature values in the mesopause region derived by lidar observations between 2001 and 2003. The white lines indicate supersaturated regions, and the yellow contours show different occurence frequencies of PMSE in the same time period. Reprinted from Lübken et al. (2009) ©Elsevier.

Regarding long term temperature trends in the upper mesosphere, the main mechanism is strongly connected to the same atmospheric constituent which induces warming at lower altitudes, namely CO_2. The upper mesosphere is not in radiative equilibrium, and emission from CO_2 at 15μm (Fomichev et al., 1998) – commonly termed *radiative cooling* – reduces the neutral temperature. Ozone (O_3) is another key component in the energy balance of the mesosphere and is in fact the main driver of the year-to-year variability in the upper mesosphere temperature since the CO_2 concentration has little variance – it has been steadily

increasing since the start of the industrial era. In a modelling study, Lübken et al. (2013) found the radiative cooling of carbon dioxide and long term reduction in O_3 to yield a net cooling of $\approx$ 1.8 K/decade at an altitude of 70 km. In an overview of temperature trends at 70 km in the mesosphere obtained after year 2003, Beig (2011) found the general trend to be negative: The mesopause temperature, where earlier reports have cloncluded with almost no trend, was found to decrease weakly.

The prediction of long term trends in the upper mesosphere temperature is complicated by the complex interplay between constituents such as CO_2, CH_4 and O_3 and aerosols. Solar forcing can also affect the temperature in the upper mesosphere (Austin et al., 2008). To parameterize minor constituents in Whole Atmosphere Models correctly, in-situ measurements are important.

As presented below, the decreasing temperature in the upper mesosphere yields an increase in the occurence of clouds consisting of icy nanoparticles. In the following, we introduce the role of nanoscale aerosols in the upper mesosphere in depth. The focus is put on the types of particles (and intrinsic properties of these) which are relevant for the MAXIDUSTY project.

2.3 Mesospheric Nanoscale Particles

Aerosols in the mesosphere, sometimes referred to as dust in their charged state, are abundant throughout the entire height region from $\sim$ 50 to 100 km. In this altitude region they can obtain charge by electron attachment, radiation-driven detachment and other ionization mechanisms and constitute a so-called "dusty" or "complex" plasma. Throughout the last few decades, a variety of aerosol types have been identified in the upper mesosphere; ice particles, meteoric smoke particles (MSPs) from re-condensation of ablation vapours, metallic layers from differential ablation and hybrid particles of ice and meteoric remnants. All of these particle types can interact with each other and influence the mesospheric chemistry to varying degrees. The present work focuses on the detection and characteristics of nanoscale particles of ice, MSPs and the hybrid of these – sometimes referred to as *dirty ice*. The aerosols types of main interest for MAXIDUSTY are described below.

Due to the inaccessibility of the mesosphere – too low pressure for even the most sophisticated balloons, too high neutral drag for satellites to keep their orbit for extended periods – the only means of in-situ observation is by sounding rock-

ets. Nanoscale particles can in many cases be observed remotely by radar, lidar or spaceborne instrumentation, however, direct probing and sampling is needed for determination of instrinsic properties like charge state and composition. The complicated detection of mesospheric aerosols is a reason for that the role of these particles in a number of physical and chemical processes are poorly understood. A motivation for the work carried out in the current project is that mesospheric aerosols are thought to be involved in processes further down in the atmosphere. Gravitational sedimentation transports the particles down to the stratosphere where they subsequently can be effective sinks for ozone and act as cloud nuclei is especially important (Voigt et al., 2005; Murad et al., 1981; Solomon, 1999).

Mesospheric Ice Particles

Mesospheric ice particles are one of the more readily observed phenomena in the mesosphere. Ice particles of sizes above $\sim$ 10 nm can manifest themselves in noctilucent clouds (NLC) during twilight. This phenomenon typically occurs in the lower parts of the mesopause at altitudes from $\sim$ 80 to 84 km during the polar summer months. Ice particles of similar sizes moreover have an important role in the radar phenomenon Polar Mesospheric Summer Echoes (PMSE). The strong dependence of radius in the optical backscatter intensity ($\beta \propto r_d^6$) makes it difficult for optical methods such as lidar and CCDs to observe a collection of particles with sizes below $\sim$ 10 nm. The increasing occurence frequency of NLCs have in several work been connected to climate change, and, if nothing else, be a clear indicator of changing ambient parameters (Thomas and Olivero, 2001; Zahn, 2003; Kirkwood et al., 2008). As shown in figure 2.2, the water concentration in the summer mesopause region is around 5-10 ppmv at the lower edge of the mesopause, and the consequence of this for nucleation of large scale ice particles is discussed in more detail below. The concentration of water vapour has been steadily increasing from around 4 ppmv at the start of the industrial era, and the general consensus is that this is the main controlling factor of NLC occurence frequency. In fact, no NLCs were reported on before 1885; this was only two years after the Krakatoa volcano eruption, and some authors have speculated that the increase in water vapour is due to this eruption. Another explanation is that water created in methane oxidation, which has increased with the release of methane from polar ice with increasing ice melting is the main driver of the increase in mesospheric water, and that the concentration before 1885 was simply not high enough to produce an observable NLC

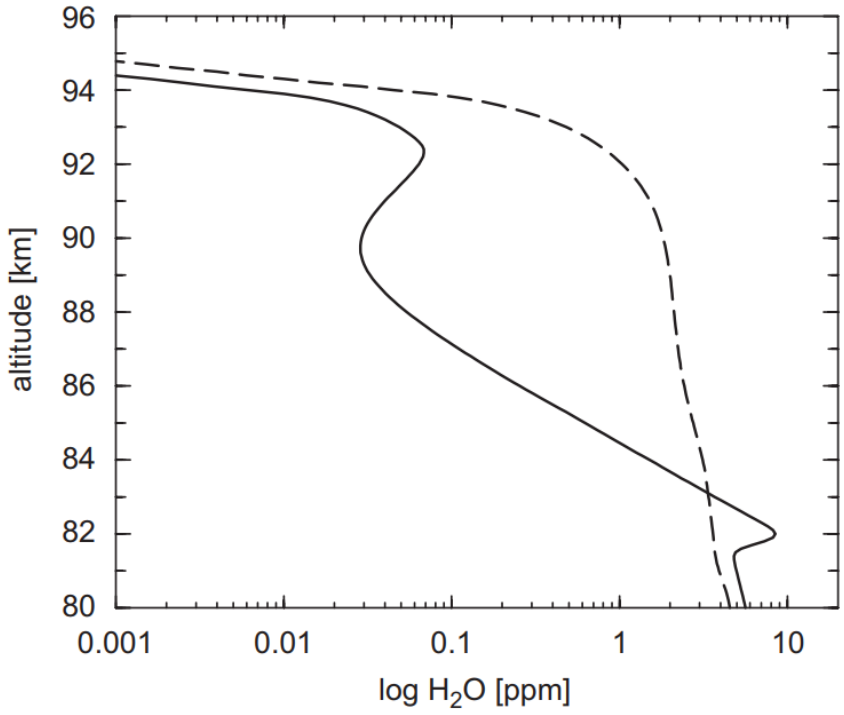

Figure 2.2: Modelled water vapor concentrations mid-summer at 78° N with (solid) and without (dashed) the effect of freeze-drying. Data from Von Zahn and Berger (2003), plot adopted from Lübken et al. (2009) ©Elsevier.

albedo (Thomas et al., 1989). The chemical process lies in the hydrogen balance; $[H] \rightleftharpoons [H_2O] + 2[CH_4] + [H_2]$. As no considerable sources or sinks of hydrogen exist in the upper stratosphere and mesosphere, the balance implies that roughly two water molecules are produces for every destroyed methane molecule. This has been confirmed by satellite observations (Jones et al., 1986).

In the following we address shortly the two possible nucleation mechanisms for mesospheric ice. This concept is important to understand which particle types the Faraday cups on MAXIDUSTY can encounter. First, let us recall Ostwald's rule which states that a thermodynamical state of a nucleation product does not need to be the most stable one, but only the one with the smallest associated free energy. This is to say that supersaturated vapour does not form hexagonal ice structures directly, and in fact for a large range of parameters forms an intermediate amorphus state without crystaline stucture. As pointed out by Zasetsky et al. (2009) and Murray and Jensen (2010), a homogeneous nucleation of ice (water bonding with water) can occur for very steep negative temperature gradients and still satisfy Ostwald's rule. However, in most cases it is more feasible that a third body – a dust grain or more specifically an MSP particle or a smaller dirty ice particle – lowers the energy barrier and promotes a much faster growth

rate than a homogeneous one. This process is called heterogeneous nuclation, which supported by the general finding that large ice particle contain MSPs up to the order of percents by volume. This is also the basis of out model of a typical ice particle, which is used consistently throughout this work. The homogeneous nucleation rate have the following porportionality to free energy (Evans, 1993):

$$R_{\mathrm{Hom}} \propto \left[r_d^{\dagger}\right]^2 \cdot \exp\left[-\frac{\Delta G_i^{\dagger}}{k_B T}\right] \tag{2.1}$$

where $r_d^{\dagger}$ is the critical grain radius and $\Delta G_i^{\dagger}$ is the Gibb's energy for adding an i^{th} molecule to the grain at thermal energy $k_B T$. The result of a third body lowering this latter term implies a faster growth.

In this thesis, Paper III and IV are mainly focussed on the observation of ice particles of sizes $\gtrsim 5$ nm and their characteristics and bulk properties.

Meteoric Smoke Particles

Cosmic dust enters the terrestrial atmosphere with meteoric ablation concentrated in the region from 70 to 110 km. The vapours of refractory elements are believed to re-condense into nanometre-sized dust particles called meteoric smoke particles (MSP) (Hunten et al., 1980; Bardeen et al., 2008; Megner et al., 2006). Despite several attempts, the composition of these particles has not been unambiguously determined, and they are often elusive to in-situ detectors deployed rockets due to their small mass/size. The detection process is elaborated on in chapter 3. Moreover, atomic metal layers in the topside mesosphere are deposited through differential ablation – a process, in which the most volatile (Na, K) elements ablate first, and the less volatile chondritic elements (Fe, Mg, Si) ablate further down (Plane, 2012). To study the role of these metallic layers and MSPs in atmospheric processes, an accurate estimate of the global influx of meteoric material is the most basic parameter. The total Interplanetary Dust Particle input (IDP), has been estimated by several methods; iron sediments in ice cores, zodiacal dust cloud observation and modelling, remote measurements by lidar and radar, and modelling of metallic layer; see Plane (2012) and references therein for a detailed review. Estimates of the IDP from these methods span two orders of magnitude, from 5 to 300 tonnes per day. As illustrated in figure 2.3, the global daily iron input – which is a proxy of the IDP – is found to vary significantly between estimation methods. As an example, sediment collection from ice cores yields higher estimates than other methods by up to two

orders of magnitude. Meteor radar measurements, the most sensitive of which is performed by the Arecibo 430 MHZ radar, give estimates in the lower end of the range (Mathews et al., 2001). On the basis of this, it is clear that the most valuable characteristics still to determine is the true meteor vapor density and true size distribution of meteoric smoke particles. The latter problem is probably best met with in-situ observation.

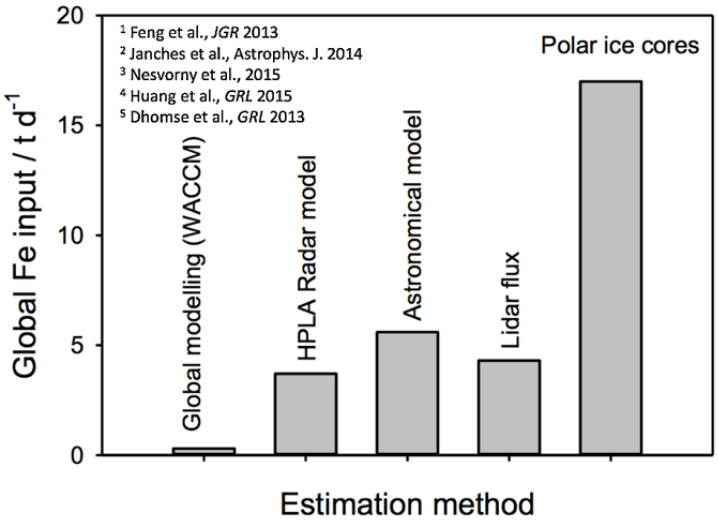

Figure 2.3: Estimation of daily iron input to the atmosphere – a proxy for meteoric influx – based on different models and measurement techniques. The data is adapted from the listed works. Courtesy of Dr. Zoltan Sternovsky, LASP.

It is our current understanding that the primary particles – vapours of nanoscale molecular and particulate matter – formed in the ablation of incoming meteorites, coagulate into particles of sizes ranging from the order of 1 Ångstrøm to a few nanometres (Rosinski and Snow, 1961; Hunten et al., 1980; Kalashnikova et al., 2000). Figure 2.4 shows a sketch of the processes a meteoroid undergoes upon entering the Earth's atmosphere, from initial ablation to the final sedimentation and large scale bulk transport of re-codensed smoke particles. The majority of incoming meteoroids have masses in the range $\sim 10^{-3} - 10^{-6}$ g which corresponds to sizes from a few tens to a few hundred microns. These bodies account for the clear majority of ablated material. Meteorites that do not completely ablate are unlikely to be of great interest due to their small contribution to the total IDP (Hunten et al., 1980). The initial re-condensation of ablation vapours takes place at the topside mesosphere, while gravitational sedimentation provides additional growth. Upwards transport of MSPs due to updraft and circulation of particles is also possible, as indicated in the principle sketch.

No successful retrievals and subsequent mass spectrum analysis of mesospheric

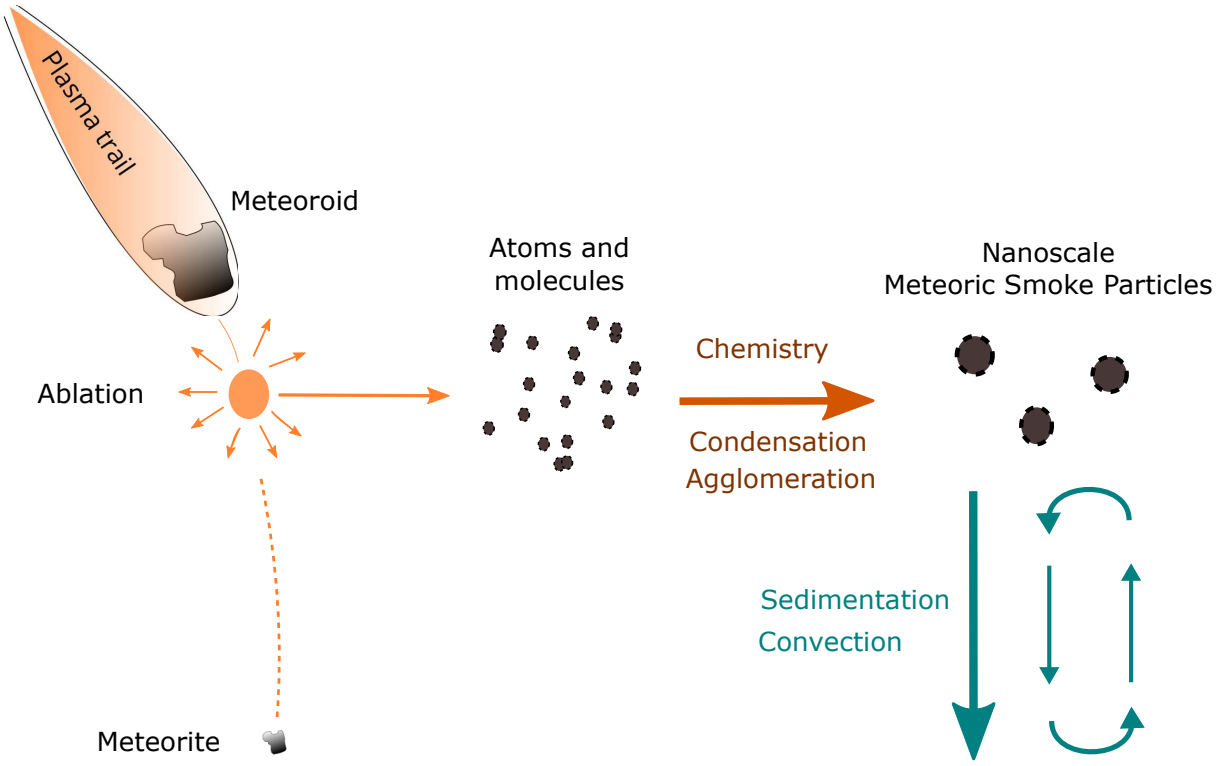

Figure 2.4: Simplified schematic of the process of MSP formation in the altitude range 70-110 km, based on an original illustration from Megner et al. (2006).

MSPs have been done at the time of writing. In the laboratory and through molecular dynamics simulations, it has been found, with the premise that ablation of olivine material injects equal amounts of Mg, Fe and Si in the upper mesosphere, that likely candidates for initial condensation nuclei and small MSPs are metal silicates and metal oxides (Saunders and Plane, 2006; Plane, 2011). The molecular dynamics calculations from these works also verified that such molecular condensation nuclei, having large dipole moments, thermodynamically favor the addition of up to 8 H_2O-molecules on molecules of certain compositions compared to homogeneous nucleation. Using Mie theory, Hervig et al. (2012) reported that the occulation spectra from polar mesospheric clouds matched particles containing up to $\sim$ 3% of either carbon, wüstite (FeO) or a non-stochiometric combination of olivine constituents.

In the present work, one of the main goals have been to design, refine and utilize new experimental methods to resolve the size distribution of MSPs inside large ice particles around the mesopause. Paper I and II along with the work by Havnes et al. (2014) are the contributions to this topic in this dissertation. The general finding, which is introduced in chapter 5, is that MSPs inside large ice

particles probably have a steeper inverse power law than that one of available model predictions. The effect of updraft on MSP growth is one of the discussion topics in Paper V. As it turns out, such transport can probably lead to dust structures and detectable radar echoes on altitudes as low as $\sim$ 70 km in the summer mesosphere – a novel feature termed *Rare Low Summer Mesospheric Clouds* first reported on in Paper V from the MAXIDUSTY campaign.

Charge state of Mesospheric Nanoparticles

The variation in the charge state of free aerosols in the upper mesosphere is mainly controlled by grain composition, size, energetic precipitation and solar irradiation. The grain composition and size controls how effective photoelectric charging, i.e. the ejection of an electron from a grain surface due do incoming photons with energies comparable or larger than the surface work function ($\sim$ a few electron Volts), is compared to collisional charging. Metals more easily yield electrons under solar irradiation compared to ice particles, and as it turns out, smaller particles have a higher affinity for photoemission than larger particles and for mesospheric ice particles larger than 10 nm, photoemission becomes negligible (Havnes and Kassa, 2009; Rapp, 2009). The charge distribution of mesospheric nanoscale particles is sensitive to several factors, that will be introduced below. This thesis deals with a charging model for aerosols in Paper IV, and the following discussion serves as a more in-depth theoretical background. Contact Charging of aerosols upon impact with rocket probes is discussed in Chapter 3.

In general, if a neutral dust grain larger than a few nanometres is placed in the plasma around the mesopause, it will become negatively charged in a matter of seconds to minutes due to electron attachment, for a plausible range of electron densities (Draine and Sutin, 1987)[1]. For the lower range of sizes, the competition between electron attachment and emission and detachment becomes important. As an illustration of the variability in the charge state, we below calculate the distribution of charges on a range of mesospeheric nanoparticles. For plasma particle attachment rates, we use the expressions by Draine and Sutin (1987) and include polarization effects (image charges). The temporal evolution of the dust density at charge state Z, denoted by $N_d(Z)$, can be stated as (Biebricher and

[1]This work discusses interstellar grains, but the attachment current terms can be generalized for mesospheric conditions

Havnes, 2012):

$$\begin{aligned}\frac{\partial N_d(Z)}{\partial t} &= J_d^i(Z-1)N_d(Z-1) - J_d^e(Z)N_d(Z) \\ &- J_d^i(Z)N_d(Z) + J_d^e(Z+1)N_d(Z+1) \\ &- J_d^{\Phi}(Z)N_d(Z) + J_d^{\Phi}(Z-1)N_d(Z-1) \\ &- J_d^{\mathrm{Det}}(Z)N_d(Z) + J_d^{\mathrm{Det}}(Z-1)N_d(Z-1) \end{aligned} \tag{2.2}$$

where $J_d^s(Z) = \tilde{J}_d^s n_s \xi \pi r_d^2 \bar{v}_{th}^s$ is the plasma attachment rates of species s for mean thermal velocity and electron attachement rate ξ from Draine and Sutin (1987). The factor $\tilde{J}_d^s$ contains the polarization contribution. Furthermore, J^{Φ} denotes the photoelectric currents and J_d^{Det} the photodetachment currents to the grain.

If we now normalize the plasma and grain potential such that $\hat{V} = eV/k_BT$ and $\hat{U} = eU/k_BT$ respectively, it can be shown that for Boltzmann distributed plasma particles – i.e. when electric forces balance plasma pressure gradients – that the quasi-neutrality for a thermalized plasma with $T_e = T_i = T$ becomes (Havnes, 2004):

$$\exp\left(\hat{V}\right) - \exp\left(-\hat{V}\right) - P\hat{U} = 0 \tag{2.3}$$

where $P = 0.695 \cdot n_d r_d T_i / n_0$ is the dusty plasma ordering parameter often referred to as the Havnes-parameter (Huba (2018), *NRL Plasma Formulary*). In many cases for the mesopause region, it turns out that quasi-neutrality can be difficult to satisfy, and Poisson's equation must be solved accordingly. However, in cases with little disturbance, e.g. updraft and gravity wave breaking, quasi-neutrality is a good approximation. Havnes et al. (1984) showed that this is valid for dust structures with length spatial scales considerably larger than the Debye-length and plasma temperatures from 150 to 3000 K. In figure 2.5 we show the equilibrium solutions from an iteration of eq. (2.3) with an initial guess of $\hat{V}$ and 12 charge states for ice particles of three different sizes, and with electron and aerosol densities representable for the summer mesopause. In this calculation the electron attachment term dominates, and particles with sizes up to ~ 10 nm are predominantly in charge state $Z = -1$. For the smallest particles photoionization becomes important, and a small portion of 5 nm ice particles (top panel) remain neutral. Large particles with radii $\gtrsim 20$ nm can reach charge state $Z = -3$ and lower for low P-values; i.e. there is an excess of available electrons for an effective collisional charging.

If we now consider the charge state of meteoric smoke particles, we note that there will be a considerable difference in charging efficiency from attachment

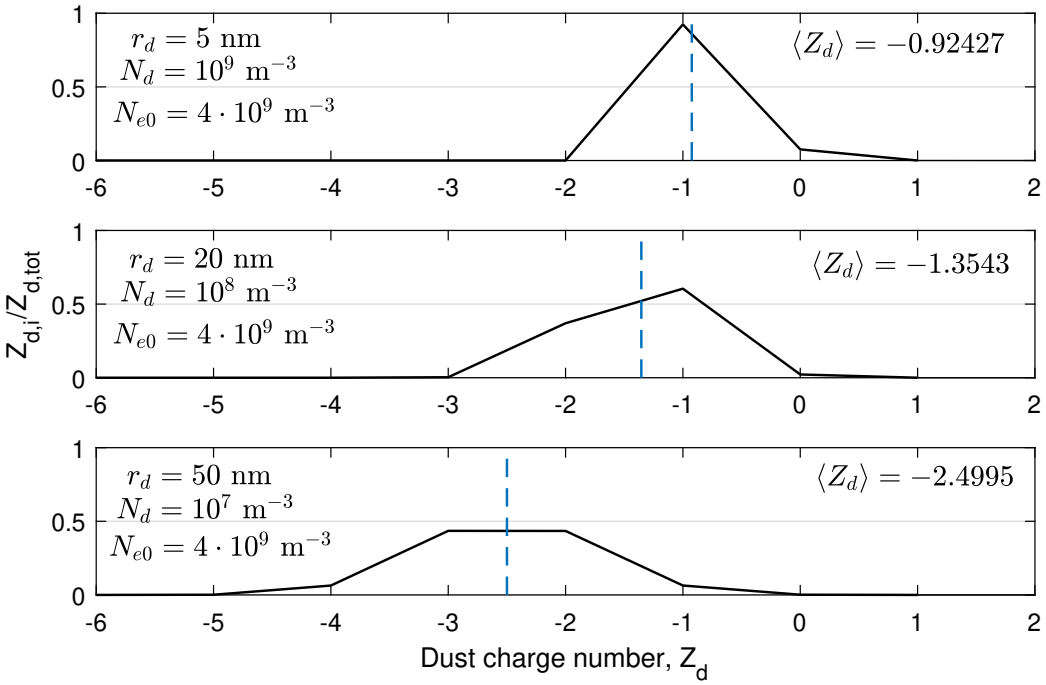

Figure 2.5: Calculated charge distributions for monodisperse mesospherice dust particles for low P-values. The size dependent photodetachment rate and image charge potential is taken into account. The electron attachment coefficient is set to 0.5, in accordance with Draine and Sutin (1987). The values in the brackets denote the average charge.

due to the smaller sizes. The composition of the particles, presumably common meteoric materials such as Fe, Mg, Si and Na, makes the MSPs more susceptible to photoionization compared to ice. In figure 2.6 we present the results of two iterations of eq. (2.3); one run *without* photodetachment (solid lines) and one run *with* photodetachment (dashed lines). The difference is striking for the particles in the lower end of the size spectrum, with photo detachment effectively neutralizing particles smaller than $\sim$ 1 nm. The main takeaway from these simple calculations is that a significant portion of MSPs tend to be neutral and even positive during sunlit (daytime) conditions. Knappmiller et al. (2011) and Asmus et al. (2015) have done thorough investigations into dust charge states when including MSPs and photoionization, and gave similar conclusions – importantly about the presence of positive MSPs in the mesosphere.

Simplified calculations like the charge state calculation presented here yield good estimates of charge distributions of mesospheric nanoparticles which can furthermore be used in discussions of remote and in-situ mesurements. A drawback of such calculations is that there are a number of dusty plasma parameters

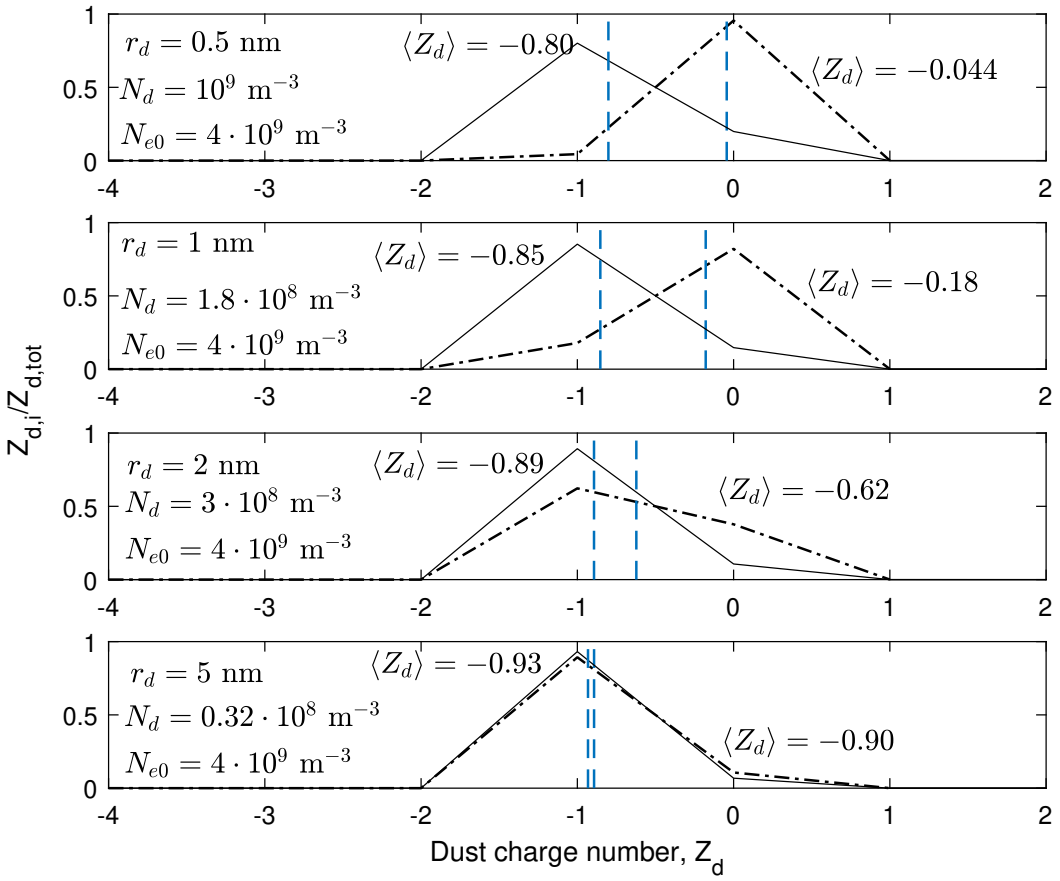

Figure 2.6: Calculated charge distributions for monodisperse MSPs of different sizes. Here, the relative MSP number density between panels follows an inverse power law of $N_{MSP} \propto r^{-2.5}$. The dashed lines show the charge distributions for sunlit conditions with size dependent photodetachment rates of $\{.05, .03, .01, .005\}$ for the four panels (top to bottom). The solid lines show the cases for *no* photodetachment. Image charge potential is taken into account for all cases.

which vary up to orders of magnitude in value throughout a cloud system around the mesopause.

In the current work, one of the main goals have been to eliminate some of the uncertainty connected to these simplified calculation of charge and size distributions by solving for particle charge, size and dust density simultaneously. The results, introduced in section 5.2 and published in Paper IV, is a new method to infer those fundamental dusty plasma properties from Faraday cup data, with high altitude resolution. With the method introduced in that paper, a more correct charging model will directly lower the uncertainty size estimates.

2.4 Remote and In-situ Observation of Mesospheric Clouds

The earliest reports of cloud-like structures at altitudes between 80 and 90 km were reported by several authors in the mid-1880s (Jesse, 1885; Leslie, 1885). It has been speculated that the 1883 eruption of Krakatoa was responsible for depositing volcanic particles at those altitudes, as no NLCs were observed before 1885 (Schröder, 1999). Wegener (1912) suggested that ice particles were abundant in NLCs. The presence of water at such high altitudes were suggested to be a consequence of the global methane (CH_4) increase due to pollution from industry. It was known that methane could oxidize to water in the stratosphere, thus increased water content in the upper atmosphere would eventually lead to condensation of the present vapour. An interesting aspect is that until the first radar observations of the same height region, clouds in the mesopause region was observed both from satellites and by astronauts in orbit (Cho and Röttger, 1997).

The rapid development of Mesosphere-Stratosphere-Troposphere (MST) radars in the 1970s (see e.g. Woodman and Guillen (1974)) provided a remote measurement technique which eventually would be used interferometrically. These radars could also obtain three-dimensional flow velocity vectors. The first observations of coherent radar echoes, polar mesospheric summer echoes (PMSE), were made at VHF frequencies around 1980. The echoes were found to be almost coincident with NLCs and related to subvisible ice particles (see Rapp and Lübken (2004) for a review).

Developments in laser technology made lidar (which was theorized as early as 1930 by Synge) more readily available throughout the 1980s and 1990s. Measurements of particles which scatter light efficiently can be used to estimate particle radii, and Fe-lidars can be used to measure temperature. For MAXIDUSTY, the RMR (Von Zahn et al., 2000) and Fe-lidars at ALOMAR were operated.

During the MAXIDUSTY campaign, the MAARSY MST radar was operated to support the rocket payloads with simultaneous common volume measurements. MAARSY (69.30° N 16.04° N) is a monostatic phased array VHF radar at 53.5 MHz with capabilities to split and steer separate beams. The system therefore allows for continuous 3D monitoring of more than one region separated in space. A feature that is highly valuable for rocket launches is that MAARSY can direct one beam in the payload trajectory direction and other beams outside that vol-

ume. In figure 2.7 we show vertical and horizontal slices of a beam directed along the payload trajectory during MXD-1 in the height range between 80 and 90 km. The PMSE was broad, layered and dynamic.

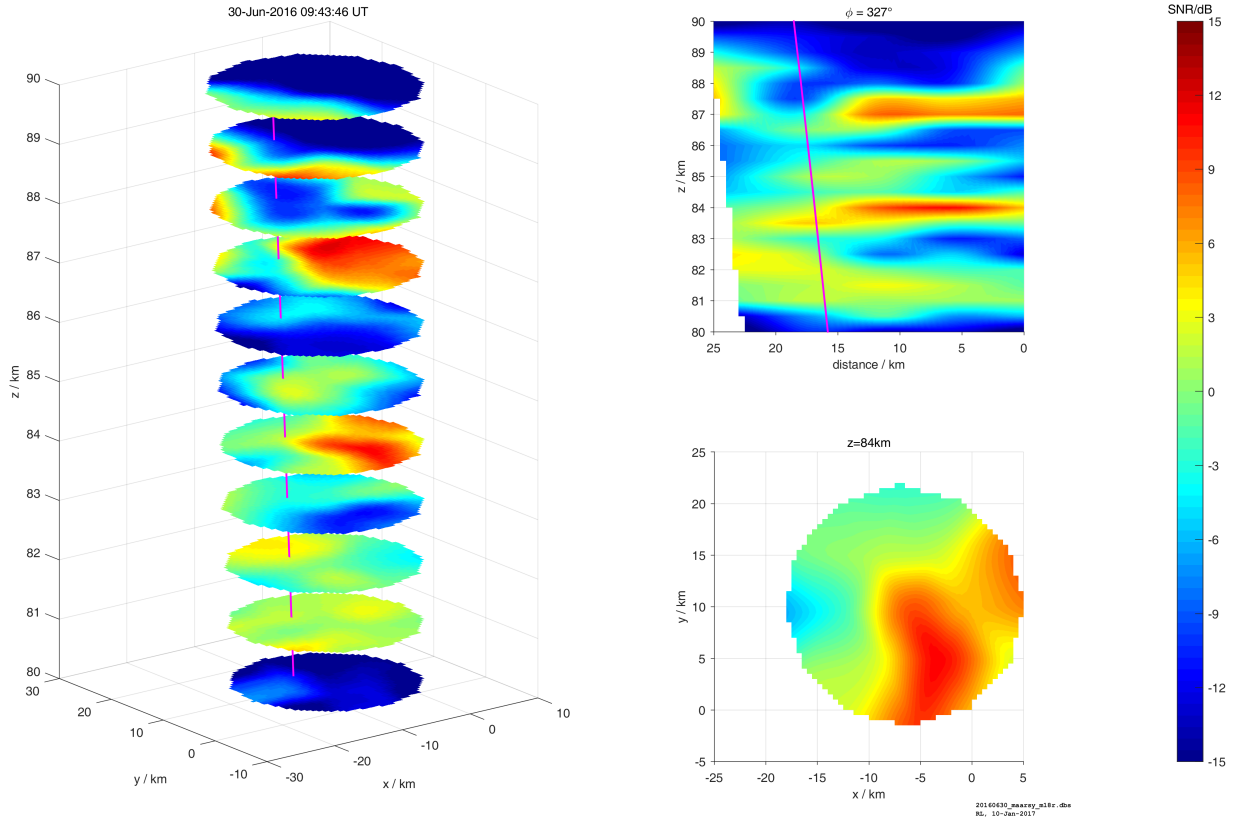

Figure 2.7: PMSE recorded at the time of launch of MXD-1 with the 53.5 MHz MAARSY radar. The radar made measurements in the same volume as the rocket, and the trajectory is indicated as a purple solid line. Courtesy of Dr. Ralph Latteck, IAP.

With the discovery of PMSE, the hypothesis quickly arose that aerosols would be effective sinks for free electrons in this height region. As mentioned in the introduction, Faraday cups were employed to solve the question of such bite-outs. Throughout the last decades, simultaneous measurements by radar and rocket have become most valuable for the investigation of dynamics in a cloud layer; also for the MAXIDUSTY campagin. In figure 2.8 we show a comparison between dust charge number density derived from DUSTY, electron density derived by mNLP and MAARSY SNR. We note, as is discussed in Paper III, that the absolute value of the electron density is probably overestimated, but the relative fluctuations are correctly presented. A clear bite-out is seen between $\sim$ 82 and 87 km. The PMSE does not appear to have a simple connection to the first or-

der plasma parameters, and spans over a larger height region than the depletion. This connection is also discussed in Paper III.

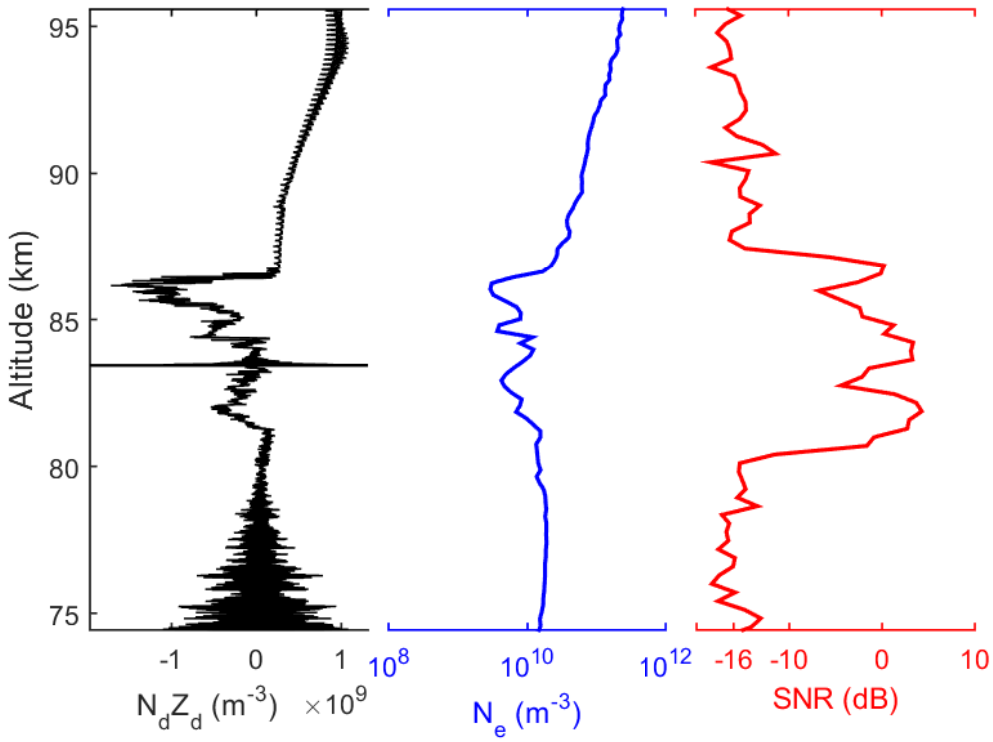

Figure 2.8: Comparison of aerosol charge number density derived from DUSTY currents, electron density from the mNLP-probes and PMSE SNR for MXD-1. A bite-out in the electron population coincides well with the aerosol measurements and SNR, however, the edge profile of the PMSE cannot easily be directly related to first order dusty plasma parameters.

Chapter 3

In-situ Detection of Mesospheric Nanoparticles

The experimental framework for the current thesis is the MAXIDUSTY sounding rocket campaign. In this chapter we introduce the theory behind the prediction of the movement of aerosols around and inside rocket probes. We put special emphasis on Faraday cups as employed on the MAXIDUSTY payload. This theory is used in the accompanying papers to estimate sizes of incoming particles, and is instrumental for correct interpretation of Faraday cup data. Impact charging and secondary charging effects, which is important in the interpretation of Faraday cup currents, is introduced. Moreover, we present a discussion on adverse effects typical for mesospheric in-situ measurements.

3.1 Dynamics of Nanoparticles in the Vicinity of Rocket Probes

There are two main factors controlling, or rather obstructing and interfering, the detection of nanoscale mesospheric particles. These are *flow fields* in the neutral gas which affect particles through collisions, and *electric fields* which interact through electric forces with charged grains. The kinetic energy of a nanoparticle of size 1 nm with a density from 1 to 10 gcm^{-3} at a rocket speed of $\sim$ 1 kms^{-1} – relevant for mesospheric rocket studies, is $\mathcal{O}(10-100)$ eV. These energies are comparable to or much larger than the electrostatic barriers of typical biased probes ($\sim$ a few eV) for grains charged with up to a few elementary charges; be it Langmuir probes or Faraday cups. A takeaway from this is that for the 'large' ice partices involved in NLCs and PMSEs, the electrostatic barrier will not affect recorded currents in DUSTY and MUDD probes significantly.

To analyse the evolution of NLCs and PMSEs, distinction between nucleation mechanisms and a number of phenomena involving the interplay between MSPs and ice particles, one needs to be able to observe particles of sizes $\lesssim$ 1 nm (Horányi et al., 1999). For these smaller particles, the aerodynamical envrionment can completely define the detection efficiency. The task to calculate this detection efficiency require subtantial simulation efforts, and since such considerations are important in many of the studies presented in this dissertation, we should discuss a few of the most important factors of nanoparticle dynamics. Antonsen and Havnes (2015) (Paper I) deals with transport of particles in the framework of MUDD. The reader is also referred to the works of Hedin et al. (2007) and Asmus et al. (2017) which have recently offered new insight on central topics regarding the detection of particles in the lower end of the size spectrum.

Pressure regime

To calculate the trajectory of a nanoparticle in the vicinity of a rocket probe, detailed knowledge about the neutral flowfield is required. As shown in table 2.1, the mean free path of neutrals traverses values from $\sim$ 1 mm to $\sim$ 40 mm in the altitude region from 70 to 90 km. In many rocket instruments, these scales can be longer than several or all characteristic length scales of a rocket robe – i.e. probe radius, length or longest internal clear path. This offers a big problem, as fluid mechanical calculations cannot be used; the explanation boils down to an undefined collision derivative in the Boltzmann transport equation. An arduous solution to this can in some cases be the Chapman-Enskog expansion – i.e. expansion of the collision term in Navier-Stokes through the parameter $\mathrm{Kn} = \lambda/L_p$, where λ is the mean free path and L_p is a characteristic system length (Boyd, 2003). A correction term for the probability that a given nanoparticle misses or *slips* a collision within a characteristic length can also be used (Cunningham slip factor; see e.g. Moshfegh et al. (2010)). However, in most cases it is easier to utilize Monte Carlo simulations of the movement of a large amount of test particles to yield a statistically probable flow field (Bird, 2005). In figure 3.1 we show a velocity field extracted from such a simulation, for the MUDD Faraday cup MUDD, which was flown on both MXD payloads. The fields can furthermore be used as input in calculation of nanoparticle trajectories. It should be noted that this example simulation is for an isolated probe, and that effects due to neighboring probes is not included. Throughout this thesis, the DSMC software for two- and three-dimension flows written by G. Bird is utilized.

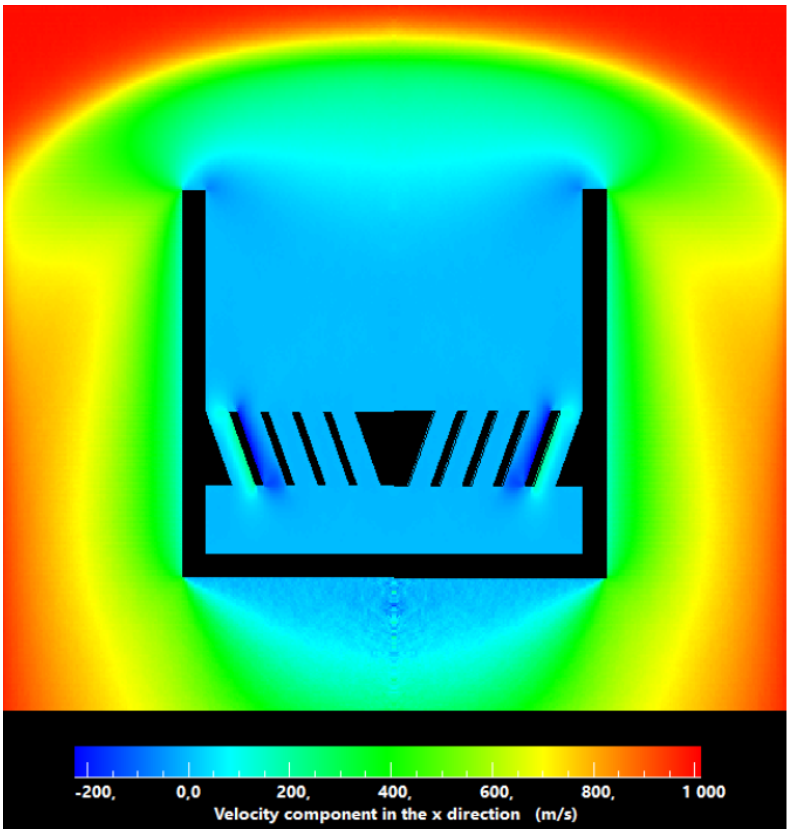

Figure 3.1: Flow speed at 70 km in the direction along the rocket payload (here termed 'x') extracted from a Monte Carlo-simulation of a rotationally symmetric flow for the MUDD Faraday cup. The thin grid wires above the impact grids were not included here.

Particle characteristics

For rocket studies, a payload can traverse orders of magnitude of characteristic length scales. The probe dimension compared to characteristic lengths such as the Debye length (λ_D) and mean free path (λ), determines the collection cross-section of a probe. However, even if one carefully use the correct probe theory and take all non-continuum flow effects into account, a significant error can still lie in the *assumptions of intrinsic parameters* of the observed particles.

In Paper I we present list of probable values of densities, surface energies, specific heats and latent heats of vaporization for smoke and ice particles, as well as their respective references. These values can differ by a factor up to a few, and certain parameters can moreover be temperature dependent. The uncertainty is lower for ice particles, as ice in all its normal forms (amorphous to hexagonal) have relatively similar characteristics. Although there is much research on meteoric analogues, there is still a large uncertainty in the MSP characteristica as their composition has not been determined unambiguously at the time of writing. The

problem is thus choosing the correct values. Consequently the thermodynamic calculations of meteoric dust have significant uncertainties.

Moreover, particles smaller than a few tens of nanometers have peculiar radiative properties. Thermal radiation peaks in the infrared part of the spectrum, at wavelengths much larger than typical grain sizes. Thus thermal re-radiation tend to deviate from Stefan-Boltzmann's law and sub-nanometer grains effectively do not radiate away heat (Rizk et al., 1991). Therefore, the size-dependent emissivity must be considered. Another factor which must be taken into account is the shape of the grains; certain molecular compositions are more probable to condense into long chain-like agglomerates, whiles other form spherical grains. The grain shape, as demonstrated below, can be parameterized as a factor in the drag force term. DeCarlo et al. (2004) and Saunders et al. (2010) found that this term varies from 1 to $\sim$ 1.6 for shapes typical for agglomerates and condensates. For the particles in the lower end of the size spectrum, the *nano-Kelvin effect* must also be considered, i.e. the curvature dependence of vapour pressure (Evans, 1993).

Modified equations for drag force and energy balance

If all intrinsic parameters of the nanoparticles were known with certainty, there is still an issue of understanding the collision process between neutrals and a grain. In practice, this means finding a good expression for the drag coefficient. The reason why this is non-trivial is that a typical grain is much smaller than the mean free path, but not necessarily small enough for Brownian effects to be important. As reviewed in Zuppardi et al. (2015), there are several models which can estimate the drag coefficient in such rarefied flows, however, there are many challenges with assigning corrections to continuum equations. Accordingly, the authors find that different existing models can in many cases disagree. There are also problems connected to surface interacations of both neutrals and aerosols with the rocket payload, which is discussed below.

For the calculation of the neutral drag on an aerosol in the works compiled in the present dissertation, we have utilized a collision model which assumes that neutral molecules interact specularly with a nanoparticle; i.e. they are reflected with the same angle as the incident. We have also assumed that a single dust particle cannot modify the density or velocity distribution of neutrals, and take the neutral velocity distribution to be Maxwellian. We also assume that the aerosol mass is much greater than 29 atomic mass units (AMU) which is the mean neu-

tral mass. The combination of these assumptions yields a model which is mathematically similar to those of Baines et al. (1965) and Smirnov et al. (2007); the latter work used the same model for neutral-dust interaction in calculations of the movement of nanodust in a fusion device.

We highlight the important physical considerations connected to our neutral drag term in the following (in spherical coordinates; (r, θ, ϕ)). We let the neutral thermal speed be defined by $v_{th}^2 = 2k_B T_N/m_N$, where m_N is the molecular mass of the neutral gas. The probability of a neutral molecule having a speed exactly within $v + \mathrm{d}v$ along the direction perpendicular to the polar direction is then, from Maxwell-Boltzmann's distribution:

$$p(v, v + \mathrm{d}v) = \frac{1}{v_{th}\sqrt{\pi}} \exp\left[\left(-\frac{v}{v_{th}}\right)^2\right] \mathrm{d}v \tag{3.1}$$

If we furthermore let $\mathbf{u}$, with $||\mathbf{u}|| = u$ be the velocity of the nanoparticle (assumed to be spherical), the momentum transferred to a surface element $\mathrm{d}A$ per unit time due to neutrals with speed v can easily be calculated as:

$$2m_N n_N \frac{1}{v_{th}\sqrt{\pi}} (v + u\cos\theta)^2 \exp\left[\left(-\frac{v}{v_{th}}\right)^2\right] \mathrm{d}v\mathrm{d}A \tag{3.2}$$

The drag force can then be obtained by integrating this contribution for all molecular speeds and all angles θ. The result is an expression which is valid for rarefied flows in both sub- and supersonic flow regimes (the latter is not covered by the normal Stokes' equation), and can be stated as:

$$\mathbf{F}_D = \chi\pi r_d^2 m_N n_N v_{th}(\mathbf{v}-\mathbf{u})\frac{1}{S}\left\{\frac{1}{\sqrt{\pi}}\left(S + \frac{1}{2S}\right)\exp(-S^2) + \left(1 + S^2 - \frac{1}{4S^2}\right)\mathrm{erf}(S)\right\} \tag{3.3}$$

where χ is the shape factor defined as the ratio between the drag of a volume equivalent sphere of a non-spherical particle and a spherical particle. The parameter $S = ||\mathbf{v} - \mathbf{u}||/v_{th}$ contains the relative speed, and $\mathrm{erf}(S)$ denotes the error function of the relative speed. This expression for the drag force self-consistently contains the drag coefficient, and the expression in the bracket is accordingly $2\sqrt{(\pi)}C_D$ for specular reflection (where C_D is the drag coefficient).

For the *energy balance*, we add to the assumptions that molecules leaving the dust grain surface does so diffusively, i.e. they have a three dimensional velocity distribution. Fundamentally, the energy balance – here used as analogous to the

heat balance – is the temporal evolution of the dust grain enthalpy, H_d. In terms of intrinsic properties of the grain we have:

$$\frac{\mathrm{d}H_d}{\mathrm{d}t} = P_H - P_C = m_d c_p \frac{\mathrm{d}T_d}{\mathrm{d}t} + L_d \frac{\mathrm{d}m_d}{\mathrm{d}t} \tag{3.4}$$

where m_d, T_d and L_d are the mass, temperature and latent heat of evaporation (no melting and grain deformation due to large temperature gradients) of the grain. The specific heat is denoted by c_p. P_H and P_C are the heating and cooling powers of the grain, respectively. We furthermore make the assumption that a nanoscale grain re-radiates poorly in the infrared part of the spectrum, thus grain cooling will only happen through surface molecules being emitted (Rizk et al., 1991). The temperature difference between a mesospheric aerosol and neutrals have been found to increase with grain size (Grams and Fiocco, 1977; Eidhammer and Havnes, 2001). The heating power will be dominated by the neutral-grain collisions. To find the contribution from this series of binary interactions, we average the flux of kinetic energy of neutrals to the grain, over their velocity distribution. If we assume that the neutral molecules have a Maxwellian velocity distribution, it can be shown that the heating power becomes (Allen et al. (2000); Smirnov et al. (2007)):

$$P_H = \pi r_d^2 n_N v_{th} k_B T_N \left\{ \frac{1}{2\sqrt{\pi}} \left[5 + 2S^2\right] \exp(-S^2) + \frac{1}{4S} \left[3 + 12S^2 + 4S^4\right] \mathrm{erf}(S) \right\} \tag{3.5}$$

where T_N is the neutral temperature. In our calculations we solve the simultaneous equations for energy balance and temporal evolution of grain radius and temperature. Example simulations for an open and a closed Faraday cup are shown below.

Adverse and poorly understood effects

In most codes for Monte Carlo simulation of rarefied gas flows, the default assumption is that surface interactions are fully diffusive; without a specular bias. According to Zuppardi et al. (2015) and references therein, this assumption is not valid in all cases. If a smooth surface has been exposed to ultra-high vacuum for a long time, the surface has a high temperature compared to its surroundings, the probe material has significantly higher molecular mass than the neutral gas or the translational energy of the neutral molecule is larger than several eV, the assumption must be reviewed. For rocket soundings, a large variety in parameters such as impact energy of the impinging molecules, surface temperature, material

and roughness of the surface can be encountered. Thus, some caution should be taken when using neutral gas flow simulations inside and around rocket instruments.

There is also some uncertainty connected to the interaction of the mesospheric aerosols with probe surfaces. In Papers I and II of this dissertation, the argumentation is used that for certain geometries and parameters, larger ice particles tend to fragment and what is recorded on the bottom detector plate is dominated by MSPs. However, particles of different materials may interact differently with the surfaces inside probes and uncertainties are naturally connected to this. A large part of this uncertainty is connected to the secondary charge production mechanism inside probes, which is not properly understood. This concept is discussed in section 3.2. As is presented there, one can control for secondary charge production by comparing the currents of the impact Faraday cup MUDD and classical Faraday cup DUSTY.

In addition to the complex aerodynamical environment around a rocket probe and the challenges arising in the characterization of it, one must also consider the electric potential structure around the payload. Aerosols readily become charged, and particles with low energy can easily be dictated by potentials as low as on the order of 1 V. A payload can be charged by direct collection of plasma, but also secondarily charged by dust grains rubbing off electron from the metal chassis of the payload body. The payload can then become positive. There are however few reliable methods to measure the payload potential, and the calibration process in such a measurement can be complicated. One method which have been shown to be reliable at altitudes above 90 km, is using the needle Langmuir probes (mNLP, University of Oslo) which were flown on both MXD payloads. Figure 3.2 shows the floating potential of the payload derived from the mNLP experiment. Above 90 km, the floating potential was situated at around -2.5 V on the upleg and around -3 V on the downleg. This indicates that the lowest biased probe (at 3 V) was likely not in the saturation region, and the absolute values of electron density derived inside the cloud layer are not reliable. The mNLP theory uses OML theory (see e.g. Jacobsen et al. (2010)) to calculate n_e, and therefore assumes a collisionless sheath, which is probably not the case at altitudes below 90 km for MXD, where the mean free path of neutrals is relatively short. Moreover, the strong positive values at altitudues below $\sim$ 90 km can also be overestimated (Priv. Comm. Andres Spicher).

From this brief discussion, it is evident that a thorough characterization of the aerodynamical and electrostatic environment outside and inside rocket probes

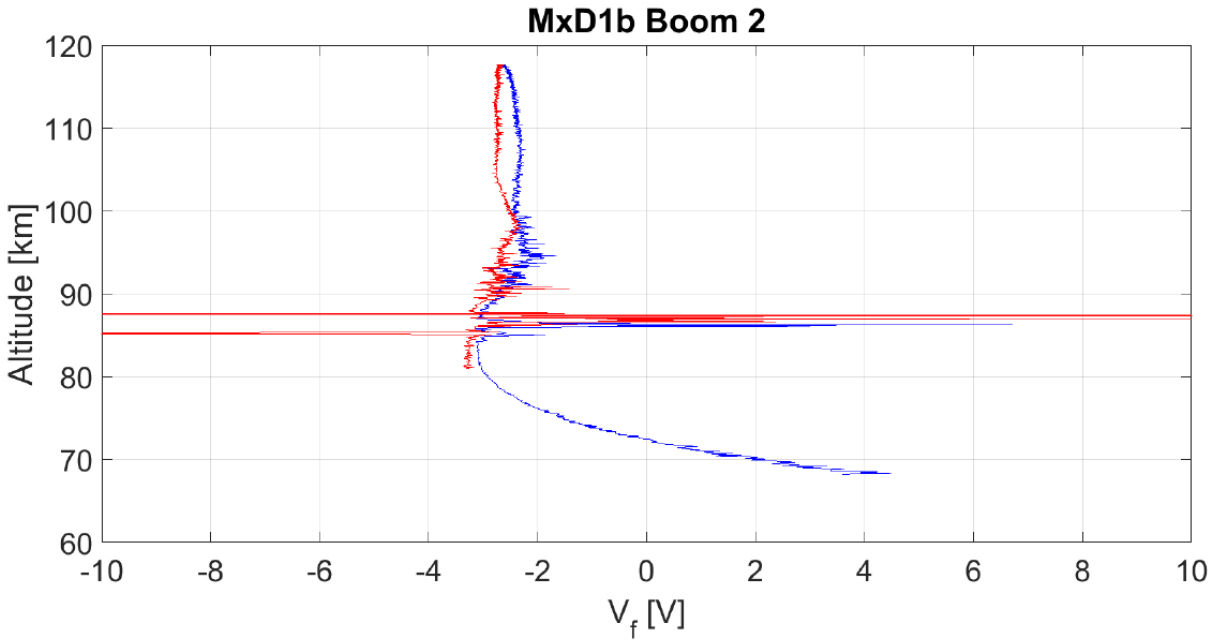

Figure 3.2: Floating potential of the MXD-1B payload derived from measurements by the multi-Needle Langmuir Probe experiment (University of Oslo). Courtesy of Andres Spicher, UiO.

must be done in order to correctly interpret the recorded signals. Paper III points on a special case during MXD-1B in which such considerations become highly important.

3.2 Interaction Between Aerosols and Rocket Probe Surfaces

Due to the probable plethora of different compositions and structures of mesospheric nanoparticles, the assumption that all particles are detected at equal rates is a questionable. The most important separation is between particles mainly consisting of ice and particles of meteoric material. Different work functions and affinity for charge transfer, among other intrinsic differences, makes the detection of these two particle types almost fundamentally different – even though the charge transfer mechanism may the same.

Impact Charging

Some of the main results of the present work is dependent on an understanding, or thorough characterization of, the charging process that takes place during a collision between a mesospheric aerosol and the surfaces of a probe. The word *during* here is key, as the collision cannot be generalized into an impulsive binary interaction. Amorphous aerosols generally have a certain degree of plasticity, and particles deform and fragment during a collision. It is difficult to generalize simple results to nanoscale particle-surface interaction.

The impact charging of micrometeorites and micrometre-sized dust grains have been studied in laboratories since the 1960s. For several years, the charge production was thought to not change significantly within a large range of velocities and particle masses, however, this is found to not be the case for collisions of either very high or very low interaction energy (Friichtenicht, 1964; Adams and Smith, 1971; John et al., 1980). In figure 3.3 we show the results from a laboratory experiment where iron particles were accelerated towards an iridium target with a large range of initial speeds. It can clearly be decided that the q/m vs. speed-relationship is non-linear. Importantly, the bouncing charge transfer mechanism for low velocity/small particle collisions ($< 1000\ \mathrm{ms}^{-1}$, $\lesssim 10$ nm) is not well understood, and few experiments have the capability to inquire about the particle energies relevant for mesospheric aerosols (Kuuluvainen et al., 2013). In energetic collisions, a cloud of plasma is formed upon interaction and charges are recollected partially or completely by the surface. The charging mechanism relevant for a typical mesospheric aerosol grazing a surface on the inside of a rocket probe is poorly represented by such a picture; it is rather likely a nanoscale analogue to triboelectric charging. To our knowledge, the triboelectic effect has only

been investigated in-depth for large – on the order of several micrometres – particles with low impact energies (Kuuluvainen et al., 2016).

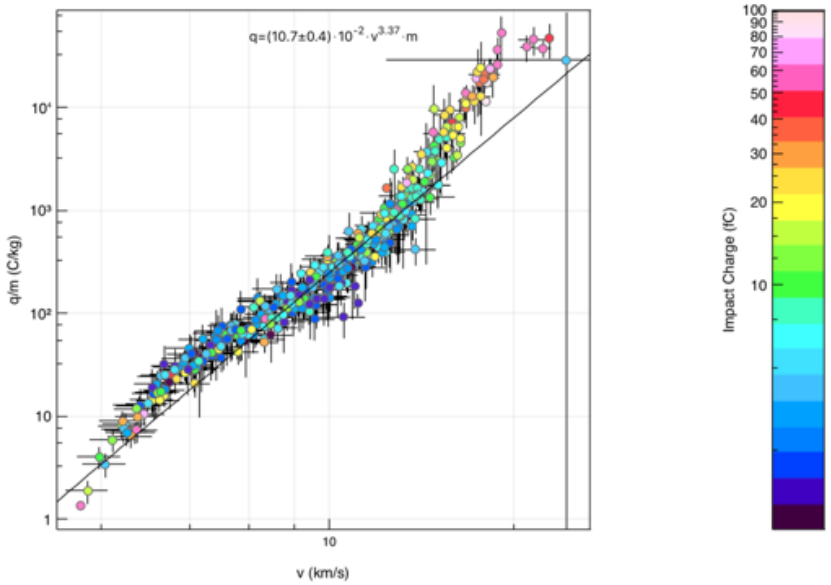

Figure 3.3: Log-Log presentation of laboratory measurements from dust accelerator experiments of iron particles on an iridium target (common for probe calibration) showing generated charge per mass compared to impact velocity. The relationship is clearly not linear. Courtesy of Dr. Zoltan Sternovsky, LASP.

John et al. (1980) derived a simple model for contact charging between a spherical grain and a smooth surface. It was later pointed out by Bailey (1984) that the grazing happening in inclined collisions affected the efficiency of the charge transfer. The general result for a particle of some elasticity, contact area A, "effective" separation between surface and particle d, and electrical capacity $C = \epsilon_0 A d$ the charge generated on contact can be written

$$Q_c = CV_c\left(1 - \mathrm{e}^{-\Delta t/\tau}\right) \tag{3.6}$$

$$= \frac{\epsilon_0 V_c}{d}\left[\frac{5}{4}\pi^2\rho_d v^2(k + k_s)\right]^{\frac{2}{5}} r_d^2\left((1 - \mathrm{e}^{-\Delta t/\tau}\right) \tag{3.7}$$

where V_c is the contact potential between the surface and particle and Δt and τ are the contact and relaxation times respectively. The expression in the square brackets describes the elastic response of the particle. For a conducting particle, $\Delta t/\tau \to 0$, and the relaxing term will vanish:

$$Q_c = \frac{\epsilon_0 V_c}{d}\left[\frac{5}{4}\pi^2\rho_d(k + k_s)\right]^{\frac{2}{5}} v^{4/5} r_d^2 \tag{3.8}$$

that is a charging probability proportional to particle cross-section. For insulating particles, the interaction time is much smaller than the relaxation, and thus $\tau/\Delta t \to 0$. It follows that the contact charge approaches $Q_c = CV_c\Delta t/\tau$. Since the relaxation time is given as the product of the permittivity times the resistivity of the material, $\tau = \epsilon\rho_R$ in which $[\rho_R] = \Omega \times m$, it can be shown dimensionally that the contact charging for insulating materials must become proportional to the particle volume:

$$Q_c \propto v^{3/5} r_d^3. \tag{3.9}$$

One immediate questions arise regarding the applicability of the results above: Is the ideal model for contact charging representable for rocket probes? This question provides motivation for the next section.

Secondary Charging Effects in Rocket Probes

The answer to the question posted above is probably not a straight yes or no. The equations presented are valid for homogeneous particles of sizes orders of magnitude larger than a typical mesospheric nanoparticle, which is arguably too ideal of a description for mesospheric aerosols. The lack of large scale crystalinity (amorphous state) and size dependent emissivity and dielectric properties may influence the affinity of a particle to absorb or release an electron.

Throughout this work, we use the term *secondary charge* when describing certain signatures in rocket probe currents. Contrary to primary charge, which is the charge delivered directly to a detector by charged aerosols (or unshielded electrons and ions), the secondary charge can be understood as the transfer of electrons *from* payload surfaces or inner parts of a probe to aerosols or fragments of aerosols. In a fragmentation process, the secondary yield per particle can be as large as 100 elementary charges, which will heavily affect or even dominate probe currents (Havnes and Næsheim, 2007; Amyx et al., 2008; Havnes et al., 2009; Kassa et al., 2012).

There is currently no consensus on what the exact mechanism and connection to classical contact charging is. The main candidate is that aerosols grazing on metal surfaces get charged in a triboelectric fashion which involves adheshion on the nanoscale. In a series of experiments with ice particles of sizes down to a few nanometres, it was found that particles colliding with gold and graphite surfaces fragmented at impact speeds comparable to those of sounding rockets (Andersson et al., 1997; Markovic et al., 1999; Tomsic et al., 2000, 2001). Tomsic et al. (2003) reported that pure ice particle of sizes larger than 6-7 nm had

a certain probability of carrying away a charge of $-1e$ for grazing impacts. The probability was found to be strongly dependent on impact angle, with a maximum around 80°. The charging for nanoscale ice was found to be proportional to r_{ice}^2 – which is not consistent with the contact charging results above. From earlier measurement, Vostrikov and Dubov (1991) had already found that approximately 1 in 10000 ice clusters of radius $\sim$ 2 nm were charged in impact at relatively low speeds. There are few similar experiments which go into the same depth as the ice experiments for nanoscale metal particles impacting at low speeds. The charging probability is therefore still an open question; In Paper II we utilized $Q \propto r_d^2$ and $Q \propto r_d^3$ when calculating the size distribution of collision fragments.

Although the theoretical aspects of the nano-triboelectric effect in rocket probes are somewhat unclear, there are empirical results which can be used to obtain a heuristic understanding of the process. Havnes and Næsheim (2007) was the first to recognize the importance of secondary charging effects in rocket probes. They concluded that the presence of MSPs inside mesospheric ice would alter the impact charging properties. Later works corroborated on that the secondary effect could be utilized to inquire about intrinsic properties of mesospheric aerosols – i.e. the effect is not necessarily only adverse (Havnes et al., 2009; Kassa et al., 2012). In Paper IV, the imperically obtained secondary charge yield is used to estimate the sizes of aerosols measured in DUSTY. As discussed in section 4.1, the MUDD probe is designed in such a way that it maximizes the secondary charge yield. This allows for detection of MSPs embedded in ice particles and can furthermore be used as a control of DUSTY measurements.

Chapter 4

The MAXIDUSTY Sounding Rocket Project

The MAXIDUSTY sounding rocket project (MXD) was initiated in 2012 by principal investigator Ove Havnes, with the aim to make detailed in-situ measurements of the Earth's polar mesosphere. The project comprised two sounding rocket launches, from hereon referred to as MXD-1 and MXD-1B. The two rockets had identical core payloads, based on dust detectors from UiT and accompanying electron density probes from the University of Oslo and TU Graz. MXD-1 and MXD-1B were launched from Andøya Space Center (69.29°N, 16.02°E) at 09:43 UT on 30 June 2016 and 13:01 UT on 8 July 2016, respectively. In Table 4.1, we present an overview of all instruments included on the MXD payloads. The UiT instruments, all relying on direct influx of dusty plasma, occupied the majority of the top deck of which the geometry is described in detail below. Apart from the 4D Space Module, which suffered from a malfunction during accerelation phase, all instruments returned data. Moreover, the main detector plate of the miniMass dust spectrometer was influenced by photoelectrons, and unambiguous results are difficult to extract from the data. The campagin ran with continuous radar support from the 53.5 MHz MAARSY radar (PI Ralph Latteck, IAP Kühlungsborn; see Latteck et al. (2012)) and the RMR-lidar at the ALOMAR observatory (see e.g. Von Zahn et al. (2000); Baumgarten et al. (2010); Fiedler et al. (2017)). These remote measurements were instrumental in the pre-launch phase for the launch decision.

The top deck geometry of the second payload, MXD-1B, is shown in Figure 4.1. The layout on the 1B-payload was almost identical to that of MXD-1, apart from the CU Boulder dust mass spectrometer miniMASS replacing DUSTY-2 (which is labelled in the sketch). Acronyms for the instruments are listed in Table 4.1, where the SRADS (Sounding Rocket Attitude Detection System) sun sensors cor-

Table 4.1: Instruments launched during the MAXIDUSTY campaign. The listed references present the instrument designs and/or theory applied to derive the corresponding plasma parameter.

	Instrument	Measured Parameter(s)	Owner†	Concept Reference
MXD-1	1 x DUSTY	Dust charge number density	UiT	Havnes et al. (1996)
	3 x Multiple Dust Detector (MUDD)	Primary/secondary ice/MSP current	UiT	Antonsen and Havnes (2015)
	Identification of the Content of NLC particles (ICON)	Neutral mass spectra of aerosol vapour	UiT	Havnes et al. (2015)
	Multiple Needle Langmuir Probes (mNLP)	Electron density	UiO	Jacobsen et al. (2010)
	Faraday Wave Propagation	Electron density	TUG	Jacobsen and Friedrich (1979)
	Positive Ion Probe (PIP)	Ion density	TUG	Blix et al. (1990)
	Capacitance Probe (CP)	Relative electron density	TUG	
	Attitude Monitoring (SRADS)	Attitude	UiO	Bekkeng (2007)
	Mesospheric Aerosol Sampling Spectrometer (miniMASS)	Aerosol/Ion mass spectra	CUB	Robertson et al. (2009)
	Side-looking NLC photometer	Optical scattering at 220 nm	SU	Gumbel and Witt (2001)
MXD-1B	2 x DUSTY	”	”	”
	3 x Multiple Dust Detector (MUDD)	”	”	”
	Identification of the Content of NLC particles (ICON)	„	”	”
	Multiple Needle Langmuir Probes (mNLP)	„	”	”
	Faraday Wave Propagation	”	”	”
	Positive Ion Probe (PIP)	”	”	”
	Capacitance Probe (CP)	”	”	”
	Attitude Monitoring (SRADS)	”	”	”
	Mini Fluxgate Magnetometer (MFM)	Magnetic field strength/orientation	UA	Miles et al. (2016)
	4D Module – Daughter Payloads	Electron density, magnetic field	ASC/UiO	

† UiO – University of Oslo, TUG – Techical University Graz, CUB – University of Colorado Boulder/LASP, SU – Stockholm University/MISU, UA – University of Alberta, ASC – Andøya Space Center

responds to 'DSS' shown in the figure. The MXD top deck layout presents a few important 'firsts' in the field of in-situ studies of the mesopause;

MXD-1B has two mechanically and electrically identically DUSTY Faraday buckets with an interspacing of $\sim$ 10 cm centre to centre. This is shorter than the characteristic dimension of the payload ram pressure bow shock, which is proportional to the top ram direction cross section diameter – $\propto d_{ram} \sim 35$ cm. This allows for rapid measurement of horizontal scales shorter than what to our knowledge has been done earlier. These measurements have the potential to reveal much information about the orientation of the smallest dust structures, comparable in size to the Bragg-scales of UHF coherent echoes. In addition, the small-scale horizontal measurements are extremely useful in quantifying the importance of adverse aerodynamic flow effects for direct influx dust probes. Preliminary results from MXD-1B show that the recorded currents of incoming dust was strongly varying between the two probes. This can probably be interpreted in that way, that aerodynamic adverse effects play a more important role than expected, at heights close to the mesopause. Moreover, it shows that aerodynamic effects can cause virtual horizontal density variations which can be, and probably have been in the past, interpreted as real 'transient' dusty plasma structures. This point forms the basis of Paper III, and is furthermore introduced in greater detail in section 6.

The MXD payloads also included the first high resolution sweeping neutral mass spectrometer (ICON) to probe the Earth's upper atmosphere. The ICON instrument is presented in section 4.1.

The triplet of MUDD Faraday impact cups on the two payloads allowed for the first measurement of the mesospheric ice particle fragment size distribution. As argued in in Paper I and Paper II, the fragment size distribution is probably directly related to the size distribution of MSPs embedded in ice particles. MSPs are also found in the latter of these two papers to be abundant inside ice particles as predicted by Havnes and Næsheim (2007).

A render of the assembled MXD-1 payload is shown in figure 4.2, below. A photo of the flight ready MXD-1B top deck is also shown in figure 4.3.

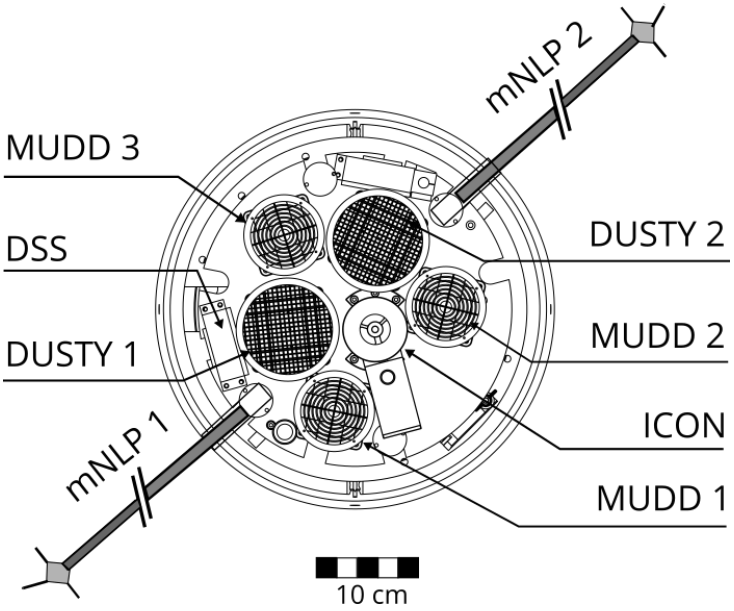

Figure 4.1: Top deck layout on the second MAXIDUSTY payload. The MUDD and DUSTY probes are the Faraday buckets from UiT. The first payload was mechanically similar but with one of the DUSTY probes replaced with the UC Boulder miniMASS. Reproduced from Antonsen et al. 2018 (Paper III), ©Copernicus.

Figure 4.2: Photorender of the MXD-1 payload with all instruments mounted. The additional yellow antennae are the Faraday rotation expertiment, while the spherical probe booms are PIP and capacitance probes.

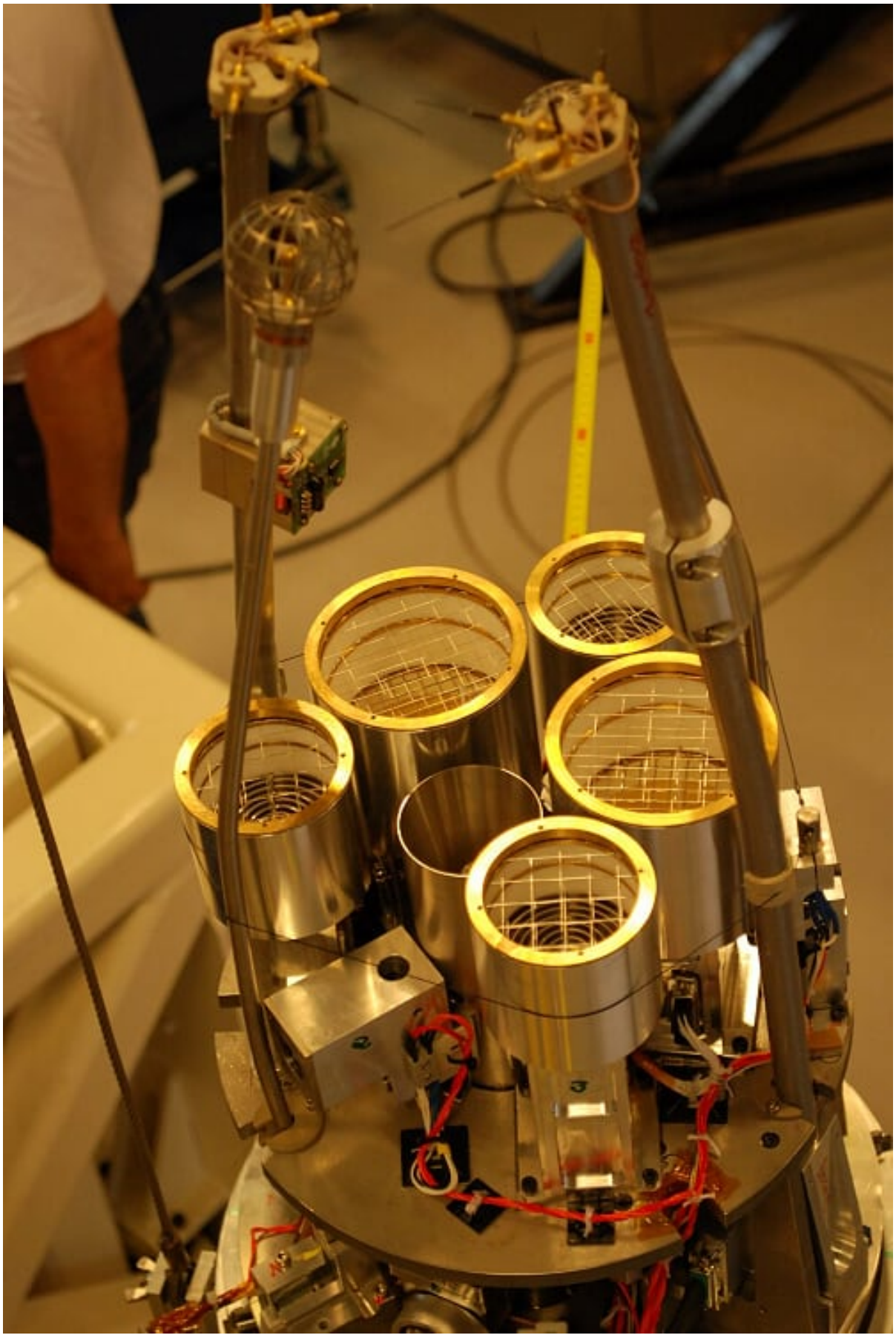

Figure 4.3: Photo of the MXD-1B topdeck displaying all Faraday cups, ICON, mNLP booms, PIP and Capacitance booms and Faraday antennae. Courtesy of Sveinung Olsen, UiT.

4.1 Instrument Principles, Design and Development

DUSTY

The DUSTY probe is fundamentally a Faraday cup – traditionally used to detect free ions and electrons in a vacuum. By choosing suitable biases on a set of detector and deflector grids, the probe can be made to detect particles in a certain energy range. By altering the grid biases, one alters the detection limits, and the probe essentially becomes a spectrometer since high biases will shield particles with low energy and vice versa. Introduced by Havnes et al. (1996), the DUSTY probe produced the first in-situ measurements of charged dust in the Earth's mesosphere. The design has through many sounding rocket flights through the last couple of decades proven to be a reliable way to measure the number charge density of dust, and the basic design has changed relatively little throughout this time.

A cross-section of the DUSTY probe with its grid biases is shown in Fig. 4.4. We show the principle of current generation in DUSTY in figure 4.5. The top grid is biased at the payload potential in order to shield neighboring probes from internal electric fields. The grid G1 is biased at +6.2 V, such that ambient ions (of energies on the order of ~ 0.01 eV) will not be able to penetrate. Ambient thermal electrons will be absorbed. The G1-potential is such that even with a few volts of payload charge due to secondary charging during upleg, ambient plasma particles are shielded effectively. The G2-grid was originally intended to absorb secondary electrons ejected from the bottomplate (BP), to correct for this loss in the derivation of the dust charge number density (Havnes et al., 1996; Havnes and Næsheim, 2007). From the first observations and theoretical considerations, however, the secondary production at G2 was found to be the dominating secondary charge source and no detectable secondary charge production takes place at BP. As it turns out, this finding facilitates the utilization of DUSTY to measure dust sizes and absolute number densities of dust particles; which is the main topic of Paper IV.

As discussed in the previous chapter, both pure ice and meteoric particles of sizes $\lesssim 1-2$ nm are influenced by air flow around the probe (see e.g. Hedin et al. (2007); Antonsen and Havnes (2015); Asmus et al. (2017) for recent works discussing this). For the DUSTY measurements on MAXIDUSTY, we have therefore assumed that these particles contribute little to the total dust number density.

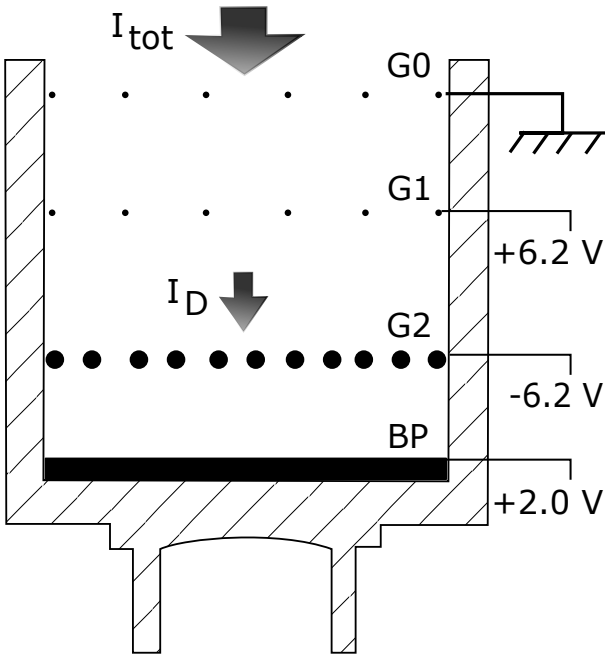

Figure 4.4: Cross section of the DUSTY probe as launched on the MXD payloads. The upper grid is payload ground intended to shield neighboring probes from internal electric fields. The Grids G1 and G2 and the bottom plate (BP) have potentials optimized to shield ambient plasma and detect mesospheric dust and ice particles.The wire thickness is exaggerated there for convenience, and we also note that the G2 wires are thicker that the G1 and shielding grid wires.

This assumption is also justified by the notion that very small particles can be neutralized effectively by photodetachment during sunlit conditions, as demonstrated in the calculations in chapter 2.3. Including the secondary current (I_{sec}, in the following), the currents to grid G2 and BP due to dust particles can be expressed as:

$$I_{G2} = \sigma I_D + I_{\text{sec}} \tag{4.1}$$
$$I_{BP} = (1 - \sigma) I_D - I_{\text{sec}} \tag{4.2}$$

where I_D is the current between G1 and G2 as shown in Fig. 4.4, and $\sigma = 0.235$ is the effective area factor of G2. We can furthermore express I_D in terms of the dust charge density $N_d Z_d$ accordingly:

$$I_D = (1 - \alpha) N_d Z_d e v_R \pi R_p^2 \cos\gamma \tag{4.3}$$

where v_R is the rocket speed, e the elementary charge, R_p is the probe radius, γ is

the coning angle and $\alpha = 0.08$ is the fraction of the probe area covered/shadowed by G1 and G0. Here we have neglected any secondary production of charge at G1, which is justified by that the effective area of G1 is only 4.6 %, which gives a secondary production area of 1.3 % of the total area; around five times smaller than that of G2. We note however, that the iteration procedure introduced in Paper IV takes into account the G1 secondary production. It has been found from laboratory measurements that the contribution of secondary currents to G2 is positive during the first few minutes of exposure to ice particles, meaning that dust particles rub off electrons from grid wires in a triboelectric fashion (Tomsic, 2001). This effect requires a grazing angle of around 80 to 85 degrees to be maximized, if the particles are pure ice (Tomsic, 2001). Note also, that combining equations (4.1) and (4.2) yields $I_D = I_{G2} + I_{BP}$, as expected.

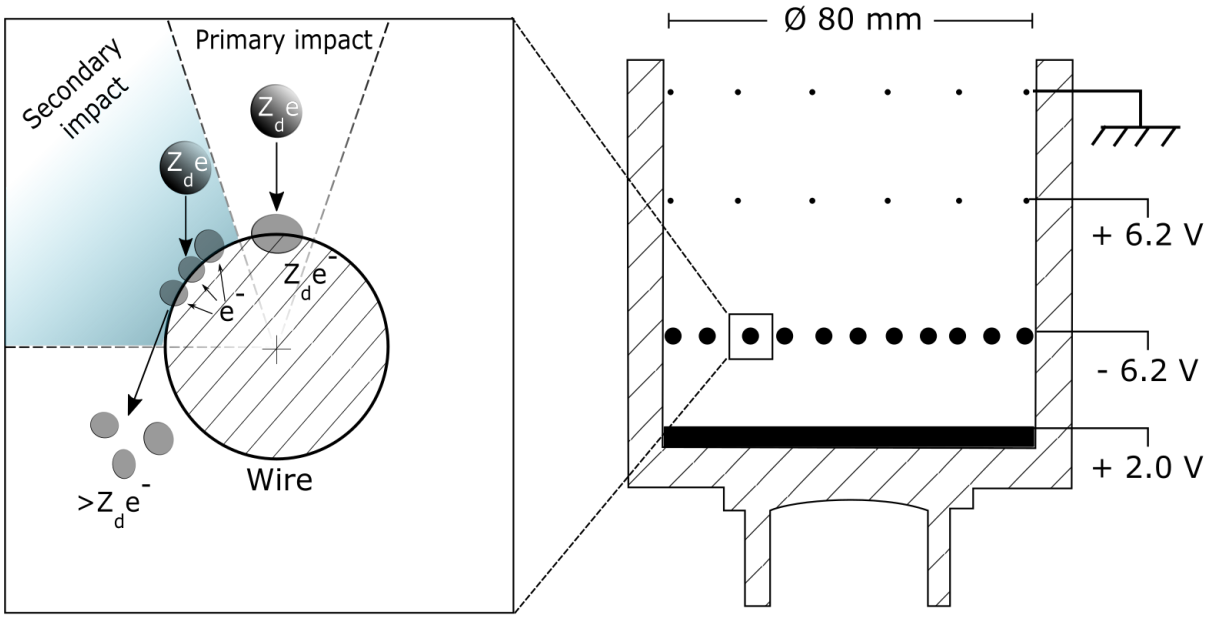

Figure 4.5: Principle sketch of large, order of 10 nm, particles entering DUSTY as launched on the MAXIDUSTY payloads. The mechanism can be described as follows: (1) A large particle deposits its charge in a primary impact and is partly fragmented, (2) If the impact is grazing, fragments can steal electrons from the grid wire. For large particles, the fragments tend to take away more electrons from the wires than the incoming charge and the net current to G2 becomes positive. For small particles, the primary charge is usually larger than the fragment current, and the net current to G2 thus becomes negative. In both cases, the bottom plate current becomes negative. We note that the secondary impact area region is exaggerated here; the true secondary charge producing area is $\gtrsim 20\%$. Adapted from Paper III, Copyright © Copernicus.

MUDD

The *MUltiple Dust Detector* – MUDD – is an impact Faraday cup with two grids biased at stationary voltages and a bottom plate detector stepping between different voltage biases sequentially. The term *impact* here refers to the mechanism which takes place on a special impact grid (G2), which is constructed in such a way that all incoming aerosols will collide with it. A sketch of MUDD with grid labelling is shown in figure 4.6.

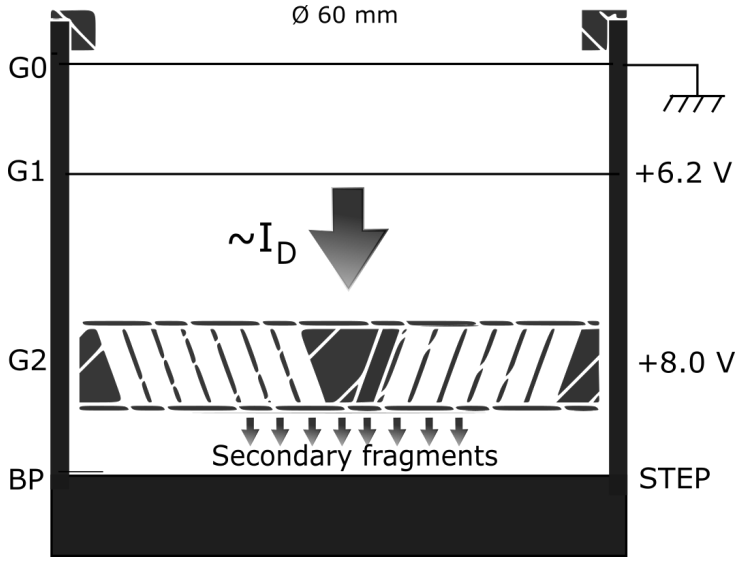

Figure 4.6: Cross section of the MUDD probe as launched during MXD. The current above G2 is analogous to the current I_D in Fig. 4.4, only with a difference due to different collecting areas. The G2 grid consist of overlapping concentric rings which implies that all primary particles hit a surface there. The G0, G1, and G2 grids have constant biases, while BP steps between different voltages every 192 samples ($F_s = 8680$ Hz) to produce the retarding potentials for detection of particles of different sizes. A single MUDD probe has three unique voltage modes and one mode that overlaps with one of the other probes for comparison and calibration. A triplet of three MUDD probes can produce a 10-point size distribution of fragments/MSPs with a height resolution of $\sim$ 100 m.

For MUDD on the MXD payloads, the G0 and G1 grids were constructed from .25 mm silver wire; in total 10 wires with five and five crossing each other perpendicularly, constituded one grid. The cross-section of these uppermost grids was 0.046 times the full cross-section of the probe. As illustrated in the principle sketch, G0 only acts as a shielding grid and is connected to payload ground and current to it is not recorded. G1 was biased at +6.2 V to shield ambient plasma. Currents were measured at G1, G2 and BP, with a noise level on the order of 1 pA for G2 and BP and an order of magnitude higher for G1 (due to amplification).

The G2 grid is what separates MUDD from a traditional Faraday cup, and the

reason why the probe is referred to as *an impact Faraday cup*. It is constructed from a number of concentric stainless steel rings with an interspacing such that no free through flux can occur[1]. The conclusion from experimental studies of nanoscale ice particles colliding on graphite and gold surfaces, is that large particles partly fragment even at low speed impacts with metal surfaces (see e.g. the works compiled in Tomsic (2001)). At an inclination of $\sim 75-85^{\circ}$, the secondary charge transfer – likely a triboelectric transfer of electrons from the grid to a ice particle fragment – is found to have a maximum. Ice particles of size 50 nm have been found from rocket measurements to produce on average $\sim 50-100$ charged fragments upon impact with the grids in Faraday cups (Havnes and Næsheim, 2007; Havnes et al., 2014; Antonsen et al., 2017). MUDD is designed to maximize, or rather guarantee, this secondary amplification of the particle current.

The bottom plate detector (BP) steps between four different voltages in order to separate fragments/particles of certain energies. On MXD-1 and MXD-1B, we combined three MUDDs with in total 10 unique BP voltages. In fact, we utilized 12 voltages of which two were overlapping in order to calibrate the probes respectively to each other in-flight. On MUDD-1 and MUDD-3, this overlapping channel had a positive bias two volts lower than that of G2, such that all particles, including possible leakage currents, were recorded. These channels are throughout the dissertation assumed to measure the total current of all incoming fragments. The stepping of the BP voltage was done every 192 samples, which with a 8680 Hz sampling rate implies that a 10-point (relative) size distribution of fragments and particles produced at G2 can be obtained at a height resolution on the order of ~ 10 m. A sketch of how the potentials step on each of the three MUDD probes flow on MXD-1 and 1B is shown in figure 4.7. As shown in Paper II, with filtering and processing, the final height distribution of fragments has a resolution of ~ 100 m.

Verification of the MUDD Secondary Currents

The secondary charging effect in MUDD can be utilized to obtain information about the volume content of MSPs inside larger ice particles – as was one of the main intentions of the design. To justify this claim, a disucssion of both theoretical and experimental inquiries is necessary. The conclusion from extended discussions on this reasoning in Paper I and II, is that the MUDD BP currents *are* indeed dominated by pure MSPs, and can furthermore be used to obtain the

[1] Very small particles *can* indeed in some cases follow the airflow and avoid direct collision with G2, but this is rarely applicable for the cases of interest in this dissertation

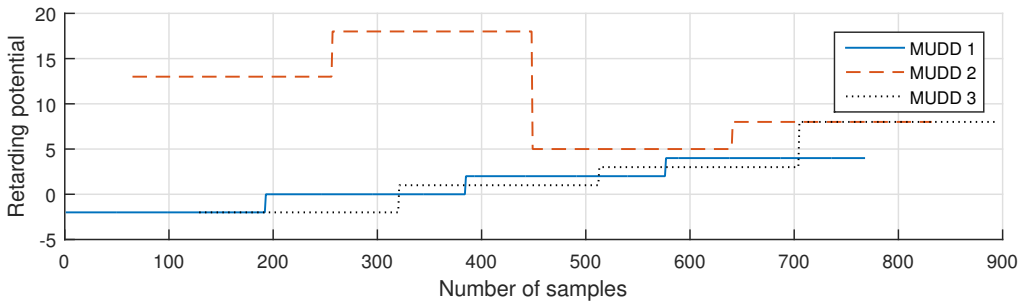

Figure 4.7: Stepping scheme of the different retarding potential modes for all MUDD probes. Note that the modes are slightly shifted in time relative to each other and the overlap between probes at retarding potentials −2 V and 8 V. The sampling frequency is 8,680 Hz, implying that a group of four steps, or 768 samples, takes ∼ 0.09 s to complete. From Paper I.

volume content. The key controlling parameter of the estimate of the volume content is the dependence of particle radius in the impactor charging probability. As shown in Paper II, the charging probability of pure MSPs is probably proportional to r_d^{-k} for k between 2 and 3, i.e. a proportionality between the cross-section and mass of the particle.

Above we claimed that a 50 nm dirty ice particle produces around 50 to 100 elementary charges at G2 which are subsequently recorded at BP. Another claim was that the charging probability, or rather the affinity to produce current, was propotional to the cross-section or mass of a particle. With the new method to derive sizes and densities of ice particles with Faraday cups presented in Paper IV, we can control these claims. We use the aerosol neutral density, N_d, and the ice particle radii, R_d, from the iteration of DUSTY data. The current produced at a grid, which is to say the effective collecting area is the probe cross-section, is as usual calculated as:

$$I = eN_d \pi R_P^2 v_R \eta_{50} \left(\frac{R_d}{50} \right)^{\alpha_C} \cdot \frac{1}{10^{-9}} \tag{4.4}$$

where e is the elementary charge, R_P is the probe radius, η_{50} is the reference number of elementary charges produced for a 50 nm particle and α_C is the proportionality exponent of the charging probability (i.e. $\alpha_C = 2$ for cross-section). To compare the secondary current in DUSTY to the true secondary current observed by MUDD, we let η_{50} be 50 elementary charges and α_C be 2. The densities and radii are estimated from DUSTY as shown in Paper IV. The resulting current is shown as a solid blue line in figure 4.8 while the true secondary currents are shown in red (MUDD 1) and orange (MUDD 3). The striking similarity reveals

a few important things: (1) The collision mechanisms producing secondary current is very similar in MUDD and DUSTY, (2) The method presented in Paper IV is justified, and (3) The assumed charging probability and reference secondary production factor fits well for the data shown here. As the critical reader will point out, there will be other (infinitely many) combinations of parameters which can produce the same plot. However, the present calculation should be regarded as highly plausible as it is based on the present knowledge about nanoscale ice particles and the reliable DUSTY probe.

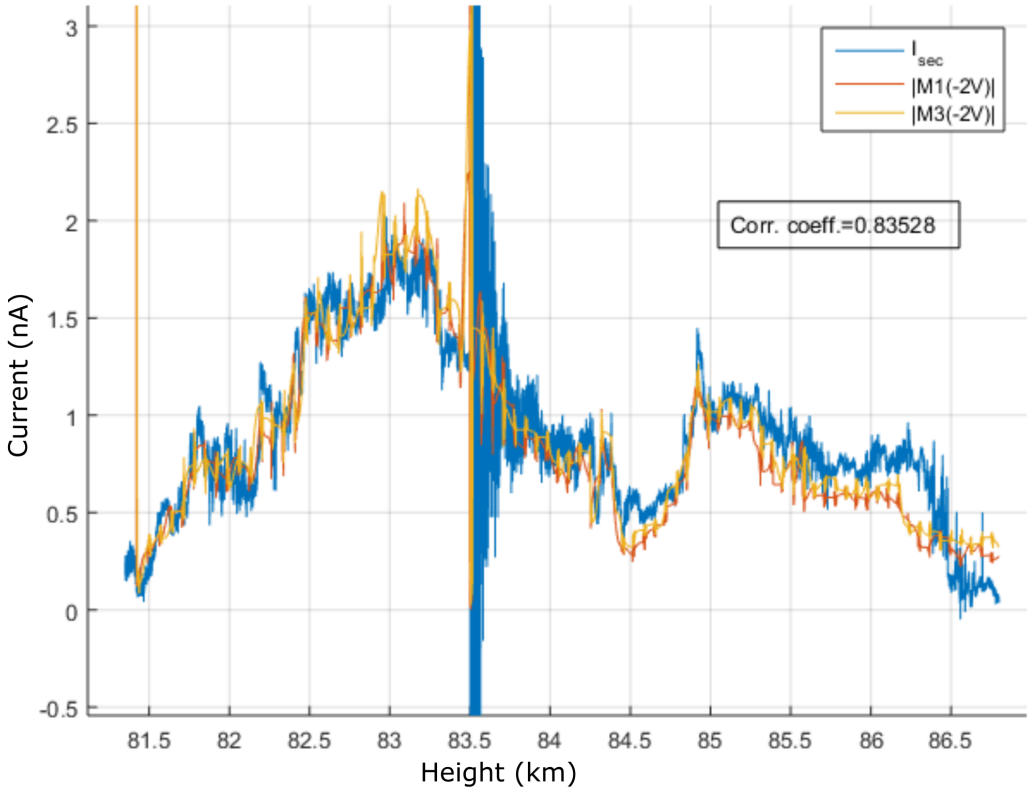

Figure 4.8: Test of the assumption that the secondary charging from ice particles at G2 in MUDD is proportional to cross-section, and that a 50 nm particle produces on average 50 elementary charges. The correlation is striking everywhere but at the very top of the cloud system.

Simulations of Particle Trajectories Around MUDD

Utilizing the theory outlined in section 3.1, we have developed a code which can be modified to calculate the trajectory of aerosols in any geometry in two or three dimensions. The code was used in Paper I to find the detection limits in MUDD and in Paper II to estimate the sizes of the particles producing current

to the bottom plate in MUDD. In the top panel of figure 4.9 we show an example simulation for a rotationally symmetric flow with zero instrument coning at an altitude of 70 km. The reason for this low altitude (lower than summer mesospheric clouds) is to study the possibility of detecting free aerosols (MSPs) with sizes below one nanometre with Faraday cups. As also mentioned in chapter 7 regarding future work, by using a modified *open* version of the MUDD, it is possible to detect free MSPs. In the example simulation shown below, all particles of sizes 0.5 nm are stopped in the upper part of the probe. For an open version of the probe (SPID = Smoke Particle Impact Detector), the detection efficiency improves dramatically.

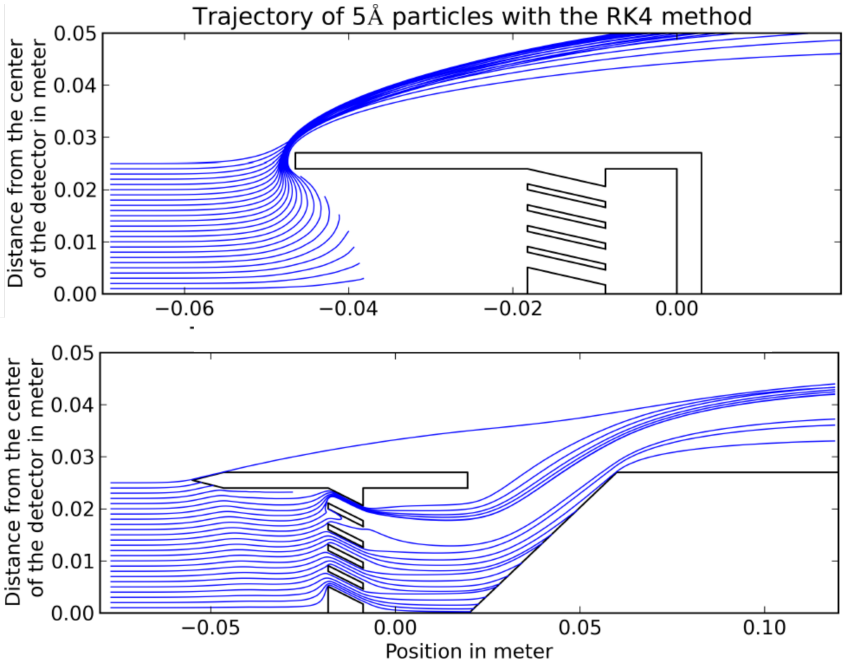

Figure 4.9: Comparison of particle flux to the closed MUDD probe (top panel) and open SPID probe (bottom panel) of 0.5 nm free neutral MSPs in the winter mesosphere at an altitude of 70 km.

ICON

As established above and proven by independent means of measurement, ice particles constituting noctilucent clouds contain meteoric smoke. In addition to molecules from smoke particles, metals such as Na, K and Fe from differential ablation of meteors are also present in their atomic form inside ice particles (Lübken and Höffner, 2004; Plane, 2004; She et al., 2006). In order to investigate whether or not the chemical composition of such atomic species and MSPs embedded in ice particles could be analyzed in-situ, the Tromsø-group have developed the Identification of the COntent of NLC particles probe (ICON); see e.g. Havnes et al. (2015). The ICON probe is the first instrument to employ a neutral quadrupole mass spectrometer for investigation of mesospheric aerosols.

Figure 4.10 shows a render and working principle of ICON. The funnel is utilized to focus and concentrate the inflowing NLC particles which are subsequently gathered and evaporated in front of the pinhole. The pinhole has an aperture of 75 micron and is kept shut by a springloaded valve until the payload is inside a cloud. A residual gas analyser (RGA) inside the ICON chamber has a mass resolution of 0.1 AMU, and can be operated in both sweeping mode and for single AMU measurement. During MAXIDUSTY, ICON was launched on both the MXD-1 and the MXD-1B payloads. On these flights, both probes were operated in a sweeping mode. ICON-1 was swept from 15 to 73 AMU in $\sim$ 4.3 seconds, and ICON-1B was swept from 15 to 56 AMU in $\sim$ 3.0 seconds. For both flights, the focusing potential was set to -15 V, while the ionizing source was calibrated to water at 70 eV and 2.0 mA current. An electron multiplier at 1.01 kV was used for amplification. With these operating parameters and a chamber pressure on the order of $10^{-7} - 10^{-5}$ mBar, the detection limit of a single AMU in terms of partial pressure was between 10^{-11} and 10^{-12} mBar. With these settings, the aim is to measure the water vapour from NLC particles and traces of meteoric material.

The ICON is a UHV system, and carefully balancing the operating parameters is necessary in order to detect the vanishingly low concentrations of atoms from meteoric ablation. For the RGA to function with best possible dection limit, the pressure must be low, however not too low as that would render the meteoric atoms and molecules undetectable. For ICON, the ideal stand-by pressure is $\sim 10^{-7}$ mBar. Traditionally, ion spectrometers have been combined with cryogenic pumps to keep low enough background pressure (see e.g. Schulte and Arnold (1992)), but as such systems are complicated to maintain and run and relatively expensive ICON uses an ion getter pump. The ion pumps require high voltage on

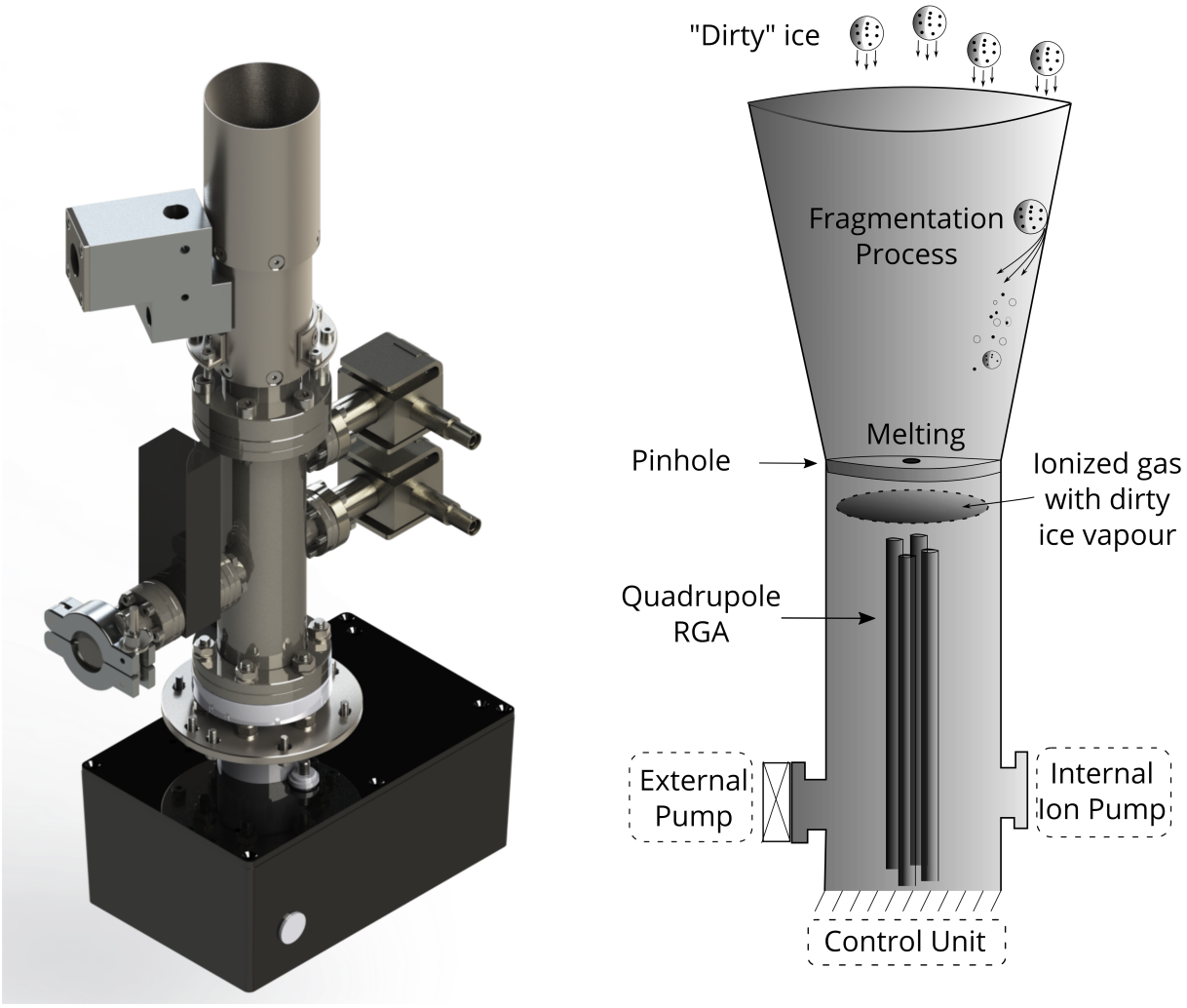

Figure 4.10: Principle sketch and rendered image of the ICON probe as flown during the MXD campaign. Due to the RGA requiring a low working pressure of $\lesssim 10^{-3}$ mBar, the probe has both internal and external pumping ports. All flanges utilize copper gaskets, except the mounting flange for the funnel, where Viton gaskets were used. Despite this, the ultimate pressure of the system was on the order of 10^{-7} mBar.

the order of 1000 V, but are small and easy to install. Moreover, ion pumps can measure the pressure of a chamber as their current is directly proportional to the number density of neutrals. In figure 4.11 we show a comparison of the pressure profiles measured with a Pirani gauge at different ambient pressures, simulating the pressure in front of the ICON pinhole at different altitudes. Combining these profiles yield a detailed picture of how the background pressure inside ICON develops during operation which is necessary for later analysis of MXD data. Importantly, the pressure remains well below a level where the collisional length becomes too short. Note that for these tests, the initial pressure *inside* ICON is not very defining for the characteristic rise time of the pressure due to the logarithmic scaling.

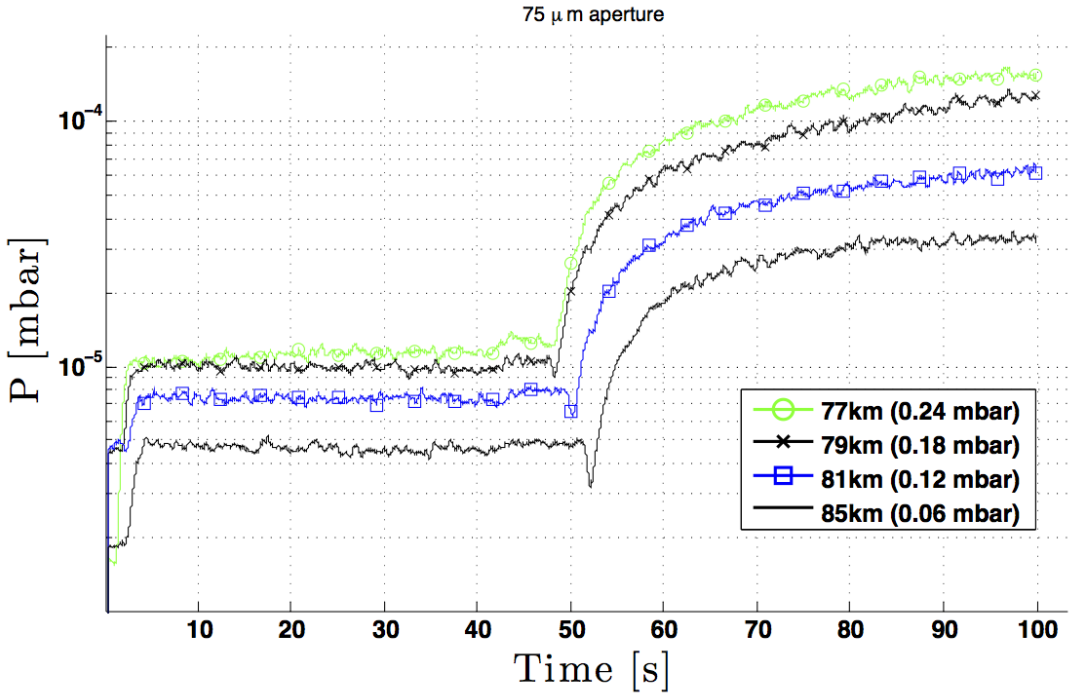

Figure 4.11: Laboratory measurements of pressure increase inside ICON chamber at different ambient pressures for an aperture diameter of 75 μm.

In figure 4.12 we show a reference sweep from ICON in both sweep and trend mode. The seemingly periodic variation over groups of $10-15$ AMU are probably contamination from pump oil or hydrocarbons deposited on the stainless steel walls during bakeout.

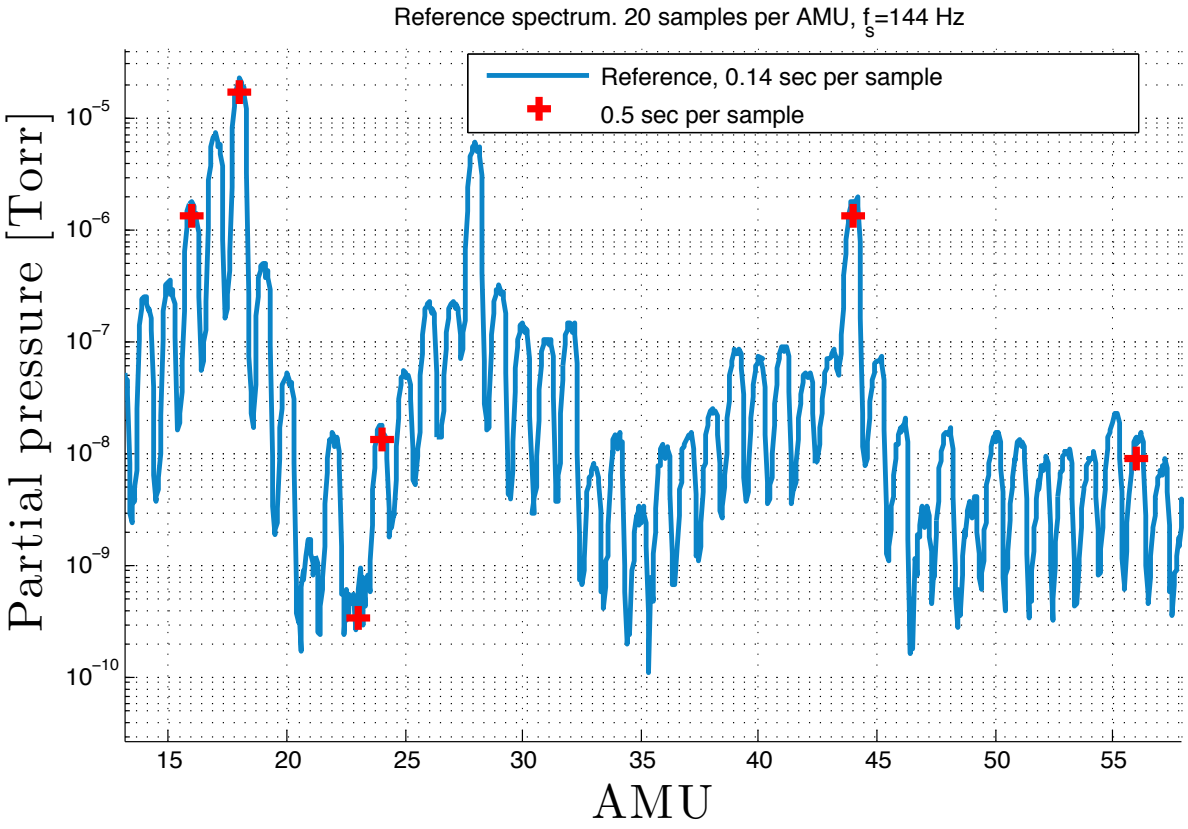

Figure 4.12: Reference spectrum of the first 56 AMUs in the ICON-I prototype comparing sweep and trend settings. The trend setting have much longer integration time and normally offers higher accuracy. In this plot it may be an artifact that there is an underlying variation with period 10-15 AMU; this can normally be attributed to hydrocarbons from pumping oils or bake-out of the stainless steel chamber. 1 Torr here is approximately 1 mBar/1.33. The electron multiplier was turned off in this test.

Chapter 5

Size Distribution of Mesospheric Dust Particles

One of the main developments included in the present thesis is the estimation of sizes of mesospheric aerosols with Faraday type cups. In Paper II we estimated the sizes of collision fragments of ice particles with the MUDD probe, which is argued to be representative for the size distribution of MSPs. In Paper IV we introduced a method to calculate the sizes and neutral density of mesospheric ice particles, by means of solving coupled equations for the dusty plasma with number charge density derived from DUSTY. This method has an advantage from optical methods in that it yields currently unmatched height resolution on the order of 10 cm. The methods are fundamentally different, and the extended DUSTY method from Paper IV yields mean absolute values of particle radii and density while the analysis in Paper II yields a relative size distribution. In this chapter we give a short introduction of sizes of mesospheric nanoparticles and the theoretical justification for the two methods used to derive particle sizes from data obtained during the MAXIDUSTY campaign.

5.1 Sizes and Growth of MSPs

Re-condensation of meteoric vapours have been considered in a handfull of works since the initial postulation by Rosinski and Snow (1961), that atomic metal from ablation can be oxidized by ambient O_2 and the metal oxides subsequently coagulate into nanoscale particles – or as they are addressed here *meteoric smoke particles*. Due to the low vapour pressures of many metal oxides in the upper mesosphere, where the temperature is very low, two colliding molecules can combine without an energy barrier. Hunten et al. (1980) presented the most well knowm coupled calculation of ablation profiles and MSP sizes; their pro-

duction rates are readily used, even today. In recent years, whole atmosphere models like WACCM have been coupled with microphysical models and a more complete parameterization of the transport of aerosols, like CARMA (see e.g. Megner et al. (2006) and Bardeen et al. (2008)). Surprisingly, the size distributions obtained by the most recent methods are very close to the original work by Hunten et al. for the low end of the size spectrum. Figure 5.1 shows a comparison of the two mentioned simulations using the CARMA model, where the discrepancy is found to grow with particle size. Such a discrepancy is mainly due to how large scale transport and turbulence is parameterized. In the following, we introduce the theory of MSP growth and size distributions from the simplest principles, i.e. no parametrization of complex transport patterns and gravity wave breaking. Subsequently we discuss how the sizes of MSPs inside larger ice particles can be obtained using MUDD.

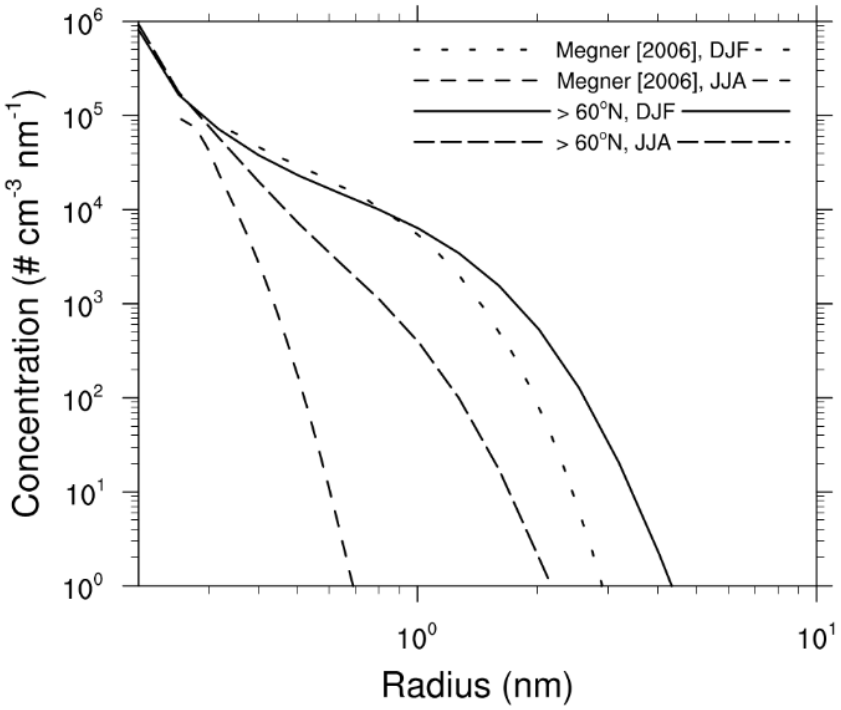

Figure 5.1: Comparison of the mean MSP size distributions obtained by two-dimensional Megner et al. (2006) and three-dimensional(Bardeen et al., 2008) whole atmosphere simulation of meteoric smoke with the CARMA code for altitudes between 80 and 90 km. The results of these simulations gave similar inverse power laws (in order of magnitude) as the original work by Hunten et al. (1980); $N_{MSP} \propto r_{MSP}^{-2.5}$. Adapted from Bardeen et al. (2008) © Wiley.

It can be assumed for a range of probable constituents of meteoric smoke particles, that they must to a large degree have been nucleated homogeneously. One simple justification of this, is that metal oxides and non-stoichiometric molecules

from ablation of olivine can be expected to have a relatively large dipole moment. Thus, homogeneous nucleation can take place without an energy barrier; three-body reactions with the other species can also take place. In the following, we examine the theoretical size distribution arising from homogeneous nucleation from a finite reservoir of ablation gas.

The rate at which atoms or molecules strike the surface of a dust grain can be calculated by calculating the first order moment of the distribution function. We let n_γ denote the density of the ablation gas, and n_d the density of the dust (smoke) particles. Allowing for a specified sticking probability, ξ_d, we have:

$$\begin{aligned} \Gamma &= \xi_d \pi r_d^2 n_\gamma \int_0^\infty \mathrm{d}v \cdot v' f(v') \\ &= 4\pi r_d^2 n_\gamma \xi_d \left(\frac{k_B T_\gamma}{2\pi M_\gamma} \right)^{\frac{1}{2}} \end{aligned} \tag{5.1}$$

where M_γ and T_γ are the molecular mass and temperature of the ablation gas species, respectively. This rate is also the rate at which ablation gas molecules are removed. If we furthermore let $n_d(r_d, t)$ be the time-dependent number of grains of radius r_d, we can express the number of removed molecules of the ablation gas per time as:

$$\frac{\partial n_\gamma}{\partial t} = -4\pi r_d^2(t) n_\gamma(t) n_d(r_d, t) \xi_d \left(\frac{k_B T_\gamma}{2\pi M_\gamma} \right)^{\frac{1}{2}} \tag{5.2}$$

where we have emphasized the time dependency of the grain radius. The rate of mass increase is simply calculated from eq. (5.1) as $\dot{m}_d = \Gamma M_\gamma$. Given that a grain grows uniformly and spherically, we can also express the mass increase in terms of the radius increase as:

$$\dot{m}_d = 4\pi r_d^2 \rho_d \dot{r}_d \tag{5.3}$$

where ρ_d is the grain material mass density. Combining equations (5.1) and (5.3) we obtain an expression for the radius rate-of-change:

$$\dot{r} = \frac{n_\gamma \xi_d}{4\pi^2 \rho_d} \left(k_B T_\gamma M_\gamma \right)^{\frac{1}{2}} . \tag{5.4}$$

If we now formalize the above manipulations into a set of coupled PDEs we have,

for the simplest case with no additional sources or sinks:

$$\frac{\partial n_\gamma}{\partial t} = -4\pi r_d^2(t) n_\gamma(t) n_d(r_d, t) \xi_d \left(\frac{k_B T_\gamma}{2\pi M_\gamma} \right)^{\frac{1}{2}} \tag{5.5}$$

$$\frac{\partial r_d}{\partial t} = \frac{n_\gamma \xi_d}{\rho_d} M_\gamma \left(\frac{k_B T_\gamma}{2\pi M_\gamma} \right)^{\frac{1}{2}} \tag{5.6}$$

This can be solved numerically, but it is possible to find an analytical approximation of the final size distribution. Differentiating (5.6) and substituting for $\partial n_\gamma / \partial t$ we obtain

$$\ddot{r}_d = \frac{\partial^2 r_d}{\partial t^2} = -4\pi r_d^2 \bar{v}_\gamma \xi_d n_d \dot{r}_d = \dot{r}_d \frac{\partial \dot{r}_d}{\partial r_d}. \tag{5.7}$$

Solving this equation yields

$$\dot{r}_d = \frac{4\pi \bar{v}_\gamma \xi_d n_d}{3} \left(r_{d,\infty}^3 - r_d^3 \right) \tag{5.8}$$

where $r_{d,\infty}$ is the final size distribution of the grains and $\bar{v}_\gamma$ is the mean thermal speed of the ablation gass molecules. Assuming $r_{d,\infty} \gg r_{d,0}$ gives that the initial growth rate can be estimated as $\dot{r}(0) \approx 4\pi \bar{v}_\gamma \xi_d n_d r_{d,\infty}^3 / 3$. At this point in time, we can assume that the gas reservoir is not significantly depleted, such that the growth rate according to eq. (5.6) can be estimated to be

$$\dot{r}_d = \frac{n_\gamma \xi_d}{\rho_d} \left(\frac{k_B T_\gamma M_\gamma}{2\pi} \right)^{\frac{1}{2}}. \tag{5.9}$$

Equating the two yields an estimate of the final size distibution is terms of the initial density of ablation molecules, $n_{\gamma,0}$:

$$n_d(r_d)_\infty \simeq \frac{3 M_\gamma n_{\gamma,0}}{4\pi \rho_d} r_{d,\infty}^{-3} \tag{5.10}$$

demonstrating an inverse power law relationship. This inverse power law is steeper than the simulation results mentioned above which indicate a proportionality close to $n_d \simeq r_d^{-2.5}$ at 90 km. This levelling can happen due to a number of mechanisms, but is probably mainly due to the parameterization of eddies and updraft in the more complex models.

Sizes of MSPs derived from MUDD measurements

The justification for why sizes of MSPs can be estimated using MUDD is given in Paper II, and we will not go into depth on that here. The conlusion is that due to sticking of small ice particles to metal surfaces, increased evaporation and smaller affinity for triboelectric charge transfer, MSPs is likely to dominate the bottom plate current in MUDD.

As specified in chapter 4.1, a triplet of MUDD (as launched on MXD) has the capability of sweeping through all 10 potential potentials in a height range of some tens of metres. On such short spatial scales, there may be large natural variations in the dusty plasma. Noise and other adverse effects might also influence the currents. Therefore, to minimize error it is preferrable to integrate the MUDD currents over relatively calm regions. By doing so, however, there is some loss of information as the size distribution can change significantly at altidudes between $\sim$ 80 and 90 km.

Figure 5.2 shows the MUDD currents integrated over an arbitrary calm part of a cloud layer and subsequently normalized. Note especially, that there is one channel with 'retarding potential' of -2V, which means that it is attractive for negative particles, and therefore presumable collects all charged fragments. This channel is also taken as the total current channel, where all charged fragments are measured. The general trend is that channels of higher retarding potential records lower currents, as expected from the theorized distributions.

A size distribution cannot be derived directly from figure 5.2 due to the following: (1) Fragments detected in the most energetic channels will also be detected in channels of lower retarding potential, and (2) The secondary impact charging occuring at G2 varies with particle size. The solution to the first problem is simple; for a given channel, we extract the current in the channel with the immediate higher retarding potential. The second issue is far more complicated to overcome. It is probable, as discussed in Paper II, that the charging probability of fragments/MSPs produced in MUDD should have a proportionality to radius somewhere between r_d^2 and r_d^3. In figure 5.3 we present the estimate of the size distibution of collision fragments calculated using the two limiting values of charging probability. The slope of the upper confidence boundaries are close to the slope of the model predictions, but we find generally steeper power laws regardless of charging probability.

Above, we provided justification for that coagulation of a depleting reservoir of ablation gas resulted in an inverse power law size distribution proportional to

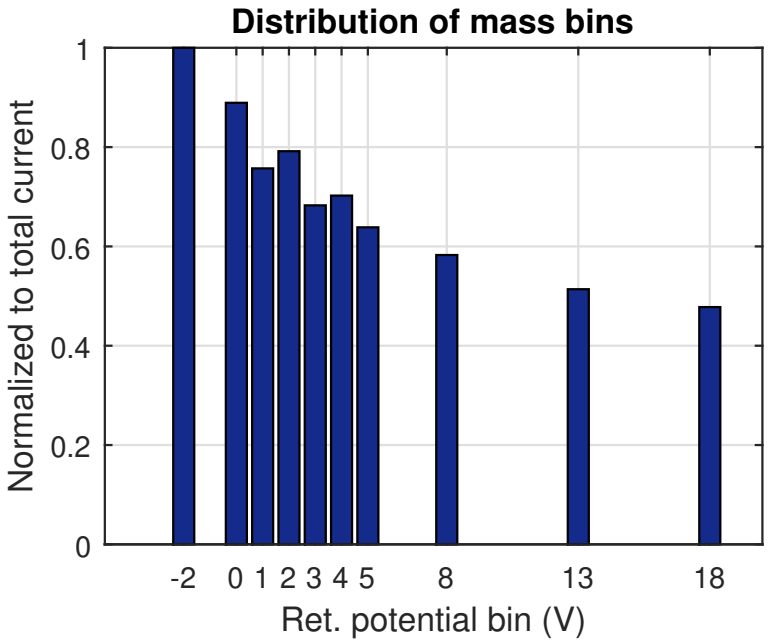

Figure 5.2: The accumulated and normalized currents for all channels (retarding potentials) on three MUDD probes in an arbitrary region of the cloud layer. This example is from the MXD-1 flight in a region with little observed variation and turbulence.

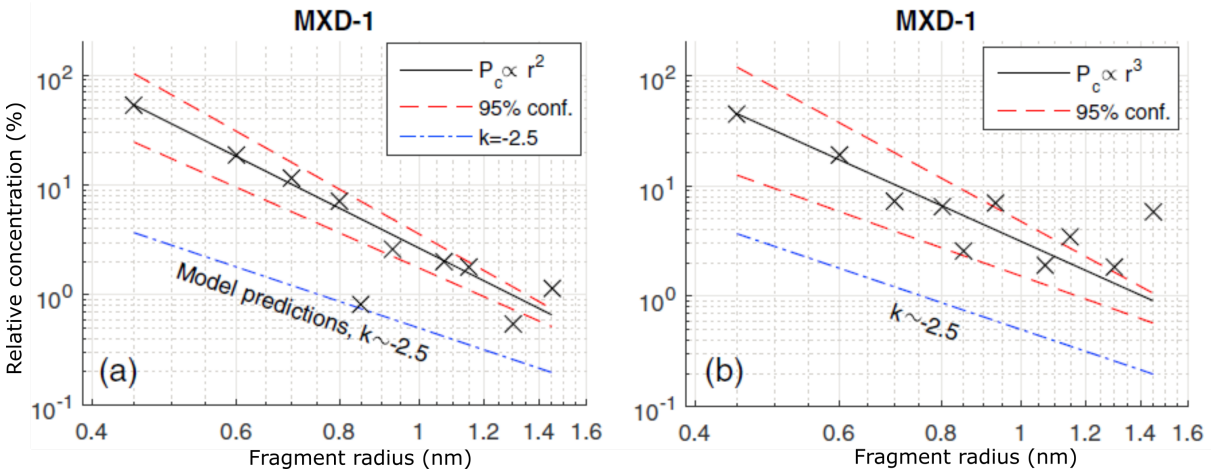

Figure 5.3: Final size distributions of collision fragments (MSPs inside ice particles) for the MXD-1 flight. The two panels show the case for two limiting values of charging probability (P_c) – either proportional to particles cross-section (panel a) or volume (panel b). The obtained distributions are plotted as solid black lines, and the red dashed lines provide the 95% confidence bounds. The blue dash-dotted lines shows a fit of modeled size distributions of free MSPs at 90 km based on Bardeen et al. (2008), Hunten et al. (1980), and Megner et al. (2006). Note that these are presented in relative terms and that the model prediciton line has been shifted down by approximately one order of magnitude for clarity.

r_d^{-3}, which is close to the values found with MUDD. We must also note however that certain collision mechanisms can yield the same proportionality, however, due to the thermodynamic and charging properties of nanoscale ice we maintain that the observed signature is due to embedded MSPs.

5.2 Sizes and Growth of Ice Particles

Due to the multiple phases of H_2O-clusters and high sensitivity to changes in temperature and saturation ratio, the nucleation and growth of ice particles is somewhat more complicated and more difficult to generalize than nucleation of meteoric smoke particles. A short introduction to nucleation theory is not adequate to give the physical insight needed to really comprehend the complex nature of mesospheric ice particles. There are, however, a few important concepts which should be introduced in order to understand how MSPs affect ice growth.

At this point, we should recall Ostwald's rule which paraphrased states that "[...] an unstable system prefers to transform into a state which is accompanied by the smallest loss of free energy, rather than to the most thermodynamically stable one" (Ostwald, 1897). This is to say that hexagonal ice – the most themodynamically stable state of H_2O-clusters – is not the most probable form under all conditions. It is possible to show that this is consistent with classical nucleation theory. The Gibbs free energy of forming a grain of i for a saturation ratio $S = p_{H_2O}/p_{amb}$ can be stated as (Pruppacher and Klett, 1997):

$$\Delta G = -\frac{4\pi\rho r_i^3}{3M} k_b T \ln S + 4\pi r_i^2 \gamma \tag{5.11}$$

where the first term on the r.h.s. is the free energy of forming internal bonds between water molecules. The last term on the r.h.s. is the free enregy connected to forming an interface, which is always positive (and therefore unfavourable). The molecular mass and initial state density is denoted by M and ρ respectively, and the energy interfacial energy is denoted by γ.

The critical radius of a grain, where effective growth can take place, is defined at the point where there is no change Gibbs energy when adding another molecule to the initial gain or cluster, i.e. $\mathrm{d}\Delta G/\mathrm{d}r_i = 0$. The critical radius is therefore

$$r^\dagger = \frac{2\gamma M}{k_B T \rho \ln S} \tag{5.12}$$

which finally yields the expression for the Gibbs energy of a critical cluster

$$\Delta G^{\dagger} = \frac{16\pi\gamma^3 M^2}{6\rho^2 k_B^2 T^2 \ln S}. \tag{5.13}$$

From this expression it is evident that that there is a strong dependence on interfacial energy. This shows, as argued by Zasetsky et al. (2009) and Murray and Jensen (2010), that Ostwald's rule applies since an amorphous state of water has a lower interfacial energy and thus a lower nucleation barrier than hexagonal ice. The consequence is that for homogeneous nucleation of ice, i.e. water nucleating with water, amorphous solid water have a more rapid growth than hexagonal ice if the water vapour is abundant.

The latter two cited works make the case for homogeneous nucleation of ice, but as pointed out by Murray and Jensen (2010) this is only possible at either very low temperatures, high saturation ratios and/or during periods of steep negative temperature gradients. Homogeneous nucleation happen to a certain degree during normal summer mesosphere conditions, and the question is whether or not (or when) homogeneous nucleation of ice can compete with heterogeneous nucleation with other mesospheric constituents. For a long time, molecules and agglomerates from meteoric ablation have been the most likely candidates for condensation nuclei of mesospheric ice (see e.g. Rapp and Thomas (2006)). The reason is that such particles can lower the nucleation barrier to virtually zero (Gumbel and Megner, 2009). As a matter of fact, there are now a few independent observations of meteoric smoke embedded in ice. Observations from the SOFIE mission on the AIM spacecraft estimated the meteoric smoke content to be up to 3% by volume (Hervig et al., 2012), while Havnes et al. (2014) and Paper II in the current work find similar volume contents. The two latter papers also point out that there is a strong dependence on charging efficiency of ice particle fragments; this is a process which MSPs can affect. Asmus et al. (2014), which provides a thorough introduction to growth of dirty ice, calculated the growth rates of ice with embedded smoke particles of different composition. Their finding was that MSP tend to cause larger but fewer grains, and the growth is strongly dependent on iron content in the smoke. Based on the discussion above, we take as a model of the typical mesospheric ice particle: a grain with embedded MSPs where the ice is not necessarily crystalline in structure.

The mean radius and size distribution of mesospheric ice is controlled by the abundance of water vapour, temperature and large scale transport of the involved species. The estimation of particle radius is complicated by the fact that meso-

spheric ice particles are generally non-spherical. Remote mesurements by satellite (Hervig et al., 2009) and ground-based lidar (Rapp et al., 2007b), have yielded axial ratios – the ratio between grain equatorial and rotational axes – of either $\sim 0.2 - 0.5$ (needle-like) or $\sim 2 - 5$ (plate-like). To which degree ambient parameters can affect the shape of the particles, is still an open question. In any case, the simplest growth models which yields spherical particles probably do not reflect reality well for the majority of mesospheric clouds.

The proportionality to radius in the optical cross-section ($\propto r_d^6$) means that optical methods such as lidar and photometers are insensitive to the smallest particles. Such instruments can only observe sizes above several nanometres; thus losing a large part of the size distribution. For the interpretation of lidar measurements, it is commonly assumed that the distribution of sizes is monomodal Gaussian. This has also been backed up by simulations (Rapp and Thomas, 2006; Baumgarten et al., 2010). Using this assumption, the mean size of particles producing NLC have been reported to be $\sim 30 - 70$ nm, with a typical width of ~ 10 nm (see e.g. Von Cossart et al. (1999); Rapp and Thomas (2006); Baumgarten et al. (2010); Megner et al. (2009)). The mean peak backscatter height as recorded by lidar is ~ 83 km, and this is found to increase on the order of ~ 80 m per decade (Fiedler et al., 2017). Particles of sizes below a few nanometres are more elusive, and their size distribution have not been investigated thoroughly. Measurements of solar occultaion by ice from satellite suggest an inverse proportionality between concentration and radius at altitudes of peak occultation (Hervig et al., 2009). The same observations also yield a broader range of mean sizes and a higher variance in the distribution width compared to lidar measurements. The variance in optical observations and poor sensitivity to the smallest sizes calls for an alternative way to obtain the key parameters of mesospheric ice.

In the following we will outline the theory of how ice particle sizes can be derived by the use of the DUSTY Faraday cups, obtaining a much better altitude resolution and theoretical size range than remote methods.

Sizes of Ice Particles derived from DUSTY measurements

We recall that the DUSTY probe, as introduced in Ch. 4, has three grids G0, G1 and G2 at respectively 0 V, + 6.2 V and - 6.2 V. The bottomplate detector has a bias of + 2 V. The cross-section of the two uppermost grids is $\sigma_0 = \sigma_1 = 0.046$ times the probe cross-section. G2 has thicker wires to increase the secondary charging effects, with $\sigma_2 = 0.235$. We recall from eqs. (4.1) and (4.2), that

the current recorded on grid 2 must be $I_{G2} = \sigma_2 I_D + I_{sec}$, where I_D is the current in front of the grid. Consequently, the bottom plate current becomes $I_{BP} = (1 - \sigma_2) I_D - I_{sec}$. The electrons which are rubbed off from G2 will produce a positive current I_{sec} to G2, which will furthermore be deposited on BP and create a negative current $-I_{sec}$ there. We can eliminate the secondary current to express I_D in terms of measured currents as

$$I_D = I_{G2} + I_{BP} \tag{5.14}$$

where the secondary production from G1 and G0 is neglected, as the small fragments will be stopped by air friction and heavy evaporation (Antonsen and Havnes, 2015). The total current into the probe is given by eq. (4.3), and amounts to $\approx 1.1 I_D$ when adjusted for σ_0 and σ_1.

In earlier papers on DUSTY, the ratio between the currents to G2 and BP have been used to extract information on how effective the secondary charging current is. In terms of previously defined terms we have

$$R = \frac{I_{G2}}{I_{BP}} = \frac{\sigma_2 I_D + I_{sec}}{(1 - \sigma_2) I_D - I_{sec}} \tag{5.15}$$

which for the limit $I_{sec} \to 0$ becomes $R = 0.31$, and in the limit $I_{sec} \gg I_D$ becomes $R = -1$. The charging of mesospheric ice by plasma scales roughly with particle radius. Thus in general, when the secondary current dominates, it can be expected that the ice particles are large – on the order of tens of nanometers (Havnes and Næsheim, 2007; Havnes et al., 2009). When the ratio is weakly positive we expect smaller particles. This is in accordance with the assumptions used in the analysis of MUDD data, that the impact charging of the particles scales with their cross-section or volume. The secondary current in DUSTY can be stated as:

$$I_{sec} = e n_d v_R A_{sec} \eta(r_d) \tag{5.16}$$

where $A_{sec} = \sigma_s \sigma_2 \sigma \approx 7\%$ is the effective area for secondary current production. The parameter σ_s describes how large portion of a grid that can produce secondary charge, and was calculated by Havnes and Næsheim (2007) to be 0.28. The secondary charging factor, $\eta(r_d)$, is here taken to be dependent on radius, and is found from earlier flights of DUSTY to be between 50 to 100 for a large reference particle. If we assume the ice particles have a charging probability proportional to cross-section and inserting for the secondary current as defined above, we obtain

$$\left(\frac{r_d}{r_{ref}} \right)^2 = \frac{(1 - \sigma_2) I_{G2} - \sigma_2 I_{BP}}{A_{sec} \eta_{ref} e n_d v_R} \tag{5.17}$$

where η_{ref} is the number of secondary charges produced for a particle of size r_{ref}. Usually, this reference value is taken to be 50 for a radius of 50 nm.

We note that the only unknown parameter in eq.(5.17) is the number density n_d. If we include a charging model, we can therefore solve self-consistently for particle radius, since DUSTY can measure the dust charge number density, $n_d Z_d$, directly. In Paper IV, we calculate the equilibrium charge by assuming quasi-neutrality and that electron collisional charging is the most significant mechanism; photo-ionization is neglected in the following. The electron density is measured by probes on the payload. The coupled system of equations can then be iterated, and only requires an initial guess of average charge number (for which a good guess is $\bar{Z}_d = -1$). In figure 5.4 we show the result of such an iteration based on from the MXD-1 flight compared to sizes estimated by RMR lidar and an in-situ photometer. The lidar generally yields smaller sizes than the iteration, which may be due to several reasons; e.g. the large difference in sampling volume or assumptions of particle intrinsic parameters. There is also some uncertainty connected to how the very smallest particles, below a few nanometres, affect the total and secondary current in DUSTY.

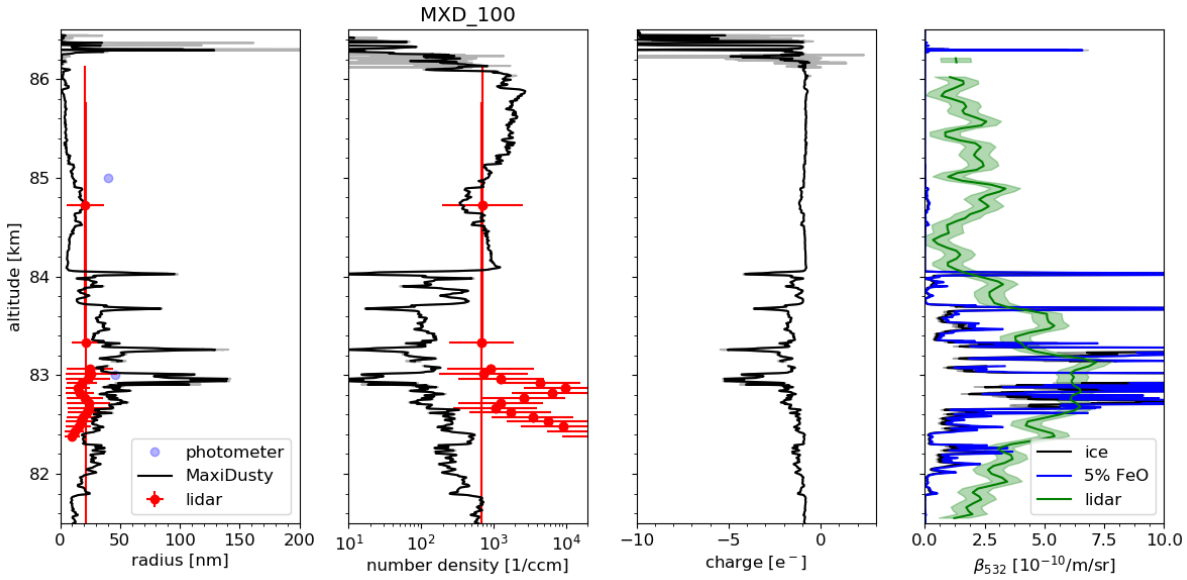

Figure 5.4: Results from iteration of equation (5.17) with a charging model. The solid black curves in panels 1, 2 and 3 show the calculated radius, number density and average charge number respectivly. The red dots represent estimated mean size (Panel 1) and density (Panel 2) from RMR lidar measurements. The rightmost panel show estimates of the optical backscatter ar 532 nm using the iteration results. Adapted from Paper IV, Copyright © Copernicus.

Chapter 6

Multi-scale Variations in the Mesospheric Dusty Plasma

The endorsement of in-situ observation of dusty plasmas or neutrals in the mesosphere, is commonly motivated by the superior height resolution of sounding rocket probes. Also, their very localized sampling normally result in a larger variance in observed parameters than integrating methods such remote radars and lidar. Rocket soundings are not, however, the only means of investigating the mesopause at very small scales. PMSEs, introduced in chapter 3, have been observed with UHF radars at frequencies as high as 1.29 GHz (Cho et al., 1992). Since PMSEs are coherent structures in the dusty plasma at the radar Bragg-scale. For UHF-radars this scale is $\sim$ 10 cm. Nevertheless, the integration in height and time makes it difficult for utilizing radars to monitor phenomena such as density variations and flow shears on the smallest scales.

Even though sounding rockets provide a most suitable platform to investigate fluctuations in the dusty plasma on the smallest spatial scales, few studies have utilized this capability. The works of Rapp et al. (2003a) and Lie-Svendsen et al. (2003) which respectively presented observations and modelling of the interconnection between aerosols and electrons on the smallest scales, are in fact some of the most recent works in this sub-field. Strelnikov et al. (2009) studied neutral fluctuation at small spatial scales, which is important to the understanding of PMSE formation.

In simultaneous measurements of PMSE and in-situ soundings, there are always differences. Some of these differences, but probably not all, are connected to the difference in sampling volume. In order to explain these, one must have a good despcription of the interconnection between aerosols and electrons for a range of ambient parameters and on a range of length scales. The ultimate reward for

such inquiries, is that the relationship between PMSE and aerosols can be better understood.

The MXD payloads were equipped with the DUSTY and MUDD probes to measure aerosols and multi-Needle Langmuir probes to measure the electron density on scales down to $\sim$ 10 cm. On MXD-1B, we launched two mechanically and electronically identical DUSTY probes with an interspacing of $\sim$ 10 cm in order to characterize horizontal differences in the charged aerosol population. The results, as presented in Paper III, show a highly complex interplay between the dusty plasma species. The flow around the payload is also found to affect recorded currents. Moreover, it is difficult to find a simple relationship (or *proxy*) between dusty plasma parameters and PMSE. In the following, we elaborate on this.

6.1 Fluctuations on the Small Scales

For particles of sizes larger than several nanometres, the neutral drag is not enough to to deflect them in the payload shock front and they will typically reach the bottom plate of DUSTY with a velocity close to that of the payload. Ideally then, with a top deck geometry as MXD-1B with two identical DUSTY probes with small interspacing, the probes would record the same current if large horizontal variations in the dusty plasma on the same scales as the interspacing are not present. Figure 6.1 shows a situation which is close to such an "ideal" scenario. From the bottom panel, we see that the ratio between DUSTY 1 and 2 currents fluctuates with the spin frequency; such oscillations are seldomly not present in mesospheric rocket soundings, and are often either left untreated or spin components are filtered. The reason these oscillations occur, as discussed in Paper III, is probably due to the smallest particles being more prone to aerodynamic modulation. Other adverse effects such as payload charging and secondary sprays of particles from other parts of the top deck may also be plausible (Kassa et al., 2012).

One motivation to look into these unwanted effects, is that similar signatures are easier to overlook when only looking at a single probe – which is typically the case. Although a spin-polluted signal is simple to correct for, it is seldomly emphasized that there may be large horizontal differences even between probes on the same deck. The threshold for wrongly interpreting observations can in such cases be significantly lowered. In figure 6.2 we show a comparison between the DUSTY probes on MXD-1B in a region with a sharp onset to strongly spin

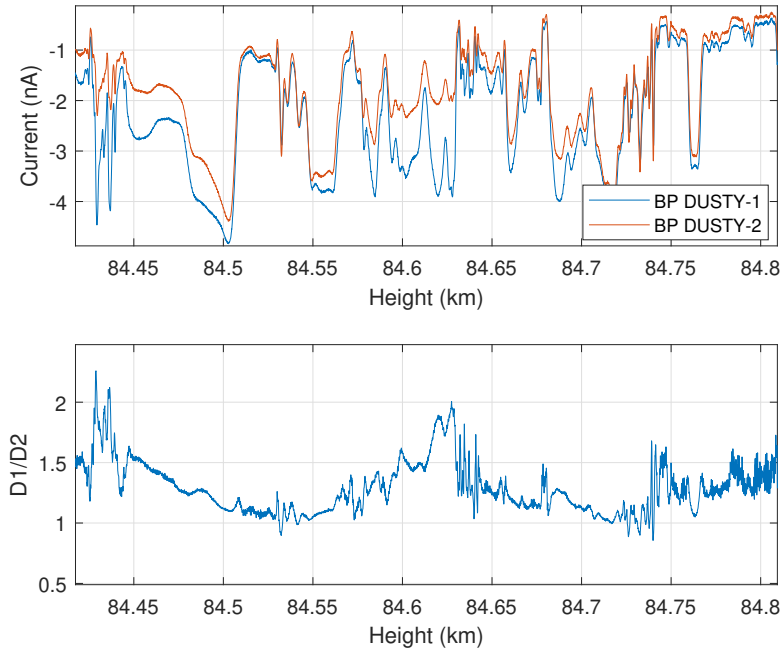

Figure 6.1: Medium scale close-up of a comparison between DUSTY 1 and DUSTY 2 on MXD-1B.The $D1/D2$-ratio is close to unity, underlining the good agreement at these scales. From Paper III.

modulated signals. The ratio of the currents display a phase shift equal to the azimuthal phase between the probes which can be interpreted as: (1) Aerodynamic modulation of (small) aerosols, or (2) A consistent difference in charge number density at the scale of the interspacing between the DUSTY probes. In Paper III we find (1) to be the most plausible explanation.

In figure 6.3 we present a comparison between electron density and DUSTY bottom plate currents in a $\sim$ 200 metre height range inside the MXD-1B cloud system. In this relatively thin slice, the correlation between the two is virtually one-to-one throughout the whole range, implying that the present ice particles absorb free electrons effectively. This is analogous to a classical bite-out in the electron population. One of the open questions addressed in Paper III, is whether or not such a bite-out is the only possible coupling between the electron and dust populations or if a postitive correlation between electrons and (negatively charged) dust can occur. This latter scenario was proposed by Lie-Svendsen et al. (2003) as a possibility during periods of sharp positive temperature gradients. For the MXD-1B flight we find that the overwhelming majority of the cloud system displays traditional bite-outs on short length scales and that positive correlations are found on longer length scales. To resolve whether or not such positive cor-

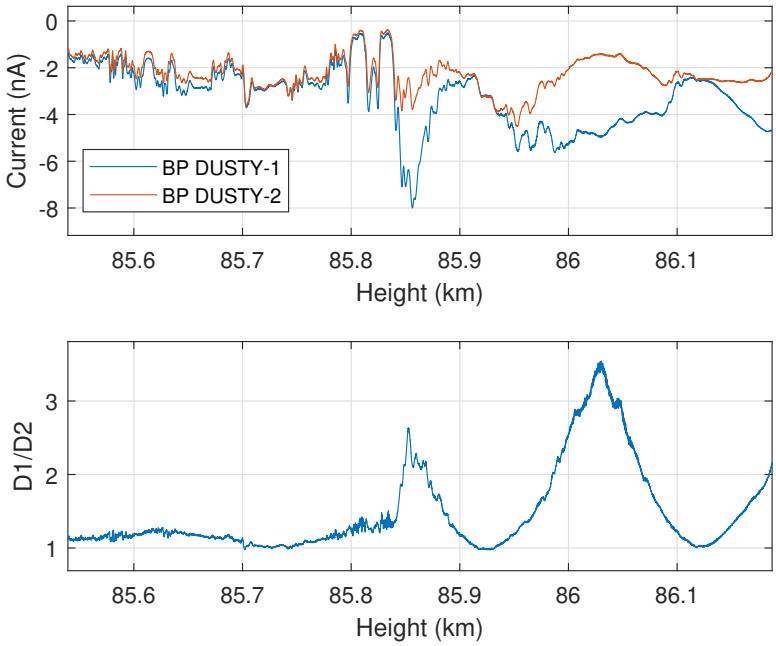

Figure 6.2: Close-up of a region where a strong disagreement between DUSTY 1 and DUSTY 2 on MXD-1B sets in. The ratio of the two DUSTY currents is modulated significantly with the spin frequency ($\sim$ 3.8 Hz). Adapted from Paper III.

relations are causal, one must also analyse the temperature and dynamics of the cloud; this is not done in Paper III.

6.2 Connection between PMSEs and Measured Plasma Parameters

There is a general consensus that charged aerosols are involved in the formation of PMSE. There have been some disscusion about the exact dependence of aerosols and/or electrons in the PMSE reflectivity (see e.g. Varney et al. (2011); Rapp et al. (2008)). For relatively low dust concentrations compared to electron density, as was the case during MXD – the application of the theory on scattering from Bragg-scales structures in a dusty plasma predict that the change in PMSE strength must depend on the square of the co-dependent dust/electron density gradient accordingly:

$$\eta \propto \bar{S}^2 \nabla \langle N_d \rangle^2 \equiv \left(\frac{Z_d N_e}{N_e + Z_i^2 N_i} \right)^2 \cdot \left(\frac{\omega_B^2 N_d}{g} - \frac{\mathrm{d}N_d}{\mathrm{d}t} - \frac{N_d}{H_n} \right)^2 \tag{6.1}$$

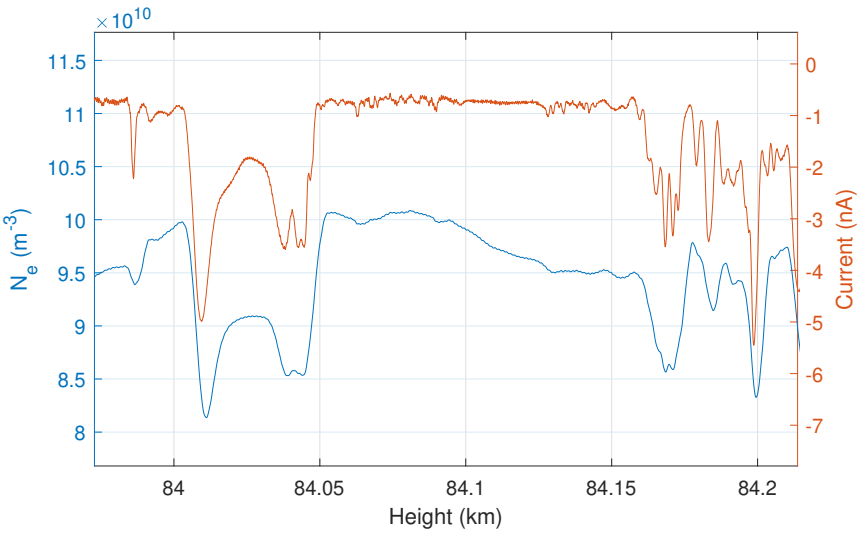

Figure 6.3: Comparison between electron density recorded by m-NLP and DUSTY current (proportional to dust charge number denstiy). The electron density height vector is shifted according to the angle between DUSTY-1 and mNLP Boom-1 ($\sim$ 20 m in height). We note a correlation on length scales $\sim$ 10 m implying anti-correlation between absolute densities. Adapted from Paper III

where $\bar{S}/Z_d$ is the mean number of Debye-sphere electrons and $\nabla\langle N_d\rangle$ is the gradient of dust density across acloud layer. In the gradient term, ω_B is the buoyancy frequency, g is the gravitational constant and H_n is the neutral scale height.

An idealized picture of the PMSE mechanism is that neutral turbulence on different length scales affect aerosols which subsequently reduce the diffusivity of electrons. Resulting gradients in the electron density, which due to the lowered diffusivity are long-lived in comparisson with thermal fluctuations, then form structures in the plasma which a radar wave can scatter from. PMSEs are thus coherent scatter from such structures on the scale of the radar Bragg-length; for the IAP MAARSY radar which was utilized during MXD, this is $\approx$ 2.8 m. A direct way to predict if fluctuations in the dusty plasma would support a PMSE, is therefore to investigate the spectral properties of the fluctuations at said Bragg scale. If the fluctuations have sufficient power, i.e. they are not attenuated in the viscous subrange, the plasma could likely support a PMSE. In figure 6.4 we show the result from a wavelet analysis done in Paper III. The wavelet power spectrum was derived from DUSTY current fluctuations, and is found to correspond reasonably well with radar SNR.

The full theoretical expression for reflectivity includes ordering parameters such as the Richardson- and Prandtl-number, in addition to microphysical parame-

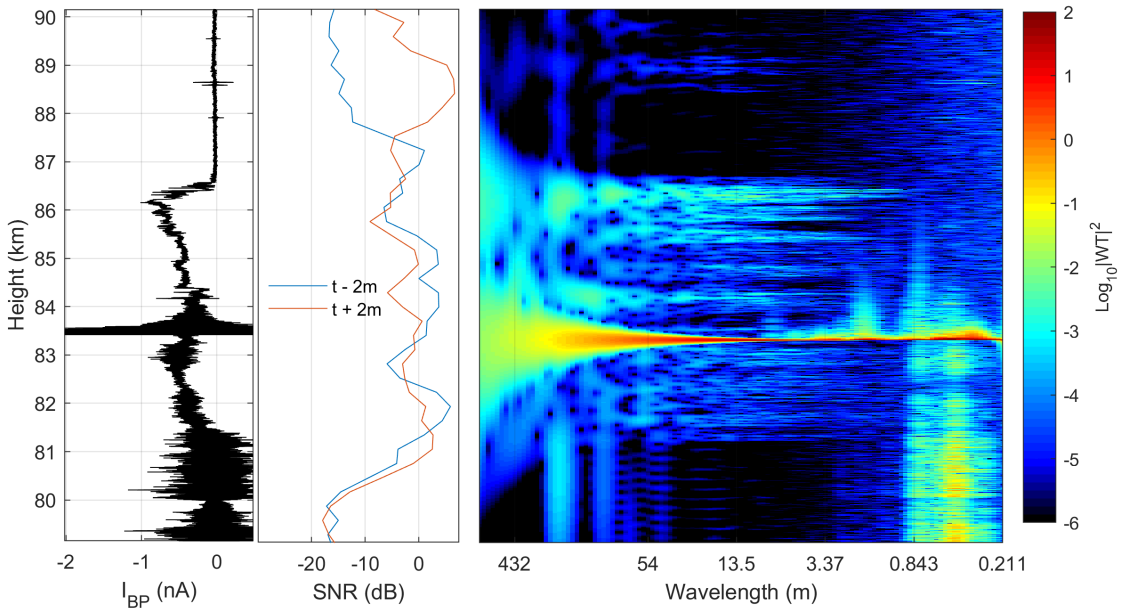

Figure 6.4: Comparison of DUSTY bottom plate current (left panel), MAARSY 53.5 MHZ radar SNR along the rocket trajectory (middle panel) and PSD from wavelet transform (right panel) – for the MXD-1 launch on the 30th of June, 2016. Conversion from frequency to spatial scales is done by using the mean rocket velocity throughout the dust cloud. Radar data courtesy of Ralph Latteck, IAP Kühlungsborn. From Paper III.

ters such as the Batchelor-scale, buoyancy frequency. Due to the complexity and impractical nature of the full expression, a few authors have suggested ordering parameters or *proxies* for PMSE formation (or strength) consisting of simple combinations of dusty plasma parameters. Paper III discusses this topic and argues that a gradient terms should probably be included in the proxy. Figure 6.5 show a comparison of four of the presumed best candidates for proxies and PMSE SNR during MXD-1B.

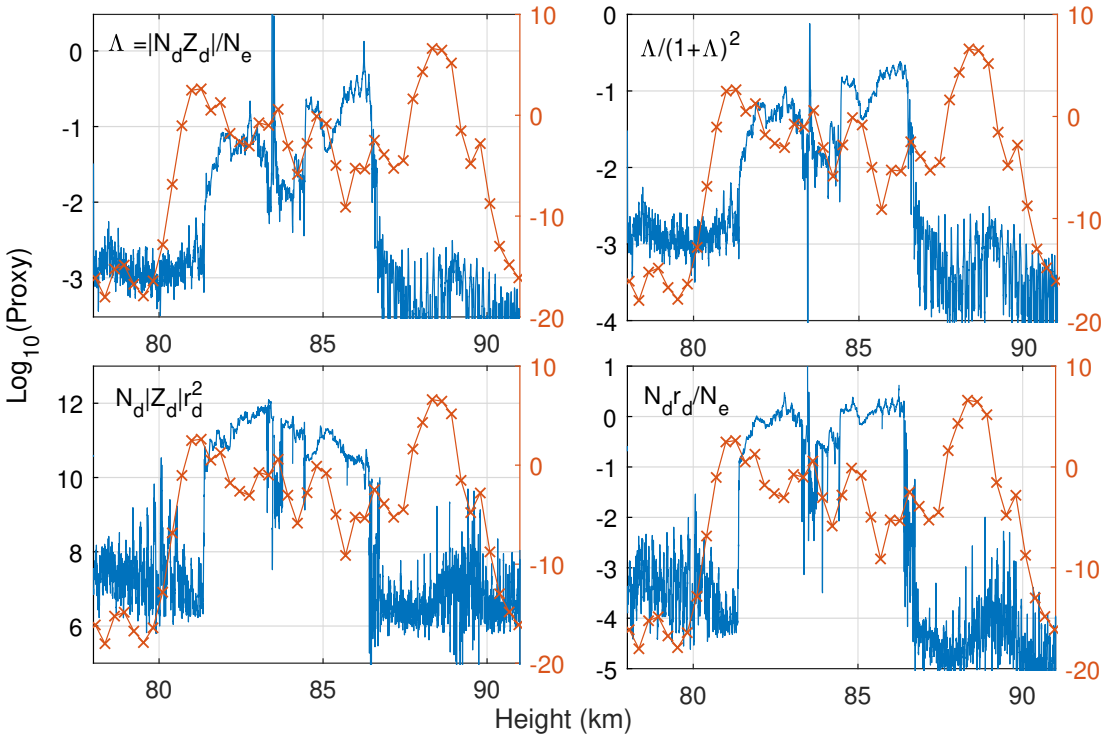

Figure 6.5: Comparison of proxies from dusty plasma parameters to PMSE SNR for the MXD-1 flight. The upper left panel is the Havnes-parameter. The upper right panel is a proxy based on the Havnes-parameter which is consistent with a one-to-one anti-correlation between electrons and charged aerosols. The proxy in the lower left panel can be recognized as the parameter utilized by Rapp et al. (2003b), while the bottom right panel is the factor used by Havnes (2004) which takes the dust radius into account. From Paper III.

Chapter 7

Future Work

The first results from the MAXIDUSTY campaign have given new insights on aerosols in the summer mesosphere. Some of the presented results in this volume pose interesting questions that warrant further investigation, but which are beyond the scope of this thesis. We shortly elaborate below on a few new ideas and ongoing endeavours that have come into being in the wake[1] of MAXIDUSTY.

7.1 In-situ observation of Meteoric Smoke Particles

As established throughout this thesis introduction, much of the recent focus for in-situ measurements in the mesosphere have been directed towards the elusive meteoric smoke particles. These particles have previously been detected in-situ, but remain the least investigated aerosol species in the upper atmosphere. From MAXIDUSTY measurement and theoretical developments during the projects, we find that Faraday cups may well be utilized to observe MSPs in their free form. We have suggested and built a new probe, SPID (see fig. 4.9 for geometry), which aims to solve the problem of adverse flow effects by using an open Faraday cup design. The Probe is to be launched on the G-Chaser Payload in January of 2019.

Figure 7.1 shows the results of a set of simulations done to determine the size threshold for detection at different altitudes for the SPID probe ('modified MUDD' in the legend) and the MUDD probe. In these simulations the composition was assumed to be a Magnesium-Silicon ferrous oxide, i.e. representable for MSPs. For MUDD at 70 km, the lowest possible detectable size is $\gtrsim 2.8$ nm, while the SPID probe can theoretically measure free MSPs smaller than 1 nm at

[1] Pun intended

the same altitude. By switching potentials in a similar manner as MUDD, it may be possible for future SPID probes to resolve a high resolution mass spectrum of *free* MSPs.

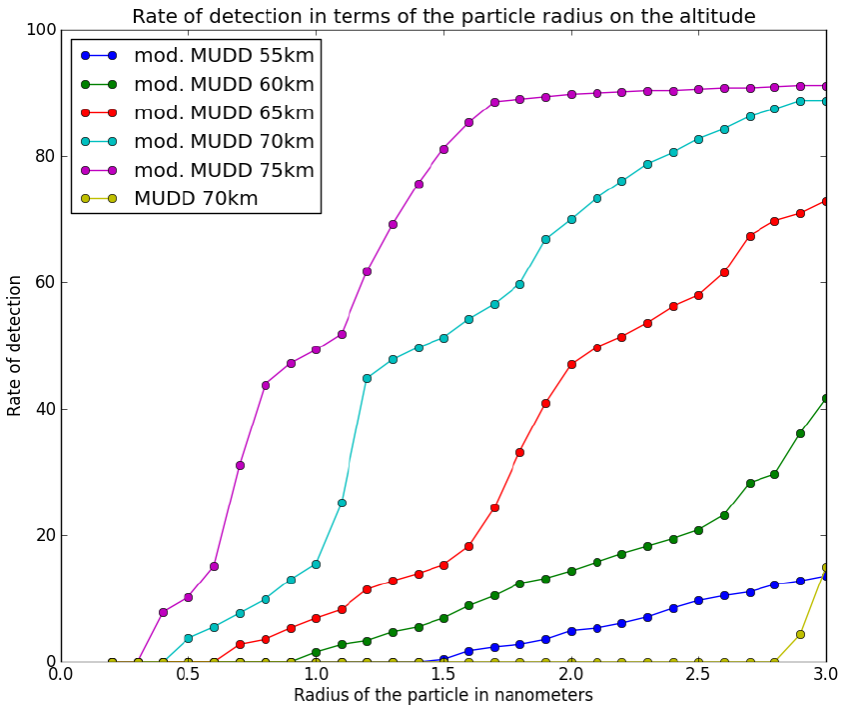

Figure 7.1: Relative detection rate in a prototype of the SPID probe (here labelled as 'modified MUDD') of neutral MSPs for different sizes at varying altitudes. The detection rate at 70 km of the original MUDD probe is also shown (yellow).

7.2 Retrieval of Meteoric Smoke Particles

In sampling and return experiments the deflection of the smallest aerosols presents a great technical challenge. As utilized in MUDD the large NLC/PMSE ice particles are more or less unaffected by the shock front of the rocket, and can be collected effectively. As described in Havnes et al. (2015), we therefore suggest a retrieval experiment (MESS = MEteoric Smoke Sampler) which collects large ice particles. A funnel will steer particles into a collection chamber with an electronic valve. The chamber will contain TEM grids to which particles will stick, and only MSPs embedded in the ice particles will be left after the ice evaporates. The TEM grids will subsequently be analysed in a clean lab. The MESS probe will have two identical sampling chambers where one stays closed during the whole flight and will eventually be compared with the real sampling chamber which is open when the clouds are passed.

Chapter 8

Conclusions

The MAXIDUSTY sounding rocket campaign was successfully completed in the summer of 2016 at the Andøya Space Centre. Two payloads contained instrumentation aimed at conducting multi-scale observation of electrons, ions and charged aerosols. In the current work, we have put special emphasis on the application of new measurement techniques using Faraday cup aerosol detectors. These efforts have yielded methods which can be used to determine intrinsic dust parameters such as charge, size, number density as well as spatial characteristics on scales of $\sim$ 10 cm.

By modelling the movement and energy balance of fragments of mesospheric ice particles inside the Faraday impact detector MUDD, we have shown that MSPs can dominate the detector current (Paper I). With this method, we used the data from two triplets of MUDD flown on the respective MAXIDUSTY payloads to derive the size distribution of embedded MSPs inside mesospheric ice particles (Paper II). The derived size distributions are sensitive to the charging probability, which we argue is proportional to r_d^k for k between 2 and 3. Moreover, the distributions were found to follow inverse power laws which are found to be slightly steeper than model predictions of free MSP size distributions. This work presents another confirmation of that MSPs are abundant in mesospheric ice particles with volume filling factors up to several percent.

This thesis supports that the secondary charging effect is important for aerosol detection with Faraday cups. In both the MUDD and DUSTY probes, this effect have been utilized to obtain information on particle characteristics. Our analysis showed that the secondary (current) yield can be estimated with good certainty by comparing MUDD and DUSTY currents. Based on this, we developed a method to calculate the sizes, charges and number densities of ice particles using DUSTY. The method shows a reasonable agreement with optical mea-

surements, but we underline that the sensitivity to electron density is relatively strong.

From the commensurate of measurements discussed in the present volume, the importance of properly characterizing effects such as flow around the payload body and electric potentials arising from payload charging becomes clear. For the MAXIDUSTY-1B flight we find a strong disagreement between aerosol currents from mechanically and electrically similar probes (Paper III). This is attributed to very small particles (of sizes $\sim$ a few nanometres) being heavily modulated in the complex aerodynamic and electric environment around the rocket payload. The question arises whether or not this is common for similar rocket sounding experiments.

We argue that Faraday cups can be instrumental in the inquiry into the exact role of aerosols in the formation of PMSEs. This relationship is difficult to reduce to a simple proxy consisting of dusty plasma parameters (Paper III), however spectral properties and simultaneous electron and aerosol measurements can be used in determining a correct reflectance expression – if the reflectance is indeed co-dependent of electrons and aerosols. Our conclusion on this topic, is that charged aerosols and electrons are in general anti-correlated even on very short scales and for very low densities (Paper III). We also report on very weak dust structures on altitudes well below the mesopause (Paper V). For these findings, it is probably necessary with a strong updraft below summer mesopause altitudes. These novel clouds in the summer mesosphere may have a mechanism which differ from PMSE

References

Adams, N. and Smith, D.: Studies of microparticle impact phenomena leading to the development of a highly sensitive micrometeoroid detector, Planetary and Space Science, 19, 195 – 204, doi: 10.1016/0032-0633(71)90199-1, 1971.

Allen, J. E., Annartone, B. M., and de Angelis, U.: On the orbital motion limited theory for a small body at floating potential in a Maxwellian plasma, Journal of Plasma Physics, 63, 299–309, 2000.

Amyx, K., Sternovsky, Z., Knappmiller, S., Robertson, S., Horanyi, M., and Gumbel, J.: In-situ measurement of smoke particles in the wintertime polar mesosphere between 80 and 85 km altitude, Journal of Atmospheric and Solar-Terrestrial Physics, 70, 61–70, 2008.

Anderson, J. G.: Rocket measurement of OH in the mesosphere, Journal of Geophysical Research, 76, 7820–7824, 1971.

Andersson, P. U., Tomsic, A., Andersson, M. B., and Petterson, J. B.: Emission of small fragments during water cluster collisions with a graphite surface, Chemical Physics Letters, 279, 100–106, doi: http://dx.doi.org/10.1016/S0009-2614(97)00990-1, 1997.

Antonsen, T. and Havnes, O.: On the detection of mesospheric meteoric smoke particles embedded in noctilucent cloud particles with rocket-borne dust probes, Review of Scientific Instruments, 86, 033 305, doi: http://dx.doi.org/10.1063/1.4914394, 2015.

Antonsen, T., Havnes, O., and Mann, I.: Estimates of the Size Distribution of Meteoric Smoke Particles From Rocket-Borne Impact Probes, Journal of Geophysical Research: Atmospheres, doi: 10.1002/2017JD027220, 2017.

Antonsen, T., Havnes, O., and Spicher, A.: Multi-scale Measurements of Mesospheric Aerosols and Electrons During the MAXIDUSTY Campaign., Atmospheric Measurement Techniques, In Review, 2018.

Asmus, H., Wilms, H., Strelnikov, B., and Rapp, M.: On the heterogeneous nucleation of mesospheric ice on meteoric smoke particles: Microphysical modeling, Journal of Atmospheric and Solar-Terrestrial Physics, 118, 180–189, 2014.

Asmus, H., Robertson, S., Dickson, S., Friedrich, M., and Megner, L.: Charge balance for the mesosphere with meteoric dust particles, Journal of Atmospheric and Solar-Terrestrial Physics, 127, 137–149, doi: 10.1016/j.jastp.2014.07.010, 2015.

Asmus, H., Staszak, T., Strelnikov, B., Lübken, F.-J., Friedrich, M., and Rapp, M.: Estimate of size distribution of charged MSPs measured in situ in winter during the WADIS-2 sounding rocket campaign, Annales Geophysicae, 35, 979–998, doi: 10.5194/angeo-35-979-2017, 2017.

Austin, J., Tourpali, K., Rozanov, E., Akiyoshi, H., Bekki, S., Bodeker, G., Brühl, C., Butchart, N., Chipperfield, M., Deushi, M., et al.: Coupled chemistry climate model simulations of the solar cycle in ozone and temperature, Journal of Geophysical Research: Atmospheres, 113, 2008.

Bailey, A.: Electrostatic phenomena during powder handling, Powder Technology, 37, 71–85, 1984.

Baines, M., Williams, I., Asebiomo, A., and Agacy, R.: Resistance to the motion of a small sphere moving through a gas, Monthly Notices of the Royal Astronomical Society, 130, 63–74, 1965.

Bardeen, C., Toon, O., Jensen, E., Marsh, D., and Harvey, V.: Numerical simulations of the three-dimensional distribution of meteoric dust in the mesosphere and upper stratosphere, Journal of Geophysical Research: Atmospheres, 113, 2008.

Baumgarten, G., Fiedler, J., and Rapp, M.: On microphysical processes of noctilucent clouds (NLC): observations and modeling of mean and width of the particle size-distribution, Atmospheric Chemistry and Physics, 10, 6661–6668, doi: 10.5194/acp-10-6661-2010, URL https://www.atmos-chem-phys.net/10/6661/2010/, 2010.

Beig, G.: Long-term trends in the temperature of the mesosphere/lower thermosphere region: 1. Anthropogenic influences, Journal of Geophysical Research: Space Physics, 116, 2011.

Bekkeng, J. K.: Prototype Development of a Low-Cost Sounding Rocket Attitude Determination System and an Electric field Instrument, Ph.D. thesis, Univeristy of Oslo, 2007.

Biebricher, A. and Havnes, O.: Non-equilibrium modeling of the PMSE Overshoot Effect revisited: A comprehensive study, Journal of Plasma Physics, 78, 303–319, 2012.

Bird, G.: The DS2V/3V program suite for DSMC calculations, in: AIP Conference Proceedings, vol. 762, pp. 541–546, AIP, 2005.

Blix, T., Thrane, E., and Andreassen, Ø.: In situ measurements of the fine-scale structure and turbulence in the mesosphere and lower thermosphere by means of electrostatic positive ion probes, Journal of Geophysical Research: Atmospheres, 95, 5533–5548, doi: 10.1029/JD095iD05p05533, 1990.

Boyd, I. D.: Predicting breakdown of the continuum equations under rarefied flow conditions, in: AIP Conference Proceedings, vol. 663, pp. 899–906, AIP, 2003.

Cho, J. Y. and Röttger, J.: An updated review of polar mesosphere summer echoes: Observation, theory, and their relationship to noctilucent clouds and subvisible aerosols, Journal of Geophysical Research: Atmospheres, 102, 2001–2020, 1997.

Cho, J. Y. N., Kelley, M. C., and Heinselman, C. J.: Enhancement of Thomson scatter by charged aerosols in the polar mesosphere: Measurements with a 1.29-GHz radar, Geophysical Research Letters, 19, 1097–1100, doi: 10.1029/92GL01155, 1992.

DeCarlo, P. F., Slowik, J. G., Worsnop, D. R., Davidovits, P., and Jimenez, J. L.: Particle morphology and density characterization by combined mobility and aerodynamic diameter measurements. Part 1: Theory, Aerosol Science and Technology, 38, 1185–1205, 2004.

Draine, B. and Sutin, B.: Collisional charging of interstellar grains, The Astrophysical Journal, 320, 803–817, 1987.

Eidhammer, T. and Havnes, O.: Size dependence of the mesospheric dust temperature and its influence on the noctilucent clouds and polar mesosphere summer echo phenomena, Journal of Geophysical Research: Space Physics, 106, 24 831–24 841, 2001.

Evans, A.: The dusty universe., Ellis Horwood, New York, NY (USA), 1993.

Fiedler, J., Baumgarten, G., Berger, U., and Luebken, F.-J.: Long-term variations of noctilucent clouds at ALOMAR, Journal of Atmospheric and Solar-Terrestrial Physics, 162, 79–89, 2017.

Fomichev, V., Blanchet, J.-P., and Turner, D.: Matrix parameterization of the 15 μm CO2 band cooling in the middle and upper atmosphere for variable CO2 concentration, Journal of Geophysical Research: Atmospheres, 103, 11 505–11 528, 1998.

Friichtenicht, J.: Micrometeroid simulation using nuclear accelerator techniques, Nuclear Instruments and Methods, 28, 70 – 78, doi: http://dx.doi.org/10.1016/0029-554X(64)90351-9, 1964.

Gelinas, L. J., Lynch, K. A., Kelley, M. C., Collins, S., Baker, S., Zhou, Q., and Friedman, J. S.: First observation of meteoritic charged dust in the tropical mesosphere, Geophysical Research Letters, 25, 4047–4050, doi: 10.1029/1998GL900089, 1998.

Goldberg, R., Pfaff, R., Holzworth, R., Schmidlin, F., Voss, H., Tuzzolino, A., Croskey, C., Mitchell, J., Friedrich, M., Murtagh, D., et al.: DROPPS: A study of the polar summer mesosphere with rocket, radar and lidar, Geophysical research letters, 28, 1407–1410, 2001.

Grams, G. and Fiocco, G.: Equilibrium temperatures of spherical ice particles in the upper atmosphere and implications for noctilucent cloud formation, Journal of Geophysical Research, 82, 961–966, 1977.

Gumbel, J. and Megner, L.: Charged meteoric smoke as ice nuclei in the mesosphere: Part 1–A review of basic concepts, Journal of Atmospheric and Solar-Terrestrial Physics, 71, 1225–1235, doi: https://doi.org/10.1016/j.jastp.2009.04.012, 2009.

Gumbel, J. and Witt, G.: Rocket-borne photometry of NLC particle populations, Advances in Space Research, 28, 1053–1058, 2001.

Havnes, O.: Polar Mesospheric Summer Echoes (PMSE) overshoot effect due to cycling of artificial electron heating, Journal of Geophysical Research: Space Physics, 109, 2004.

Havnes, O. and Kassa, M.: On the sizes and observable effects of dust particles in polar mesospheric winter echoes, Journal of Geophysical Research: Atmospheres, 114, 2009.

Havnes, O. and Næsheim, L. I.: On the secondary charging effects and structure of mesospheric dust particles impacting on rocket probes, Annales Geophysicae, 25, 623–637, doi: 10.5194/angeo-25-623-2007, 2007.

Havnes, O., Morfill, G., and Goertz, C.: Plasma potential and grain charges in a dust cloud embedded in a plasma, Journal of Geophysical Research: Space Physics, 89, 10 999–11 003, 1984.

Havnes, O., Trøim, J., Blix, T., Mortensen, W., Næsheim, L. I., Thrane, E., and Tønnesen, T.: First detection of charged dust particles in the Earth's mesosphere, Journal of Geophysical Research: Space Physics, 101, 10 839–10 847, doi: 10.1029/96JA00003, 1996.

Havnes, O., Surdal, L. H., and Philbrick, C. R.: Mesospheric dust and its secondary effects as observed by the ESPRIT payload, Annales Geophysicae, 27, 1119–1128, doi: 10.5194/angeo-27-1119-2009, 2009.

Havnes, O., Gumbel, J., Antonsen, T., Hedin, J., and Hoz, C. L.: On the size distribution of collision fragments of NLC dust particles and their relevance to meteoric smoke particles, Journal of Atmospheric and Solar-Terrestrial Physics, 118, 190–198, doi: http://dx.doi.org/10.1016/j.jastp.2014.03.008, 2014.

Havnes, O., Antonsen, T., Hartquist, T., Fredriksen, Å., and Plane, J.: The Tromsø programme of in situ and sample return studies of mesospheric nanoparticles, Journal of Atmospheric and Solar-Terrestrial Physics, 127, 129–136, 2015.

Havnes, O., Antonsen, T., Baumgarten, G., Hartquist, T., Fredriksen, Å., Friedrich, M., and Hedin, J.: A new method to inference the size, number density, and charge of mesospheric dust from its in situ collection by the DUSTY probe., Atmospheric Measurement Techniques, In Review, 2018a.

Havnes, O., Latteck, R., Hartquist, T. W., and Antonsen, T.: First simultaneous rocket and radar detections of rare low summer mesospheric clouds., Geophysical Research Letters, 45, 5727–5734, doi: 10.1029/2018GL078218, 2018b.

Hedin, J., Gumbel, J., and Rapp, M.: On the efficiency of rocket-borne particle detection in the mesosphere, Atmospheric Chemistry and Physics, 7, 3701–3711, doi: 10.5194/acp-7-3701-2007, 2007.

Hedin, J., Giovane, F., Waldemarsson, T., Gumbel, J., Blum, J., Stroud, R. M., Marlin, L., Moser, J., Siskind, D. E., Jansson, K., et al.: The MAGIC meteoric smoke particle sampler, Journal of Atmospheric and Solar-Terrestrial Physics, 118, 127–144, 2014.

Hervig, M. E., Gordley, L. L., Stevens, M. H., Russell III, J. M., Bailey, S. M., and Baumgarten, G.: Interpretation of SOFIE PMC measurements: Cloud identification and derivation of mass density, particle shape, and particle size, Journal of Atmospheric and Solar-Terrestrial Physics, 71, 316–330, 2009.

Hervig, M. E., Deaver, L. E., Bardeen, C. G., III, J. M. R., Bailey, S. M., and Gordley, L. L.: The content and composition of meteoric smoke in mesospheric ice particles from SOFIE observations, Journal of Atmospheric and Solar-Terrestrial Physics, 84-85, 1 – 6, doi: http://dx.doi.org/10.1016/j.jastp.2012.04.005, 2012.

Hervig, M. E., Bardeen, C. G., Siskind, D. E., Mills, M. J., and Stockwell, R.: Meteoric smoke and H2SO4 aerosols in the upper stratosphere and mesosphere, Geophysical Research Letters, 44, 1150–1157, 2017.

Horányi, M., Gumbel, J., Witt, G., and Robertson, S.: Simulation of rocket-borne particle measurements in the mesosphere, Geophysical Research Letters, 26, 1537–1540, 1999.

Huba, J. D.: NRL: Plasma formulary, Tech. rep., NAVAL RESEARCH LAB WASHINGTON DC BEAM PHYSICS BRANCH, 2018.

Hunten, D. M., Turco, R. P., and Toon, O. B.: Smoke and Dust Particles of Meteoric Origin in the Mesosphere and Stratosphere, Journal of the Atmospheric Sciences, 37, 1342–1357, doi: 10.1175/1520-0469(1980)037<1342:SADPOM>2.0.CO;2, 1980.

Jacobsen, K., Pedersen, A., Moen, J., and Bekkeng, T.: A new Langmuir probe concept for rapid sampling of space plasma electron density, Measurement Science and Technology, 21, 085 902, 2010.

Jacobsen, T. and Friedrich, M.: Electron density measurements in the lower D-region, Journal of Atmospheric and Terrestrial Physics, 41, 1195 – 1200, doi: http://dx.doi.org/10.1016/0021-9169(79)90022-9, 1979.

Jesse, O.: Auffallende erscheinungen am abendhimmel, Met. Zeit, 2, 311–312, 1885.

John, W., Reischl, G., and Devor, W.: Charge transfer to metal surfaces from bouncing aerosol particles, Journal of Aerosol Science, 11, 115–138, 1980.

Jones, R., Pyle, J., Harries, J., Zavody, A., Russell, J., and Gille, J.: The water vapour budget of the stratosphere studied using LIMS and SAMS satellite data, Quarterly Journal of the Royal Meteorological Society, 112, 1127–1143, 1986.

Kalashnikova, O., Horanyi, M., Thomas, G., and Toon, O.: Meteoric smoke production in the atmosphere, Geophysical research letters, 27, 3293–3296, 2000.

Kassa, M., Rapp, M., Hartquist, T., and Havnes, O.: Secondary charging effects due to icy dust particle impacts on rocket payloads, Annales Geophysicae, 30, 433–439, 2012.

Kirkwood, S., Dalin, P., and Réchou, A.: Noctilucent clouds observed from the UK and Denmark–Trends and variations over 43 years, Annales geophysicae: atmospheres, hydrospheres and space sciences, 26, 1243, 2008.

Knappmiller, S., Rapp, M., Robertson, S., and Gumbel, J.: Charging of meteoric smoke and ice particles in the mesosphere including photoemission and photodetachment rates, Journal of Atmospheric and Solar-Terrestrial Physics, 73, 2212–2220, doi: http://dx.doi.org/10.1016/j.jastp.2011.01.008, 2011.

Kuuluvainen, H., Arffman, A., Saukko, E., Virtanen, A., and Keskinen, J.: A new method for characterizing the bounce and charge transfer properties of nanoparticles, Journal of Aerosol Science, 55, 104–115, 2013.

Kuuluvainen, H., Saari, S., Mensah-Attipoe, J., Arffman, A., Pasanen, P., Reponen, T., and Keskinen, J.: Triboelectric charging of fungal spores during resuspension and rebound, Aerosol Science and Technology, 50, 187–197, 2016.

Latteck, R., Singer, W., Rapp, M., Vandepeer, B., Renkwitz, T., Zecha, M., and Stober, G.: MAARSY: The new MST radar on Andøya—System description and first results, Radio Science, 47, 2012.

Lübken, F.-J., Lautenbach, J., Höffner, J., Rapp, M., and Zecha, M.: First continuous temperature measurements within polar mesosphere summer echoes, Journal of Atmospheric and Solar-Terrestrial Physics, 71, 453 – 463, doi: 10.1016/j.jastp.2008.06.001, 2009.

Leslie, R.: Sky glows, Nature, 32, 245, 1885.

Lie-Svendsen, Ø., Blix, T., Hoppe, U.-P., and Thrane, E.: Modeling the plasma response to small-scale aerosol particle perturbations in the mesopause region, Journal of Geophysical Research: Atmospheres, 108, 2003.

Lübken, F.-J.: Thermal structure of the Arctic summer mesosphere, Journal of Geophysical Research: Atmospheres, 104, 9135–9149, 1999.

Lübken, F.-J. and Höffner, J.: Experimental evidence for ice particle interaction with metal atoms at the high latitude summer mesopause region, Geophysical research letters, 31, 2004.

Lübken, F.-J., Hillert, W., Lehmacher, G., Von Zahn, U., Bittner, M., Offermann, D., Schmidlin, F., Hauchecorne, A., Mourier, M., and Czechowsky, P.: Intercomparison of density and temperature profiles obtained by lidar, ionization gauges, falling spheres, datasondes and radiosondes during the DYANA campaign, Journal of Atmospheric and Terrestrial Physics, 56, 1969–1984, 1994.

Lübken, F.-J., Strelnikov, B., Rapp, M., Singer, W., Latteck, R., Brattli, A., Hoppe, U.-P., and Friedrich, M.: The thermal and dynamical state of the atmosphere during polar mesosphere winter echoes, Atmospheric chemistry and physics, 6, 13–24, 2006.

Lübken, F.-J., Berger, U., and Baumgarten, G.: Temperature trends in the midlatitude summer mesosphere, Journal of Geophysical Research: Atmospheres, 118, 13,347–13,360, doi: 10.1002/2013JD020576, 2013.

Markovic, N., Andersson, P. U., Någård, M. B., and Pettersson, J. B.: Scattering of water from graphite: simulations and experiments, Chemical Physics, 247, 413 – 430, doi: http://dx.doi.org/10.1016/S0301-0104(99)00233-5, 1999.

Mathews, J., Janches, D., Meisel, D., and Zhou, Q.-H.: The micrometeoroid mass flux into the upper atmosphere: Arecibo results and a comparison with prior estimates, Geophysical Research Letters, 28, 1929–1932, 2001.

Megner, L., Rapp, M., and Gumbel, J.: Distribution of meteoric smoke – sensitivity to microphysical properties and atmospheric conditions, Atmospheric Chemistry and Physics, 6, 4415–4426, doi: 10.5194/acp-6-4415-2006, 2006.

Megner, L., Siskind, D., Rapp, M., and Gumbel, J.: Global and temporal distribution of meteoric smoke: A two-dimensional simulation study, Journal of Geophysical Research: Atmospheres, 113, 2008.

Megner, L., Khaplanov, M., Baumgarten, G., Gumbel, J., Stegman, J., Strelnikov, B., and Robertson, S.: Large mesospheric ice particles at exceptionally high altitudes, Annales Geophysicae, 27, 943–951, doi: 10.5194/angeo-27-943-2009, 2009.

Meriwether, J. W. and Gerrard, A. J.: Mesosphere inversion layers and stratosphere temperature enhancements, Reviews of Geophysics, 42, 2004.

Miles, D. M., Mann, I. R., M., C., D., B., Narod, B. B., Bennes, t. J. R., Pakhoti, n. I. P., A., K., B., B., Nokes, C. D. A., C., C., Haluza-DeLay, T., Elliott, D. G., and Milling, D. K.: A miniature, low-power scientific fluxgate magnetometer: A stepping-stone to cube-satellite constellation missions, Journal of Geophysical Research: Space Physics, 121, 11,839–11,860, doi: 10.1002/2016JA023147, 2016.

Moshfegh, A., Shams, M., Ahmadi, G., and Ebrahimi, R.: A new expression for spherical aerosol drag in slip flow regime, Journal of Aerosol Science, 41, 384–400, 2010.

Murad, E., Swider, W., and Benson, S. W.: Possible role for metals in stratospheric chlorine chemistry, Nature, 289, 273–274, 1981.

Murray, B. J. and Jensen, E. J.: Homogeneous nucleation of amorphous solid water particles in the upper mesosphere, Journal of Atmospheric and Solar-Terrestrial Physics, 72, 51–61, doi: 10.1016/j.jastp.2009.10.007, 2010.

Pedersen, A., Troim, J., and Kane, J.: Rocket measurements showing removal of electrons above the mesopause in summer at high latitude, Planetary and Space Science, 18, 945–947, doi: https://doi.org/10.1016/0032-0633(70)90092-9, 1970.

Plane, J. M.: On the role of metal silicate molecules as ice nuclei, Journal of Atmospheric and Solar-Terrestrial Physics, 73, 2192–2200, 2011.

Plane, J. M.: Cosmic dust in the Earth's atmosphere, Chemical Society Reviews, 41, 6507–6518, 2012.

Plane, J. M. C.: A time-resolved model of the mesospheric Na layer: constraints on the meteor input function, Atmospheric Chemistry and Physics, 4, 627–638, doi: 10.5194/acp-4-627-2004, 2004.

Pruppacher, H. R. and Klett, J. D.: Microphysics of clouds andrecipitation, Wiley, 1997.

Rapp, M.: Charging of mesospheric aerosol particles: the role of photodetachment and photoionization from meteoric smoke and ice particles, Annales Geophysicae, 27, 2417, 2009.

Rapp, M. and Lübken, F.-J.: Polar mesosphere summer echoes (PMSE): Review of observations and current understanding, Atmospheric Chemistry and Physics, 4, 2601–2633, doi: 10.5194/acp-4-2601-2004, 2004.

Rapp, M. and Thomas, G. E.: Modeling the microphysics of mesospheric ice particles: Assessment of current capabilities and basic sensitivities, Journal of Atmospheric and Solar-Terrestrial Physics, 68, 715 – 744, 2006.

Rapp, M., Gumbel, J., and Lübken, F.-J.: Absolute density measurements in the middle atmosphere, Annales Geophysicae, 19, 571–580, 2001.

Rapp, M., Lübken, F.-J., and Blix, T.: Small scale density variations of electrons and charged particles in the vicinity of polar mesosphere summer echoes, Atmospheric Chemistry and Physics, 3, 1399–1407, 2003a.

Rapp, M., Lübken, F.-J., Hoffmann, P., Latteck, R., Baumgarten, G., and Blix, T. A.: PMSE dependence on aerosol charge number density and aerosol size, Journal of Geophysical Research: Atmospheres, 108, 2003b.

Rapp, M., Strelnikova, I., and Gumbel, J.: Meteoric smoke particles: Evidence from rocket and radar techniques, Advances in Space Research, 40, 809–817, 2007a.

Rapp, M., Thomas, G. E., and Baumgarten, G.: Spectral properties of mesospheric ice clouds: Evidence for nonspherical particles, Journal of Geophysical Research: Atmospheres, 112, 2007b.

Rapp, M., Strelnikova, I., Latteck, R., Hoffmann, P., Hoppe, U.-P., Häggström, I., and Rietveld, M. T.: Polar mesosphere summer echoes (PMSE) studied at Bragg wavelengths of 2.8 m, 67 cm, and 16 cm, Journal of Atmospheric and Solar-Terrestrial Physics, 70, 947–961, 2008.

Rapp, M., Strelnikova, I., Strelnikov, B., Friedrich, M., Gumbel, J., Hoppe, U.-P., Blix, T., Havnes, O., Bracikowski, P., Lynch, K., and Knappmiller, S.: Microphysical Properties of Mesospheric Aerosols: An Overview of In Situ-Results from the ECOMA Project, in: Aeronomy of the Earth's Atmosphere and Ionosphere, chap. 4, pp. 67–74, Springer Netherlands, Dordrecht, 2011.

Rizk, B., Hunten, D., and Engel, S.: Effects of size-dependent emissivity on maximum temperatures during micrometeorite entry, Journal of Geophysical Research: Space Physics, 96, 1303–1314, 1991.

Robertson, S., Horanyi, M., Knappmiller, S., Sternovsky, Z., Holzworth, R., Shimogawa, M., Friedrich, M., Torkar, K., Gumbel, J., Megner, L., Baumgarten, G., Latteck, R., Rapp, M., Hoppe, U.-P., and Hervig, M. E.: Mass analysis of charged aerosol particles in NLC and PMSE during the ECOMA/MASS campaign, Annales Geophysicae, 27, 1213–1232, doi: 10.5194/angeo-27-1213-2009, 2009.

Rosinski, J. and Snow, R.: Secondary particulate matter from meteor vapors, Journal of Meteorology, 18, 736–745, 1961.

Saunders, R., Möhler, O., Schnaiter, M., Benz, S., Wagner, R., Saathoff, H., Connolly, P., Burgess, R., Murray, B., Gallagher, M., et al.: An aerosol chamber investigation of the heterogeneous ice nucleating potential of refractory nanoparticles., Atmospheric Chemistry & Physics, 10, 2010.

Saunders, R. W. and Plane, J. M.: A laboratory study of meteor smoke analogues: Composition, optical properties and growth kinetics, Journal of Atmospheric and Solar-Terrestrial Physics, 68, 2182–2202, 2006.

Schröder, W.: Were noctilucent clouds caused by the Krakatoa eruption? A case study of the research problems before 1885, Bulletin of the American Meteorological Society, 80, 2081–2086, 1999.

Schulte, P. and Arnold, F.: Detection of upper atmospheric negatively charged microclusters by a rocket-borne mass spectrometer, Geophysical research letters, 19, 2297–2300, 1992.

Seibert, G. and Battrick, B. T.: The history of sounding rockets and their contribution to European space research, ESA Publications division, 2006.

She, C., Williams, B., Hoffmann, P., Latteck, R., Baumgarten, G., Vance, J., Fiedler, J., Acott, P., Fritts, D., and Lübken, F.-J.: Simultaneous observation of sodium atoms, NLC and PMSE in the summer mesopause region above ALOMAR, Norway (69°N, 12°E), Journal of Atmospheric and Solar-Terrestrial Physics, 68, 93 – 101, doi: https://doi.org/10.1016/j.jastp.2005.08.014, phenomena of the Summertime Mesosphere, 2006.

Smirnov, R., Pigarov, A. Y., Rosenberg, M., Krasheninnikov, S., and Mendis, D.: Modelling of dynamics and transport of carbon dust particles in tokamaks, Plasma Physics and Controlled Fusion, 49, 347, 2007.

Solomon, S.: Stratospheric ozone depletion: A review of concepts and history, Reviews of Geophysics, 37, 275–316, 1999.

Strelnikov, B., Rapp, M., Strelnikova, I., Engler, N., and Latteck, R.: Small-scale structures in neutrals and charged aerosol particles as observed during the ECOMA/MASS rocket campaign, Annales Geophysicae, 27, 1449–1456, 2009.

Stroud, W., Nordberg, W., Bandeen, W., Bartman, F., and Titus, P.: Rocket-grenade measurements of temperatures and winds in the mesosphere over Churchill, Canada, Journal of Geophysical Research, 65, 2307–2323, 1960.

Thomas, G. and Olivero, J.: Noctilucent clouds as possible indicators of global change in the mesosphere, Advances in Space Research, 28, 937–946, 2001.

Thomas, G. E., Olivero, J. J., Jensen, E. J., Schroeder, W., and Toon, O. B.: Relation between increasing methane and the presence of ice clouds at the mesopause, Nature, 338, 490, 1989.

Tomsic, A.: Collisions between water clusters and surfaces, Ph.D. thesis, Göteborg University, 2001.

Tomsic, A., Marković, N., and Pettersson, J. B.: Direct scattering and trapping–desorption of large water clusters from graphite, Chemical Physics Letters, 329, 200 – 206, doi: http://dx.doi.org/10.1016/S0009-2614(00)01002-2, 2000.

Tomsic, A., Andersson, P. U., Markovic, N., Piskorz, W., Svanberg, M., and Pettersson, J. B. C.: Molecular dynamics simulations of cluster-surface collisions: Emission of large fragments, The Journal of Chemical Physics, 115, 10 509–10 517, doi: http://dx.doi.org/10.1063/1.1413740, 2001.

Tomsic, A., Schröder, H., Kompa, K.-L., and Gebhardt, C. R.: Impact dynamics of molecular clusters on surfaces: Fragmentation patterns and anisotropic effects, The Journal of Chemical Physics, 119, 6314–6323, doi: http://dx.doi.org/10.1063/1.1603213, 2003.

Varney, R. H., Kelley, M. C., Nicolls, M. J., Heinselman, C. J., and Collins, R. L.: The electron density dependence of polar mesospheric summer echoes, Journal of Atmospheric and Solar-Terrestrial Physics, 73, 2153–2165, 2011.

Voigt, C., Schlager, H., Luo, B., Dörnbrack, A., Roiger, A., Stock, P., Curtius, J., Vössing, H., Borrmann, S., Davies, S., et al.: Nitric acid trihydrate (NAT) formation at low NAT supersaturation in polar stratospheric clouds (PSCs), Atmospheric chemistry and physics, 5, 1371–1380, 2005.

Von Cossart, G., Fiedler, J., and Von Zahn, U.: Size distributions of NLC particles as determined from 3-color observations of NLC by ground-based lidar, Geophysical Research Letters, 26, 1513–1516, 1999.

Von Zahn, U. and Berger, U.: Persistent ice cloud in the midsummer upper mesosphere at high latitudes: Three-dimensional modeling and cloud interactions with ambient water vapor, Journal of Geophysical Research: Atmospheres, 108, 2003.

Von Zahn, U., Von Cossart, G., Fiedler, J., Fricke, K., Nelke, G., Baumgarten, G., Rees, D., Hauchecorne, A., and Adolfsen, K.: The ALOMAR Rayleigh/Mie/Raman lidar: objectives, configuration, and performance, Annales Geophysicae, 18, 815–833, 2000.

Vostrikov, A. and Dubov, D. Y.: Surface induced ionization of neutral water clusters, Zeitschrift für Physik D Atoms, Molecules and Clusters, 20, 61–63, 1991.

Wegener, A.: Die Erforschung der obersten Atmosphärenschichten, Zeitschrift für anorganische Chemie, 75, 107–131, 1912.

Woodman, R. F. and Guillen, A.: Radar observations of winds and turbulence in the stratosphere and mesosphere, Journal of the Atmospheric Sciences, 31, 493–505, 1974.

Zahn, U.: Are noctilucent clouds a "Miner's Canary" for global change?, EOS, Transactions American Geophysical Union, 84, 261–264, 2003.

Zasetsky, A., Petelina, S. V., and Svishchev, I.: Thermodynamics of homogeneous nucleation of ice particles in the polar summer mesosphere, Atmospheric Chemistry and Physics, 9, 965–971, 2009.

Zuppardi, G., Morsa, L., Savino, R., Sippel, M., and Schwanekamp, T.: Rarefied aerodynamic characteristics of aero-space-planes: a comparative study of two gas–surface interaction models, European Journal of Mechanics-B/Fluids, 53, 37–47, 2015.

PAPER I

Antonsen, T. and Havnes, O.: On the detection of mesospheric meteoric smoke particles embedded in noctilucent cloud particles with rocket-borne dust probes, Review of Scientific Instruments, 86, 033 305, doi: http://dx.doi.org/10.1063/1.4914394, 2015

On the detection of mesospheric meteoric smoke particles embedded in noctilucent cloud particles with rocket-borne dust probes

T. Antonsen[a] and O. Havnes
Department of Physics and Technology, University of Tromsø, NO-9037 Tromsø, Norway

(Received 26 June 2014; accepted 25 February 2015; published online 20 March 2015)

Mesospheric nanoparticles in the forms of water ice particles and meteoric smoke particles (MSPs) exist in the middle atmosphere where they often play a decisive role in cloud formation and in chemical processes. Direct *in situ* observations of mesospheric nanoparticles have been made possible by rocket probes developed during the last two decades. Although progress has been made in mapping properties such as electric charge, sizes, and interaction with the plasma and neutral gas, more observations are needed on the size distribution, chemical content, and structure of the MSP to determine their role in cloud formation and chemistry in the mesosphere and stratosphere. We here present the result of a detailed analysis of the performance of a new dust probe MUltiple Dust Detector (MUDD) [O. Havnes *et al.*, J. Atmos Soll.-Terr. Phys. **118**, 190 (2014); O. Havenes *et al.*, *ibid.* (in press)], which should give information of the size distribution of MSP by fragmenting impacting ice particles and releasing a fraction of the MSP which most probably are embedded in them [O. Havnes and L. I. Naesheim, Ann. Geophys. **25**, 623 (2007); M. E. Hervig *et al.*, J. Atmos. Sol.-Terr. Phys. **84-85**, 1 (2012)]. We first determine the electric field structure and neutral gas condition in the interior of the probe and from this compute, the dynamics and current contribution of the charged fragments to the currents measured as the probe scans the fragment energy. For the single MUDD probe flown in July 2011 on the PHOCUS payload, we find that the fragment currents at the three retarding potentials for MUDD of 0, 10, and 20 V correspond to fragment sizes of $\gtrsim$0.6 nm, >1.5 nm, and >1.8 nm if the fragments have a negative unit charge. We also discuss the optimum choice of retarding potentials in future flights of MUDD probes. By launching 2 to 3 mechanically identical MUDD probes but with different retarding potentials, we will obtain a much more detailed and reliable fragment (MSP) size distribution. © *2015 AIP Publishing LLC.* [http://dx.doi.org/10.1063/1.4914394]

I. INTRODUCTION

Dust particles, or aerosols, are abundant throughout the entire terrestrial atmosphere. In the high latitude mesosphere, at heights between ~80 and 90 km, dust or ice particles are found mainly in the form of nanoscale ice grains which can be optically detected as noctilucent clouds (NLCs)[5,6] or their related sub-visual phenomenon, polar mesospheric summer echoes (PMSEs).[7,8] A common factor of many of these studies is the connection between the icy dust forms and meteoric smoke particles (MSPs) which are discussed in more depth below.

The mesospheric dust has received a considerable amount of attention over the last couple of decades, much because of the implications they are suggested to have for the middle atmosphere chemistry. Strong evidence exists for the effective depletion of Potassium (K) and Sodium (Na) layers in the presence of icy dust particles.[9,10] The direction of the polar middle atmosphere wind draught is upwards during the summer and is thought to be important for the rapid growth of NLC particles. During winter, the wind draught changes direction and dust can acquire momentum downwards.[11–13] At lower altitudes, dust particles supply surface area where chemical reactions both indirectly and directly can remove ozone.[14,15] The temperature in the mesosphere has sunk $O(1)$ K since 1979, with cooling rates up to 0.4 Kyr^{-1}.[16,17] This offers an explanation for the significant increase in NLC frequency since 1979.[18,19] Mesospheric dust has moreover been suggested to indicate changes in the climate;[20,21] however, such capabilities have been challenged.[22]

Basic research on nucleation and growth mechanisms, the complex chemistry of the particles and their possible connection with neighboring atmospheric layers are other fields which are constrained by the limitations of observational studies. In the troposphere, long-time measurements by balloon and *in situ* measurements by airplane are much used techniques (see, e.g., Cziczo, Thomson, and Murphy[23] and Bigg[24] for recent reviews); however, these methods cannot be applied for mesospheric probing. Indirect remote methods such as ground based and space borne radar may be used, but have limitations. For this reason, rockets have become indispensable for mesosphere research as it is the only method which allows for *in-situ* operation. In addition, the sensitivity of rocket instrumentation is far superior of that of remote methods making the rocket the only tool to probe small scale phenomena.

Since the first direct evidence for charged particles in the mesosphere was presented by Havnes *et al.*,[25] a faraday cup design such as their DUSTY probe has often been the basic design for attempts of *in situ* measurement of various dust and aerosol particles. Gelinas *et al.*,[26] Lynch *et al.*,[27] and Rapp *et al.*[28] all used modified designs to successfully detect charged

[a]Electronic mail: tarjei.antonsen@uit.no

particles in the mesosphere. These studies represent important steps towards an experimental verification of theoretical MSP size distributions and charge state. *In situ* studies, such as the previous, have confirmed the elusive nature of MSPs and have pointed out problems with decisively determining their characteristics. By using alternative mass spectrometer designs, Schulte and Arnold[29] and Robertson *et al.*[30] detected aerosols with sizes of up to a few nanometers in the mesosphere. A major problem for MSP detection experiments is that particles at their sizes tend to be swept away from rocket probes by the airflow around them.[31,32] This greatly complicates the utilization of faraday cup designs. However, recent observations and new considerations presented in this paper that NLC particles probably contain a significant number of embedded MSPs which suggest that a simple cup design can indeed be used to detect MSPs.

The daily mass influx of meteoric material into the middle atmosphere is generally thought to be on the order of 1–100 metric tons (Love and Brownlee;[33] see Plane[34] for a recent review). The majority of the meteoric ablation occurs in the height range between 70 and 110 km where they deposit layers of atomic metals.[35,36] Rosinski and Snow[37] proposed early that the oxidization of ablation vapor could create species such as iron oxide (FeO) and silicon oxides (SiO/SiO_2) which were likely to subsequently re-condense into nanometer-scale solid particles, so called MSPs. This work was further developed by Hunten, Turco, and Toon[38] who introduced a microphysical model considering not only the initial re-condensation, but also subsequent growth of the particles by coagulation, and particle transport by eddy-diffusion. The calculations in the latter work predicted number densities of MSPs up to several thousand cm^{-3} for sizes up to a few nanometers.

The chemical composition of these smoke particles has been discussed since their theorization. Current studies from both laboratory and remote measurements by satellite have proposed compositions consistent with a chondritic origin.[4,39] Moreover, electron structure theory has been used to justify that metal silicates with large dipole moments should form in the mesosphere and subsequently, act as efficient nucleation sites for water to form icy dust particles.[40] This latter work extends the view that MSPs are the most likely nuclei for mesospheric ice particles (see Rapp and Thomas[41] for a detailed review) to a nuclei of few or single molecules of meteoric origin. Early models of NLC particle nucleation relied on the idea that NLCs contained cores of single MSPs and had few other contaminants in the ice layer,[42] a view that was withheld for a long time and even backed up by experiments.[6,43] However, impurities such as molecules of meteoric origin and larger MSPs may amplify the growth significantly by lowering the surface energy barrier for nucleation.[44,45] On the basis of rocket measurements and modeling, Havnes and Næsheim[3] shifted this view of the traditional NLC particle towards an ice dust particle with *many* embedded MSPs, uniformly distributed as the different nucleation and growth mechanisms compete until a depletion of the local water density. Recently, this embedded MSP prediction has obtained further support from satellite observations,[4] which estimates a volume filling factor of meteoric material between 0.01% and 3% in dust from polar mesospheric clouds (PMCs). It should be noted, however, that by modeling the global MSP distribution, Megner *et al.*[46,47] found that the concentrations of MSPs at the polar summer mesopause were not high enough to account for the high number density of the NLC particles alone, opening for the ongoing discussion on NLC nucleation and growth mechanisms and MSP transport. Those works propose that a pure heterogeneous mechanism may be insufficient for explaining nucleation, but that free smoke particles can be effective nuclei when accompanied by moderate temperature gradients. This could significantly increase the number of available nucleation sites compared to a situation where MSP of sizes ~1 nm was required for condensation into larger ice particles. Homogeneous mechanisms, where the mesospheric water vapor condenses to amorphous and even solid states, have furthermore been shown to compete with heterogenous nucleation when the temperature gradient is moderately negative, as can be the case in temporarily strong cooling forced by gravity waves propagating upwards.[44,48] Measurements of NLC particle radii have been found to be consistent with a mean of around 50 nm for a monodispersive distribution and shifted downwards for polydisperse distributions.[49–51] These "large" particles must therefore have grown substantially, even if the initial nucleus was a MSP with a radius in the upper tail of their theoretical size distribution (see Hunten, Turco, and Toon[38] and Megner, Rapp, and Gumbel[52]).

The present paper aims to utilize the "new" NLC particle and simulate the dynamics of its fragments inside a bucket probe. For this purpose, we use the MUDD probe (MUltiple Dust Detector) which was developed at the University of Tromsø and flown in the PHOCUS campaign in July 2011, as our simulation domain. Several studies have found that dust particles colliding with surfaces on rockets will rub off secondary charges, a process which in some cases has been found to dominate the recorded signal.[3,25,53–55] It has been argued[1,3,55] that the large secondary production is mainly caused by the presence of the embedded MSPs which will not evaporate even if similarly small ice particles would. The majority of the smallest fragments may therefore reflect the true size distribution of MSPs. We report the results of modeling collision fragment motion and current contribution to the grids inside bucket dust probes similar to the DUSTY probe.[25] The motion is calculated on basis of E-field and neutral gas condition simulations. The numerical model we have developed is aimed at being used both to improve the analysis of results from MUDD probes which have been, and will be, launched and to assist in developing new rocket probes for measuring dust in the mesosphere. The MUDD probe[1,2] is nearly identical to the DUSTY probe except that its lowest grid (G2) is made up of concentric inclined strips. Due to this, no ambient dust particle entering the probe can pass and directly hit the bottom plate of the probe. They will all hit G2 and we expect the majority of the icy NLC/PMSE particles to partly fragment and that many of the fragments will rub off charge from G2 and carry them to the bottom plate. We do not expect "free" MSP, which are not embedded into NLC/PMSE particles, to contribute significantly to the currents measured at the bottom plate of MUDD. The majority of such "free" MSP, having sizes below ~2 nm, will be carried away from the

probe by the airstream around the payload. Larger MSP may enter the probe, but for sizes up to ~5 nm, the impact velocities will be low, resulting in a low probability for charging, or in attachment to the impact grid G2.

In Sec. II, we present the technical details of the MUDD detector. Section III is dedicated to our theoretical model, including E-field simulations, neutral gas simulations, and charged dust dynamics. The model equations for transport and evaporation of dust particles and the closure of these based on static background simulations are presented. The results from our simulations of pure MSP fragments and pure ice fragments resulting from the collision of NLC particles in MUDD are presented in Sec. IV. A discussion is given in Sec. V.

II. THE MUDD PROBE

Figure 1 shows a principle sketch of the MUDD probe, which is an augmentation of the original bucket design of Havnes *et al.*[25] The detector is a faraday cup with two biased square meshes, G0 and G1, and a lower biased fragmentation grid, G2, which consists of partly overlapped inclined (≈20° with normal) concentric rings, allowing for no direct dust particle influx to the bottom detector plate, BP. The uppermost grid, G0, is set to the rocket payload potential; ideally at 0 V, however, rocket payloads often acquire small negative voltages during flight.[56] Small bias voltages on the probe (~1 V) will not significantly affect the grid voltages, as the grids are isolated from the payload, and the field from the probe walls does not affect the vertical motion of fragments. The G1 grid is biased to a constant value of +6.2 V, which will shield out ambient positive ions, while electrons may pass. The ion flux can be affected by boundary E-field effects, as will be discussed. The dust particles which hit G2 are mainly NLC or PMSE particles, and their fragments will move towards BP if they are not stopped by the electric field or neutral gas drag. "Free" MSP particles in the ambient dust population are either deflected away from the MUDD probe or, if entering it, they are broken so much that their probability for charging is very low, or they attach to G2. They do not contribute significantly to the current at BP. G2 has a constant voltage of +10 V, while BP alternates between +10 V, 0 V, −10 V, and back to 0 V and then repeats this cycle. Details on the sampling scheme for the MUDD probe launched in 2011 can be found in Havnes *et al.*[1] The BP current sampling frequency was then 1920 Hz, but the scheme will be improved for the launch of MaxiDusty-I. The electric field—and retarding potential—is zero between BP and G2 for the mode in which V_{BP} = 10 V. This mode measures all charged fragments which are not stopped by neutral drag and will also measure the current of a significant number of free electrons for which a correction must be made.[1,2] In regions where dust is absent, this electron "leakage" current is the only contribution to BP. The other voltage modes of retarding potentials 10 V and 20 V will not measure free electron current, as they are stopped by the electric fields. By altering the G2-BP E-fields, fragments from different regions of the energy spectrum will hit BP, and this study is concerned with how to obtain a fragment size distribution from the measured currents.

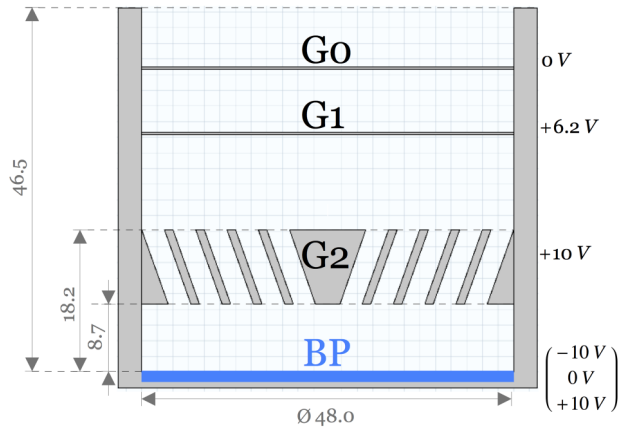

FIG. 1. Vertical cross section of the MUDD probe. Length measures are in millimeters.

III. MODELING

In our efforts to solve the problem of single dust fragment dynamics inside MUDD, we present a model based on parameters from different background simulations. We have split the modeling into three parts: electric field structure, neutral gas field fields, and charged dust grain dynamics including heating and evaporation. The E-field and neutral gas simulations are used as static inputs for the dust simulations.[57] The neutral gas and dust calculations are presented in Secs. III A and III B below. The E-field simulations will not be addressed in depth here. A FEM-procedure solving Poisson's equation in radial symmetry from COMSOL[57] was used to calculate the different field configurations for the rotational symmetric MUDD probe. The E-field configuration for the case when the BP voltage is $V_{BP} = -10V$, i.e., the mode of largest retarding potential which will detect the highest energy particles, is presented in Fig. 2.

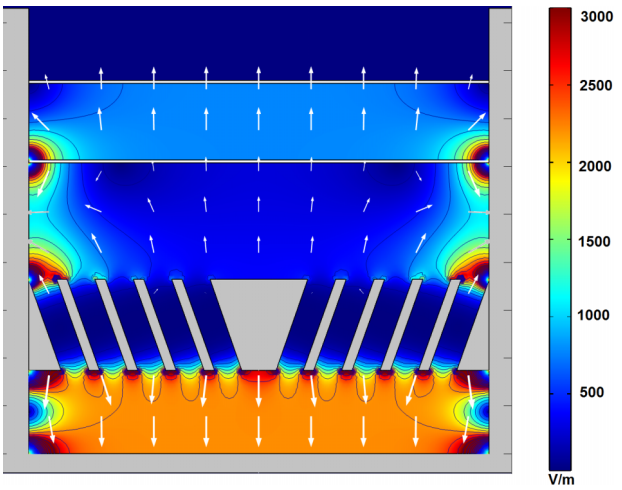

FIG. 2. Electric field in Vm^{-1} inside MUDD for a bottom plate potential of −10 V. The field values are cutoff at 3000 V/m, although the fields around sharp edges can be a factor of 10 larger than this; however, this effect is very local.

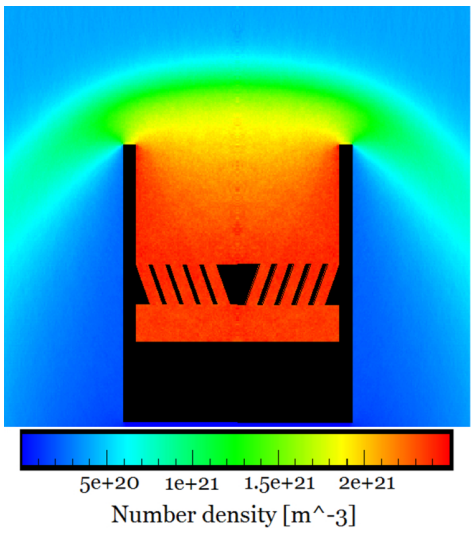

FIG. 3. Simulated neutral gas number density around MUDD at 82 km altitude, for $v_r = 750$ ms^{-1}.

A. Neutral gas fields

The degree to which a gas is rarefied can be quantified by the dimensionless Knudsen number, Kn, defined as the ratio of the mean free path of undisturbed flight of a gas molecule to a characteristic dimension, e.g., an instrument dimension or dust radius, of a system,

$$Kn = \frac{\lambda_{mfp}}{L}. \tag{1}$$

For a typical dust bucket probe, i.e., $L \sim 0.1$ m, inside and in the vicinity of rocket probes during operation in the mesosphere, the mean free path is large enough so that the collision derivative in Boltzmann's transport equation is not well defined. The continuous flow Navier-Stokes equations or other modified versions of Boltzmann's equation can thus not be used to derive neutral gas fields inside the probe.[58] The solution is to treat the gas flow with probabilistic methods; the Direct Simulation Monte Carlo (DSMC) method proposed by G. Bird (described in Bird[59]) to obtain quasi-steady solutions. We will in this study use the DS2V code written by Bird to treat the problem in rotational symmetry, searching for steady flows at large times. The flow fields are subsequently used as input to the dust fragment simulations and is shown in Fig. 3.

B. Dust dynamics

The relatively low ambient gas density in the height region of NLCs, generally between 80 and 90 km, ensures that the compressed air outside, in front and inside of a bucket probe is dominated by transitional flow Knudsen numbers (~0.01 – 1 for our system). For the neutral gas-dust drag force, we therefore use an expression modified for this regime, valid for sub- and supersonic dust speeds, assuming a specular reflection of neutrals in a collision with a dust grain,[60,61]

$$\mathbf{F}_{gd} = \chi \pi r_d^2 m_g n_g v_{th,g} (\mathbf{v}_g - \mathbf{v}_d) \frac{1}{u} \left\{ \frac{1}{\sqrt{\pi}} \left(u + \frac{1}{2u} \right) \exp(-u^2) + \left(1 + u^2 - \frac{1}{4u^2} \right) \mathrm{erf}(u) \right\}, \tag{2}$$

where r_d and $\mathbf{v}_d$ are the dust fragment radius and velocity, respectively; $m_g, n_g, \mathbf{v}_g$, and $v_{th,g} = (2k_B T_g/m_g)^{\frac{1}{2}}$ are the local neutral gas parameters, and $u = |\mathbf{v}_g - \mathbf{v}_d|/v_{th,g}$ is the relative Mach number of the dust particles. The factor $\chi = F_{gd}^p / F_{gd}^{ve}$ is the dynamic shape factor defined as the ratio of the neutral air drag on a non-spherical particle to the drag introduced by its volume equivalent sphere.[62] This correction factor is useful for modeling dynamics of non-spherical agglomerates, but its dependence of particle orientation, flow regime, and particle size can introduce uncertainties.[63]

When ignoring incoming radiation and thermal emission, as motivated by the finding of Rizk, Hunten, and Engel[64] that sub-micron particles of meteoric origin tend to not radiate away heat easily, the energy balance energy equation becomes[31,61]

$$\begin{aligned} \hat{P}_N &= \frac{\pi}{4} r_d^2 n_g v_{th,g} k_B T_g \left\{ \frac{2}{\sqrt{\pi}} \left[5 + 2u^2 \right] \exp(-u^2) + \frac{1}{\sqrt{u^2}} \left[3 + 12u^2 + 4u^4 \right] \mathrm{erf}(u) \right\} \\ &= \frac{4\pi}{3} \rho_d r_d^3 c_p \frac{dT_d}{dt} + L_d \frac{dm_d}{dt}, \end{aligned} \tag{3}$$

where ρ_d, m_d, and L_d are the mass density, mass, and latent heat of evaporation of a dust grain, respectively; c_p denotes the specific heat of the dust grains. The numeric values of the parameters used in the simulations are summarized in Table I. The expression denoted $\hat{P}_N$ on the lhs is the heating power of dust grains due to collisions with neutrals modified for

TABLE I. The basic set of dust parameters used in the simulations.

Parameter	Value	Note
MSP mass density, ρ_s	3000 kgm^{-3}	Plane,[40] Klekociuk *et al.*[80]
Ice mass density, ρ_i	980 kgm^{-3}	
Fragment charge, q_d	−1 e	Discussed in Sec. III C
Mean dust weight, m_D	140/18 a.m.u.	For MSP/ice, respectively
Initial fragment velocity, v_0	450 ms^{-1}	Tomsic[68]
Latent heat of vaporization of ice, L^{ice}	2.78×10^6 J kg^{-1}	Lichtenegger and Kömle[81]
Latent heat of vaporization of MSP, L^{smoke}	6×10^6 J kg^{-1}	Hunten, Turco, and Toon[38]
Specific heat of ice, c_p^i	$90+7.5T_d$ J kg^{-1}K^{-1}	Klinger[82]
Specific heat of smoke, c_p^s	1000 J kg^{-1}K^{-1}	Hunten, Turco, and Toon[38]
Mean surface energy of smoke, $\bar{\gamma}_{smoke}$	0.200 J m^{-2}	Gundlach *et al.*[83]
Surface energy of ice, γ_{ice}	0.190 J m^{-2}	Heim *et al.*[84]

diffusive reflection of the neutral gas molecules which leave with the characteristic temperature of the dust.[61] The rhs terms originate from the heat due to increased temperature and the heat loss due to vaporization of the grain, respectively.

By assuming local thermodynamic equilibrium and that surface molecules leave diffusively from the dust grain, we can express the rate of change in radius as a function of intrinsic dust properties (cf. Evans[45]),

$$\frac{\mathrm{d}r_d}{\mathrm{d}t} = -\frac{P_{vap}(T_d,r_d)}{\rho_d}\left(\frac{m_D}{2\pi k_B T_d}\right)^{\frac{1}{2}}, \tag{4}$$

where $P_{vap}(T_d,r_d)$ is the material specific vapor pressure, m_D is the mass of *one* dust surface molecule, and ρ_d is the grain density.

Podolak, Pollack, and Reynolds[65] give the vapor pressure terms for ice and MSP-like components as

$$P_{vap}(T_d) = \begin{cases} 3.89\cdot 10^{10}\exp\left(-4845/T_d\right) & \text{for ice} \\ 1.51\cdot 10^{12}\exp\left(-56655/T_d\right) & \text{for smoke} \end{cases}. \tag{5}$$

However, we must correct this for very small surfaces. The term which allows for spherical ejection of material from small bodies is given in Evans[45] as

$$P_{vap}(T_d,r_d) = P_{vap}(T_d)\cdot\exp\left(\frac{2\gamma m_D}{\rho_d k_B T_d r_d}\right), \tag{6}$$

where $P_{vap}(T_d)$ is the term from Eq. (5), and γ is the specific surface energy of the dust grain.

We calculate the dust grain temperature self-consistently from Eq. (3) by rewriting the mass derivative,

$$\frac{\mathrm{d}T_d}{\mathrm{d}t} = \frac{\hat{P}_N - L_d\cdot 4\pi r_d^2\left(\frac{m_D}{2\pi k_B T_d}\right)^{\frac{1}{2}}\cdot P_{vap}(T_d,r_d)}{\frac{4\pi}{3}\rho_d r_d^3 c_p}. \tag{7}$$

Neutral gas field solutions from the DSMC simulations as well as electric field solutions and dust material specific parameters were used to close the model equations for single dust particle movement. Most emphasis was put on the movement of single charged fragments, as NLC particles are expected to be partly crushed and that fragments are ejected from the concentric rings of G2. This process is discussed in more detail in Sec. V A. In Figure 4, we present typical results from the idealized situation where the fragmentation at one of the inclined concentric rings is considered. The local deviation from a homogeneous electric field between G2 and BP and inside G2 was neglected. The particles were traced from the point of fragmentation through a certain integration time, until their radii were reduced to 1 Å or until they hit a system boundary. A larger fraction of the 1.6 nm radius MSP trajectories (Fig. 4, top) hits BP compared to the 3 nm pure ice particle trajectories (54% vs. 38%). The ice particles experience a much larger neutral gas friction, as well as evaporation due to their intrinsic properties which leads to that relatively large ice particles would contribute less to the measured current at BP than MSPs in the upper part of the theoretical size distribution, as will be discussed in depth below.

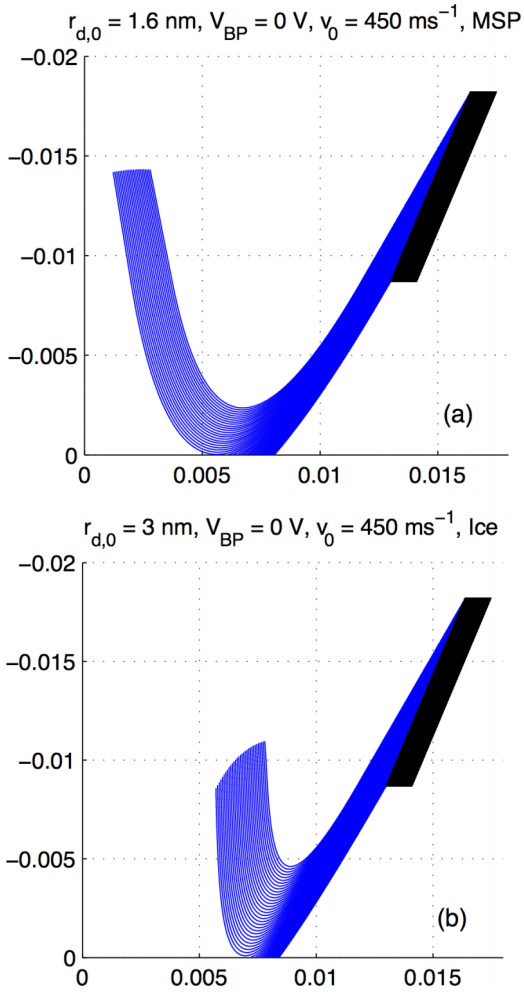

FIG. 4. Traced trajectories (blue solid lines) of 1.6 nm radius MSPs (top) and 3.0 nm pure ice particles (bottom) for a bottom plate potential of 0 V. The black structure is a cross section of one inclined ring in G2. The y-axis and x-axis give the vertical and (arbitrary) radial position from the center of the probe, of the ring and the fragment orbits. Units are (m).

C. Choice of dust parameters

The calculations performed in this work require knowledge about a range of intrinsic dust properties to close the model equations. To find recent, or even any, material specific data which apply to MSPs can be a challenge due to the limited knowledge of their chemistry. This issue is often resolved by using data from analogues of smoke particles, and we summarize the set of dust parameters used in this study in Table I. A few comments on the choices of MSP parameters should however be made.

The MSP material density is often assigned a value of $\rho_d = 2000$ kg m^{-3}.[38,46,66,67] However, on the basis of both observations (e.g., Hervig *et al.*[4]) and theoretical discussions (see, e.g., references listed in Table I), this number may be too low. If the MSPs are indeed formed from chondritic material, the density could be at least $\rho_d = 3000$ kg m^{-3} as set here (non-stoichiometric olivine compound), and possibly higher, even for amorphous states.

The choice of initial velocity for the fragments at G2 in MUDD, $v_0 = 450$ ms^{-1} for a rocket velocity of around $v_r = 750$ ms^{-1}, is the parameter containing the largest uncertainty

at this point. The collision dynamics of nanoparticles is not very well known, and our assumptions about nanoscale ice particles are based on studies by Tomsic,[68] Tomsic, Marković, and Pettersson,[69] Tomsic *et al.*,[70,71] and Andersson *et al.*[72] of impacting pure ice particles. For nanoscale ice particles, their experiments show that $O(100)$ eV-particles may conserve up to 70% of their initial energy when colliding with gold or graphite coated surfaces at an incident angle of 70°. Extrapolating these results to lower energy particles gives a conservation of around 40% of the initial energy, on which we have appended an uncertainty of $\pm 100\ \mathrm{ms}^{-1}$ (corresponding to ~36% ± 15%). This energy loss is valid for pure ice particles; however, it is conceivable that the energy loss for the MSPs will be similar to the characteristic one for ice particles, if they are embedded within or bounded on the surface of, e.g., a NLC particle. Sato, Chen, and Pui[73] also find that silica, silver, and nickel nanoparticles colliding with silver surfaces lose a large amount of their perpendicular velocity. We find it conceivable that the MSPs, unlike many ice particles, will keep much of their velocity parallel to the surface due to, e.g., lubrication by water layers.

The charge state of the fragments should be discussed. As noted by Kuuluvainen *et al.*,[74] the transfer of charge to nanoparticles impacting on surfaces as well as their bouncing properties is not well understood. In studies of pure ice particles,[68–72] it is found that surface impacts of smaller particles generally lead to that they stick to the surface and evaporate while larger particles bounce off and appear to be more or less intact. Such a scenario cannot explain the large production of charged fragments which has been observed in several rocket experiments,[1,3,55] where the secondary charge production in a triboelectric mechanism corresponds to that a particle of radius 50 nm should produce between 50 and 100 charged fragments, while a smaller particle of radius say 10 nm produces around five charged fragments. It is not likely that all released fragments are charged. In moderate to high energy collisions of ice particles[68,75,76] and MSP-like particles[77] with metal surfaces, it is found that the particles can break into fragments of which a proportion ($\sim 0.01\% - 0.1\%$) become charged, a probability proportional to $m_{ice}^{2/3}$ and m_{MSP}, respectively. The discrepancy between these results and those from rocket experiments points towards a structure of NLC/PMSE particles which is more loosely bound than a pure ice particle. It seems likely that the effect of a large number of embedded MSPs[1,3,4] could lead to just this. The fact that so many of the small fragments from impacting NLC/PMSE particles do not stick to the impact surface, as similar ice particles tend to do, also suggests that their velocity can be larger than what we find for ice particles at the relevant energies for the MUDD observations. For very small dually or more strongly charged particles, the electric potential at the surface can, depending on the material, exceed the surface tensile potential.[78] In view of that the probability for a fragment to acquire one unit charge is less than unity, possibly considerably so, we find the assumption that fragments at most carry one unit charge to be reasonable. We also assume that the majority of fragments will have a negative charge, as is observed during the first minutes of exposure of a metal surface to impacting nanoscale ice particles.[68] Two unit charges can probably not be totally excluded, but it seems very unlikely that such fragments can carry a substantial fraction of the BP current. It may also be that electric field emission prevents the existence of two or more unit charges on dust particles of the order of one nm radius.[79]

It is assumed throughout this study that the ejection angle of a fragment is 6° to the G2 surface, based on results for ice particles of similar size (e.g., Tomsic[68]) which show that fragments scatter diffusively around angles very close to the collision surface at our inclination angles, although uncertainty may be present in this parameter. We do not expect this to have large effect on the results, as small deviations around this angle is found to introduce around 2% more or less hits per degree for typical fragment sizes.

IV. RESULTS FROM FRAGMENT SIMULATIONS

Neutral gas simulations were performed for the polar summer mesosphere with density data from Rapp, Gumbel, and Lübken.[85] Calculations were carried out for an assumed altitude of 82 km and an ambient temperature of $T = 150$ K.[86] This is consistent with the observed NLC height during the PHOCUS campaign.[1] Dust simulations were run for single dust fragments which were singly charged. For each chosen dust radius, we simulated the motion of 50 fragments, with initial coordinates evenly spaced over the entire G2 fragmentation surface. A set of simulations of 50 nm NLC particles flowing in to the probe, through the shock front, was also performed. Those particles were found to preserve most of their initial energy, hitting G2 with a velocity just below $700\ \mathrm{ms}^{-1}$ which corresponds to around 85% of their initial energy. The sizes of the simulated fragments were chosen so that the maximum and minimum detectable radius in a specific voltage mode of MUDD was included.

Presented below are the main results from the simulation of pure MSPs and pure ice fragments in the original voltage modes of MUDD as flown on PHOCUS.[1] Simulations of alternative voltage modes to be used in future flights of MUDD probes are also presented.

A. MSP fragments

We now assume that the fragments, which are produced when PMSE/NLC particles hit G2, are pure MSP. For each set of 50 fragments with given radius and velocity, we calculate the fraction of them which will reach the bottom plate and contribute to the BP current. Figure 5 shows this as the relative current, for the two retarding potentials of 10 and 20 V corresponding to bottom plate potentials of 0 and −10 V. In the case of a bottom plate potential of $V_{BP} = 0$ V, i.e., a retarding field of approximately $1100\ \mathrm{Vm}^{-1}$, MSPs with radii as small as 1.4 nm can contribute to the BP current for an initial velocity of $450\ \mathrm{ms}^{-1}$ (solid line). All fragments larger than 1.8 nm will contribute to the current, and fragments with radii between around 1.4 nm and larger can be inferred with this mode. The adopted uncertainty in velocity shifts the smallest detectable radius down about 0.2 nm for a $100\ \mathrm{ms}^{-1}$ higher initial velocity, and up between 0.3 and 0.4 nm for the lower bound. The situation is very similar for

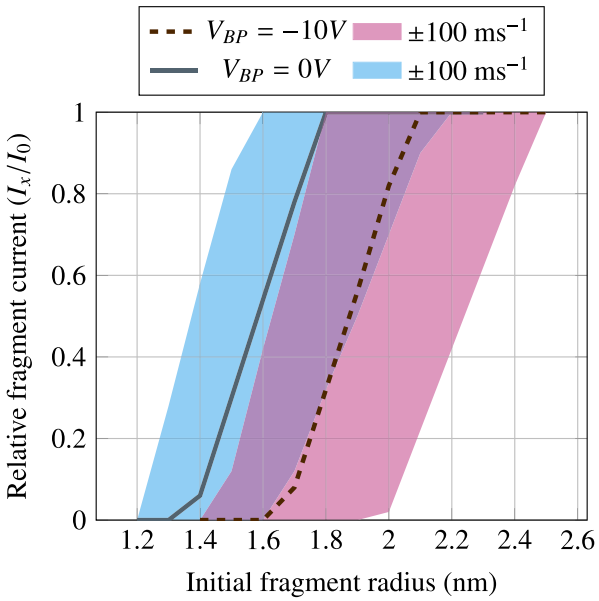

FIG. 5. Currents of pure MSP fragments at BP relative to the zero retarding field mode ($V_{BP} = +10$ V). The lines represent an initial velocity at G2 of $v_0 = 450$ ms^{-1}. I_x denotes the current at BP when $V_{BP} = x$ V.

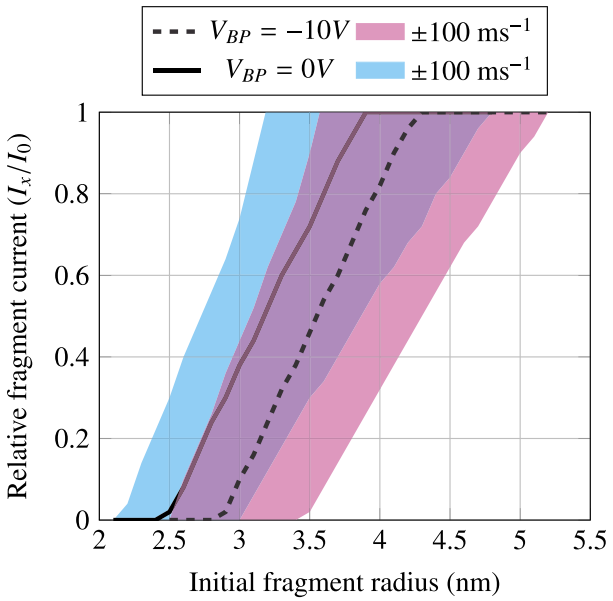

FIG. 6. Currents of pure ice fragments at BP relative to the mode with zero retarding potential.

the case when $V_{BP} = -10V$, i.e., a ≈2200 Vm^{-1} retarding field, where the 450 ms^{-1}-particles (dashed line) are theoretically detectable at radii above 1.7 nm. Particles larger than 2.1 nm will all reach the bottom plate, and the uncertainty in velocity shifts the distribution down around 0.2 nm or up 0.3 to 0.4 nm depending on the radius. In the mode, where there are no retarding fields, i.e., when $V_{BP} = 10$ V, our simulations show that MSP particles smaller than ~0.6 nm are stopped completely. In view of the assumed uncertainty in initial fragment velocity, this range becomes 0.5–0.8 nm. In reality, because of the MUDD geometry, small to moderate retarding fields can be present in this mode, which is discussed in Sec. V D. If we require that $I_x/I_0 \geq 30\%$ to detect the charged fragments, MUDD detects MPSs with sizes above ~1.5 nm in the 10 V retarding potential mode, and sizes above ~1.8 nm in the 20 V retarding potential mode. For the zero potential mode ($V_{BP} = +10$ V), MSPs larger than ~0.7 nm can contribute to the BP current, where the uncertainty in initial velocity will shift this limit down to 0.6 nm or up to 0.9 nm. All fragments larger than 0.9 nm are found to reach the bottom plate in the zero field mode.

B. Pure ice fragments

The results for simulations of pure ice fragments are presented in Figure 6 for retarding potentials of 10 V and 20 V between G2 and BP inside MUDD.

In the mode with a retarding potential of 10 V, we observe that particles with radii above 2.5 nm may contribute to the BP current if they are not obstructed at impact. The uncertainty in the smallest detectable radius is around 0.3 nm smaller and 0.5 nm larger than the mean (450 ms^{-1}-fragments). In the second voltage mode, where the retarding potential is 20 V, ice fragments with sizes above around 3 nm will contribute to the BP current. The uncertainty in detectable radius for this mode is slightly larger, 0.4 nm smaller and 0.6 nm larger than the mean value. As has been discussed, ice particles of sizes smaller than around 3 nm tend to stick to surfaces in collisions.[68] Combined with the small charging probability of these smaller ice fragments, they probably do not contribute significantly to the measured current at BP.

We find that the ice particles experience a significant evaporation within the integration time, typically ~$O(10^{-4})$ s. As shown in the bottom panel of Figure 7, a pure ice fragment of 3.5 nm can lose as much as 1/4 of their initial mass before hitting BP. This result, alongside simulations of MSPs with layers of ice a few Ångstrøm thick, supports that if ice were to stick to the MSP particles in the fragmentation process, this layer of ice would evaporate quickly and not distort the measured energy distribution of MSPs significantly. Although the MSPs are found to rapidly acquire heat, no significant evaporation is observed as can be inferred from the top panel of Fig. 7. We may also note that the breaking of these small fragments by neutral air can be substantial, resulting in a large difference in energy of the impacting fragments coming from the top and bottom of G2.

C. Alternative fragment detecting modes

Motivated by the goal of improving the resolution of the observed fragment energy spectrum, especially for lower energies, we present a summary of the simulations carried out for pure MSP fragments in voltage modes with lower retarding potentials.

Figure 8 shows a comparison between the three original potential modes and three additional modes at lower retarding potentials of 1V, 2V, and 5V, respectively. It shows the fraction of hits to BP by fragments of a certain energy (or size). Fragments with radii smaller than 1 nm can be detected both with the 1 V retarding mode ($V_{BP} = 9$ V) and the 2 V retarding mode ($V_{BP} = 8$ V). Inclusion of such low energy

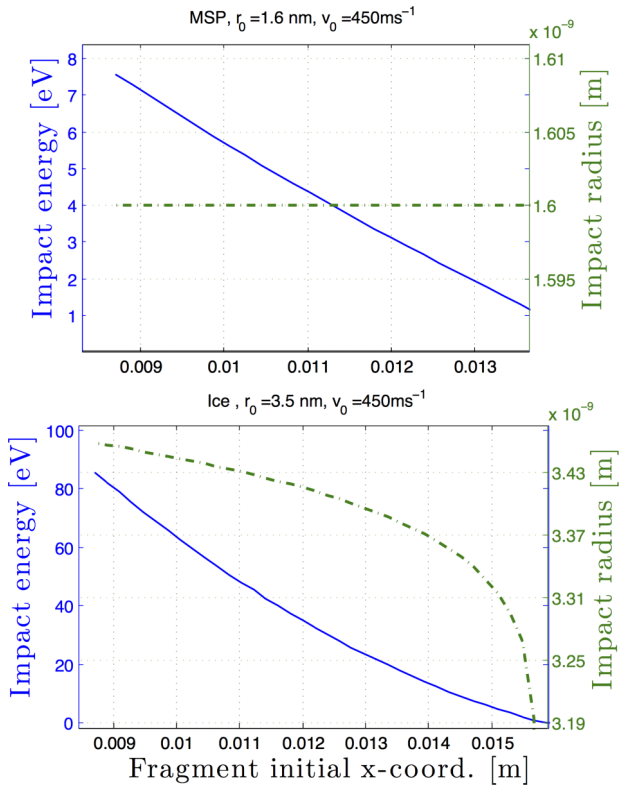

FIG. 7. Energy (solid line) and radius (dashed) at impact with BP for 1.6 nm radius MSP particles (top) and 3.5 nm pure ice particles (bottom) as a function of initial position.

modes should give a significantly increased resolution in the lower end of the fragment size spectrum, which can be related to the energy spectrum of MSPs, cf. the discussion in Sec. V C. To measure charged fragments with sizes which would normally be stopped by the air drag in the zero potential mode, we plan to include modes with small attractive potentials (e.g., $V_{BP} = +11$ V) as part of the voltage scheme in future flights of MUDD.

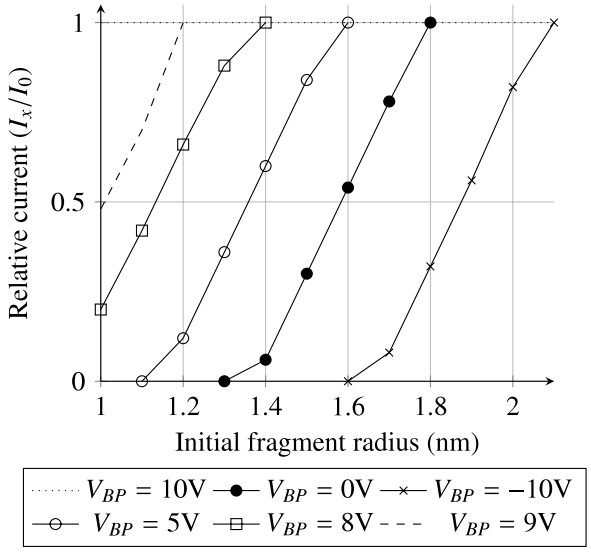

FIG. 8. Ratio between the current of the zero retarding potential mode and several modes with retarding potentials ($V_{BP} \neq 10$ V) for pure MSPs. The initial velocity is 450 ms^{-1}. I_x denotes the current at BP when $V_{BP} = x$ V.

V. DISCUSSION

A. Fragmentation process

Our model of a NLC particle is based on recent studies which show that they probably contain a relatively large amount—up to several percent by volume—of MSPs embedded in them.[1,3,4] There are, however, few experiments which apply directly to the collision and fragmentation dynamics of nanoparticles in a system like ours. Tomsic[68] presents experimental data and molecular dynamics simulations for collisions between ice particles down to a few nanometers and various surfaces. Their velocity regime is similar to ours, however, their experiments utilize collision surfaces with temperatures up to 1400 K, which is above what is relevant for our applications. Nevertheless, studies of lower temperature collisions (see, e.g., Tomsic *et al.*,[70] Andersson *et al.*,[72] and Markovic *et al.*[87]) show that the preservation of initial kinetic energy is very similar for low and high temperature collisions; however, in the latter case, the final energy spectrum tends to include a significant amount of low energy particles. In addition to this, Tomsic *et al.*[71] found that surfaces with temperatures ~300 K produce relatively narrow velocity distributions of the scattered fragments, so our uncertainty in initial fragment energy of about 30% will cover much of the variance. For low temperature collisions, Tomsic,[68] Tomsic, Marković, and Pettersson[69] find that small ($\lesssim$3 nm) water clusters tend to stick to the impact surfaces.

Kassa *et al.*[55] modeled the observations by different dust probes on the ECOMA-4 payload (see Rapp *et al.*[88] for details), where a probe with four times less geometric cross section than a larger one with similar geometry, could measure up to twice the current of the large probe. They found that this apparently had as an explanation that the smaller probe, located further back on the payload structure, was sprayed with collision fragments from ice particles impacting on the payload body in front and adjacent the smaller probe. The observations required that a 50 nm particle should produce between 50 and 100 charged fragments in a collision. A calculation based on the observations of MSP content by volume from Hervig *et al.*[4] and Havnes *et al.*,[1] shows that even if only the outermost layer of evenly distributed MSPs on a contact area equal to 1/4 of the dust surface area is released, then between 50 and 400 meteoric particles will be released if we assume a monodisperse distribution with $r_{MSP} = 1.4$ nm. Even if only a modest fraction of these become charged, they can contribute significantly to the total current (see also Havnes *et al.*[1]), thus reducing the requirement that the NLC particle itself is porous. However, the large difference in, e.g., specific heat between MSPs and ice may still cause the NLC particles to become more brittle and thus fragment more easily than pure ice particles.

To correctly interpret the MUDD data to obtain information on the MSP contribution, we need knowledge about to what extent the ice fragments will affect the observed current on BP. The key to answering this question lies in the fragmentation process. If the NLC/PMSE particles, even if they have up to a few percent of MSPs embedded by volume, behave like pure ice particles, they should primarily rebound

from the impact surface without severe fragmentation. Their probability of acquiring substantial charge is small and they will not contribute much to the current at BP. Smaller NLC/PMSE particles of sizes of several nm and below tend to stick to the surface and evaporate. They should therefore also not contribute much to the current at BP.[69–71]

If large ice particles, of say 50 nm, rebound and carry with them an initial charge of around $-4e$, they could only contribute a current of 4%–8% of the maximum current measured at BP. This follows from the results of Havnes *et al.*,[2] Havnes and Næsheim,[3] Kassa *et al.*[55] that an impacting 50 nm particle can typically produce 50–100 charged fragments. Even though fragmentation releasing small MPSs may seem to be required, large charged ice fragments may constitute a small part of the fragment currents in the highest energy ranges.

B. Detection limits for MUDD on PHOCUS

The BP voltage settings for the first MUDD launch were presented in Sec. II. The detecting scheme allowed for observation of fragments at three different BP voltages; two modes of retarding potentials between G2 and BP ($V_{BP} = -10$ V and $V_{BP} = 0$ V) and one with zero potential ($V_{BP} = +10$ V). During the time dust fragments are inside the probe, no significant evaporation from the MSP fragments is observed, even though the heating of these may be artificially high due to that the thermal radiation from grains has been neglected. Thus, we propose that the size distribution of measured fragments, presumably MSPs, is equal or very closely related to their true size distribution inside the NLCs.[1] On the basis of our simulations of spherical NLC fragments, we present in Table II the theoretical detection limits for pure ice fragments and MSPs in MUDD. Due to discussion above that ice particles of radii smaller than ~3 nm tend to stick impact surfaces and also experience a rapid evaporation, we have not included these in the mode with no retarding fields ($V_{BP} = +10$ V). The requirement for a significant detection is set to that 30% of the fragments of a given size will reach BP.

The dynamic shape of the particles, deflection angle from G2, as well as the uncertainty in MSP density are factors which will introduce shifts in the obtained size limits; however, these contributions will not be discussed in this paper. One particular factor which has not been included, but may become important is the transport of small fragments which stop between G2 and BP due to air drag. Our calculations predict that most MSP fragments with radii $\lesssim$0.6 nm will be stopped by neutral air drag between G2 and BP in the zero potential mode ($V_{BP} = +10$ V). Pure ice fragments of such sizes are found to evaporate fast and lose their charge; however, this should not be true for MSPs. Since the theoretical size distribution of MSPs predicts that they are abundant at small radii,[38,46] we must also consider their fate if they are stopped completely by neutral gas particles. A simple solution to this problem is that random walk processes move the fragments to whichever is closest of G2 and BP. For future probes, we will also include an accelerating potential between G2 and BP to ensure the detection of very small MSPs; however, this will also increase the free electron current which must be corrected for.[1]

TABLE II. Theoretical detection limits for the MUDD probe flown on PHOCUS in July 2011. EB denotes the error bound for the minimum detectable radius where [L,U] are the lower and upper limits due to an uncertainty of ± 100 ms^{-1} in initial fragment velocity.

	V_{BP} (V)	Mean (nm)	EB [L,U]
MSP	−10	1.8	[1.6, 2.2]
	0	1.5	[1.3, 1.8]
	+10	0.7	[0.6, 0.9]
ICE	−10	3.3	[3.0, 4.0]
	0	2.9	[2.5, 3.5]

C. Alternative potential modes

The MUDD probe as launched on the PHOCUS rocket in 2011[1] is a coarse mass spectrometer for charged dust or aerosol fragments. The mass resolution is dependent on the choice of retarding potentials between G2 and BP. The use of more potentials than in the first flight will, in principle, lead to a better resolution of the observed fragment energy spectrum, but the longer sweep time; this implies will reduce the height resolution. In a future flight of MUDD planned for 2015, we will use up to three mechanically identical MUDD probes which cycle through different sets of retarding potentials. The potential switching times will not be simultaneous so measurements from the different MUDDs will overlap. This will yield an increased accuracy and better spatial and energy resolution.

From the analysis of the first flight data from the MUDD probe, Havnes *et al.*[1] found that approximately 30% of the charged fragments, which were detected when the retarding potential between G2 and BP was zero, were stopped when the retarding potential was switched to 10 V. When the potential subsequently switched to 20 V, 50% were stopped. This implies that approximately 30% of the fragments were found to have energies below 10 eV, while 20% of fragments were found to have energies between 10 eV and 20 eV. The last 50% of the fragments, which have estimated energies $>$ 20 eV, were not stopped even by the largest potential. Large ice particles with masses up to the initial NLC mass may contribute to this current but should not dominate. We found for the ice fragments that particles with radii smaller than around 2.5 nm will not reach BP due to electrostatic forces, neutral gas friction, and evaporation. The previously discussed results from Kassa *et al.*,[55] Tomsic,[68] Adams and Smith,[77] and Friichtenicht[89] show that small ice fragments tend to stick to impact surfaces in a collision and moreover have a lower charging probability than MSPs. This suggests that the distinguishable BP currents in the modes with low potential is likely to be dominated by pure MSPs.

Figure 9 shows possible choices of retarding potentials in a future flight of MUDD, compared to the theoretical MSP size spectrum. The black lines give the choice of BP potentials (the corresponding retarding potentials being $V_{BP} = -10$ V) and indicate the minimum sizes which can be stopped by

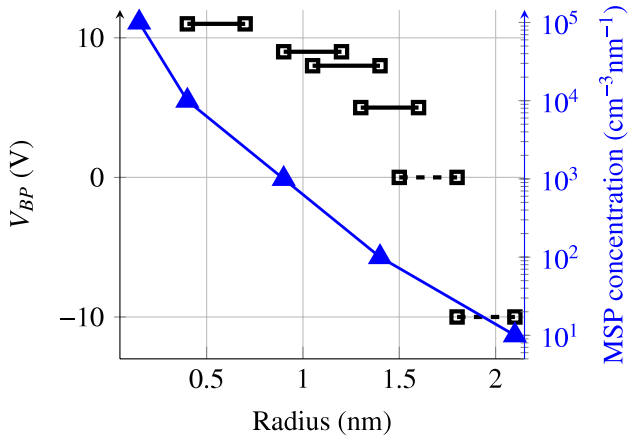

FIG. 9. Coverage of the theoretical MSP size spectrum with MUDD for an initial fragment velocity of 450 ms^{-1} (black with squares) with different retarding and accelerating potentials. The MSP spectrum (blue solid line) is the theoretical distribution at around 90 km.[38,52] The dashed lines represent the modes utilized in the PHOCUS campaign, July 2011.

those potentials. The uncertainties in the sizes are indicated by the horizontal extent of the lines. The upper limit of a size interval (squares) is the radius above which all charged fragments will contribute to the current in a certain mode. If the abundance of MSPs in the lower part of the spectrum implies that the concentration of these small MSPs is also present at large numbers inside NLC particles, there is a definite need to improve the resolution of MUDD and similar probes at low energies.

D. E-field edge effects

In the results from the fragment transport calculation presented here, we utilized an idealized electric field to reduce possible unrealistic numerical instabilities due to small fragments starting off in an extreme electric field. The electric field is observed to have values on the order of 10 000 Vm^{-1}, i.e., a decade higher than the infinite conducting plane solutions. However, these anomalies might not introduce unwanted effects, such as decelerating particles or deflecting them to the walls, because anomalous fields between G2 and BP are directed towards the probe in the modes with retarding potentials. Furthermore, the strong fields between the bucket and the outermost G2 ring will probably not represent the real fields, since G2 in reality is insulated from the bucket by a teflon ring which is not included in the simulations, and will probably reduce the outermost anomalies. For V_{BP} = +10 V, when the theoretical field is zero, the boundary effect might become important; in the regions below the two outermost rings of G2, the E-fields can become as large as ∼1000 Vm^{-1}, which is sufficient to significantly slow down or even stop small particles completely. If the particle flux through this region was effectively reduced, the current which we have regarded as the current due to all charged fragments will be reduced, possibly by a significant fraction. If this was the case, the total secondary charge production should be increased by a similar fraction. If the E-fields above and between the two outermost rings of G2 were to effectively shield out the charged fragments, the fraction would become just above 20%. Although the fields between G1 and G2 also have irregularities, the NLC particles are too energetic to be significantly affected.

VI. CONCLUSIONS

In this paper, we have studied the transport and dynamics of collision fragments created when mesospheric PMSE/NLC particles impact with an interior grid G2 on the rocket-borne MUDD probe, using computer simulations with a dedicated model. The model for dust fragment dynamics included the heating and evaporation of grains, and the model equations were closed by background simulations of the electric fields and neutral gas flow inside and around the probe. Our studies support the conclusion by Havnes *et al.*[1] Our simulations indicate that they observed MSP particles with radii >1.5 nm for a bottom plate potential of 0 V, >1.8 nm for a bottom plate potential of −10 V, and >0.6 nm for a bottom plate potential of +10 V. At radii above 1.8 nm and 2.1 nm in the two modes with V_{BP} = 0 V and V_{BP} = −10 V, respectively, all charged MSPs would reach BP. We observed a rapid evaporation of pure ice fragments, and when discussing our results in the light of the observations of pure ice particles by Tomsic,[68] Tomsic, Marković, and Pettersson,[69] Tomsic *et al.*,[70,71] and Andersson *et al.*,[72] e.g., that ice particles smaller than ∼3 nm tend to stick to impact surfaces, we conclude that few low energy ice fragments are observed in MUDD. The detection limit for ice fragments for the lowest potential mode is thus ∼3 nm and for the highest potential mode ∼3.5 nm. Finally, we find that ice fragments most likely contribute only a minor part of the observed energy spectrum. Since the MUDD probe from Havnes *et al.*[1] only contained the three discussed voltage modes, it is uncertain whether larger ice fragments contributed significantly to the BP current.

An uncertainty in initial fragment velocity of ±100 ms^{-1} is found to shift the observed size distribution of MSPs down between 0.2 and 0.3 nm and up between 0.3 and 0.4 nm; for ice fragments, these errors are slightly larger. The neutral gas fields inside the probe are found to brake/retard the smallest fragments to some extent. We have not considered the effect of local turbulence between G2 and BP, as the DSMC simulations[59] indicate no significant turbulent gas motion inside MUDD. Electric fields may however decrease the flux of small fragments near the edges of probes, as anomalous large fields can reduce the effective cross section of the G2 grid.

Even if MSPs carry small ice layers of up to 3 Å around them, they will have a very similar observed energy spectrum as the MSPs without ice, since the ice evaporates quickly. Our model does not include the heating of fragments during the fragmentation process; however, simple calculations of the contact heating during collision suggest that both ice fragments and MSPs at the surface of the NLCs are found to acquire significant heat at time scales on the order of 10^{-11} s. Such an initial heating strengthen our assumption that few small ice particles will be detected in MUDD. The MSPs are unaffected by this heating, since their acquired heat is not sufficient to cause significant evaporation. It is not improbable that an evaporating ice layer will reduce the friction on the

released MSPs, resulting in higher velocities than what we have used.

From our study of alternative potential modes in MUDD, we find a clear advantage in adding several new potential modes. These, together with more than one mechanically identical MUDD probes on future flights, will ensure a higher resolution and an improved accuracy of the lower part of the energy spectrum and thus, MSP fragments.

[1]O. Havnes, J. Gumbel, T. Antonsen, J. Hedin, and C. L. Hoz, J. Atmos. Sol.-Terr. Phys. **118**, 190 (2014).
[2]O. Havnes, T. Antonsen, T. Hartquist, Å. Fredriksen, and J. Plane, "The Tromsø programme of *in situ* and sample return studies of mesospheric nanoparticles," J. Atmos. Sol-Terr. Phys. (in press).
[3]O. Havnes and L. I. Næsheim, Ann. Geophys. **25**, 623 (2007).
[4]M. E. Hervig, L. E. Deaver, C. G. Bardeen, J. M. Russell III, S. M. Bailey, and L. L. Gordley, J. Atmos. Sol.-Terr. Phys. **84-85**, 1 (2012).
[5]G. E. Thomas, Rev. Geophys. **29**, 553, doi:10.1029/91RG01604 (1991).
[6]M. Hervig, R. E. Thompson, M. McHugh, L. L. Gordley, J. M. Russell, and M. E. Summers, Geophys. Res. Lett. **28**, 971, doi:10.1029/2000GL012104 (2001).
[7]B. Inhester, J. Klostermeyer, F. J. Lübken, and U. von Zahn, J. Geophys. Res.: Atmos. **99**, 20937, doi:10.1029/94JD01619 (1994).
[8]M. Rapp and F.-J. Lübken, Atmos. Chem. Phys. **4**, 2601 (2004).
[9]F.-J. Lübken and J. Höffner, Geophys. Res. Lett. **31**, L08103, doi:10.1029/2004GL019586 (2004).
[10]C. She, B. Williams, P. Hoffmann, R. Latteck, G. Baumgarten, J. Vance, J. Fiedler, P. Acott, D. Fritts, and F.-J. Lubken, J. Atmos. Sol.-Terr. Phys. **68**, 93 (2006).
[11]C. G. Bardeen, O. B. Toon, E. J. Jensen, D. R. Marsh, and V. L. Harvey, J. Geophys. Res. **113**, D17202, doi:10.1029/2007JD009515 (2008).
[12]M. E. Hervig, L. L. Gordley, L. E. Deaver, D. E. Siskind, M. H. Stevens, J. M. Russell III, S. M. Bailey, L. Megner, and C. G. Bardeen, Geophys. Res. Lett. **36**, L18805, doi:10.1029/2009GL039737 (2009).
[13]O. Havnes and M. Kassa, J. Geophys. Res.: Atmos. **114**, D09209, doi:10.1029/2008JD011276 (2009).
[14]M. J. Prather and J. Rodriguez, Geophys. Res. Lett. **15**, 1, doi:10.1029/GL015i001p00001 (1988).
[15]C. Voigt, H. Schlager, B. P. Luo, A. Dornbrack, A. Roiger, P. Stock, J. Curtius, H. Vossing, S. Borrmann, S. Davies, P. Konopka, C. Schiller, G. Shur, and T. Peter, Atmos. Chem. Phys. **5**, 1371 (2005).
[16]P. Keckhut, A. Hauchecorne, and M. L. Chanin, J. Geophys. Res.: Atmos. **100**, 18887, doi:10.1029/95JD01387 (1995).
[17]P. Keckhut, Adv. Space Res. **28**, 955 (2001).
[18]E. P. Shettle, M. T. DeLand, G. E. Thomas, and J. J. Olivero, Geophys. Res. Lett. **36**, L02803, doi:10.1029/2008GL036048 (2009).
[19]M. Gadsden, Adv. Space Res. **20**, 2097 (1997).
[20]G. Thomas and J. Olivero, Adv. Space Res. **28**, 937 (2001).
[21]M. Andreae and D. Rosenfeld, Earth-Sci. Rev. **89**, 13 (2008).
[22]U. von Zahn, Eos, TAGU **84**, 261 (2003).
[23]D. J. Cziczo, D. S. Thomson, and D. M. Murphy, Science **291**, 1772 (2001).
[24]E. K. Bigg, Meteorit. Planet. Sci. **47**, 799 (2012).
[25]O. Havnes, J. Trøim, T. Blix, W. Mortensen, L. I. Næsheim, E. Thrane, and T. Tønnesen, J. Geophys. Res.: Space Phys. **101**, 10839, doi:10.1029/96JA00003 (1996).
[26]L. J. Gelinas, K. A. Lynch, M. C. Kelley, S. Collins, S. Baker, Q. Zhou, and J. S. Friedman, Geophys. Res. Lett. **25**, 4047, doi:10.1029/1998GL900089 (1998).
[27]K. A. Lynch, L. J. Gelinas, M. C. Kelley, R. L. Collins, M. Widholm, D. Rau, E. MacDonald, Y. Liu, J. Ulwick, and P. Mace, J. Geophys. Res.: Space Phys. **110**, A03302, doi:10.1029/2004JA010502 (2005).
[28]M. Rapp, J. Hedin, I. Strelnikova, M. Friedrich, J. Gumbel, and F.-J. Lübken, Geophys. Res. Lett. **32**, L23821, doi:10.1029/2005GL024676 (2005).
[29]P. Schulte and F. Arnold, Geophys. Res. Lett. **19**, 2297, doi:10.1029/92GL02631 (1992).
[30]S. Robertson, M. Horanyi, S. Knappmiller, Z. Sternovsky, R. Holzworth, M. Shimogawa, M. Friedrich, K. Torkar, J. Gumbel, L. Megner, G. Baumgarten, R. Latteck, M. Rapp, U.-P. Hoppe, and M. E. Hervig, Ann. Geophys. **27**, 1213 (2009).
[31]M. Horanyi, J. Gumbel, G. Witt, and S. Robertson, Geophys. Res. Lett. **26**, 1537, doi:10.1029/1999GL900298 (1999).
[32]J. Hedin, J. Gumbel, and M. Rapp, Atmos. Chem. Phys. **7**, 3701 (2007).
[33]S. G. Love and D. E. Brownlee, Science **262**, 550 (1993).
[34]J. M. C. Plane, Chem. Soc. Rev. **41**, 6507 (2012).
[35]J. M. C. Plane, Chem. Rev. **103**, 4963 (2003).
[36]J. Höffner and J. S. Friedman, Atmos. Chem. Phys. **4**, 801 (2004).
[37]J. Rosinski and R. H. Snow, J. Meteorol. **18**, 736 (1961).
[38]D. M. Hunten, R. P. Turco, and O. B. Toon, J. Atmos. Sci. **37**, 1342 (1980).
[39]R. W. Saunders and J. M. Plane, J. Atmos. Sol.-Terr. Phys. **68**, 2182 (2006).
[40]J. M. Plane, J. Atmos. Sol.-Terr. Phys. **73**, 2192 (2011).
[41]M. Rapp and G. E. Thomas, J. Atmos. Sol.-Terr. Phys. **68**, 715 (2006).
[42]R. Turco, O. Toon, R. Whitten, R. Keesee, and D. Hollenbach, Planet. Space Sci. **30**, 1147 (1982).
[43]M. N. Eremenko, S. V. Petelina, A. Y. Zasetsky, B. Karlsson, C. P. Rinsland, E. J. Llewellyn, and J. J. Sloan, Geophys. Res. Lett. **32**, L16S06, doi:10.1029/2005GL023013 (2005).
[44]A. Y. Zasetsky, S. V. Petelina, and I. M. Svishchev, Atmos. Chem. Phys. **9**, 965 (2009).
[45]A. Evans, *The Dusty Universe*, Series in Astronomy (John Wiley & Sons, 1994), pp. 59–99.
[46]L. Megner, D. E. Siskind, M. Rapp, and J. Gumbel, J. Geophys. Res.: Atmos. **113**, D03202, doi:10.1029/2007JD009054 (2008).
[47]L. Megner, J. Gumbel, M. Rapp, and D. Siskind, Adv. Space Res. **41**, 41 (2008).
[48]B. J. Murray and E. J. Jensen, J. Atmos. Sol.-Terr. Phys. **72**, 51 (2010).
[49]G. von Cossart, J. Fiedler, and U. von Zahn, Geophys. Res. Lett. **26**, 1513, doi:10.1029/1999GL900226 (1999).
[50]C. von Savigny, C. E. Robert, G. Baumgarten, H. Bovensmann, and J. P. Burrows, Atmos. Meas. Tech. **2**, 523 (2009).
[51]L. Megner, M. Khaplanov, G. Baumgarten, J. Gumbel, J. Stegman, B. Strelnikov, and S. Robertson, Ann. Geophys. **27**, 943 (2009).
[52]L. Megner, M. Rapp, and J. Gumbel, Atmos. Chem. Phys. **6**, 4415 (2006).
[53]A. M. Zadorozhny, A. A. Vostrikov, G. Witt, O. A. Bragin, D. Y. Dubov, V. G. Kazakov, V. N. Kikhtenko, and A. A. Tyutin, Geophys. Res. Lett. **24**, 841, doi:10.1029/97GL50866 (1997).
[54]B. Smiley, M. Rapp, T. Blix, S. Robertson, M. Horányi, R. Latteck, and J. Fiedler, J. Atmos. Sol.-Terr. Phys. **68**, 114 (2006).
[55]M. Kassa, M. Rapp, T. W. Hartquist, and O. Havnes, Ann. Geophys. **30**, 433 (2012).
[56]T. A. Bekkeng, A. Barjatya, U.-P. Hoppe, A. Pedersen, J. I. Moen, M. Friedrich, and M. Rapp, Ann. Geophys. **31**, 187 (2013).
[57]See http://www.comsol.com/acdc-module for PDE module.
[58]A. Beskok and G. E. Karniadakis, J. Thermophys. Heat Transfer **8**, 647 (1994).
[59]G. Bird, *Molecular Gas Dynamics and the Direct Simulation of Gas Flows*, Oxford Science Publications (Oxford University Press, Incorporated, 1994).
[60]M. J. Baines, I. P. Williams, and A. S. Asebiomo, Mon. Not. R. Astron. Soc. **130**, 63 (1965).
[61]R. D. Smirnov, A. Y. Pigarov, M. Rosenberg, S. I. Krasheninnikov, and D. A. Mendis, Plasma Phys. Controlled Fusion **49**, 347 (2007).
[62]N. A. Fuchs, Q. J. R. Meteorol. Soc. **91**, 249 (1965).
[63]P. F. DeCarlo, J. G. Slowik, D. R. Worsnop, P. Davidovits, and J. L. Jimenez, Aerosol Sci. Technol. **38**, 1185 (2004).
[64]B. Rizk, D. M. Hunten, and S. Engel, J. Geophys. Res.: Space Phys. **96**, 1303, doi:10.1029/90JA01998 (1991).
[65]M. Podolak, J. B. Pollack, and R. T. Reynolds, Icarus **73**, 163 (1988).
[66]I. Strelnikova, M. Rapp, S. Raizada, and M. Sulzer, Geophys. Res. Lett. **34**, L15815, doi:10.1029/2007GL030635 (2007).
[67]J. M. C. Plane, Atmosp. Chem. Phys. **4**, 627 (2004).
[68]A. Tomsic, "Collisions between water clusters and surfaces," Ph.D. thesis (Göteborg University, 2001).
[69]A. Tomsic, N. Marković, and J. B. Pettersson, Chem. Phys. Lett. **329**, 200 (2000).
[70]A. Tomsic, P. U. Andersson, N. Markovic, W. Piskorz, M. Svanberg, and J. B. C. Pettersson, J. Chem. Phys. **115**, 10509 (2001).
[71]A. Tomsic, H. Schrder, K.-L. Kompa, and C. R. Gebhardt, J. Chem. Phys. **119**, 6314 (2003).
[72]P. U. Andersson, A. Tomsic, M. B. Andersson, and J. B. Petterson, Chem. Phys. Lett. **279**, 100 (1997).
[73]S. Sato, D.-R. Chen, and D. Y. Pui, Aerosol Air Qual. Res. **7**, 278 (2007).
[74]H. Kuuluvainen, A. Arffman, E. Saukko, A. Virtanen, and J. Keskinen, J. Aerosol Sci. **55**, 104 (2013).
[75]D. Dubov and A. Vostrikov, Journal of Aerosol Science **22**(1), S245 (1991), proceedings of the 1991 European Aerosol Conference Abstracts of the Nineteenth Annual Conference of the Gesellschaft für Aerosolforschung

e.V. Association for Aerosol Research Association Pour La Recherche des Aerosols.
[76]A. Vostrikov and D. Dubov, Z. Phys. D: At., Mol. Clusters **20**, 61 (1991).
[77]N. Adams and D. Smith, Planet. Space Sci. **19**, 195 (1971).
[78]P. Bliokh, V. Sinitsin, and V. Yaroshenko, *Dusty and Self-Gravitational Plasmas in Space*, Astrophys. Space Sci. Libr. (Springer, 1995).
[79]B. T. Draine and B. Sutin, Astrophys. J. **320**, 803 (1987).
[80]A. R. Klekociuk, P. G. Brown, D. W. Pack, D. O. ReVelle, W. N. Edwards, R. E. Spalding, E. Tagliaferri, B. B. Yoo, and J. Zagari, Nature **436**, 1132 (2005).
[81]H. Lichtenegger and N. Kömle, Icarus **90**, 319 (1991).
[82]J. Klinger, Icarus **47**, 320 (1981).
[83]B. Gundlach, S. Kilias, E. Beitz, and J. Blum, Icarus **214**, 717 (2011).
[84]L.-O. Heim, J. Blum, M. Preuss, and H.-J. Butt, Phys. Rev. Lett. **83**, 3328 (1999).
[85]M. Rapp, J. Gumbel, and F.-J. Lübken, Ann. Geophys. **19**, 571 (2001).
[86]F.-J. Lübken, J. Lautenbach, J. Höffner, M. Rapp, and M. Zecha, J. Atmos. Sol.-Terr. Phys. **71**, 453 (2009).
[87]N. Markovic, P. U. Andersson, M. B. Någård, and J. B. Pettersson, Chem. Phys. **247**, 413 (1999).
[88]M. Rapp, I. Strelnikova, B. Strelnikov, M. Friedrich, J. Gumbel, U.-P. Hoppe, T. Blix, O. Havnes, P. Bracikowski, K. Lynch, and S. Knappmiller, *Aeronomy of the Earth's Atmosphere and Ionosphere*, IAGA Special Sopron Book Series Vol. 2, edited by M. A. Abdu and D. Pancheva (Springer Netherlands, 2011), pp. 67–74.
[89]J. Friichtenicht, Nucl. Instrum. Methods **28**, 70 (1964).

PAPER II

Antonsen, T., Havnes, O., and Mann, I.: Estimates of the Size Distribution of Meteoric Smoke Particles From Rocket-Borne Impact Probes, Journal of Geophysical Research: Atmospheres, doi: 10.1002/2017JD027220, 2017

AGU PUBLICATIONS

JGR

Journal of Geophysical Research: Atmospheres

RESEARCH ARTICLE

10.1002/2017JD027220

Estimates of the Size Distribution of Meteoric Smoke Particles From Rocket-Borne Impact Probes

Tarjei Antonsen[1], **Ove Havnes**[1], **and Ingrid Mann**[1]

[1]Department of Physics and Technology, University of Tromsø, Tromsø, Norway

Key Points:
- Meteoric smoke particles are abundant inside mesospheric ice particles
- The size distribution of fragments of ice particles can be determined with an impact/Faraday cup probe
- The size distribution of fragments of mesospheric ice particles is directly connected to meteoric smoke particles

Correspondence to:
T. Antonsen,
tarjei.antonsen@uit.no

Citation:
Antonsen, T., Havnes, O., & Mann, I. (2017). Estimates of the size distribution of meteoric smoke particles from rocket-borne impact probes. *Journal of Geophysical Research: Atmospheres*, *122*, 12,353–12,365. https://doi.org/10.1002/2017JD027220

Received 29 MAY 2017
Accepted 1 NOV 2017
Accepted article online 3 NOV 2017
Published online 26 NOV 2017

Abstract Ice particles populating noctilucent clouds and being responsible for polar mesospheric summer echoes exist around the mesopause in the altitude range from 80 to 90 km during polar summer. The particles are observed when temperatures around the mesopause reach a minimum, and it is presumed that they consist of water ice with inclusions of smaller mesospheric smoke particles (MSPs). This work provides estimates of the mean size distribution of MSPs through analysis of collision fragments of the ice particles populating the mesospheric dust layers. We have analyzed data from two triplets of mechanically identical rocket probes, MUltiple Dust Detector (MUDD), which are Faraday bucket detectors with impact grids that partly fragments incoming ice particles. The MUDD probes were launched from Andøya Space Center (69°17′N, 16°1′E) on two payloads during the MAXIDUSTY campaign on 30 June and 8 July 2016, respectively. Our analysis shows that it is unlikely that ice particles produce significant current to the detector, and that MSPs dominate the recorded current. The size distributions obtained from these currents, which reflect the MSP sizes, are described by inverse power laws with exponents of $k \sim [3.3 \pm 0.7, 3.7 \pm 0.5]$ and $k \sim [3.6 \pm 0.8, 4.4 \pm 0.3]$ for the respective flights. We derived two k values for each flight depending on whether the charging probability is proportional to area or volume of fragments. We also confirm that MSPs are probably abundant inside mesospheric ice particles larger than a few nanometers, and the volume filling factor can be a few percent for reasonable assumptions of particle properties.

1. Introduction

The polar summer mesopause, located at ~80–90 km altitude, is the coldest region of the terrestrial atmosphere, with temperatures sometimes approaching 100 K (Lübken, 1999; Zahn & Meyer, 1989). The low temperatures allow for growth of nanoscale ice particles, despite the low water mixing ratio around the order of a few ppmv (Hervig et al., 2003; Murray & Jensen, 2010). Cloud phenomena like the visible noctilucent clouds (NLC) and polar mesospheric summer echoes (PMSEs) observed by radar are related to the presence of water ice particles. NLCs consist of particles, typically of sizes around some tens of nanometers (see, e.g., von Cossart et al., 1999; Baumgarten et al., 2008), large enough to scatter light effectively and therefore detectable by a variety of optical remote sensing methods. PMSEs are coherent radar echoes observable at frequencies from the HF to the UHF regime, which are controlled by smaller subvisual particles. Smoke and/or ice particles can effectively reduce the mobility of electrons and allow for persisting electron gradients created by neutral turbulence, which subsequently can produce Bragg scattering (see, e.g., Rapp & Lübken, 2004 for a review). Ice particles $\gtrsim$10 nm become predominantly negatively charged due to the work function of ice making photoemission and photodetachment less effective than the collection of free electrons in the D layer ionosphere (Knappmiller et al., 2011). Because of the charge state of the particles, electrostatic rocket probes are one of the preferred tools for in situ measurements. The first unambiguous detection of mesospheric charged particles was done by Havnes et al. (1996) with the rocket-borne Faraday bucket detector DUSTY. Their measurements confirmed the existence of negatively charged particles but did not exclude the possible effect of large positively charged dust grains or particles of meteoric origin on the measured currents.

Although water ice can form homogeneously around the polar summer mesopause during periods of relatively sharp negative temperature gradients (Murray & Jensen, 2010; Zasetsky et al., 2009), homogeneous nucleation between water vapor and condensation nuclei of meteoric material is generally thought to be the dominant growth mechanism for creating large ice particles ($\gtrsim$1 nm) (Gumbel & Megner, 2009; Reid, 1997; Rapp & Thomas, 2006). Meteoroids ablate at heights between 70 and 110 km, and the resulting vapor condenses into agglomerates with radii ~0.1 to ~2 nm, commonly named meteoric smoke particles (MSPs),

which can subsequently partake in the ice particle formation process (Hunten et al., 1980; Megner et al., 2006). Exactly how MSPs are embedded inside larger ice particles was unclear for a long time and is still not completely resolved. Mesospheric ice particles were initially considered to be pure ice or contain a single or few MSP nuclei (Plane, 2003; Rapp & Thomas, 2006). Through revisiting measurements done with DUSTY, Havnes and Næsheim (2007) found that MSPs are probably abundant inside NLC particles. Based on analysis of rocket measurements where a small dust detector recorded much higher currents than a larger similar probe placed on the top deck, Kassa et al. (2012) also concluded that secondary charge production can dominate impact detectors and that embedded MSPs would amplify the secondary charging. Satellite measurements (Hervig et al., 2012) later confirmed that mesospheric ice particles are likely to contain meteoric material. Due to the neutral air flow around rocket payloads, particles of sizes $\lesssim 2$ nm are swept away in the shock front and direct detection of MSPs is difficult (Hedin et al., 2007). To deal with this problem, Havnes et al. (2014) developed a new rocket probe based on their earlier findings — the MUltiple Dust Detector (MUDD) — which aimed to detect MSPs by fragmenting large ice particles and releasing embedded smoke particles in the collision with a fragmentation grid. The first version of MUDD was launched successfully in July 2011 on the PHOCUS (Particles, Hydrogen and Oxygen Chemistry in the Upper Summer mesosphere) payload, and measurements yielded information on distribution of collision fragments. It was found that $\sim 70\%$ of fragments are smaller than $\sim$1.2 nm, 20% between 1.2 and 10% larger than 1.6 nm, when assuming the charging probability of fragments is proportional to their mass. This latter work also estimated the volume filling factor of MSPs inside NLC particles to be between $\sim 0.05\%$ and several percent, consistent with the findings of Hervig et al. (2012).

From the first flight of MUDD, it was argued that the size distribution of the collision fragments was proportional to, if not directly transferable to the size distribution of free MSPs. Simulations of fragment dynamics and evaporation inside MUDD have showed that this is a plausible assumption (Antonsen & Havnes, 2015). To obtain an absolute size distribution of MSPs from the MUDD detector, however, uncertainties in the charge transfer mechanism (i.e., triboelectric) during a collision between ice particles and the fragmentation grid must be resolved. Such charging mechanisms are not well understood for ~ 1 nm particles in the mesosphere. Therefore, we rely on experimental work on pure ice particles (Tomsic, 2001) and meteoric analogues (Adams & Smith, 1971), along with theoretical considerations on the topic (Antonsen & Havnes, 2015; Havnes et al., 2014; Kuuluvainen et al., 2013). For nanoscale ice particles, the experiments showed that fragments have predominantly negative charge, up to a few minutes after bombardment on a clean metal surface. After the initial few minutes, a significant number of the fragments can become positively charged. We assume for this reason that the fragments are negatively charged in our simulations of fragments inside MUDD.

In the present study, we aim for a higher resolution in MSP sizes and of the spatial variation of dust/ice layers around the mesopause compared to the 2011 flight of MUDD. Due to technical difficulties (i.e., electrometer settling) there is a trade-off between size and height accuracy in a single probe. We therefore use three mechanically identical probes with partially overlapping detection modes (voltage biases), so that a large part of the mass spectrum can be covered while probes can be referenced to each other continuously to make recalibration of the instruments more convenient.

In section 2 we present the new version of the MUDD dust detector. Section 3 presents the measurements obtained by, and technical details of, two triplets of MUDD probes on two sounding rocket launches, MAXIDUSTY 1 (MXD-1) and MAXIDUSTY 1B (MXD-1B), during the summer of 2016. In section 4 we present and discuss the size distribution of collision fragments of mesospheric ice particles detected by MUDD and their relation to MSP size spectra. In section 5 we give a short summary, discussion, and concluding remarks on the results.

2. The New MUltiple Dust Detector — MUDD

A cross section of MUDD is shown in Figure 1. The MUDD probe is a Faraday bucket-type detector with two statically biased grids and a bottom plate detector varying between four different voltage biases sequentially. The shielding grid, G0, is set to the floating payload ground and shields neighboring instruments from interior electric fields. The positive ion shielding grid, G1, is biased to +6.2 V, which is sufficient to shield from the positive ambient species. The fragmentation grid, G2, consists of inclined rings that partly overlap to prevent the direct influx of large ice particles to the bottom plate. An ice particle with a radius around 50 nm will be partially fragmented at impact with G2 and normally produce between 50 and 100 charged fragments,

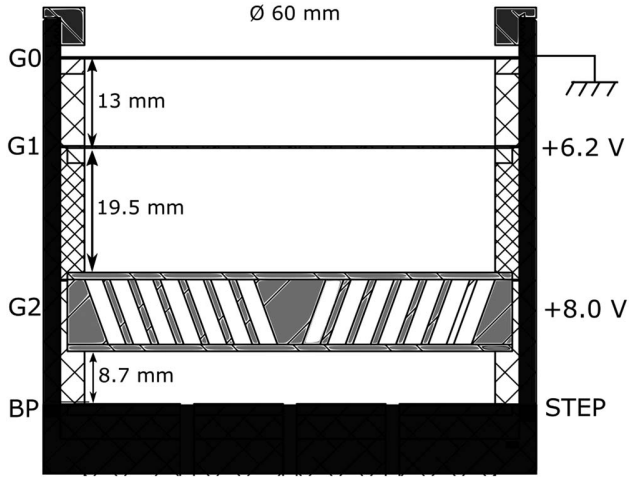

Figure 1. Principle sketch of the MUDD detector. The G0, G1, and G2 grids have a constant bias, while BP steps between different voltages to produce the retarding potentials for detection of particles of different sizes. A single MUDD probe has three unique voltage modes and one mode that overlaps with one of the other probes for comparison and calibration.

depending on the radius proportionality of the triboelectric charging of the fragments (Havnes & Næsheim, 2007). The fragments will subsequently travel toward the bottom plate (BP), almost parallel with the G2 planes, with an energy of around 40% of the initial energy (Antonsen & Havnes, 2015; Havnes et al., 2014; Tomsic, 2001).

On two separate payloads, MAXIDUSTY 1 and MAXIDUSTY 1B, identical triplets of MUDD were launched. The probe layout on the payload top deck for the MXD-1B payload is shown in Figure 2. The top deck geometry was identical to the one of the MXD-1, apart from the UC Boulder instrument miniMASS (mini Mesospheric Aerosol Sampling Spectrometer) that substituted DUSTY 1 on the first flight. The electrostatic dust probe measurements were supported by boom probe measurements of electron density; both by Faraday rotation (Jacobsen & Friedrich, 1979) and multineedle Langmuir probes (Bekkeng et al., 2010; Jacobsen et al., 2010). A new mass spectrometer, ICON (Identification of the COntent of Noctilucent cloud particles) (Havnes et al., 2015), was included on both payloads to analyze the chemical composition of NLC particles. The three MUDD probes had four unique voltage steps totaling to 10 different voltage modes, that is, two overlapping voltage modes for referencing and calibrating probes relative to each other. The respective voltage modes of each of the MUDDs are listed in Table 1, in terms of retarding potential for negatively charged fragments. A negative retarding potential implies attracting forces for negatively charged fragments. The potentials were chosen on the basis of the extensive modeling and experimental results of Antonsen and Havnes (2015) and Havnes et al. (2014), respectively, such that a large part of the theoretical size distribution is covered. Positive retarding potentials will stop all fragments up to a certain size, and the raw current of a single channel will correspondingly represent a cumulative distribution. By subtracting bins of higher retarding potential, an absolute distribution can be obtained. We have also included a mode in which all negative fragments will be attracted to the bottom plate ($U_R = -2$ V), even down to a couple of Ångstrøms in size, to yield a higher sensitivity in the lowest part of the size spectrum (which is thought to contain the highest number of particles) and a more correct total current.

The currents to G1, G2, and BP were sampled at a rate of 8,680 Hz, and the voltage modes switched every 192 samples (~15 m in altitude around the mesopause). The three probes ran in parallel with identical sampling rates, but with a 64-sample interval between the first voltage mode in each group, such that the first voltage mode of MUDD-2 started 64 samples after the first mode in MUDD-1 and so on. This means that in every full cycle (four voltage modes) MUDD-1 overlapped with MUDD-3 in the −2 V retarding mode for 64 samples (~6 m); correspondingly, MUDD-2 overlapped for the same number of samples with MUDD-3 in the +8 V mode. The stepping scheme of the potentials for the different probes is illustrated in Figure 3.

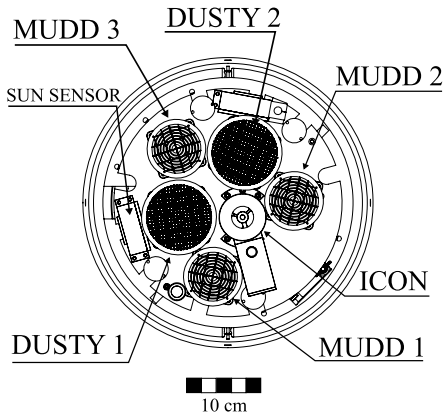

Figure 2. Top deck layout on the second MAXIDUSTY payload. The MUDD and DUSTY probes are the Faraday buckets from UiT. The first payload was mechanically similar but with one of the DUSTY probes replaced with the UC Boulder miniMASS.

3. MUDD Observations During the MaxiDusty Campaign

Two triplets of MUDD probes were launched from Andøya Space Center (69.29°N, 16.02°E) at 09:43 UT on 30 June 2016 and 13:01 UT on 8 July 2016, respectively, on the MXD-1 and MXD-1B sounding rocket payloads. MXD-1 was launched through a relatively broad NLC, reaching from ~80 to 86 km, as detected by the RMR-lidar at the ALOMAR observatory (see Gerding et al., 2016; Von Zahn et al., 2000 for technical details). This NLC had a strong volume backscatter coefficient from 80 to 82 km and a more diffuse appearance in the upper part. Observations of PMSE were made simultaneously and in the same volume as the rocket path by the MAARSY radar during the entire campaign. The PMSE structure during the MXD-1 launch, as shown in Figure 4, was highly dynamic with moderate echo strength. At the time of launch, the PMSE stretched from around 80 to 90 km in a nonhomogenous structure. The radar beam along the rocket flight path showed that the payload passed through three moderately strong PMSE layers but missed

Table 1
Voltage Modes of the MUDD Probes in Terms of Retarding Potential in Volts

Probe	Ret. Potential (V)
MUDD-1	(−2, 0, 2, 4)
MUDD-2	(13, 18, 5, 8)
MUDD-3	(−2, 1, 3, 8)

the regions of strongest backscatter. For the MXD-1B launch, clouds obscured the NLC measurements, but PMSE backscatter from the height region between ∼ 84 km and ∼ 88 km was very strong and appeared relatively homogeneous in comparison to the PMSE from the first launch.

3.1. MUDD Measurements on MXD-1

The analysis of the raw MUDD currents requires some in-depth explanation. Due to the settling time of the MUDD electrometers after switching between voltage modes, the first 10–20 samples in every voltage step (192 samples in total) cannot be directly used. To be certain of minimizing the effect of electrometer settling, we removed the 20 first samples in every voltage step for all potential modes. For most of the potential modes, a weak settling could still be observed after the removal of the initial 20 samples. The remaining 172 samples of all voltage steps were consequently fitted with an exponential function in region with no dust (example shown in Figure 5a), and the slow settling components were subtracted.

Furthermore, an issue with electron current leakage must be resolved. Ideally, no electron current would be measurable on the bottom plate for all retarding potential modes. This implies in theory that only the $U_R = -2$ V and $U_R = 0$ V could show signs of ambient electrons reaching BP, since these modes do not retard negative particles. In reality, due to the complex E field structure inside MUDD and other possible effects such as payload charging, minor current contributions from ambient electrons are present for retarding potential modes up to ∼ 5 V. In these cases, currents from the regions 79 km to 81 km (below NLC) and 86.7 km to 90 km (above NLC) were fitted by cubic polynomials to a very good agreement. An example of the fitted curves for one of the MUDD probes is shown in Figure 5b, where we note that the voltage mode with $U_R = 8$ V does not require background subtraction. Such a fitting procedure is valid when there is no clear bite-out in the G2 current and does not require an iteration process as employed in Havnes et al. (2014). For the PHOCUS payload, the least retarding channel had $U_R = 10$ V and electron leakage was only observed in the zero potential mode, which agrees with the MXD-1 results.

Figure 6 shows the recorded upleg currents of G1 and G2 for MUDD-1. The same channels for the other two probes in the MUDD triplet show almost identical current strengths and features. The spike at ∼83.5 km is due to the firing of a squib on the ICON instrument, also situated on the top deck. Both of these channels display a spin modulation of 3.8 Hz, which is expected for G1 and also for G2 whenever secondary particles produced at G1 or the probe walls hit the lower grid. This modulation was removed in postprocessing, as discussed later. We note that no clear electron bite-out was observed by MUDD; although a slight tendency of a weakening of the negative dust current may be seen, in contrast to the 2011 flight on the PHOCUS payload (Havnes et al., 2014). The Faraday rotation electron density probes and mNLP Langmuir probes on MXD-1 observed a strong bite-out for a background electron density of ∼ $10^9 m^{-3}$, with two pronounced peaks at 83 km and 86 km (M. Friedrich and E. Trondsen, private communication, 2017). This confirms that the ice particles residing in the NLC were predominantly charged negatively.

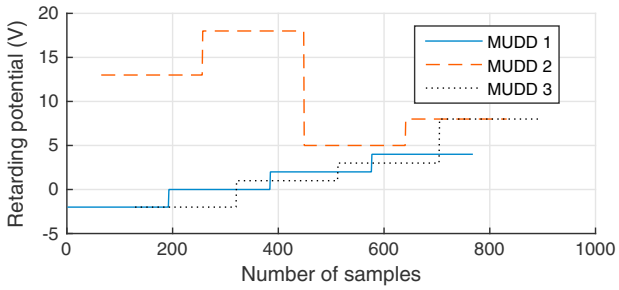

Figure 3. Stepping scheme of the different retarding potential modes for all MUDD probes. Note that the modes are slightly shifted in time relative to each other and the overlap between probes at $U_R = -2$ V and $U_R = 8$ V. The sampling frequency is 8,680 Hz, implying that a group of four steps, or 768 samples, takes ∼0.09 s to complete.

The bottom plate currents from MaxiDusty-1 are shown in Figure 7. The noise due to the squib firing at 83.5 km is present also in this data. Currents for equal voltage modes from the different probes, as well as evolution with altitude, match very well. The calibration factor between probes is addressed below. The regions where BP currents show clear signs of dust fragments matches with the lidar backscatter from the NLC; however, the PMSE strength does not follow the bottom plate current well, especially in the upper part of the echo. The currents above ∼86 km are weak, apart from a few short scale signatures on the order of ∼ 10 m. From the combined remote measurements and MUDD currents we shall therefore assume that there resided a population of relatively large ice particles in two layers: up to 84 km and around 85 km. Preliminary calculations of NLC particle sizes from RMR-lidar and the onboard photometer from the Department of Meteorology at Stockholm University also support this assumption (G. Baumgarten and J. Hedin, private communication, 2017). Further analysis of the DUSTY results confirms this. A population of smaller (PMSE) ice particles were probably present throughout the height region between 81 and 86 km.

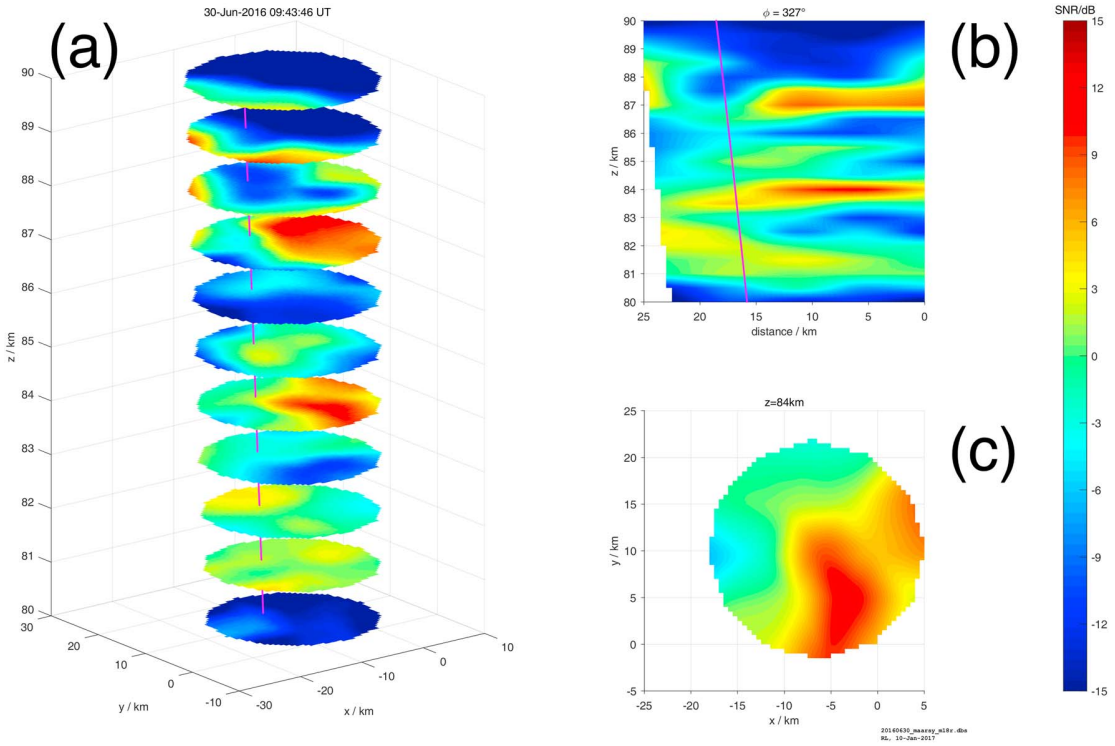

Figure 4. PMSE profile along rocket trajectory (marked as solid line) obtained with MAARSY for the MXD-1 flight. (a) Two-dimensional slices with a radius of 10 km, throughout the region containing PMSE. (b) A vertical slice in the plane of the rocket trajectory. (c) A two-dimensional snapshot of the PMSE at 84 km. Courtesy of Dr. Ralph Latteck, IAP Kühlungsborn.

The recorded BP currents increase with decreasing retarding potential, and the attracting mode $U_R = -2$V consistently records the strongest currents. For the neighboring modes $U_R = 1$ V and $U_R = 2$ V, the latter gives a bigger contribution to the total raw current; however, the effective current is still smaller when taking charging probability into account, as will be discussed below.

We must also address the calibration of the probes. MUDD-1 and MUDD-2 are, as mentioned above, referenced to MUDD-3 at potential modes $U_R = -2$ V and $U_R = 8$ V, respectively. For further analysis, we recalibrate the probes to MUDD-3 in the overlapping potential modes and use the same calibration factor for all potential modes. Using the same calibration is analogous to assuming that the dusty plasma has no fluctuations on length scales comparable to the payload diameter. This should most often be the case since the power spectral

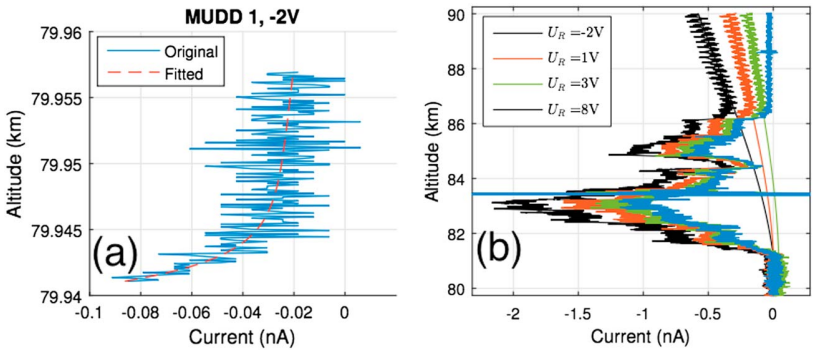

Figure 5. Steps in the postflight preparation of MUDD data. (a) Varying current in a single voltage mode when there is no dust, due to electrometer settling. The 20 first samples of the group have been removed, such that the length is 172 samples. (b) Changing BP current with height due to leakage electron current. Both these effects are removed by fitting and extracting fitted curves.

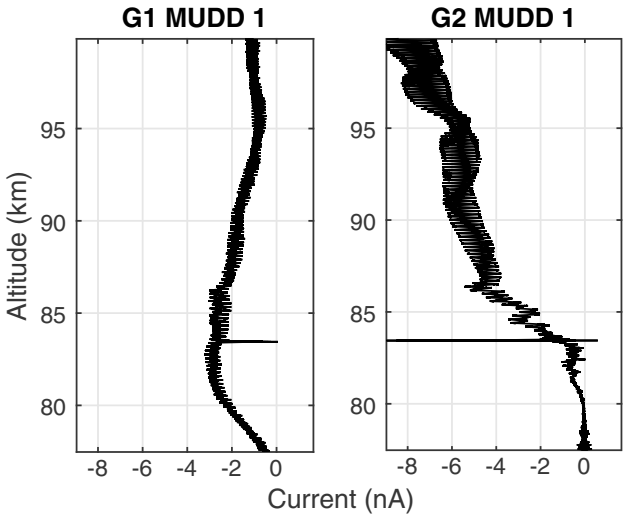

Figure 6. Raw currents to shielding grid (G1) and fragmentation grid (G2) from MUDD-1 on MXD-1. A bite-out in the electron population can be inferred by the G1 currents. The sharp peak around 83.5 km is due to a squib firing.

density in the neutral gas, for which the dusty plasma is a passive tracer, normally decreases rapidly at length scales less than a few meters (Rapp & Lübken, 2004). The payload diameter is 0.356 m. Figure 8 shows the two calibration factors through the ice layer for the MXD-1 flight. The probe currents are chosen as the median value for each voltage step of 172 samples, to reduce noise from very short current fluctuations. The ratio is close to unity throughout the whole layer with the exception of the height region near the squib firing at ~ 83.5 km and the very rapid change in current at ~ 84.2 km. A weak variation due to spin modulation is also observed. In the calculation of the total current contribution from the different potential modes, we have utilized the median value of every voltage step and rescaled the all currents according to the calibration curves in Figure 8.

3.2. MUDD Measurements on MXD-1B

The data handling and analysis procedures of the MXD-1B MUDD data are identical to the procedures utilized on MXD-1 data described in the previous section. Although the probe settings on the two payloads were identical, the recorded MUDD currents from the MXD-1B flight are difficult to explain with — or compare to — the previous MUDDs and also other Faraday bucket probes. For MXD-1, MUDD records currents that can be expected when the ice population consists of a significant number of large particles. This was also confirmed by DUSTY measurements for MXD-1, by employing methods used in several earlier works to characterize the charged particle population (see, e.g., Havnes & Næsheim, 2007; Havnes et al., 1996). For MXD-1B, all G1 and G2 grids on MUDD probes show very large negative currents but only a relatively weak bite-out and with heavy spin modulation even though attitude measurements show very little coning. The BP currents also behave unexpected but consistently with the G1 and G2 currents shown in Figure 9. These very negative currents are also seen in the two DUSTY probes flown on MXD-1B, for which we at present time do not have one single plausible explanation. The unusual signatures from the Faraday buckets on MXD-1B will be the topic of future work. Due to the highly variable currents, the calibration factor for MXD-1B is also variable and deviates significantly from unity at certain altitudes, as shown below. There is, however, little doubt that parts of the dust layer contain the typical ice particles as observed during the MXD-1 launch, and the results derived from MXD-1B data should to a certain degree yield valid estimates of fragment sizes. A natural consequence of the high variance is that the error becomes larger in the fitted size distribution.

Figure 10 shows all the raw bottom plate (BP) currents for the MXD-1B flight after subtraction of the electron leakage contribution. The altitude profile follows the shielding and fragmentation grid currents fairly well,

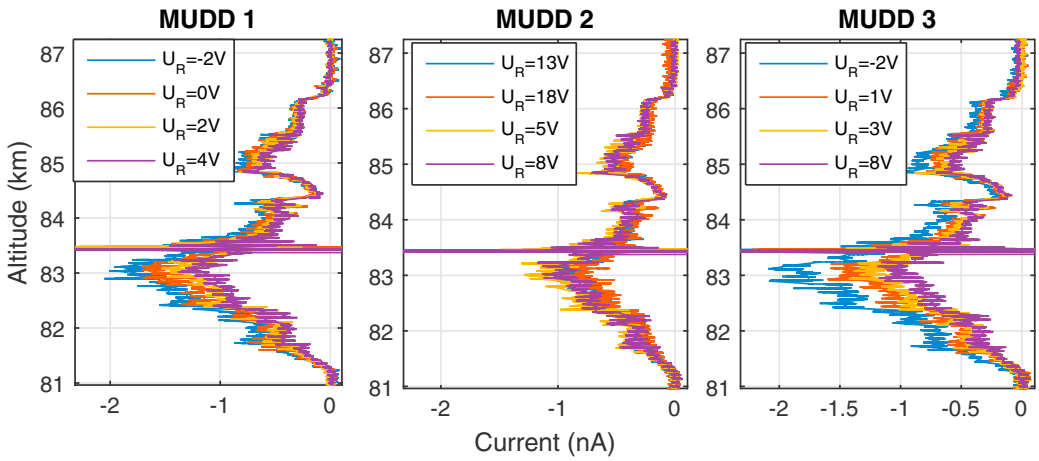

Figure 7. Raw currents corrected for increasing leakage electron current from the BP channel of all the MUDD probes on MXD-1.

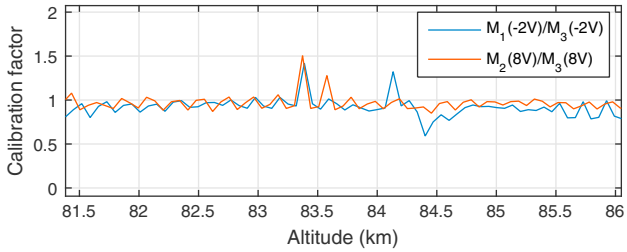

Figure 8. Calibration factor for equal potential modes on different probes. The probes are calibrated in flight by the ratio of overlapping potentials between probes. For MUDD-1 and MUDD-3 (blue line), the overlapping modes had retarding potential $U_R = -2$ V. For MUDD-2 and MUDD-3 (red line), the $U_R = 8$ V modes overlapped.

but a closer inspection reveals that structures are not completely coincident. This points toward a complicated relationship between the ambient dusty plasma parameters that cannot be resolved through analysis of the MUDD probes alone. Instrumental effects such as payload charging cannot be ruled out, but analysis of the floating potential of the onboard Langmuir probes (E. Trondsen, private communication, 2017) probably cannot explain the profile. It can also be speculated that UV radiation can affect the recorded current. The ~ 3.8 Hz spin modulation is prominent in the dust structure in the middle, however not as visible in the lower and upper layers. In general, the MXD-1B flight lacks the characteristics typical of large secondary charging effects where the current to G2 can become partly positive in the DUSTY probe. This would be a clear confirmation that a fragmentation charging process is dominating the G2 current and significantly influences BP currents.

The in-flight calibration curve, as discussed above, is shown in Figure 11. This deviates from the ideal situation where both curves are close to unity.

It is a likely possibility that the PMSE is partly populated by high concentrations of very small ice particles, many of which can be uncharged but may severely influence on the payload potential, by scavenging electrons from its surface. Artificial variations in the currents to the dust probes may also occur due to the airstream around the payload affecting smaller incoming particles. The deviation is only present for MUDD-1B, which has the lowest retarding potentials. A possible explanation is that the irregularity originates from a relatively high concentration of small charged ice particles with radii of a few nanometers that are barely energetic enough to penetrate G1 down to G2, but not further. However, the difference between equal potential on different probes cannot easily be explained. Another possible explanation of a calibration factor of ~10 could be that one of the booms measuring electron density (mNLP) was stuck in a (partly) vertical position such that the payload top deck was sprayed with fragments during certain periods of the rotation (Friedrich, private communication). Nevertheless, the fragment currents are stronger in the height region from 85.5 km to 86.7 km for all probes, and in the further analysis we use this region but recalibrate the currents for MUDD-1B.

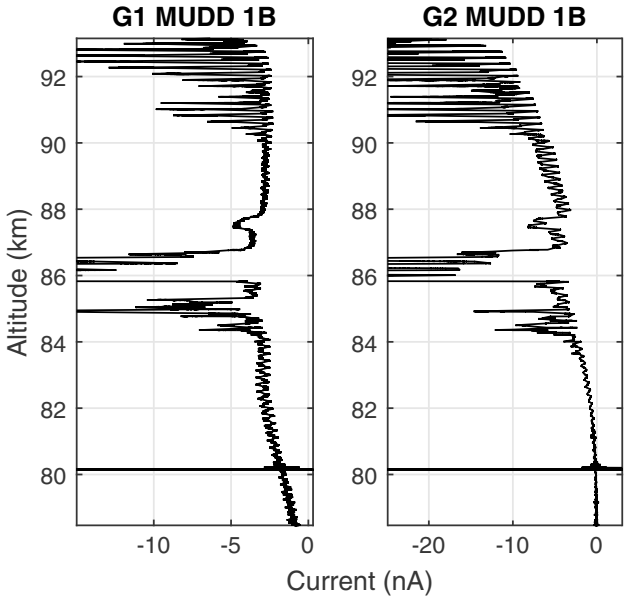

Figure 9. Raw currents to shielding grid (G1) and fragmentation grid (G2) from MUDD-1B on MXD-1B. The G1 current is more dynamic than on the first flight, but a bite-out can still be inferred from the profile. The peak at ~ 80 km is due to a squib firing.

4. Derived Size Distributions of Collision Fragments

Each potential step is 192 samples long (in the raw form), which corresponds to ~17.5 m along the payload orbit within the ice layer. Relatively large fluctuations on length scales smaller than this can readily occur, and we therefore utilize the median of each potential step when calculating a mean size distribution. With this method we obtain 10-point mean size distributions with an altitude resolution of ~ 70 m. Due to the internal mechanical structure of MUDD not being perfectly axisymmetric—for example, two cross beams strengthening G2—there is also spin modulation present in the BP currents. This effect was reduced by Fourier transforming and attenuating the 3.8 Hz frequency bins and the pronounced harmonics.

Currents from within the ice layer from the three MUDD probes on MXD-1, normalized to the $U_R = -2$ V mode, are shown in Figure 12. When two probes measure in the same mode simultaneously, an average of the currents is used. As confirmed by the raw currents, less retarding potential modes observe larger currents more or less consistently, as expected. An interesting feature is that the normalized contribution from the lower potential modes decrease with altitude, while higher retarding potentials record relatively larger currents. In multilayered dust clouds, it is possible that respective layers can have certain differences in size distributions, but even with homogeneity there are a few different possible explanations for this observed feature.

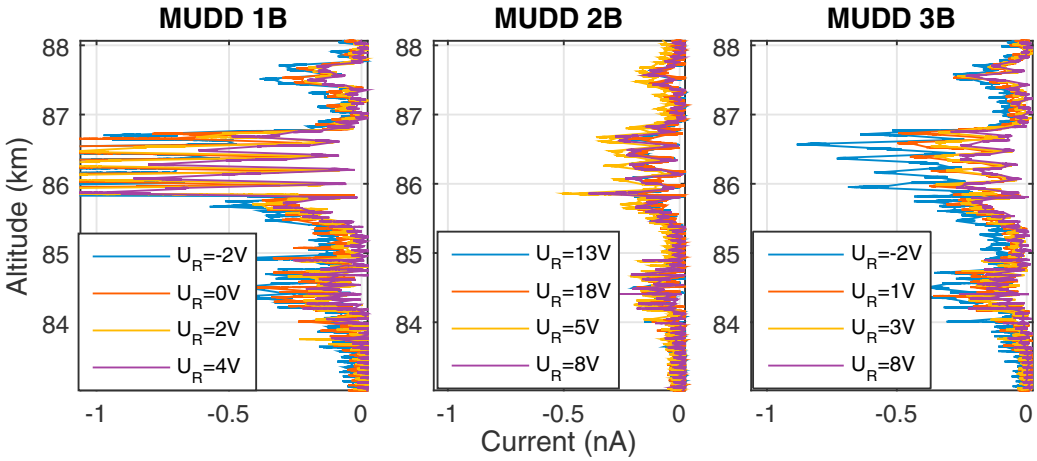

Figure 10. Raw currents corrected for increasing leakage electron current from the BP channel of all the MUDD probes on the MXD-1B payload.

Larger fragments topside. The variation in current with potential may be interpreted as fragments being larger at the topside of the dust cloud, which would be opposite from what is expected. However, this is unlikely in both of the main models of the mesospheric ice particle. First, if the large ice particles are solely made up of pure water ice throughout the cloud, this indicates that ice fragments increase in size with altitude. A physical description of such a situation cannot be obtained easily. Second, if the fragment size distribution is directly linked to the MSP size distribution, it would require that MSPs increase in size with altitude—opposite from what one would expect from growth and sedimentation mechanisms.

Changing production factor. Alternatively, the narrowing of the response versus potential with height in Figure 12 could indicate that the production factor of fragments decreases with altitude, which is consistent with the lidar measurements indicating fewer and/or smaller ice particles on the topside of the dust layer. Larger particles at the bottom would have more kinetic energy available to partly break the ice particle upon impact with the G2 grid and probably produce more fragments. We do not expect a strong influence on the MXD-1 observations due to particle sedimentation into warmer regions, since temperature measurements with iron lidar recorded consistent low temperatures $\sim$ 120 K throughout the whole region (J. Höffner, private communication, 2017). Also, the changing rocket speed throughout the layer will probably add to the effect. For MXD-1 the rocket velocity is approximately 838 m s^{-1} at 81 km and 772 m s^{-1} at 86 km, yielding a $\approx$ 15% reduction in impact energy at G2. This conclusion is also supported by mass spectrometer measurements indicating that the topside of the layer contains smaller particles, possibly free MSPs, which would not enter MUDD (Robertson et al., 2009).

"Nanodust shedding" effect. As a third explanation, we must mention a recent development in charging mechanisms for mesospheric nanoparticles that may explain a possible physical mechanism, where larger MSPs can be more abundant in the fragment distribution at the top of a NLC/PMSE layer. In a recent work, Havnes and Hartquist (2016) proposed a new mechanism where MSPs can scavenge electrons from larger ice particles (so called "nanodust shedding") that can further affect the internal distribution of MSP sizes inside ice particles. The physical explanation is that the switching time of the polarized ("image") potential on the surface of an ice particles is *slow* compared to the charging and escape rate of an impinging MSP. The result is that small MSPs are effectively shed, and large ice particles contain an overrepresentation of relatively large MSPs. The effect is stronger for low neutral temperatures ($\lesssim$ 120 K, which was the case for MXD-1, as measured by iron lidar; Höffner, private communication). Near the top layer of the dust cloud, the number density of the larger NLC particles may be low enough for the nanodust shedding effect to effectively quench the sticking of the smallest MSPs to the ice particle surface. In the lower part of the ice cloud, the number

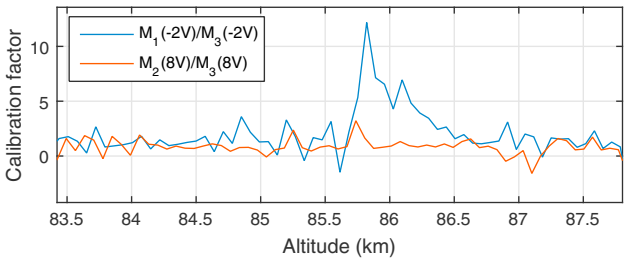

Figure 11. Calibration factor for equal potential modes on different probes for MXD-1B. The relatively high correction suggested by the ratio of the $U_R = -2$ V modes (blue line) is discussed in the text.

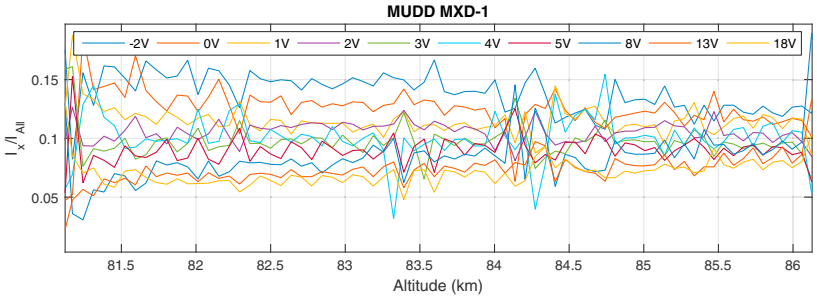

Figure 12. Ratio between MUDD currents from each retarding potential channel, respectively, (I_X) and the sum of all currents (I_{All}), that is, relative contribution to the total current, on the MXD-1 payload.

densities are high enough to absorb a large proportion of smoke particles, regardless. The shedding effect is suggested to affect short time scale charging events but depends on many intrinsic parameters that introduce uncertainties.

The normalized currents from the dust layer centered at $\sim$ 86.5 km during the MXD-1B launch are shown in Figure 13. The trend with decreasing currents with altitude, as seen during MXD-1, can be observed also here. The arguments given above for this observed trend should be valid for both flights. We note that the attracting channel current ($U_R = -2$ V) is comparatively larger for MXD-1B, and that the analyzed height region is much shorter for the second flight.

To obtain the fragment size distribution from the MUDD currents, we need to determine the true current contribution of fragments. Without knowing the size distribution of the incident particles that produce the fragments, it may be difficult to get accurate estimates of how the fragment size distribution develops with altitude (cf. the discussion above). We therefore calculate the integral contribution of all modes to yield a mean fragment size distribution throughout the dust layer. Figure 14 shows the integrated but otherwise untreated current distribution normalized to the current of the $U_R = -2$ V mode. In this distribution, all different potential modes contain currents from modes of higher retarding potentials, which need to be removed. For some neighboring bins, the mode with the highest retarding potential observes larger current than the lower potential mode. This may seem unphysical, but we note that the charging probabilities of fragments are not taken into account here and must be included to yield a correct size distribution.

To obtain the general size distribution we need also to calculate what fragment sizes correspond to each retarding potential and their respective charge state. The problem of relating the MUDD currents to fragment sizes was treated in depth by Antonsen and Havnes (2015). In that work, the movement inside MUDD of both pure MSPs and MSPs coated with ice layers of different thicknesses was simulated, and it was found that the recorded currents at BP (for the potential modes used here) are most likely from pure MSPs, rather than pure ice or a mixture of ice and meteoric material. In the present work we have utilized the dust dynamics model from the previously cited work and calculated the size bins for each potential mode. A short comment on a few

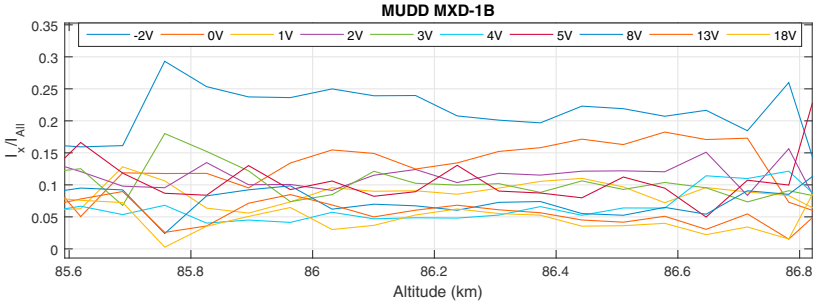

Figure 13. Relative contribution to the total currents for all retarding potential modes in the dust layer from 85 to 87 km on MXD-1B.

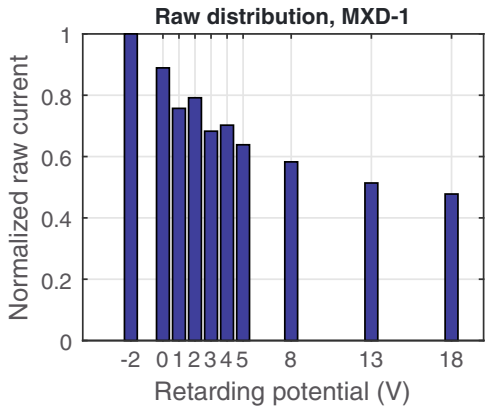

Figure 14. Distribution of integrated MUDD fragment currents from all channels of MUDD on MXD-1, corresponding to a cumulative mass distribution normalized to the current in the $U_R = -2$ V mode (total current, such that $I(-2V) = 1$). This is not adjusted for difference in charging probability.

central simulation parameters should be made. We have here assumed that 40% of the initial kinetic energy is preserved for movement of fragments, while the rest is dissipated to internal degrees of freedom in the fragmentation progress, that is, partial fragmentation, heating, and evaporation, as justified by experiments (Havnes et al., 2014; Tomsic, 2001). A change in the set initial fragment energy of ±10% then yields a difference in initial velocity of around ±50 m s^{-1}. The difference in estimates of the fragment size subsequently translates to roughly ±0.1 nm (Antonsen & Havnes, 2015). Furthermore, the MSP mass density is set to 3,000 kg m^{-3} (Klekociuk et al., 2005; Plane, 2011), and fragments are assumed to be singly negatively charged.

The charging probability of the fragmented dust particles introduces a relatively large uncertainty in the final mass distribution. The principal assumption to utilize for the charging state is that the charging probability is $P_c \propto m_{frag} \propto r^3$ for pure MSP fragments, following Friichtenicht (1964) and Adams and Smith (1971). This may not, however, be directly applicable to the case of relatively low velocity collisions. The dominating charging mechanism is triboelectric, so that we have also included the possibility of $P_c \propto r^2$, which should be a probable scaling. The obtained final size distribution, shown in Figures 15a and 15b for the first launch and Figures 15c and 15d for the second launch, shows similar trends as the theoretical distributions of free MSPs of Bardeen et al. (2008), Hunten et al. (1980), and Megner et al. (2006) (at 90 km), with the size range, 0.45–1.5 nm, spanning about 2 orders of magnitude in concentration. The theoretic distributions

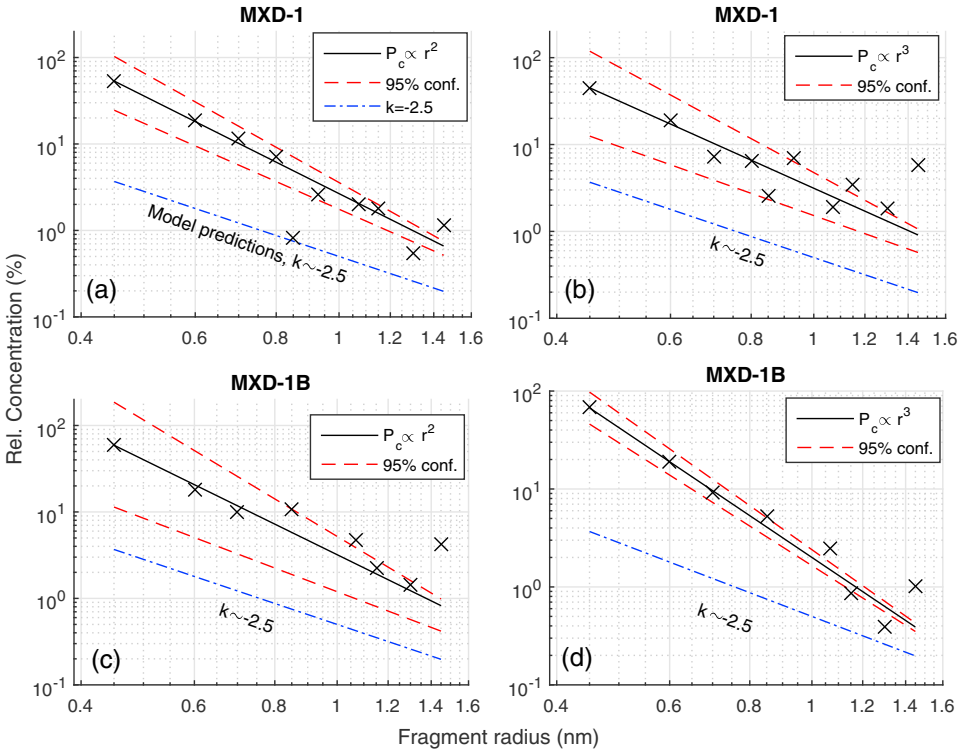

Figure 15. Obtained size distributions of collision fragments (MSPs inside ice particles) in MUDD on the MaxiDusty payloads for limiting values of charging probability (P_c). The obtained distributions are plotted as solid black lines, while the 95% confidence bounds are plotted in red dashed lines. The blue dash-dotted lines shows a fit of modeled size distributions of free MSPs at 90 km based on Bardeen et al. (2008), Hunten et al. (1980), and Megner et al. (2006). We note that the model prediction fit have been shifted down to emphasize the gradient; that is, the relative concentration is not accurate. (a) The MXD-1 case for P_c proportional to the fragment cross section. (b) The MXD-1 for P_c proportional to fragment volume. (c and d) The same respective limits of P_c for the MXD-1B flight.

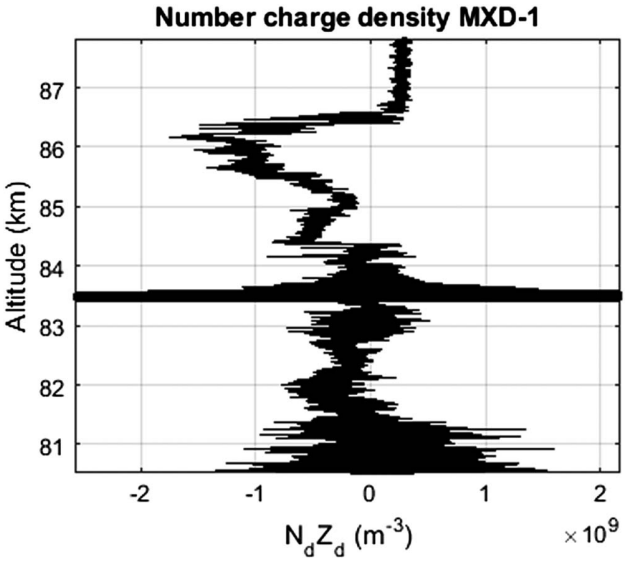

Figure 16. Charge number density throughout the layer containing dust/ice particles during MXD-1 derived from the DUSTY probe. The noisy nature of the profile around 83.5 km and below 81 km is due to mechanical stress from squib firings.

presented in the three modeling papers, plotted in blue dash-dotted lines, agree very well in the size range detectable in MUDD and a mean fit is presented. We note that the theoretic MSP distributions around 90 km can have a dependence on the production curve for meteoric ablated material, and some variation can be expected. If we look closer at the inverse power law size distributions that arise from the different charging probabilities, $n(r) \propto r^{-k}$, the exponent for the free MSPs is $k \sim 2.5$. However, in the distributions derived from MUDD, we obtain exponents of $k \sim 3.3 \pm 0.7$ for $P_c \propto r^2$ and $k \sim 3.7 \pm 0.5$ for $P_c \propto r^3$ for MXD-1, and $k \sim 3.6 \pm 0.8$ and $k \sim 4.4 \pm 0.3$ for MXD-1B, where the errors are based on the 95% prediction bounds. These values ($k \gtrsim 3$; Evans, 1994) may indicate that the distribution of the fragments reaching the bottom plate has not changed significantly from G2. Such a result may not agree with earlier work (Antonsen & Havnes, 2015) that indicate that only MSPs survive, and that the initial fragment distribution created in the collision with G2 changes toward lower k values as a result of fragment evaporation. From experiments, it has been found that ice particles $\lesssim$ 7 nm have a charging probability $\propto m^{3/2}$, and small water ice grains are found to stick effectively to metal surfaces (Tomsic, 2001). Moreover, very small ice grains that will also thermalize evaporate rapidly, according to extensive modeling of fragment dynamics and evaporation (Antonsen & Havnes, 2015). In that case, the inverse power law will be stronger than the one for pure MSPs and will probably have a cutoff and deviate from an ideal inverse power scaling. This makes ice particles an unlikely candidate to dominate the size distribution. We must also note that the uncertainties are many, and the inverse power law obtained here is nothing more than indicative of the expected size distribution. A significant source of error in the fitted distribution may lie in the determination of the sizes in the attracting potential mode, as dynamics of such small grains are difficult to simulate reliably. If the sizes from the smallest potential bins were shifted up only a few Ångstrøms, then the resulting size distribution would follow a significantly weaker inverse power law.

5. Discussion

We have in this work presented measurements from two triplets of the Faraday bucket probe MUDD launched on the MaxiDusty payloads MXD-1 and MXD-1B in the summer of 2016. In principle, the probes provide a simple technique to analyze the fragments of mesospheric ice particles larger than ~10 nm and are expected to separate between signatures of pure ice and meteoric agglomerates contained inside the particles entering the probes. From the combined measurements of the three probes and through numerical simulations of dust movement inside them (see Antonsen & Havnes, 2015), we have derived two 10-point size distributions of collision fragments. The size distributions can be fitted by inverse power laws. From considerations of fragment evaporation and dynamics, we find it unlikely that the measured currents are from pure ice, and thus, the derived size distribution should reflect the one of the MSPs. The exponents of the obtained power laws, $k \sim [3.3 \pm 0.7, 3.7 \pm 0.5]$ and $k \sim [3.6 \pm 0.8, 4.4 \pm 0.3]$ for the two flights, respectively, show as expected from theory (Hunten et al., 1980; Megner et al., 2006) and measurements of an earlier version of MUDD (Havnes et al., 2014) that the number of fragments of sizes around a few Ångstrøms, assumably MSPs, is at least 1 order of magnitude larger than the number of $\sim$ 1 nm particles. The obtained distribution would, by these arguments, be dominated by MSPs embedded in the ice particles. The power laws should not, however, be utilized as the size distribution of free MSPs as the growth and fragmentation process might also affect the distribution. Havnes et al. (2014) and Antonsen and Havnes (2015) discussed the possibility of larger ice fragments "disguising" as MSPs as a possible source of error. Another uncertainty in deriving the size distributions lies in the fragment charging and especially the triboelectric charging, which is thought to be dominant for nanometer size dust particles in the fragmentation process.

To provide additional justification for our conclusions, we can estimate the volume filling factor of presumable MSPs inside the NLC particles. The volume filling factor is a measurement of the content by volume of meteoric material in the ice particles. Following Havnes et al. (2014), the collected current on the bottom plate can be expressed as $I_{BP} = \xi N_d e A_M v_R$, where ξ is the number of charged fragments produced in a single

particle collision with G2, N_d is the number density of ice particles, $A_M = \pi \cdot 0.045^2$ m^2 is the MUDD cross section, $e = 1.6 \cdot 10^{-19}$ C is the elementary charge, and $v_R = 800$ m s^{-1} is the rocket velocity. For a simple estimate of ξ, we use values from MXD-1 at ~ 85 km. Inserting for the MUDD current, $|I_{BP}| = 1$ nA, we obtain $\xi N_d = 1.23\times10^9$m^{-3}. The charge number density, shown in Figure 16 for MXD-1, was obtained from measurements with the Faraday cup probe DUSTY and can be found in Figure 16 to be $|N_d Z_d| \approx 1.5\times10^9$ m^{-3}, where Z_d is the charge number of ice particles (typically $\bar{Z}_d = -1$ or a few times this in very active regions). Furthermore, assuming that monodispersive NLC particles with radii of 15 nm and concentration N_{15} produced the electron bite-out while a population of particles with radii 50 nm and concentration N_{50} produced the optical scattering, we can estimate that the measured charge number density was produced by ice particle concentrations of $N_{15} \approx 10^9$ m^{-3} and $N_{50} \approx 5\times10^7$ m^{-3} by using realistic charge distributions. We are then left with the equation $N_{50}\xi + N_{15}\xi(15/50)^3 = 1.23 \times 10^9$ m^{-3} that yields $\xi = 16$. The volume filling factor is dependent on the MSP size distribution; but for a homogeneous example population of 0.9 nm particles, the volume filing factor becomes $\approx 16 \times (0.9/50)^3 \times 100\% = 0.01\%$ for an ice particle with radius 50 nm and $\approx 0.075\%$ for a 25 nm ice particle. This is of course for the case when all fragments are charged, so that the actual filling factor can probably be at least 1 order of magnitude larger when accounting for charging probabilities. If assuming that all fragments are pure ice and accounting for their charging probability, we obtain unphysical filling factors of > 100%. This feature agrees well with the findings of Hervig et al. (2012) who found filling factors within the range 0.01–3% and Havnes et al. (2014) (for the first flight of MUDD on the PHOCUS payload) where the conclusion was that MSPs are abundant inside NLC particles with filling factors between 0.05% and several percent.

Acknowledgments
The MAXIDUSTY rocket campaign with related research was supported by the Norwegian Research Council and the Norwegian Space Centre. We would also like to thank Ralph Latteck and Gerd Baumgarten at IAP for providing MAARSY radar data and RMR lidar data, respectively, and Martin Friedrich for providing electron density data. All data related to MUDD, as well as raw data for all instruments, are available from the UiT Open Research repository at https://dataverse.no/dataset.xhtml?persistentId=doi:10.18710/KSGADN or through the DOI identifier. Raw PCM data from all instruments are also available from Andøya Space Center.

References

Adams, N. G., & Smith, D. (1971). Studies of microparticle impact phenomena leading to the development of a highly sensitive micrometeoroid detector. *Planetary and Space Science*, *19*(2), 195–204. https://doi.org10.1016/0032-0633(71) 90199-1

Antonsen, T., & Havnes, O. (2015). On the detection of mesospheric meteoric smoke particles embedded in noctilucent cloud particles with rocket-borne dust probes. *Review of Scientific Instruments*, *86*(3), 033305. https://doi.org10.1063/1.4914394

Bardeen, C. G., Toon, O. B., Jensen, E. J., Marsh, D. R., & Harvey, V. L. (2008). Numerical simulations of the three-dimensional distribution of meteoric dust in the mesosphere and upper stratosphere. *Journal of Geophysical Research*, *113*, D17202. https://doi.org10.1029/2007JD009515

Baumgarten, G., Fiedler, J., Lübken, F.-J., & von Cossart, G. (2008). Particle properties and water content of noctilucent clouds and their interannual variation. *Journal of Geophysical Research*, *113*, D06203. https://doi.org10.1029/2007JD008884

Bekkeng, T. A., Jacobsen, K. S., Bekkeng, J. K., Pedersen, A., Lindem, T., Lebreton, J. P., & Moen, J. I. (2010). Design of a multi-needle Langmuir probe system. *Measurement Science and Technology*, *21*(8), 085903.

Evans, A. (1994). *The dusty universe*, Series in Astronomy. Chichester, New York: John Wiley.

Friichtenicht, J. F. (1964). Micrometeoroid simulation using nuclear accelerator techniques. *Nuclear Instruments and Methods*, *28*(1), 70–78. https://doi.org10.1016/0029-554X(64)90351-9

Gerding, M., Kopp, M., Höffner, J., Baumgarten, K., & Lübken, F.-J. (2016). Mesospheric temperature soundings with the new, daylight-capable IAP RMR lidar. *Atmospheric Measurement Techniques*, *9*(8), 3707–3715. https://doi.org10.5194/amt-9-3707-2016

Gumbel, J., & Megner, L. (2009). Charged meteoric smoke as ice nuclei in the mesosphere: Part 1—A review of basic concepts. *Journal of Atmospheric and Solar-Terrestrial Physics*, *71*(12), 1225–1235.

Havnes, O., & Hartquist, T. W. (2016). Nanodust shedding and its potential influence on dust-related phenomena in the mesosphere. *Journal of Geophysical Research: Atmospheres*, *121*, 12,363–12,376. https://doi.org10.1002/2016JD025037

Havnes, O., & Næsheim, L. I. (2007). On the secondary charging effects and structure of mesospheric dust particles impacting on rocket probes. *Annales Geophysicae*, *25*(3), 623–637. https://doi.org10.5194/angeo-25-623-2007

Havnes, O., Trøim, J., Blix, T., Mortensen, W., Næsheim, L. I., Thrane, E., & Tønnesen, T. (1996). First detection of charged dust particles in the Earth's mesosphere. *Journal of Geophysical Research*, *101*(A5), 10,839–10,847. https://doi.org10.1029/96JA00003

Havnes, O., Gumbel, J., Antonsen, T., Hedin, J., & Hoz, C. La (2014). On the size distribution of collision fragments of NLC dust particles and their relevance to meteoric smoke particles. *Journal of Atmospheric and Solar-Terrestrial Physics*, *118*, 190–198. https://doi.org10.1016/j.jastp.2014.03.008

Havnes, O., Antonsen, T., Hartquist, T. W., Fredriksen, Å., & Plane, J. M. C. (2015). The Tromsø programme of in situ and sample return studies of mesospheric nanoparticles. *Journal of Atmospheric and Solar-Terrestrial Physics*, *127*, 129–136. https://doi.org10.1016/j.jastp.2014.09.010

Hedin, J., Gumbel, J., & Rapp, M. (2007). On the efficiency of rocket-borne particle detection in the mesosphere. *Atmospheric Chemistry and Physics*, *7*(14), 3701–3711. https://doi.org10.5194/acp-7-3701-2007

Hervig, M., McHugh, M., & Summers, M. E. (2003). Water vapor enhancement in the polar summer mesosphere and its relationship to polar mesospheric clouds. *Geophysical Research Letters*, *30*(20), 2041. https://doi.org10.1029/2003GL018089

Hervig, M. E., Deaver, L. E., Bardeen, C. G., Russell, J. M. III, Bailey, S. M., & Gordley, L. L. (2012). The content and composition of meteoric smoke in mesospheric ice particles from SOFIE observations. *Journal of Atmospheric and Solar-Terrestrial Physics*, *84-85*, 1–6. https://doi.org10.1016/j.jastp.2012.04.005

Hunten, D. M., Turco, R. P., & Toon, O. B. (1980). Smoke and dust particles of meteoric origin in the mesosphere and stratosphere. *Journal of the Atmospheric Sciences*, *37*(6), 1342–1357. https://doi.org10.1175/1520-0469(1980)037<1342:SADPOM>2.0.CO;2

Jacobsen, K. S., Pedersen, A., Moen, J. I., & Bekkeng, T. A. (2010). A new Langmuir probe concept for rapid sampling of space plasma electron density. *Measurement Science and Technology*, *21*(8), 085902.

Jacobsen, T. A, & Friedrich, M. (1979). Electron density measurements in the lower *D*-region. *Journal of Atmospheric and Terrestrial Physics*, *41*(12), 1195–1200. https://doi.org10.1016/0021-9169(79)90022-9

Kassa, M., Rapp, M., Hartquist, T. W., & Havnes, O. (2012). Secondary charging effects due to icy dust particle impacts on rocket payloads. *Annales Geophysicae*, *30*(3), 433–439. https://doi.org10.5194/angeo-30-433-2012

Klekociuk, A. R., Brown, P. G., Pack, D. W., ReVelle, D. O., Edwards, W. N., Spalding, R. E., … Zagari, J. (2005). Meteoritic dust from the atmospheric disintegration of a large meteoroid. *Nature*, *436*(7054), 1132–1135. https://doi.org10.1038/nature03881

Knappmiller, S., Rapp, M., Robertson, S., & Gumbel, J. (2011). Charging of meteoric smoke and ice particles in the mesosphere including photoemission and photodetachment rates. *Journal of Atmospheric and Solar-Terrestrial Physics*, *73*(14–15), 2212–2220. https://doi.org10.1016/j.jastp.2011.01.008

Kuuluvainen, H., Arffman, A., Saukko, E., Virtanen, A., & Keskinen, J. (2013). A new method for characterizing the bounce and charge transfer properties of nanoparticles. *Journal of Aerosol Science*, *55*, 104–115. https://doi.org10.1016/j.jaerosci.2012.08.007

Lübken, F-J. (1999). Thermal structure of the arctic summer mesosphere. *Journal of Geophysical Research*, *104*(D8), 9135–9149.

Megner, L., Rapp, M., & Gumbel, J. (2006). Distribution of meteoric smoke—Sensitivity to microphysical properties and atmospheric conditions. *Atmospheric Chemistry and Physics*, *6*(12), 4415–4426. https://doi.org10.5194/ acp-6-4415-2006

Murray, B. J., & Jensen, E. J. (2010). Homogeneous nucleation of amorphous solid water particles in the upper mesosphere. *Journal of Atmospheric and Solar-Terrestrial Physics*, *72*(1), 51–61. https://doi.org10.1016/j.jastp. 2009.10.007

Plane, J. M. C. (2003). Atmospheric chemistry of meteoric metals. *Chemical Reviews*, *103*(12), 4963–4984. https://doi.org10.1021/cr0205309

Plane, J. M. C. (2011). On the role of metal silicate molecules as ice nuclei. *Journal of Atmospheric and Solar-Terrestrial Physics*, *73*(14–15), 2192–2200. https://doi.org10.1016/j.jastp.2010.07.008

Rapp, M., & Lübken, F.-J. (2004). Polar mesosphere summer echoes (PMSE): Review of observations and current understanding. *Atmospheric Chemistry and Physics*, *4*(11/12), 2601–2633. https://doi.org10.5194/acp-4-2601-2004

Rapp, M., & Thomas, G. E. (2006). Modeling the microphysics of mesospheric ice particles: Assessment of current capabilities and basic sensitivities. *Journal of Atmospheric and Solar-Terrestrial Physics*, *68*(7), 715–744.

Reid, G. C. (1997). The nucleation and growth of ice particles in the upper mesosphere. *Advances in Space Research*, *20*(6), 1285–1291. https://doi.org10.1016/S0273-1177(97)00788-6

Robertson, S., Horanyi, M., Knappmiller, S., Sternovsky, Z., Holzworth, R., Shimogawa, M., … Hervig, M. E. (2009). Mass analysis of charged aerosol particles in NLC and PMSE during the ECOMA/MASS campaign. *Annales Geophysicae*, *27*(3), 1213–1232. https://doi.org10.5194/angeo-27-1213-2009

Tomsic, A. (2001). Collisions between water clusters and surfaces (PhD thesis), Göteborg University, Gothenburg, Sweden.

von Cossart, G., Fiedler, J., & von Zahn, U. (1999). Size distributions of NLC particles as determined from 3-color observations of NLC by ground-based lidar. *Geophysical Research Letters*, *26*, 1513–1516. https://doi.org10.1029/1999GL900226

Von Zahn, U., Von Cossart, G., Fiedler, J., Fricke, K. H., Nelke, G., Baumgarten, G., … Adolfsen, K. (2000). The ALOMAR Rayleigh/Mie/Raman lidar: Objectives, configuration, and performance. *Annales Geophysicae*, *18*(7), 815–833.

Zahn, U., & Meyer, W. (1989). Mesopause temperatures in polar summer. *Journal of Geophysical Research*, *94*(D12), 14,647–14,651.

Zasetsky, A. Y., Petelina, S. V., & Svishchev, I. M. (2009). Thermodynamics of homogeneous nucleation of ice particles in the polar summer mesosphere. *Atmospheric Chemistry and Physics*, *9*(3), 965–971. https://doi.org10.5194/acp-9-965-2009

PAPER III

Antonsen, T., Havnes, O., and Spicher, A.: Multi-scale Measurements of Mesospheric Aerosols and Electrons During the MAXIDUSTY Campaign., Atmospheric Measurement Techniques, In Review, 2018

Multi-scale Measurements of Mesospheric Aerosols and Electrons During the MAXIDUSTY Campaign

Tarjei Antonsen[1], Ove Havnes[1], and Andres Spicher[2]

[1]Department of Physics and Technology, UiT- The Arctic University of Norway
[2]Department of Physics, University of Oslo

Correspondence: T. Antonsen (tarjei.antonsen@uit.no)

Abstract. We present measurements of small scale fluctuations in aerosol populations as recorded through a mesospheric cloud system by the Faraday cups DUSTY and MUDD during the MAXIDUSTY-1B flight on the 8th of July, 2016. Two mechanically identical DUSTY probes mounted with an inter-spacing of ~ 10 cm, recorded very different currents, with strong spin modulation, in certain regions of the cloud system. A comparison to auxiliary measurement show similar tendencies in the MUDD data. Fluctuations in the electron density are found to be generally anti-correlated on all length scales, however, in certain smaller regions the correlation turns positive. We have also compared the spectral properties of the dust fluctuations, as extracted by wavelet analysis, to PMSE strength. In this analysis, we find a relatively good agreement between the power spectral density (PSD) at the radar Bragg scale inside the cloud system, however the PMSE edge is not well represented by the PSD. A comparison of proxies for PMSE strength, constructed from a combination of derived dusty plasma parameters, show that no simple proxy can reproduce PMSE strength well throughout the cloud system. Edge effects are especially poorly represented by the proxies addressed here.

1 Introduction

The terrestrial mesosphere, situated at $\sim 50 - 100$ km, contains the ambient prerequisites to house a number of different types of nanoparticles. From nanometer sized meteoric smoke particles (MSP) coagulated from ablation vapors of meteors, to ice particles with radii of several tens of nanometers, aerosols in this region vary greatly in composition and size. Such variation consequently makes mesospheric ice and dust particles important in many physical and chemical processes in the atmosphere. The summer mesosphere is particularly interesting in the study of ice and dust particles due to extremely low temperatures, often $\lesssim 120$ K at the mesopause (Lübken, 1999; Gerding et al., 2016), which lowers the nucleation threshold of said aerosols. The mesopause region, located between ~ 80 and 90 km, is the only region with consistently low temperatures for ice particles to form regularly. Ice particles of sizes $\gtrsim 10$ nm can scatter light effectively and consequently give rise to the phenomenon called noctilucent clouds (NLC). Subvisual particles can also produce coherent radar echoes at frequencies between some tens of MHz and ~ 1 GHz, by reducing the electron diffusivity such that gradients in electron density can persist for long time periods and produce radar backscatter at the radar Bragg-scales. Such echoes are called Polar Mesospheric Summer Echoes (PMSE; see e.g. Rapp and Lübken (2004); Rapp and Thomas (2006) for comprehensive reviews).

Due to the height range of the mesosphere, it is unaccessible for balloons and rocket probes is the only means of in situ observation. Remote measurements are readily carried out from ground and satellites, but some ground measurements are contingent on lower atmosphere conditions while satellite measurements depend on orbit type. For a full characterization of the dusty plasma in the mesopause region, conventional payloads for this purpose must contain probes for detection of electrons, ions and dust and ice particles. Conventional Langmuir probes are convenient in measuring ambient plasma densities, however, different problems may arise in the calibration of these (Bekkeng et al., 2013; Havnes et al., 2011). Dust particle measurements are often carried out with Faraday buckets, which are electrostatic probes designed to separate charged particles from ambient ions and electrons (see e.g. Havnes et al. (1996); Gelinas et al. (1998)). As with Langmuir probes, calibration of Faraday buckets is a possible issue. Further problems connected to particle dynamics are also typical for mesospheric rocket probes, and modeling of neutral gas flow and electric field structure is often required. Studies of the cut-off of observable sizes in Faraday buckets have shown that at altitudes around 85 km, MSPs with radii $\lesssim 1-2$ nm are swept away in the shock in front of the probes, while the cut-off radius for ice particles is somewhat higher (Hedin et al., 2007; Antonsen and Havnes, 2015). Furthermore, secondary charging effects must be considered to correctly interpret measured currents (Havnes and Næsheim (2007); Kassa et al. (2012), Havnes et al. (2018a) – this issue).

1.1 Small-scale measurements in the mesopause region

Observations of mesospheric dust structures on the smallest scales possible are especially interesting in explaining UHF PMSE, diffusion processes and size sorting among other phenomena in the mesopause region. These phenomena are not particularly well understood, and small scale density variations of aerosols and their connection to neutral turbulence and electron density still require substantial observational and theoretical work to be fully comprehended. Few previous studies have emphasized on simultaneous measurements of dust and electron populations. Rapp et al. (2003a) studied the simultaneous variation of electrons and aerosols, and the spectral properties of their fluctuations. They found that there was a general anti-correlation between electrons and charged particles, and that the connection to neutral turbulence was clear. The anti-correlation has been observed on large scales since the early days of mesospheric rocket studies (see e.g. Pedersen et al. (1970)), but its precence on the smallest scales is not the general rule. Lie-Svendsen et al. (2003) showed that a correlation between ions and electrons, thus complicating the relationship with dust particles, can be positive in regions of high aerosol evaporation and large particles. Strelnikov et al. (2009) studied the connection to neutral turbulence, substantiating the connection between mesospheric dust and VHF PMSE.

In this work, we present the measurements from theMAXIDUSTY campaign, with special emphasis on the MAXIDUSTY-1B payload launched from Andøya Space Center, 8th of July 2016. The top deck contained, among other probes, two mechanically and electrically identical DUSTY Faraday buckets with an interspacing of ~ 10 cm. The DUSTY probe (see (Havnes et al., 1996)) can yield absolute dust charge number density, and the setup on MAXIDUSTY-1B is intended to study horizontal density variations of dust on very short length scales. As is shown, the probes recorded very different currents in certain parts of the dust layer, while almost identical currents in other parts of the layer, suggesting that the assumption of homogeneity of the dust and/or flow structure across the payload top deck is not always valid. Three modified Faraday cups of the type

MUDD (see Havnes et al. (2014); Antonsen and Havnes (2015); Antonsen et al. (2017)) with similar interspacing, confirm the DUSTY measurements and display a similar difference between probe currents. A comparison between electron currents from needle Langmuir probes (U. of Oslo) shows that the correlation is generally clearly negative between dust number densities and electron densities, but in some regions of the cloud system the correlation is more variable and not as unambiguous. We also perform a spectral analysis of fluctuations in the aerosol population, and we discuss these results in the framework of simultaneous PMSE observations done with the IAP MAARSY radar. Lastly, we discuss the applicability and validity of simple proxies composed of the dusty plasma parameters in predicting PMSE strength and shape.

2 The DUSTY Faraday Bucket

The schematics of the DUSTY probe are shown in Fig. 1, and the principle of current generation in DUSTY is shown in Fig. 2. The top grid is set to payload potential and is intended to shield neighboring probes from internal electric fields. The grid G1 is biased at +6.2 V in order to deflect ambient ions and absorb ambient thermal electrons. The G2-grid was originally intended to absorb secondary electrons ejected from the bottomplate (BP), to correct for this loss in the derivation of the dust charge number density (Havnes et al., 1996; Havnes and Næsheim, 2007). However, as justified by observations and theoretical considerations, the secondary production at G2 is the dominating secondary charge source and no detectable secondary charge production takes place at the bottom plate. This finding facilitates the utilization of DUSTY to measure dust sizes and absolute number densities of dust particles (Havnes et al., this issue) .

As indicated above, it has been found that particles of sizes $\lesssim 1-2$ nm are heavily affected by air flow around the probe in the mesopause region (Hedin et al., 2007; Antonsen and Havnes, 2015; Asmus et al., 2017). In the following, we will therefore assume that these particles contribute little to the total dust number density. Such an assumption can be further justified by the notion that very small particles can be neutralized effectively by photo-detachment during sunlit conditions. The dust currents to grid G2 and BP can then be expressed as:

$$I_{G2} = \sigma I_D + I_{sec} \tag{1}$$

$$I_{BP} = (1-\sigma) I_D - I_{sec} \tag{2}$$

where I_D is the current between G1 and G2 as shown in Fig. 1, and $\sigma = 0.28$ is the effective area factor of G2. We can furthermore relate I_D to the dust charge density $N_d Z_d$ according to:

$$I_D = (1-\alpha) N_d Z_d e v_R \pi R_p^2 \cos\gamma \tag{3}$$

where v_R is the rocket speed, $e = 1.6 \cdot 10^{-19}$ C the elementary charge, R_p is the probe radius, γ is the coning angle and $\alpha = 0.08$ is the fraction of the probe area covered/shadowed by G1 and G0. Here we have neglected any secondary production of charge at G1, and the secondary contribution to the currents is denoted by I_{sec}. From earlier flights and laboratory studies is

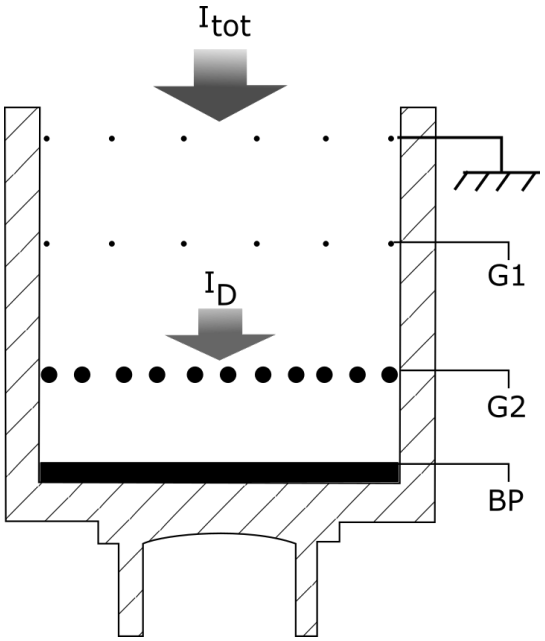

Figure 1. Cross section of the DUSTY probe. The upper grid is payload ground intended to shield neighboring probes from E-fields. The Grids G1 and G2 and the bottom plate (BP) have potentials optimized to shield ambient plasma and detect mesospheric dust and ice particles. The wire thickness is exaggerated there for convenience, and we also note that the G2 wires are thicker that the G1 and shielding grid wires.

has been found that the net contribution of this term is positive during exposure to ice particles less than a few minutes, meaning that dust particles rub off electrons from grid wires in a triboelectric fashion, as illustrated in Fig. 2 (Tomsic, 2001; Havnes and Næsheim, 2007; Kassa et al., 2012). This effect requires a grazing angle of around 70 to 75 degrees to be maximized, if the particles are pure ice (Tomsic, 2001). We also note that combining the equation yields $I_D = I_{G2} + I_{BP}$, as expected.

Figure 3 shows the mechanical layout of the topdeck on the MXD-1B payload. The layout was similar to the MXD-1 topdeck layout, only with one DUSTY probe replacing the miniMASS aerosol spectrometer (CU Boulder). In total five dust detectors were included on the second flight, of which three were of the type MUltiple Dust Detector (MUDD) and two were identical DUSTY probes. The topdeck also contained sun sensors (denoted DSS in the figure) for orientation measurements, and the Identification of the COntent of NLC particles (ICON) neutral mass spectrometer (see Havnes et al. (2015)). Measurements of electron density where made by Faraday rotation (TU Graz) and multi-needle Langmuir probes (mNLP, U. of Oslo). A Positive Ion Probe (PIP) and a Capacitance probe were mounted on booms (TU Graz). Due to the high sampling rate of the mNLP-instrument, its data is best suitable for comparison of simultaneous small scale fluctuations in aerosol and electron populations and it will therefore be utilized in the comparison between aerosol and electron fluctuations below.

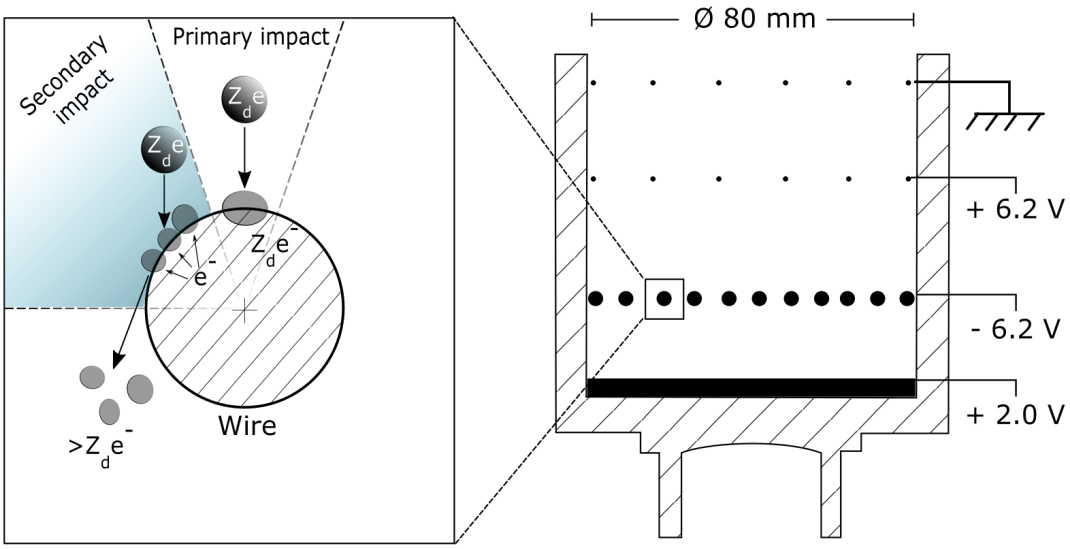

Figure 2. Principle sketch of large, order of 10 nm, particles entering DUSTY as launched on the MAXIDUSTY payloads. The mechanism can be described as follows: (1) A large particle deposits its charge in a primary impact and is partly fragmented, (2) If the impact is grazing, fragments can steal electrons from the grid wire. For large particles, the fragments tend to take away more electrons from the wires than the incoming charge and the net current to G2 becomes positive. For small particles, the primary charge is usually larger than the fragment current, and the net current to G2 thus becomes negative. In both cases, the bottom plate current becomes negative. We note that the secondary impact area region is exaggerated here; the true secondary charge producing area is $\gtrsim 20\%$.

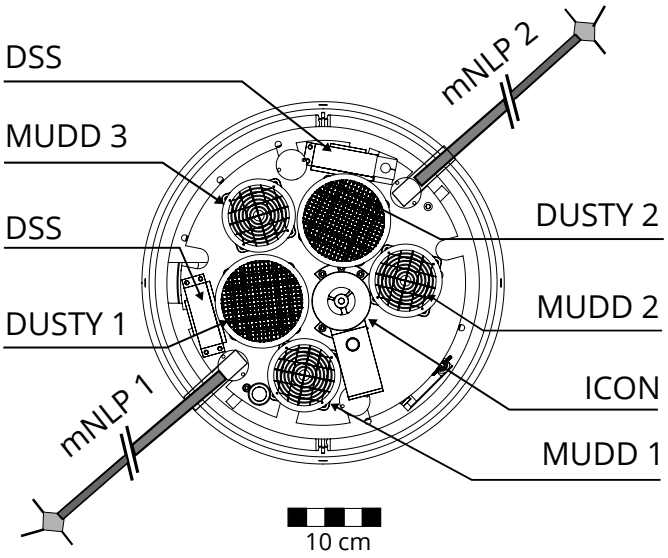

Figure 3. Layout of the topdeck and mNLP booms on the MXD-1B payload. The two identical DUSTY probes have a distance between them of 10 cm from center to center. The length of the booms was ~ 60 cm, with the aim to minimize aerodynamic and electric adverse effects from the main payload structure.

3 DUSTY measurements from the MXD-1B launch

As this work focuses on small-scale measurements of fluctuations in the mesospheric dusty plasma, we use the MXD-1B flight in a case study as it had the dual DUSTY configuration introduced above. DUSTY data from the first flight (MXD-1) gives the basis for the two recent papers of Havnes et al. (2018b) and Havnes et al. (2018, this issue), and in this work we also briefly discuss measurements from that payload. The MXD-1B payload was launched from Andøya Space Center (69.29°N, 16.02°E) at 13:01 UT on July 8, 2016. Simultaneous PMSE measurements done with the MAARSY 53.5 MHz VHF radar, recorded an unusually strong PMSE stretching from ~ 84 to ~ 88 km in altitude. Due to visibility issues, NLC observation by lidar was unavailable at the time of launch.

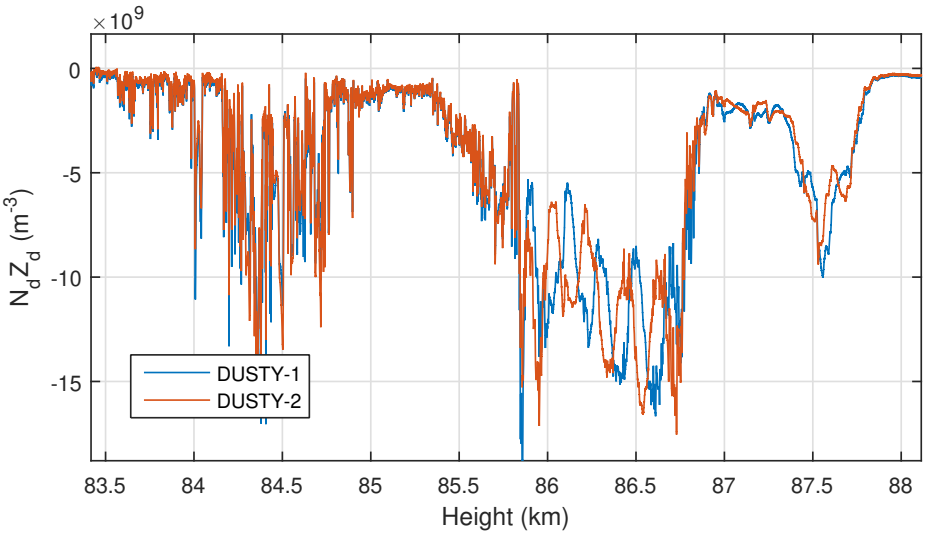

Figure 4. Dust charge number density for the identical DUSTY probes launched on the MXD-1B payload on the 8th of July 2016.

A main motivation behind launching two identical probes with a short distance between them, is to characterize the two dimensional structure of dust clumps and holes throughout the cloud region on the shortest scales – i.e. scales on which UHF PMSE are produced. If the dust clumps are made up of dust particles which are large enough to be unaffected by the airflow around the payload, and that the DUSTY probes have no leakage of ambient plasma, the currents measured by DUSTY-1 and DUSTY-2 should be identical. Discrepancies between probe signals imply that aerodynamic effects or other adverse effects are important. We see from the dust charge density derived from the two DUSTY probes in Fig. 4, however, that such a simple similarity is not the case at all heights. Taking the ratio between probe BP currents, $I_{BP,1}/I_{BP,2}$, yields a ratio near unity in the lower part of the cloud system, but from the middle of the cloud the ratio deviates from 1. Between 86 and 86.8 km the difference between the two probes is particularly large. Figure 5 shows the onset of the first disagreement region which starts at ~ 85.85 km. Below this altitude the ratio between DUSTY-1 and DUSTY-2 measurements follow each other closely, but at altitudes above, the currents are strongly influenced by the rotation of the payload and we see that the two probes here vary

roughly in antiphase. The phase difference is very close to the 125° azimuth angle difference between the probes on the front deck (see Fig. 3).

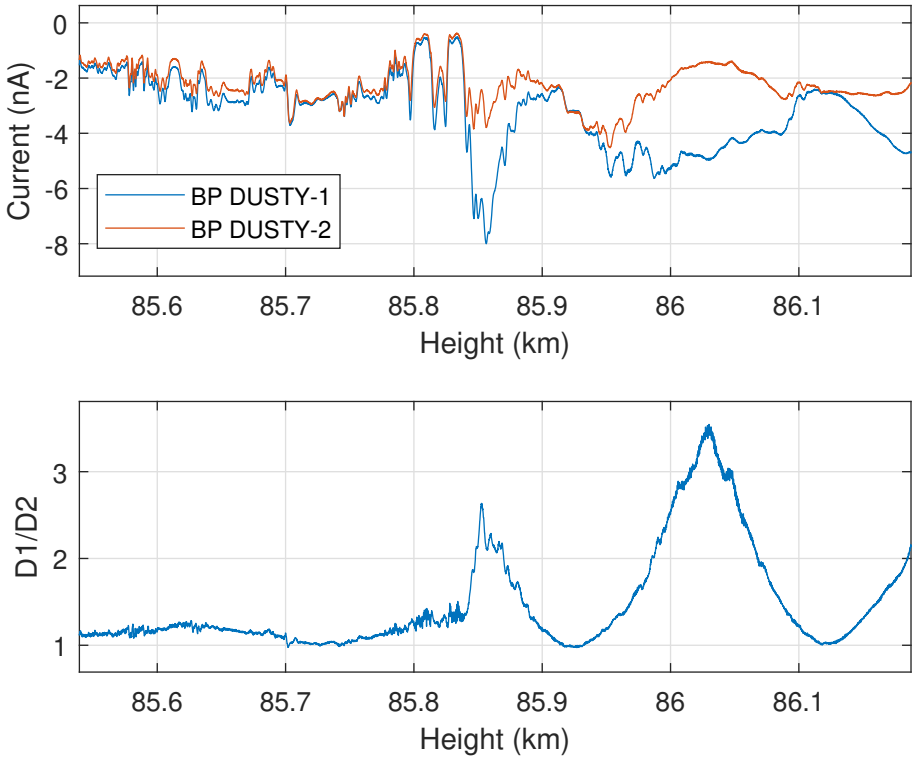

Figure 5. Magnification of the immediate region around the onset height (~ 85.85 km) of the large disagreement between the DUSTY probes. Above this height, the ratio of the two DUSTY currents becomes heavily modulated with a characteristic oscillation at the payload spin frequency.

Figure 6 shows the BP currents over approximately two rotation periods below the onset altitude. A weak modulation of the ratio $I_{BP,1}/I_{BP,2}$ with payload rotation is present (≈ 3.8 Hz), but the agreement is very good down to the smallest scales $\lesssim 1$ m.

It seems obvious that the main factor in the disagreement between the probes has to be the air stream around the payload which can affect dust particles, particularly the very small ones below one or two nanometer which can be totally swept away from the probes. However, also the somewhat larger dust particles will be affected by the air stream and have their velocity direction affected. If the payload had no coning, so that the payload velocity is directed along its axis, we would expect no change due to rotation unless a strong external wind, at a large angle to the payload axis, could introduce some asymmetry in the air stream. For mesospheric rockets with apogees $\lesssim 140$ km, we expect an angle between payload velocity and axis of

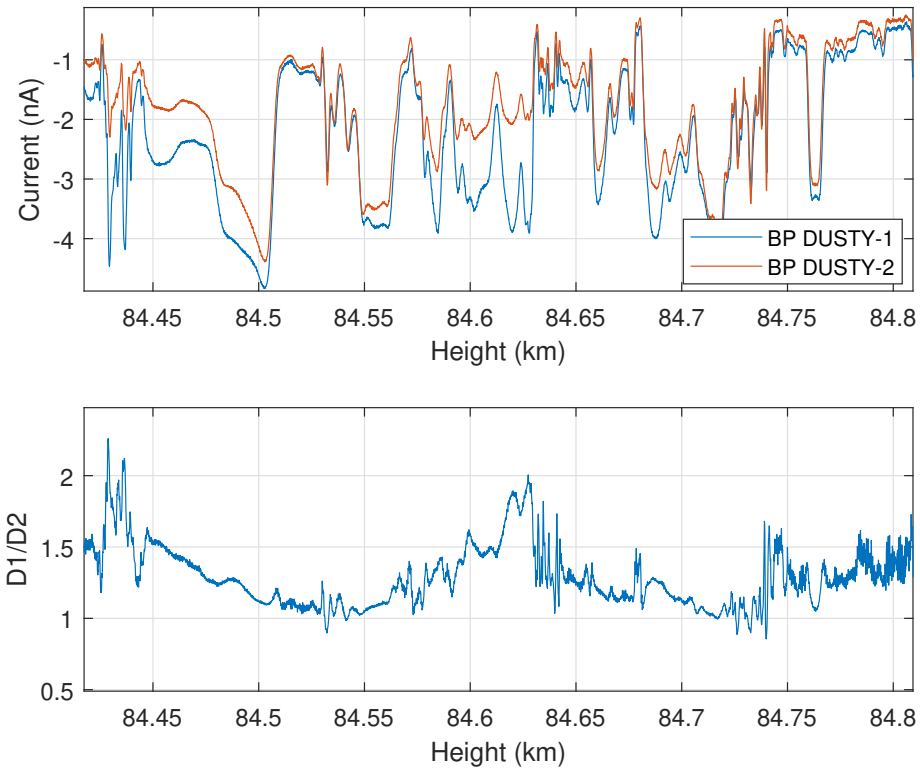

Figure 6. Magnification of region with relatively strong probe currents below disagreement onset. A generally good agreement is found down to the lowest height scales ($\sim$ 10 cm), which is justified by the $D1/D2$-ratio being near unity.

8-10 degrees throughout the cloud region, which was confirmed by magnetometer orientation data. Also, the asymmetry of the instruments on the front deck could lead to an asymmetry of the air stream even with zero coning. Additionally, ambient plasma may affect recorded currents if the payload becomes substantially charged. The complete characterization of the aerodynamic environment around the supersonic payload flying through a mesospheric dusty plasma is a phenomenal problem to attack, and will not be the main focus of this work. Nevertheless, it is very probable that findings about adverse effects related to aerodynamics and payload charging on the MXD payloads can be transferred with some generality to similar datasets.

Moreover, we have a new tool to further substantiate the claim of small dust particles. By iterating the dusty plasma equations for charge balance and equilibrium between charge states simultaneously (Havnes et al. 2018, this issue), it is possible to calculate the mean dust radius with very good height resolution in a layer of dust from DUSTY-currents. In Fig. 7 we show the result of such a calculation for the MXD-1B. The thin and high peaks occurring at certain heights are regions where the equation for radius approaches 1/0 in the iteration. Such cases usually occur around cloud edges, so the method is more reliable inside clouds. In general, the particle sizes are relatively small throughout the cloud system and only passes 20 nm below ~ 84

km. The results above 88 km may be difficult to interpret due to the very low amount of dust there. Since DUSTY currents are directly proportional to the charge number density of dust particles, the iteration scheme mentioned above can be used to obtain the total density of aerosols, N_d, also seen in Fig. 7. In the further discussion of how DUSTY currents relate to electron density, we note from the figure that the number density of aerosols is $\sim 10^8 - 10^{10}$ m^{-3}. Compared to electron density measurements from Faraday rotation (Friedrich, M., private communication, 2018), this is one to three order of magnitude lower than N_e throughout the layer, which justifies that we can utilize theory on PMSE reflectivity which is valid for low values of $\Lambda = N_d Z_d / N_e$ when investigating the relationship of aerosols to PMSE strength below.

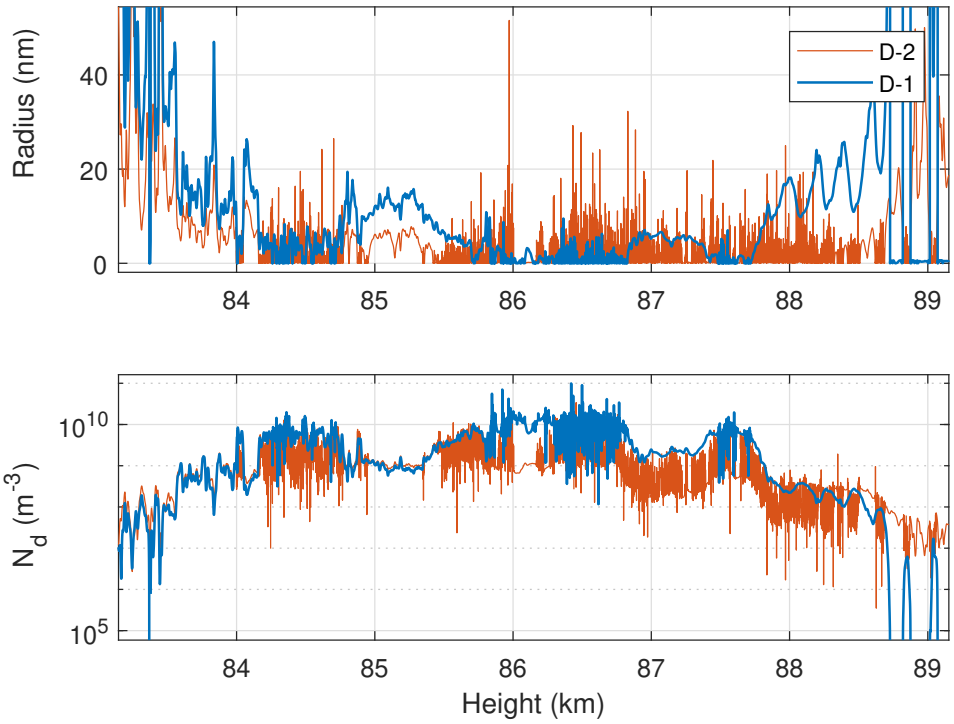

Figure 7. Particle radius and number densities derived from DUSTY-1 (blue) and DUSTY-2 (red) data through the method introduced by Havnes et al. (2018, this issue). The sizes are generally small and densities are generally high compared to earlier flights and values usually found in lidar studies.

4 Comparison to auxiliary mesurements

4.1 Secondary Impact Currents: MUDD measurements

As a control of the DUSTY measurements we address the similarity of the MUDD measurements to the measurements from the DUSTY probes. The principal difference between a DUSTY and a MUDD probe is that in the latter, the G2 grid is replaced with an opaque grid consisting of inclined concentric rings to ensure that all particles hit a ring. The principle is that the secondary current should become large compared to DUSTY, since in MUDD the area producing secondary charging now is equal to the full opening of DUSTY (i.e. $\rho = 1$ in eqs. 1 and 2). On the MXD-1B payload, three MUDD probes were mounted on the topdeck with an azimuthal angle of $\sim 120^\circ$ between them. For comparison to DUSTY, we look at the currents from the MUDD-1 and MUDD-3 probes since these had observation modes with attracting potentials to ensure that even the smallest impact fragments were measured. A comparison of the bottom plate current of MUDD to charge number density derived from DUSTY is shown in Fig. 8. There is a good agreement between the two throughout the cloud. In the region starting at ~ 85.9 km, the disagreement between the MUDD probes is even more pronounced than for the two DUSTY probes. The phase difference between peaks in this region is also here consistent with the azimuthal difference between the probes. The MUDD currents differ from DUSTY above ~ 88 km. In this region, the MUDD currents are stronger than below the lower layer dust cloud, as opposed to DUSTY where the topside currents are effectively zero. In Fig.9 we show the correlation between MUDD-1 and MUDD-3 total current. These two probes had channels which could measure the total current of incoming charged aerosols, and all their charged fragments produced on impact with the probe. Such a measurement can be directly related to DUSTY by assuming the same secondary charging efficiency of the probes, and can accordingly be compared to DUSTY without any particular loss of generality. Due to the angle between the probes of 120°, if the currents were completely dominated by payload rotation, the correlation would be negative. Consequently, if the angle between the probes were 180° the correlation would be -1 in such a situation. At the bottom of the cloud at ~ 83 km, the correlation rises to almost unity, indicating that large particles dominate the currents. The correlation analysis also reveal that there is a strong variation in the relationship between the MUDD-1 and MUDD-3 currents above this region. Since this analysis is unaffected by spin modulation, it is possible to infer structures which normally would be difficult to separate from the background. Interestingly, two regions above 90 km, one centered at ~ 91 km and one centered at ~ 93 km, show a tendency of a weaker correlation than the expected value which is close to unity. This might suggest that there are populations of very small particles which control the electrons and thus the electron leakage current to MUDD at these altitudes. If the payload potential is negligible, we would expect the correlation to very close to unity at these heights.

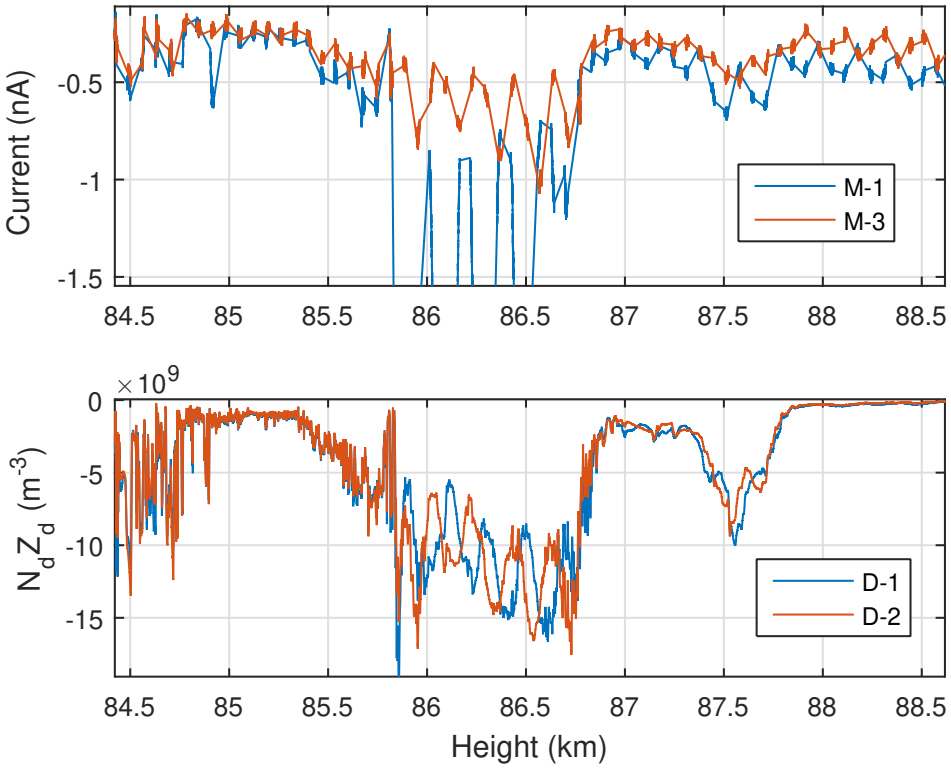

Figure 8. Comparison of MUDD-1 and MUDD-3 currents (top) and DUSTY-1 and DUSTY-2 charge number densities (bottom). Both probe pairs display the same heavily spin modulated feature at $\sim$ 86 km, suggesting the presence of very small dust particles.

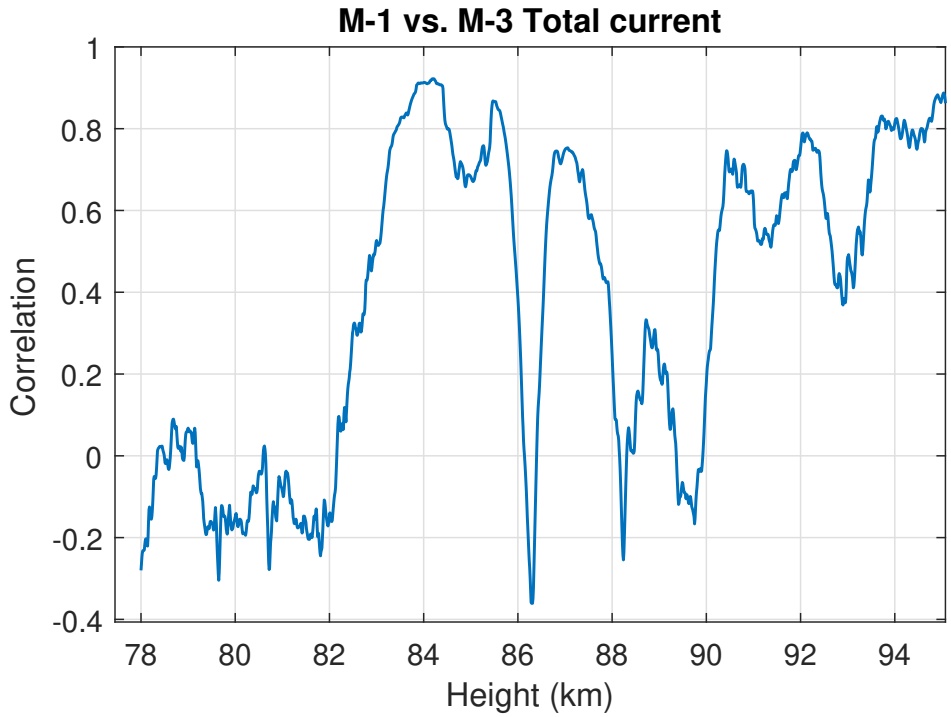

Figure 9. Correlation between the total current channels ($U_R = -2$ V) on MUDD-1 and MUDD-3 evaluated for a moving window of 1000 samples corresponding to $\sim$ 100 meters in altitude.

4.2 Electron density measurements

We must also address the electron population. In a number of studies, a large scale bite-out comparable to the largest dust structure scales have been observed. From earlier studies on small scale correlation between aerosols and electrons it has been found that density variations should follow the same general anti-correlation. However, in some cases, there can be an anti-correlation due to high evaporating rates and other proposed mechanisms (Rapp et al., 2003a; Lie-Svendsen et al., 2003).

There were two instruments measuring electron density on the MXD payloads, by Faraday rotation and needle Langmuir probes (mNLP; see Jacobsen et al. (2010); Bekkeng et al. (2010)). For reasons which will not be addressed here, the needle Langmuir probes overestimated the electron density in the mesopause region.However, due to its high sampling frequency, and thus ability to resolve relative fluctuations, the m-NLP instrument is much more convenient to compare with DUSTY currents, even though uncertainties may occur due to changes in the floating potential and aerodynamic effects (Private communication, Friedrich, Torkar and Spicher, 2018). For aboslute value comparisons, the Faraday rotation experiment from TU Graz yield accurate absolute electron densities with a lower height resolution. In Fig. 10 we show the comparison of the electron density derived from the UiO mNLP-instrument, using three probes on boom 2 biased at 4.5 V, 6 V and 7.5 V repectively, and DUSTY raw current throughout the entire cloud region. Since particles are predominantly negatively charged, a positive correlation between the curves means a negative correlation between aerosols and electrons. Somewhat surprising, the large scale correlation between electron density and DUSTY current is not as unambiguously positive as expected, but a clear bite-out is present. The variation of the correlation on the largest scales ($\sim 0.1 - 1$ km) are discussed in more detail below. If we look

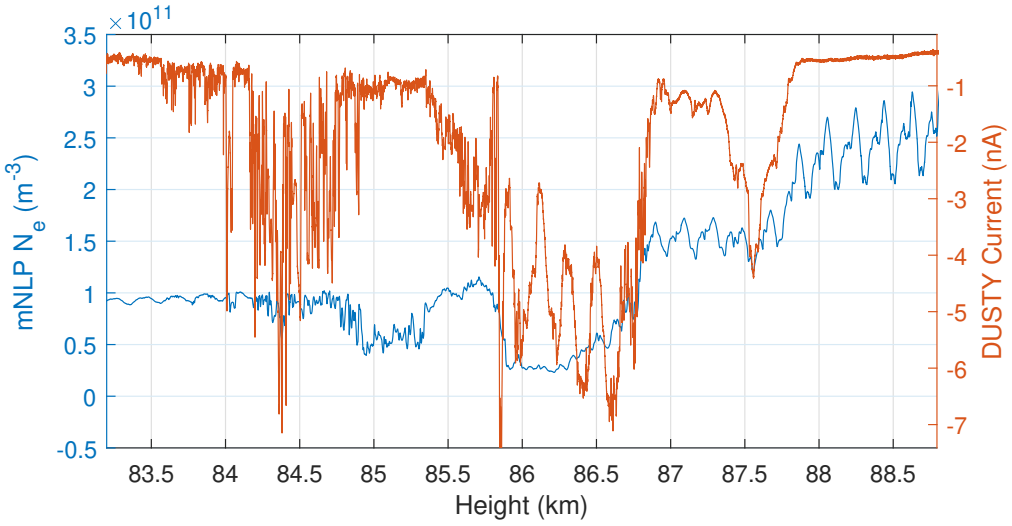

Figure 10. Comparison of electron density measure by the mNLP probes (blue) and DUSTY bottom plate current (red).

at the correlation, thus anti-correlation between N_e and N_d, on scales of length ~ 10 m, we see a high similarity between the DUSTY and mNLP curves more or less throughout the dust cloud. In Fig. 11, we show the situation in a ~ 200 m thick

slice around 84 km. The correlation is close to unity down to scales of a few metres. This should confirm that dust particles are dictating electron dynamics and lower their diffusivity. Since the PMSE during MXD-1B was particularly strong, the scattering structures are probably associated with very steep electron density gradients. A deep look into turbulence and diffusivity of the species will not be done here, but may further corroborate that small particles are in fact accountable for the disagreement between DUSTY-1 and DUSTY-2 currents in parts of the cloud system, as opposed to pure payload potential and aerodynamic adverse flow effects of larger particles. In figure 12 we present the correlations between electron density and DUSTY currents

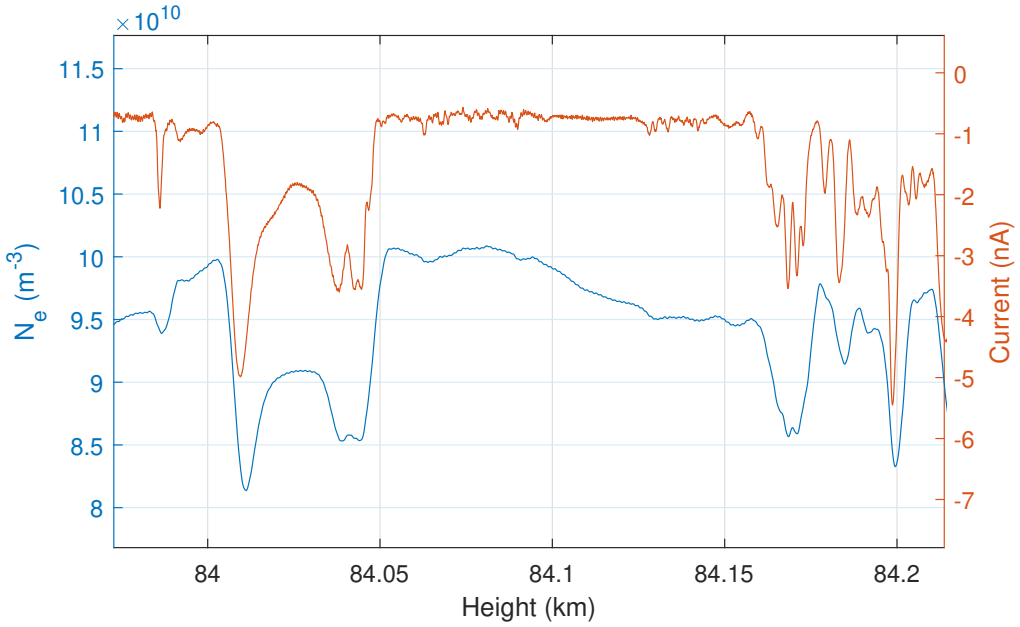

Figure 11. Close-up of structure where the electron density and DUSTY-1 currents agree well, during the MXD-1B launch. We note that the electron density height vector is shifted according to the angle between DUSTY-1 and mNLP Boom-1 ($\sim$ 20 m in height). We note a correlation on length scales $\sim$ 10 m implying anti-correlation between absolute densities.

at three different characteristic length scales, corresponding to moving windows of $\sim$ 10, 100 and 1000 m. In this calculation, a correlation between electron density and DUSTY currents implies – here as earlier – an anti-correlation between the electron and aerosol population. This is well demonstrated in figure 11, where the curves following each other closely implies that there is almost a one-to-one anti-correlation between electron and aerosol densities. This, of course meaning that the dominating electron loss mechanism is attachment to aerosols. The curves expectedly show a high degree of similarity, however, by changing the window size we aim to reveal large scale effects which are otherwise masked by small to mid-scale fluctuations. The overall correlation between electron density and DUSTY current is clearly positive – implying anti-correlation between the densities. With increasing window size, it becomes evident that in the region around ~ 85.5 km, where the gradient in the aerosol density and to a certain degree also electron density are steep and the DUSTY currents do not match, the correlation between electron density and the aerosol population becomes positive. This is noteworthy, as a mechanism in which this would

happen is difficult to construct. Lie-Svendsen et al. (2003) and Rapp et al. (2003a) points out that a possible positive correlation between dusty plasma species densities could happen if the particles are particularly large with high evaporation rates. As shown in figure 7, the particle sizes are small throughout the cloud system here, so this latter mechanism might be difficult to reconcile with our data. As a last note on the correlation, we look at the situation at ~ 86.25 km. This is where the iteration scheme yields the lowest sizes throughout the layer, and it is in the middle of the most active region where the two DUSTY probes show a strong spin modulation. At this point, there is a small region of relatively strong positive correlation between the species densities. A possible effect might be that parts of the payload (a stuck boom, etc.) created a spray of smaller ice particles with a high production of secondary electrons. This is partly consistent with one of the booms on MXD-1B recording peculiar currents and furthermore that the floating payload potential increases in this region. It is also clear that wake effects should play a role, i.e. booms entering and exiting the wake periodically will influence the measurements. The degree to which such wake effects will affect the electron-dust coupling is not however simple to estimate. Nevertheless, calculation of recombination rates, evaporation rates and flow modelling must be done to give a definitive answer to the question about the observed positive correlation.

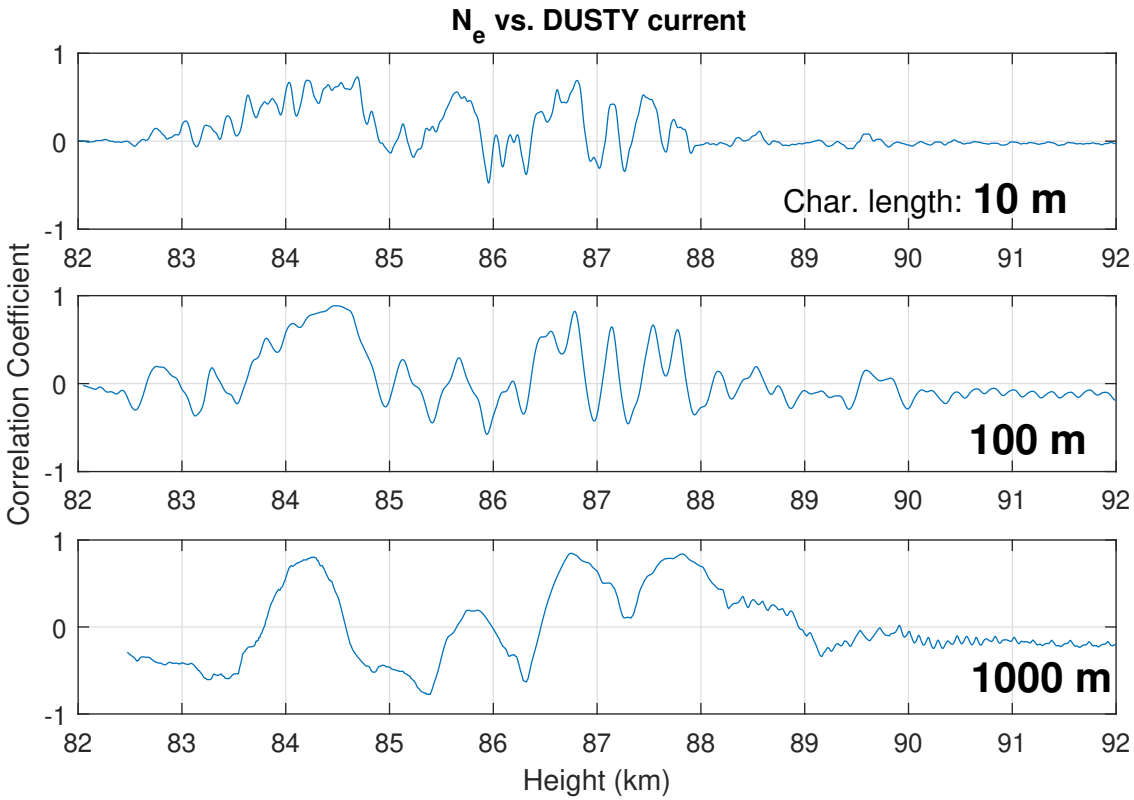

Figure 12. Comparison of correlation between needle Langmuir-probe electron density and DUSTY-2B currents. The correlation coefficients are Spearman Rank values for moving windows of three different characteristic lengths; 10, 100 and 1000 m. The 10- and 100 m components were further filtered to remove spin components.

4.3 Spectral properties

The connection between the mesospheric aerosol population(s) and PMSE strength, can be characterized through the spectral properties of the cloud sysytem. To assess the spectral properties we utilize wavelet analysis to compute power spectra of the DUSTY currents, as wavelets are much more robust than Windowed Fourier Transforms (WFT) with respect to unwanted features induced by the length of the signal; wavelet transforms conserve both high time and frequency resolution, while in WFT the window length introduces a trade-off between time and frequency resolution. The wavelet transform (WT) is determined theoretically through a convolution between a wavelet and the raw probe current (see e.g. Torrence and Compo (1998)):

$$(I_{BP} * \Psi_\Omega)(\xi) = W_n(s) = \sum_{k=0}^{N-1} I_{BP,k} \Psi_\Omega^* \left[\frac{(k-n)\delta\xi}{s} \right] \tag{4}$$

where I_{BP} is the DUSTY bottomplate current, Ψ_Ω is the wavelet for a non-dimensional frequency denoting the number of voices per octave, $\delta\xi$ is the sampling time increment and s the wavelet temporal scales. In the following, we have used the complex Morlet wavelet

$$\Psi_\Omega(\xi) = \Gamma e^{-\xi^2/2} e^{i\Omega\xi} \tag{5}$$

for normalization constant Γ and a number of voices per octave of $\Omega = 16$. Similar wavelet transforms have been used by e.g. Brattli et al. (2006), Strelnikov et al. (2009) and Asmus et al. (2017) for spectral analysis of rocket probe data. To obtain the power spectral density (PSD) of the DUSTY signal, we calculate $|W(s)|^2 = WW^*$, which is arbitrarily normalized.

Figure 13 shows a comparison of DUSTY-1B currents, PMSE recorded by the MAARSY radar (IAP Kühlungsborn) along the rocket trajectory and the PSD from wavelet transform in the height region of the dust cloud system during the MXD-1B launch. A striking feature is the strength of the PMSE which peaks at ~ 50 dB. The currents recorded by DUSTY-1B are also relatively strong compared to earlier flights. In general the three main 'bumps' in the DUSTY-1B current agree well in altitude with the regions of strongest PSD. The PMSE strength shows no clear agreement with any single feature of the DUSTY signal, but we must note that the PSD strength at wavelengths close to the radar Bragg-scale (≈ 2.8 m) is sufficient to be consistent with PMSE throughout the entire region between ~ 82.5 and ~ 86 km. That is, at these altitudes, the PSD have not reached the steep spectral slope consistent with the viscous convective subrange. A noteworthy feature related to the spectral slope above 85 km should be addressed; When looking at PSD at single heights above this point, it becomes evident that the decay of the curves are in fact generally steeper than what is expected for turbulent layers, and thus edge effects become important (Alcala et al., 2001; Alcala and Kelley, 2001). The implication of this to PMSE proxies is discussed in section 5.

The sharp peak in DUSTY current at just above 80 km is due to a squib firing, and is found to induce noise in a number of harmonics at wavelengths shorter than a few metres in the power spectrum. That the features at these wavelength can be traced to mechanical vibrations induced by a squib firing is confirmed by the power spectrum from the MXD-1 flight, shown in figure 14, where the squib firing at ~ 83.5 km produces very similar (transient) noise and harmonics. The noise at short wavelengths below the squib firing can be traced to nosecone separation. The apparent wavelength of the oscillations

induced by squib firings are worthwhile discussing. Due to their proximity in wavelength to the radar Bragg-scale – both for the VHF and UHF regime – some caution should be taken when comparing PMSE and PSD. Some harmonics, e.g. at ~ 0.5 m in figure 13 are only slowly decaying. Moreover, there seems to be another component modulating the slowly decaying oscillations which in some cases might suggest that such feature is in fact real (which is not the conclusion here). A region of particular interest for the MXD-1B flight is that at the lower edge of the cloud system, between ~ 82.5 and ~ 83.5 km. In this region, the dust currents are very weak, but there is still significant strength in the PSD, even at wavelengths down to some tens of cm. It is difficult to conclude whether or not UHF PMSE would be observable for these conditions, due to the noise induced by the squib firing. Nevertheless, as is confirmed by the density and radius calculations presented above, there should be a small population of large ice particles present in this region which can sustain turbulent structures at short length scales. This may be another reason to expect UHF PMSE more often at the lower edge of of the dust system. The fact that the VHF PMSE is strong in this region, and furthermore stays relatively stationary over a four minute time window around launch, is another confirmation of the presence of particles lowering electron diffusivity. One key observation from the PMSE case during the MXD-1B launch is that even though the VHF PMSE was extremely strong, it does not necessarily imply that the probability for UHF PMSE is high.

For comparison, we present in figure 14 the analogous plot to figure 13 for the MXD-1 flight. We note that the spatial scales indicated for the power spectrum are similar, but we have included a slightly wider range for the MXD-1 flight clearly see the spin noise and its harmonics. The spin components are especially pronounced at wavelengths between ~ 200 m and ~ 20 m, and the dominant wavelength is consistent with the recorded spin period of 3.7 Hz. There are significant differences between the overall spectral properties of the respective flights. In the MXD-1B flight, the recorded currents and power spectral densities are much stronger in general, compared to the first flight. We note that a strong dust charge number density does not necessarily imply a strong PSD by causality. Similar to the MXD-1B flight, there is a significant strength in the PSD at the lower edge of the cloud system, however we cannot trace the PSD down to scales of tens of cm, due to the noise induced by mechanical vibrations. One feature worth noting, is that it seems that the PSD in general extends down to shorter length scales at lower altitudes, however not significantly stronger in value than expected.

4.4 Aerosol Dependence in PMSE Reflectivity and Proxies

The radar reflectivity in PMSEs have been subjected to much scrutiny since the first observation of coherent VHF echoes, and the exact scattering mechanism is still not agreed upon. However, there is consensus that for relatively low dust concentrations – as falls out from the application of the theory on scattering from Bragg-scales structures in a dusty plasma – that the main part of PMSE modulation must be dependent on the square of the co-dependent dust/electron density gradient (see e.g. Rapp et al. (2008); Varney et al. (2011)) accordingly:

$$\eta \propto \bar{S}^2 \nabla \langle N_d \rangle^2 \equiv \left(\frac{Z_d N_e}{N_e + Z_i^2 N_i} \right)^2 \cdot \left(\frac{\omega_B^2 N_d}{g} - \frac{\mathrm{d}N_d}{\mathrm{d}t} - \frac{N_d}{H_n} \right)^2 \tag{6}$$

where $\bar{S}/Z_d$ is the mean number of Debye-sphere electrons and $\nabla \langle N_d \rangle$ is the gradient of dust density across an active cloud layer. In the gradient term, ω_B is the buoyancy frequency, g is the gravitational constant and H_n is the neutral scale height.

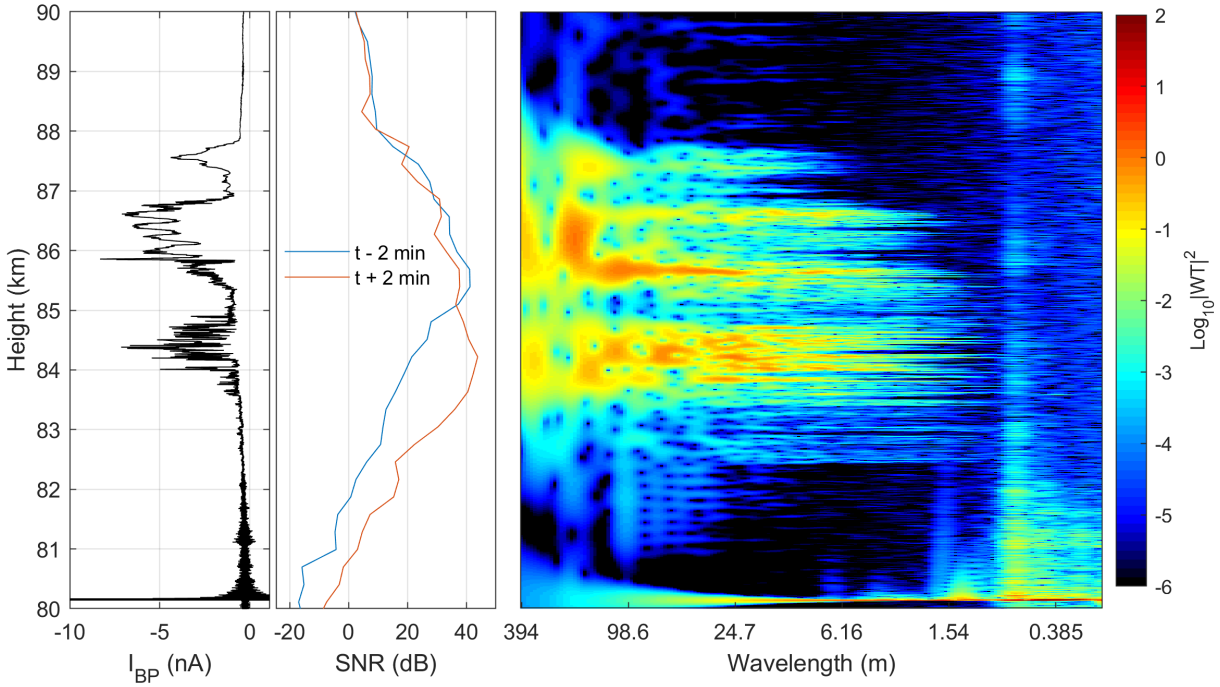

Figure 13. Comparison of DUSTY-1B bottomplate current (left panel), MAARSY 53.5 MHZ radar SNR along the rocket trajectory (middle panel) and PSD from wavelet transform (right panel) – for the MXD-1B launch. The spatial scales in the right panel were converted from frequency to approximate wavelength through $\lambda = 2\pi v_R/\omega$, where the rocket velocity was set to that of the middle of the dust cloud; $v_R = 800$ ms^{-1}. Radar data courtesy of Ralph Latteck, IAP Kühlungsborn.

The full expression for the reflectivity, as provided for the electron-aerosol dusty plasma in the mentioned works, includes a number of ordering parameters, such as the Richardson- and Prandtl-number, as well as microphysical parameters such as the Batchelor-scale, buoyancy frequency and more. A quick application of the expression is complicated and impractical. Due to this fact, a few ordering parameters and proxies have been suggested as central for the existence of PMSE. The most fundamental dust plasma ordering parameter is the ratio of dust charge number density to electron density, $\Lambda = |N_d Z_d|/N_e$. As pointed out by Bellan (2010), if PMSE is purely from spatial modulation of gas phase electrons due to aerosols, the reflectivity would scale as some power of $\Lambda/(1+\Lambda)^2$. A few other authors have proposed proxies for PMSE; Rapp et al. (2003b) and Blix et al. (2003) found $N_d|Z_d|r_d^2$ to a consistent proxy for the fossil and active turbulence mechanism of PMSE, while Havnes et al. (2001) did a comparison to $|N_d Z_d|$ – all works with reasonable agreement between proxies and PMSE strength. Furthermore, Havnes (2004) uses the ordering parameter $P \sim N_d r_d/N_e$ for a time dependent cloud model for a Boltzmann distributed plasma, which has been used to predict over- and undershoots of PMSE.

In figure 15 we show the comparison of the four key proxies introduced above to PMSE for the MXD-1 flight. The reason why we use the first flight for comparison is due the extraordinary strength and lack of fine structures in the MXD-1B

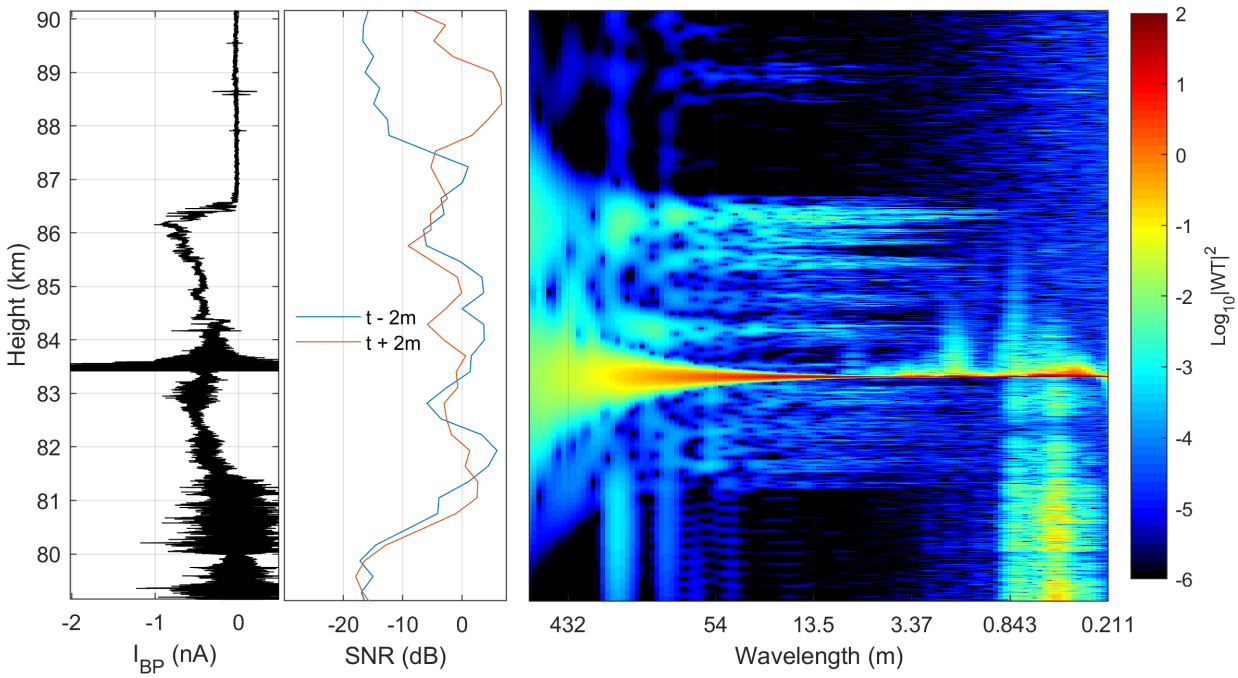

Figure 14. Comparison of DUSTY bottom plate current (left panel), MAARSY 53.5 MHZ radar SNR along the rocket trajectory (middle panel) and PSD from wavelet transform (right panel) – for the MXD-1 launch on the 30th of June, 2016. Conversion from frequency to spatial scales is done as in figure 13, by using the mean rocket velocity though out the dust cloud. Radar data courtesy of Ralph Latteck, IAP Kühlungsborn

PMSE, thus a comparison with the moderate strength and dynamic situation during the first flight is better suited for proxy comparison. There is a weak total positive correlation for all proxies. It should be noted that none of the proxies predict the reduction in PMSE strength at ~ 83 and 85.5 km well, and the upper and lower edges of the cloud system are poorly represented by all parameters. In a general comparison of proxies, we computed the correlation between all proxies on the form $\log_{10}(N_d^i|Z_d|^j r_d^k/N_e^l)$ with PMSE SNR, for $\{i,j,k,l\}$ running from 0 to 4. No single proxy scored significantly higher than others, but all proxies in figure 15 were among the highest scoring with correlation coefficients $\lesssim 0.2$. From this simple analysis it is not possible to conclude about the PMSE mechanism, however, it is reasonable to assume that a gradient term should be included.

In the same manner as Rapp et al. (2003b), we look at the relationship between PMSE SNR and $|N_d Z_d|$ in figure 16. In their figure 10, a pronounced slope of ~ 1 supported the validity of a proxy with linear dependence on the dust charge number density. This is not the case for the MXD-1B, where an unambiguous slope cannot be derived.

As a last point of attack in our inquiry into the aerosol/PMSE relationship, we compare in figure 17 the wavelet PSD at a wavelength of 2.8 m, equal to the MAARSY Bragg-scale, to the PMSE SNR throughout the layer for both MXD flights.

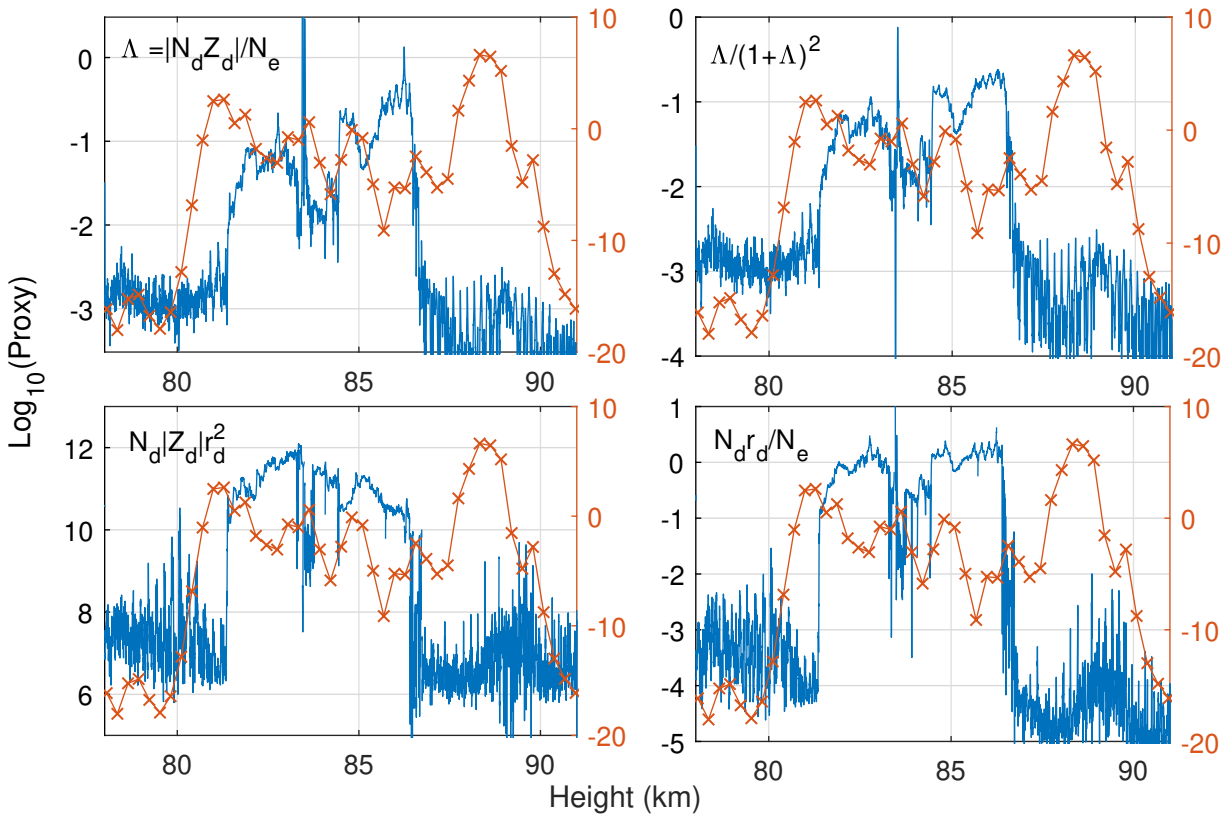

Figure 15. Comparison of proxies from dusty plasma parameters to PMSE SNR for the MXD-1 flight. The upper two panels are proxies based on the ratio of dust charge number density to electron density. The proxy in the lower left panel can be recognized as the parameter utilized by Rapp et al. (2003b), while the bottom right panel is the P-factor introduced by Havnes et al. as an ordering parameter in dust cloud modelling.

If the PMSE mechanism was purely from aerosols dictating gas phase electrons, the SNR and PSD would follow each other closely. Although the PMSE SNR does not display the strong reductions in strength as the PSD, the curves correlate fairly well non-linearly. Again the agreement is low at the edges. These PMSE profiles were obtained with 2 minute integration time, and plasma flow in and out of the scattering volume must be considered in a more rigorous comparison.

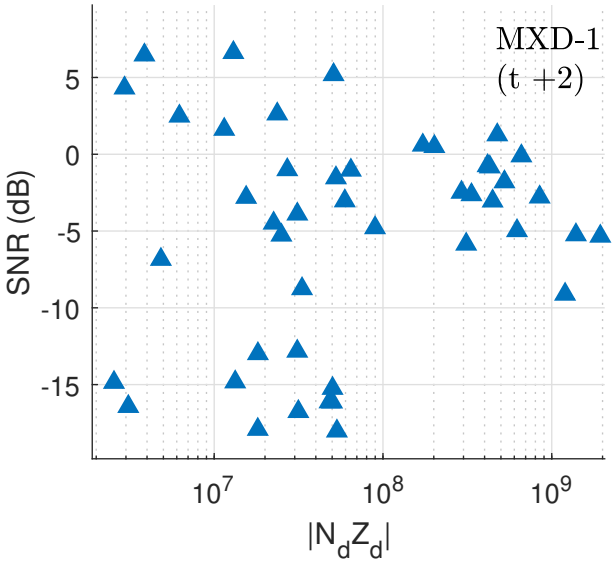

Figure 16. Scatter plot of Charge number density derived from DUSTY and PMSE SNR in decibels for the MXD-1 flight. Note that the SNR scale has a range of three orders of magnitude, thus a one-to-one correlation would yield a line with $\lesssim 45^\circ$ angle in this plot. No principal axis can be derived significantly for this cluster, i.e. the variance is too large.

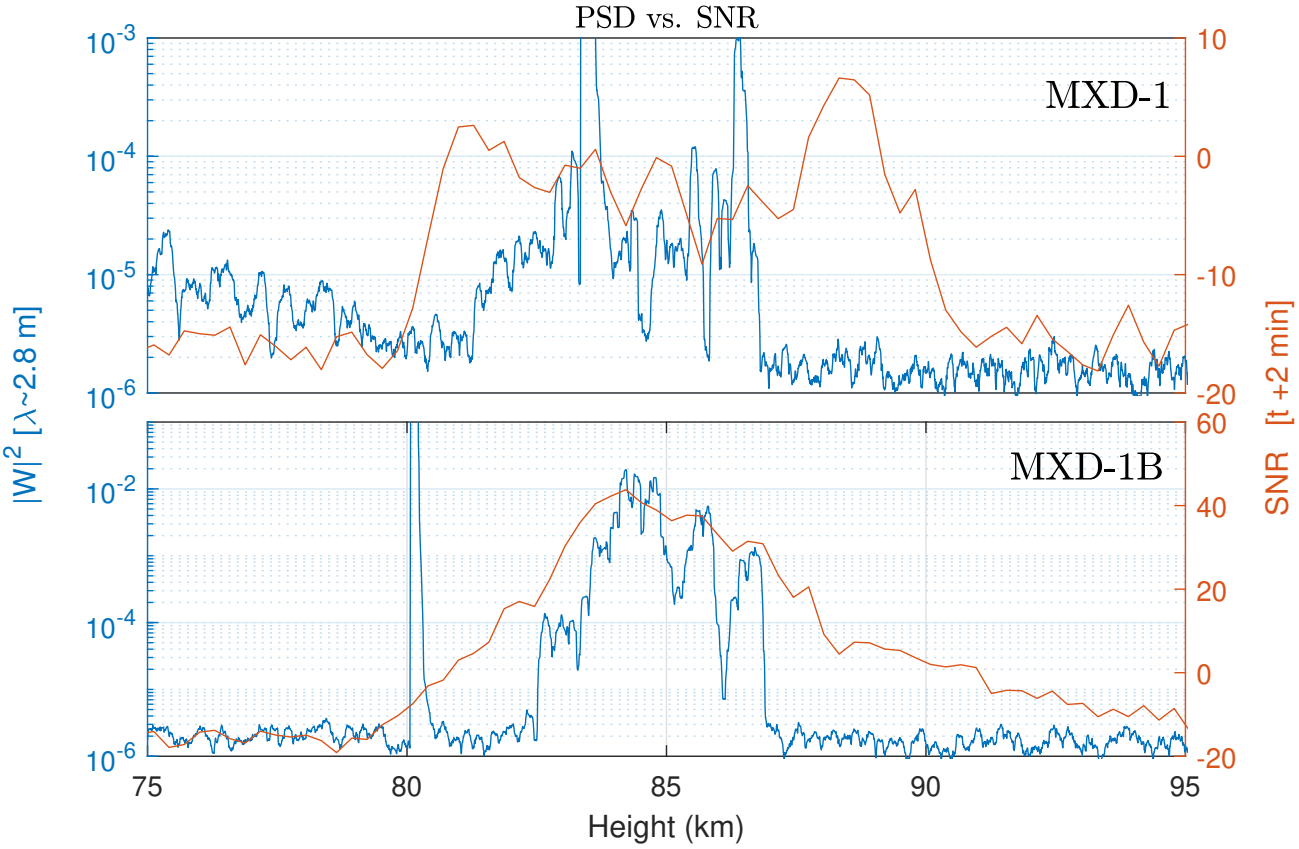

Figure 17. Comparison of MAARSY SNR (red, 2 minutes after launch), and PSD from the wavelet transform of DUSTY bottom plate currents (blue), evaluated at a wavelength of ≈ 2.8 m $= \lambda_{\mathrm{Bragg}}$. The top and bottom panels show the situation for the MXD-1 and MXD-1B launches respectively. Note the different scales for the two panels.

5 Discussion

The recorded currents during MXD-1B with large spin modulation, which yield a large spread in horizontal gradients for DUSTY and MUDD, have two plausible explanations; adverse effects from payload charging with resulting electron leakage or small particles combined with strong aerodynamic modulation. From preliminary estimation of the floating potential from the m-NLP assuming that the probes were in the saturation region, we find that the payload floating potential is only offset with about 3 V on average in the dust cloud region, which would not be enough to let 2-3 eV electrons into DUSTY or MUDD. Another possibility is the presence of very small particles, possibly MSPs, with high enough fraction of the dust charge density to affect the BP currents significantly. From modelling studies it has shown MSPs smaller than $\sim 1-2$ nm are swept away or heavily influenced by the neutral flow field in the shock front of the payload (Hedin et al., 2007; Antonsen and Havnes, 2015). In the summer mesopause, the density of MSPs of sizes larger than this cut-off is found to be relatively low in modelling studies, so an in depth analysis of the dynamics of small dust particles around the MXD-1B payload must be carried out. Small particles/MSPs have a rapid density diffusion which implies a rapid smoothing of dust clumps/holes. Particles of sizes $\sim 1-2$ nm generally have a charging time much longer than L/v_R (where L is a characteristic length of the payload), so they have the time to spatially modulate electrons even after they enter the shock of the payload without producing a bite-out – or anti-correlation in the respective densities. The last candidate mentioned in this paper as a possible candidate for the strong modulation in DUSTY currents, is the adverse effect of a spray of fragments and secondary charges from a stuck boom above the top deck. To unambiguously confirm this, a rigorous analysis of the three dimensional geometry and orientation as a function of time must be done. This is a complicated exercise and will not be discussed in this paper.

The combination of different perspectives on small scale measurements of mesospheric aerosols and electrons in this work, underlines especially one thing: aerodynamic effects can completely dominate recorded signals in the presence of aerosols. In missions where a relatively high resolution of particle sizes cannot be inferred, particular caution must be taken when analyzing small scale dust phenomena.

In our comparison of the DUSTY currents from MXD-1B with auxiliary measurements of electrons with needle Langmuir probes and dust with the MUDD probe, we find that the agreement is good below a height of ~ 85.5 km. Above this, the agreement on shorter scale is less pronounced, however, a large scale bite-out is present. This is to say that all instruments were affected by the same modulation at spin frequency. Interestingly, the electron data displayed little rotational modulation in the layer which DUSTY showed a strong spin component. The explanation of this boils down to the same situation as mentioned above, where aerosols cannot absorb electron quickly enough; this is plausible as the electron attachment rate for both pure ice and MSP particles with sizes below 10 nm is much larger than the time is takes for a particle to traverse the distance from the front of the rocket to the top deck. A more rigorous calculation of electron attachment rates may reveal possible combinations of parameters which produce more effective recombination rates, but generally with $N_e \sim 10^8 - 10^{11}$ m^{-3}, the attachment rates for particles $\lesssim 10$ nm are on the order of seconds to hundreds of seconds.

If the aerodynamic environment in front of the payload can be characterized properly, the dual-probe configuration of DUSTY on MXD-1B can also be used to investigate the horizontal differences in small scale dust structures. In the case of

MXD-1B, the interpretation of the data from the region with the strong spin modulation, a possible interpretation could be that there are highly elongated structures consisting of small dust particles which persist in the cloud system for relatively long times. To confirm this, and give a detailed description of the multi-scale structures in the cloud, a rigorous treatment of the dust and electron gradients – in both the vertical and horizontal direction – must be carried out.

We must also mention the modest inquiry into the comparison between PMSE and aerosol fluctuations. Generally, the power spectra from fluctuations in the DUSTY currents – directly connected to the aerosol charge number density – agree well *inside* the cloud at the radar Bragg scale, for both flights. How edge effects are manifested in the aerosol fluctuation spectra have not to our knowledge been thoroughly investigated earlier. In addition, a straight forward comparison between PMSE and DUSTY currents give similar conclusions: PMSE edges cannot be described easily from aerosol measurements. Moreover, as MAXIDUSTY is one of few flights where 'all' the relevant dusty plasma parameters are either measured or can be inferred from measurements, we made a comparison of simple proxies for PMSE strength. In this context it may be noted, as found by Alcala et al. (2001); Alcala and Kelley (2001), that for power spectra steeper than the -5/3 slope of Kolmogorov-scale dominated systems, cloud edges dominate the PSD. Consequently, if such steep gradients are seen, it is plausible that a cloud potential model as the one used in Havnes (2004) is the most descriptive for the cloud structures, as edges may be better described from electrostatic effects and Boltzmann distributed plasma species. Regarding a PMSE proxy, this means that the parameter $N_d r_d / N_e$ would be a good ordering parameter, as it is the principal ordering parameter in the mentioned cloud potential model. However, this is not clear in our measurements, as is also the case for the remaining calculated proxies.

6 Conclusions

The key findings are summarized as follows:

1. The measurements from two mechanically and electrically identical DUSTY Faraday cups with an interspacing of ~ 10 cm show very different measurements in parts of a cloud system (MXD-1B flight). We attribute this to the precence of small particles of sizes $\sim$ a few nanometres which are heavily modulated in the complex aerodynamic environment around the rocket payload.

2. A correlation analysis between charged aerosols and electrons show very strong negative correlation coefficients on vertical scales of lengths down to ~ 10 metres. In a few smaller regions of the dust cloud system, we find weak to medium strong positive correlation between the two species. This effect is difficult to reconcile with the earlier proposed mechanism that the aerosols in this case must be large with a significant evaporation rate. In fact, in the parts of the cloud where positive correlation is seen, the particle sizes are only a few nanometres large.

3. The difference in wavelet power spectra between the MXD-1B flight, where the PMSE was very strong, and the MXD-1 flight, where the PMSE was weak, is significant. For MXD-1B, the PSD keeps its strength to shorter wavelengths compared to MXD-1. There does not, however, seem to be a clear tendency here for the case of a strong PSD in the VHF regime (on MAARSY with Bragg scales of 2.8 m), that the PSD keeps it strength down to the UHF length scales.

4. We find a generally weak agreement between simple proxies from dusty plasma parameters and recorded PMSE strength. Edge effects cannot be reproduced with the proxies or PSD extracted through wavelet analysis at the radar Bragg scale presented in this paper.

Acknowledgements. We thank Ralph Latteck at IAP Kühlungsborn for the MAARSY radar profiles for the MAXIDUSTY Campaign, and kind contributions from the University of Oslo by the 4DSpace strategic research initiative. The rocket campaign and the construction of the rocket instrumentation was supported by grants from the Norwegian Space Centre (VIT.04.14.7, VIT.02.14.1, VIT.03.15.7, VIT.03.16.7) and the Research Council of Norway, grant 240065. The replication data for the figures in this paper can be found through the UiT Open Research repository at https://doi.org/10.18710/N8GF1U.

Competing interests. The authors declare that they have no conflicts of interest.

References

Alcala, C. and Kelley, M.: Nonturbulent layers in polar summer mesosphere: 2. Application of wavelet analysis to VHF scattering, Radio Science, 36, 891–903, 2001.

Alcala, C., Kelley, M., and Ulwick, J.: Nonturbulent layers in polar summer mesosphere: 1. Detection of sharp gradients using wavelet analysis, Radio Science, 36, 875–890, 2001.

Antonsen, T. and Havnes, O.: On the detection of mesospheric meteoric smoke particles embedded in noctilucent cloud particles with rocket-borne dust probes, Review of Scientific Instruments, 86, 033 305, https://doi.org/http://dx.doi.org/10.1063/1.4914394, 2015.

Antonsen, T., Havnes, O., and Mann, I.: Estimates of the Size Distribution of Meteoric Smoke Particles From Rocket-Borne Impact Probes, Journal of Geophysical Research: Atmospheres, https://doi.org/10.1002/2017JD027220, 2017.

Asmus, H., Staszak, T., Strelnikov, B., Lübken, F.-J., Friedrich, M., and Rapp, M.: Estimate of size distribution of charged MSPs measured in situ in winter during the WADIS-2 sounding rocket campaign, Annales Geophysicae, 35, 979–998, https://doi.org/10.5194/angeo-35-979-2017, 2017.

Bekkeng, T., Jacobsen, K., Bekkeng, J., Pedersen, A., Lindem, T., Lebreton, J., and Moen, J.: Design of a multi-needle Langmuir probe system, Measurement science and technology, 21, 085 903, 2010.

Bekkeng, T.-A., Barjatya, A., Hoppe, U.-P., Pedersen, A., Moen, J., Friedrich, M., and Rapp, M.: Payload charging events in the mesosphere and their impact on Langmuir type electric probes, Annales Geophysicae, 31, 187–196, 2013.

Bellan, P.: Comment on comment by Markus Rapp and Franz-Josef Lübken on "Ice iron/sodium film as cause for high noctilucent cloud radar reflectivity", Journal of Geophysical Research: Atmospheres, 115, 2010.

Blix, T. A., Rapp, M., and Lübken, F.-J.: Relations between small scale electron number density fluctuations, radar backscatter, and charged aerosol particles, Journal of Geophysical Research: Atmospheres, 108, 2003.

Brattli, A., Blix, T. A., Lie-Svendsen, Ø., Hoppe, U.-P., Lübken, F.-J., Rapp, M., Singer, W., Latteck, R., and Friedrich, M.: Rocket measurements of positive ions during polar mesosphere winter echo conditions, Atmospheric Chemistry and Physics, 6, 5515–5524, https://doi.org/10.5194/acp-6-5515-2006, 2006.

Gelinas, L. J., Lynch, K. A., Kelley, M. C., Collins, S., Baker, S., Zhou, Q., and Friedman, J. S.: First observation of meteoritic charged dust in the tropical mesosphere, Geophysical Research Letters, 25, 4047–4050, https://doi.org/10.1029/1998GL900089, 1998.

Gerding, M., Kopp, M., Höffner, J., Baumgarten, K., and Lübken, F.-J.: Mesospheric temperature soundings with the new, daylight-capable IAP RMR lidar, Atmospheric Measurement Techniques, 9, 3707–3715, https://doi.org/10.5194/amt-9-3707-2016, 2016.

Havnes, O.: Polar Mesospheric Summer Echoes (PMSE) overshoot effect due to cycling of artificial electron heating, Journal of Geophysical Research: Space Physics, 109, 2004.

Havnes, O. and Næsheim, L. I.: On the secondary charging effects and structure of mesospheric dust particles impacting on rocket probes, Annales Geophysicae, 25, 623–637, https://doi.org/10.5194/angeo-25-623-2007, 2007.

Havnes, O., Trøim, J., Blix, T., Mortensen, W., Næsheim, L. I., Thrane, E., and Tønnesen, T.: First detection of charged dust particles in the Earth's mesosphere, Journal of Geophysical Research: Space Physics, 101, 10 839–10 847, https://doi.org/10.1029/96JA00003, 1996.

Havnes, O., Aslaksen, T., and Brattli, A.: Charged dust in the Earth's middle atmosphere, Physica Scripta, 2001, 133, 2001.

Havnes, O., Hartquist, T. W., Kassa, M., and Morfill, G. E.: In-flight calibration of mesospheric rocket plasma probes, Review of Scientific Instruments, 82, 074 503, https://doi.org/10.1063/1.3611007, 2011.

Havnes, O., Gumbel, J., Antonsen, T., Hedin, J., and Hoz, C. L.: On the size distribution of collision fragments of NLC dust particles and their relevance to meteoric smoke particles, Journal of Atmospheric and Solar-Terrestrial Physics, 118, 190–198, https://doi.org/http://dx.doi.org/10.1016/j.jastp.2014.03.008, 2014.

Havnes, O., Antonsen, T., Hartquist, T., Fredriksen, Å., and Plane, J.: The Tromsø programme of in situ and sample return studies of mesospheric nanoparticles, Journal of Atmospheric and Solar-Terrestrial Physics, 127, 129–136, https://doi.org/http://dx.doi.org/10.1016/j.jastp.2014.09.010, 2015.

Havnes, O., Antonsen, T., Baumgarten, G., Hartquist, T., Fredriksen, Å., Friedrich, M., and Hedin, J.: A new method to inference the size, number density, and charge of mesospheric dust from its in situ collection by the DUSTY probe., ACT/AMT, This issue, 2018a.

Havnes, O., Latteck, R., Hartquist, T. W., and Antonsen, T.: First simultaneous rocket and radar detections of rare low summer mesospheric clouds., Geophysical Research Letters, 0, –, https://doi.org/10.1029/2018GL078218, 2018b.

Hedin, J., Gumbel, J., and Rapp, M.: On the efficiency of rocket-borne particle detection in the mesosphere, Atmospheric Chemistry and Physics, 7, 3701–3711, https://doi.org/10.5194/acp-7-3701-2007, 2007.

Jacobsen, K., Pedersen, A., Moen, J., and Bekkeng, T.: A new Langmuir probe concept for rapid sampling of space plasma electron density, Measurement Science and Technology, 21, 085 902, 2010.

Kassa, M., Rapp, M., Hartquist, T. W., and Havnes, O.: Secondary charging effects due to icy dust particle impacts on rocket payloads, Annales Geophysicae, 30, 433–439, https://doi.org/10.5194/angeo-30-433-2012, 2012.

Lie-Svendsen, Ø., Blix, T., Hoppe, U.-P., and Thrane, E.: Modeling the plasma response to small-scale aerosol particle perturbations in the mesopause region, Journal of Geophysical Research: Atmospheres, 108, 2003.

Lübken, F.-J.: Thermal structure of the Arctic summer mesosphere, Journal of Geophysical Research: Atmospheres, 104, 9135–9149, 1999.

Pedersen, A., Troim, J., and Kane, J.: Rocket measurements showing removal of electrons above the mesopause in summer at high latitude, Planetary and Space Science, 18, 945 – 947, https://doi.org/https://doi.org/10.1016/0032-0633(70)90092-9, 1970.

Rapp, M. and Lübken, F.-J.: Polar mesosphere summer echoes (PMSE): Review of observations and current understanding, Atmospheric Chemistry and Physics, 4, 2601–2633, https://doi.org/10.5194/acp-4-2601-2004, 2004.

Rapp, M. and Thomas, G. E.: Modeling the microphysics of mesospheric ice particles: Assessment of current capabilities and basic sensitivities, Journal of Atmospheric and Solar-Terrestrial Physics, 68, 715 – 744, 2006.

Rapp, M., Lübken, F.-J., and Blix, T.: Small scale density variations of electrons and charged particles in the vicinity of polar mesosphere summer echoes, Atmospheric Chemistry and Physics, 3, 1399–1407, 2003a.

Rapp, M., Lübken, F.-J., Hoffmann, P., Latteck, R., Baumgarten, G., and Blix, T. A.: PMSE dependence on aerosol charge number density and aerosol size, Journal of Geophysical Research: Atmospheres, 108, 2003b.

Rapp, M., Strelnikova, I., Latteck, R., Hoffmann, P., Hoppe, U.-P., Häggström, I., and Rietveld, M. T.: Polar mesosphere summer echoes (PMSE) studied at Bragg wavelengths of 2.8 m, 67 cm, and 16 cm, Journal of Atmospheric and Solar-Terrestrial Physics, 70, 947–961, 2008.

Strelnikov, B., Rapp, M., Strelnikova, I., Engler, N., and Latteck, R.: Small-scale structures in neutrals and charged aerosol particles as observed during the ECOMA/MASS rocket campaign, Annales Geophysicae, 27, 1449–1456, 2009.

Tomsic, A.: Collisions between water clusters and surfaces, Ph.D. thesis, Göteborg University, 2001.

Torrence, C. and Compo, G. P.: A Practical Guide to Wavelet Analysis, Bulletin of the American Meteorological Society, 79, 61–78, https://doi.org/10.1175/1520-0477(1998)079<0061:APGTWA>2.0.CO;2, 1998.

Varney, R. H., Kelley, M. C., Nicolls, M. J., Heinselman, C. J., and Collins, R. L.: The electron density dependence of polar mesospheric summer echoes, Journal of Atmospheric and Solar-Terrestrial Physics, 73, 2153–2165, 2011.

PAPER IV

Havnes, O., Antonsen, T., Baumgarten, G., Hartquist, T., Fredriksen, Å., Friedrich, M., and Hedin, J.: A new method to inference the size, number density, and charge of mesospheric dust from its in situ collection by the DUSTY probe., Atmospheric Measurement Techniques, In Review, 2018a

A new method to infer the size, number density, and charge of mesospheric dust from its in situ collection by the DUSTY probe.

Ove Havnes[1], Tarjei Antonsen[1], Gerd Baumgarten[2], Thomas W. Hartquist[3], Alexander Biebricher[4], Åshild Fredriksen[1], Martin Friedrich[5], Jonas Hedin[6].

[1] Institute of Physics and Technology, Arctic University of Norway, Tromsø, Norway

[2] Leibniz-Institute of Atmospheric Physics at Rostock University, Kühlungsborn, Germany

[3] School of Physics and Astronomy, University of Leeds, Leeds, UK

[4] Norwegian Center for Space-related Education, N-8480 Andenes, Norway

[5] Graz University of Technology, 8010 Graz, Austria

[6] Department of Meteorology, Stockholm University, 10691 Stockholm, Sweden.

Correspondence to: Ove Havnes (ove.havnes@uit.no)

Abstract. We present a new extended method of analyzing measurements of mesospheric dust made with DUSTY rocket-borne Faraday cup probes. It yields the variation of fundamental dust parameters through a mesospheric cloud with an unrivalled altitude resolution down to 10 cm or less. A DUSTY probe was the first probe which unambiguously detected charged dust/aerosol particles in the Earth's mesosphere. DUSTY excluded the ambient plasma by various biased grids, which however allowed dust particles with radii above a few nanometer to enter, and it measured the flux of charged dust particles. The flux measurements directly yielded the total ambient dust charge density.

We extend the analysis of DUSTY data by using the impact currents on its main grid and the bottom plate as before, together with a dust charging model and a secondary charge production model, to allow the determination of fundamental parameters, such as dust radius, charge number and total dust density. We demonstrate the utility of the new analysis technique by considering observations made with the DUSTY probes during the MAXIDUSTY rocket campaign in June-July 2016 and comparing the results with those of other instruments (Lidar and photometer) also used in the campaign.

1 Introduction.

The Earth's mesosphere has for a long time been the least known part of the Earth's atmosphere, and it probably still is. One reason for this is its inaccessibility to direct in situ observations – it being too high for balloons and planes, and too low for satellites. Its main cloud phenomena, the noctilucent clouds (NLC) which occurs in its polar regions, were first observed in 1885 (Jesse, 1885; Backhouse, 1885; Symons, 1888, Gadsden and Schröder, 1989). They are the highest altitude clouds in the Earth's atmosphere. It now appears that the NLC occurrence frequency is increasing with time and that the NLC spread further away from the poles with time (de Land et al., 2007), possibly due to changes in the composition of trace elements, like water vapor, in the mesosphere region. As such, one reason for the interest to understand the mesosphere is that it may be an indicator of climatic changes in the troposphere and stratosphere (Thomas, 1996). Another reason is that the mesosphere is the transition zone, between the outer space and the lower part of the atmosphere, where energetic particle precipitation, meteors and UV radiation normally deposits most of their energy. Disturbed magnetosphere conditions, with high energy particle precipitation, can create large amounts of reactive NO_x molecules which, when transported downwards, react with and reduce the ozone content (Reddman et al., 2013). Also, there is an influx of meteorites into the Earth's atmospheres, the total mass of which has been claimed to be from 4 to 300 t/day (Plane 2012; Asmus et al., 2015). Much of the meteorites evaporate as they are heated due to air friction when they enter the atmosphere, and the evaporated material re-condenses and creates nanometer sized particles, the meteoric smoke particles (MSP) (Rosinski and Snow, 1961; Hunten et al., 1980). The MSPs are thought to be crucial in creating NLC, where they probably act as condensation sites for water vapor to form the larger icy NLC particles, but homogeneous condensation may also be part of the cause of this (Turco et al., 1982; Rapp and Thomas, 2006). In the growth process the icy NLC particles, growing by water vapor condensing on them, also capture MSP, so that NLC particles will have MSPs embedded in them (Havnes and Naesheim, 2007; Havnes et al., 2009; Hervig et al., 2012, 2017). It also appears that the MSPs, when transported downwards, can influence on the cloud formation in the stratosphere and possibly also the troposphere (Ogurtsov and Raspopov, 2011).

In order to understand the mesosphere it is crucial to understand the evolution and role of various types of dust particles in it, such as the icy NLC and Polar Mesospheric Summer Echoes (PMSE) particles, and MSPs which probably also are present in the winter mesosphere to create

the weak radar PMWE (Polar Mesospheric Winter Echoes) clouds (Czechovsky et al., 1979; Zeller et al., 2006; Latteck and Strelnikova, 2015). The progress in ground based instrumentation and observing techniques during the last few decades has been impressive. For example, lidars now routinely observe in full daylight to determine NLC particle sizes and densities (Baumgarten et al., 2007) and they also measure the metallic content in the mesosphere (Huang et al, 2015) and mesospheric temperatures (Höffner and Lautenbach, 2009). The powerful new MST radar MAARSY with its large increase in sensitivity has profoundly changed our knowledge of PMSE occurrence rates and the altitude ranges in which they can be found (Latteck and Strelnikova, 2015). Satellites have identified MSP cloud layers by observing along them (Hervig et al., 2009) and have also confirmed earlier predictions (Havnes and Næsheim, 2007; Havnes et al., 2009; Kassa et al., 2012) that MSPs are embedded in the icy NLC/PMSE particles with from 0.01 to 3% by volume (Hervig, 2012).

One of the obvious advantages of the ground based instrumentation and satellites, is that they can observe the mesospheric clouds continuously. However, they have a limited space resolution (ca. 100 m and upwards) and time resolution (seconds and upwards). Rocket instrumentation, on the other hand, although presenting only a snapshot of the conditions along its trajectory, observe with a time resolution typically of ~ 10^{-3} to 10^{-4} seconds, corresponding to a spatial resolution of ~ 0.1 to 1 m. Various rocket probes are developed to observe the plasma conditions (Friedrich and Rapp, 2009), the dust charge density (Havnes et al., 1996a), the total density of small dust (MSP) by a flashing technique (Rapp and Strelnikova, 2009) while MASS is a coarse dust mass spectrometer (Knappmiller et al., 2008; Amyx et al., 2008; Robertson et al., 2009, 2014). The MUDD (Multiple Dust Detector) mass analyze the collision fragments of the icy NLC particles and relate this to the mass distribution of embedded MSP (Havnes et al., 2014; Antonsen and Havnes, 2015; Antonsen et al., 2017).

In spite of the progress made with rocket instrumentation, there is a lack of high time/space resolution instruments to measure parameters as dust size, number density and charge. In the present paper we consider the principles of the much used DUSTY impact probe (Havnes et al., 1996a) and how its performance can be improved. The DUSTY probe, the principle of which is shown in Fig.1, is equipped with grids to prevent ambient plasma from reaching G2 and the bottom plate BP but allow dust particles to enter and collide with the grids and the BP. The potentials of the grids are given in Fig.1. The observed currents to the probe were originally used to find only the dust charge density of the ambient dust cloud, but in the present paper we will show how to extend the analysis of the DUSTY probe currents to allow it to also determine

other dust parameters. The extension of the original method of analysis is based on earlier works, which have demonstrated the importance of secondary charge and secondary current production in glancing dust impacts on rocket probes and payload bodies (Havnes and Næsheim, 2007; Havnes et al., 2009; Kassa et al., 2012).

In Sec.2 we extend the earlier analysis method for the DUSTY impact probe and now use the currents to G2 and BP to find not only the dust charge density as before, but also the total dust density, the dust radius and the mean dust charge. In Sec. 3 we show the values for dust density and dust radius by this new method, used on the observations by the DUSTY probe on the payload MXD-1, which was launched on 30.06.2016 at 09:43:18 UT in the MAXIDUSTY rocket campaign. In Sec.4 we compare the DUSTY results with those from the RMR Lidar at Andøya (von Cossart et al, 1999; von Zahn et al, 2000; Baumgarten et al, 2007) and the on board MISU photometer (Gumbel et al., 2001; Hedin et al., 2008; Megner et al., 2009) and conclude the paper in Sec.5.

2 The extended analysis of dust observations made with DUSTY type Faraday cup probes.

The DUSTY probe (Havnes et al., 1996a; Havnes and Næsheim, 2007), the design of which is shown in Fig. 1, has grids G0, G1 and G2 and a solid bottom impact plate BP. The probe must point forward along the payload axis. The dust impact currents to G1, G2 and BP are all registered but not the current to G0, which is at the payload potential Φ_P. The registered currents are I_{G1}, I_{G2} and I_{BP}. The current I_{G1} will not be used in the analysis. It is the grid which is most influenced by effects like payload charging and the plasma environment and as such not directly connected to the measurements of dust. G0 and G1 are made of thin cylindrical wires and they each cover only 4.6% of the opening cross section of DUSTY. G2 is made of thicker wires to increase the secondary charging effect. It covers 23.5 % of the DUSTY cross section.

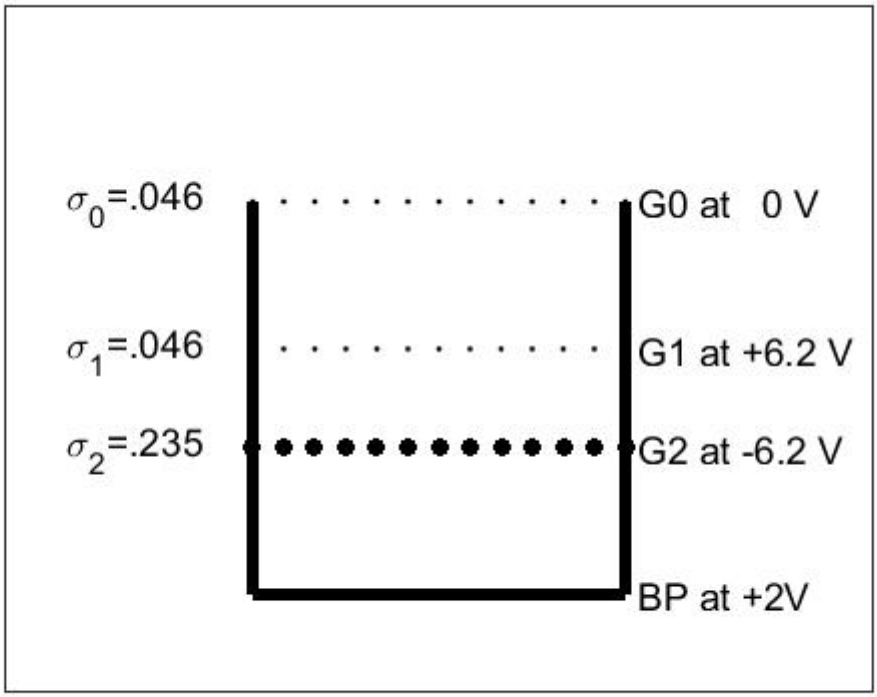

Figure 1. The design of the DUSTY probe used in the MAXIDUSTY campaign. The fractional coverage of the different grids, relative to the total probe cross section, are $\sigma_0 = \sigma_1 = 0.046$ and $\sigma_2 = 0.235$. The electric potentials of all the grids and the bottom plate are relative to the payload potential Φ_P. The currents are measured on G1, G2 and BP, but not on G0.

The dust current into the probe in front of G2, is designated I_D and is part of the expressions for the total current I_{G2} measured on G2

$$I_{G2} = \sigma_2 I_D + I_S \quad (1)$$

and for I_{BP} measured on the BP.

$$I_{BP} = (1 - \sigma_2) I_D - I_S \quad (2)$$

The current to G2 is made up of $\sigma_2 I_D$ which is the part of I_D which hits G2 and deposits its charge, plus the secondary current I_S which is produced by glancing dust impacts on G2 which rubs off electrons from it. If this last process is effective it can lead to that the total current I_{G2} can become positive even if the impacting dust particles are charged negatively. The current I_{BP}

to the bottom plate is made up of the direct hits on to BP by the dust which was not hitting G2, and minus the secondary current I_S. The electrons which are rubbed off from G2, producing a positive current I_S to G2, will be deposited on BP and create a negative current $-I_S$ there. We can eliminate I_S to find I_D by

$$I_D = I_{G2} + I_{BP} \quad . \tag{3}$$

The two upper grids G0 and G1 are made of thin wires and each cover only 4.6 % of the DUSTY cross section (Fig. 1). Much of the small negatively charged fragments produced on them by will be stopped by air friction and probe internal electric fields (Antonsen et al., 2017). We therefore neglected a possible contribution of their secondary production to the currents to G2 and BP. However, they will together stop ~9.2 % of the incoming dust current from passing G0 and G1. The current I_{Total} into the probe just above G0 can be expressed as $I_{Total} = I_D (1-\sigma_0)^{-2} = 1.1 \times I_D$ which gives us directly the observed ambient dust charge density $\Sigma (N_Z Z_D)$ from the relationship

$$I_{Total} = \pi R_p^2 V_R e \sum(N_Z Z_D) \quad . \tag{4}$$

Here R_p is the probe radius, and e = 1.6 x 10^{-19} C. The number density of dust particles with charge number Z_D is N_Z and the rocket velocity is V_R. We should note that the dust charge density $\sum(N_Z Z_D)$ which can be extracted from Eq. (4) is independent of the model for secondary production of charge since this cancels in Eq. (3).

Some information on the expected size of the dust particles, and the role of secondary charge production, can be found from examining the ratio

$$R = \frac{I_{G2}}{I_{BP}} = \frac{\sigma_{G2} I_D + I_S}{(1-\sigma_{G2}) I_D - I_S} \quad . \tag{5}$$

This ratio R should have values between $R = \frac{\sigma_{G2}}{1-\sigma_{G2}} = 0.31$ when the secondary charging current $I_S \rightarrow 0$, and R= -1 for $I_S >> I_D$. In Fig.2 we show R and I_D as function of altitude. It is reassuring that R, even though it varies significantly with altitude, stays so well within the above limits. This has been shown to be the case also in several earlier launches of the DUSTY probe (Havnes and Næsheim, 2007; Havnes et al., 2009).

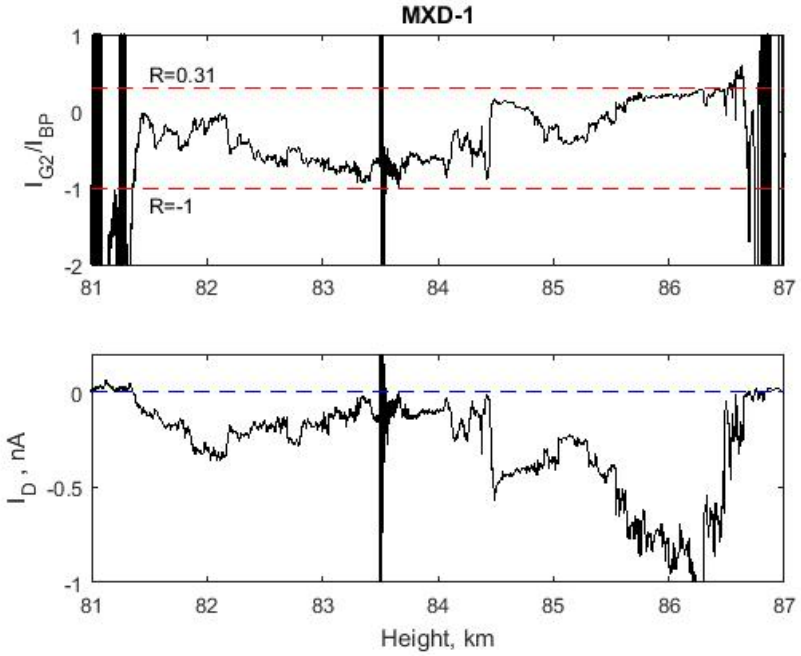

Figure 2. The ratio of the currents to G2 and BP in the upper panel, compared to the current I_D in the lower panel. The large disturbance at ~ 83.5 km altitude is caused by a squib being fired to open for another experiment on the payload. The values of R, at and outside the borders of the cloud are to be neglected since the dust density there is low or zero and R is therefore dominated by noise and uncertainties in their background level.

We see from Fig. 2 that the ratio R is dominated by secondary charging effects in the middle of the cloud system at ~82.5 to ~84.4 km, while at the upper edge around 86 km secondary charging is not very significant. This is in accordance with a scenario where small cloud particles normally can be expected to be found in the upper parts of the clouds (Robertson et al, 2009), from where they sink and grow, to reach maximum sizes in the middle regions of the clouds. In the lower parts, melting should lead to a reduction of dust sizes and release of embedded MSPs. Laboratory experiments show that the secondary production for fast impacts on metals by iron particles of radius above ~100 nm, is proportional to the volume of the impacting particle (Friichtenicht, 1964; Adams and Smith, 1971). Impacts of small ice particles below a radius ~100 nm, at impact velocities ~ 1400 m/s, indicate that the secondary production is proportional to the cross section of the impacting ice particle (Tomsic, 2001). Since the charge on a dust particle at given plasma conditions is roughly proportional to its radius, and since the cross section is proportional to the square of the radius, a significant secondary current (R<0) indicates large particles, while small secondary production (R>0) indicate small dust particles. We will later show that this is what we get for the dust size from the extended method.

The secondary charging, or the rubbing off effect by impacting dust on surfaces, is strongly dependent on the impact angle θ_i, the angle between the surface normal and the direction to the impacting particle. In the experiments with ice particles (Tomsic 2001) the maximum of the secondary production was at θ_i~ 86 degrees and it was reduced to 0 at 90 deg. Little secondary charge production took place below θ_i ~ 70 deg. This means that of the dust particles impacting on the cylindrical grid wires, only a fraction will rub off electrons from the grid. Havnes and Næsheim (2007) analyzed in detail the rotational effect on the currents to the grids of two DUSTY probes, launched in the summer of 1994 (Havnes et al., 1996a). They found that a substantial secondary charge production was needed to model the payload rotational effects on the grid impact currents. The effect of secondary charging has since been mapped in several other rocket flights (Havnes et al., 2009; Kassa et al., 2012; Havnes et al., 2014; Antonsen and Havnes, 2015; Antonsen et al., 2017). One result of the analysis of the secondary impact effects of NLC particles on the main grids of DUSTY type probes, was that it had to be very much more efficient than what has been found for impact of ice particles in laboratory experiments. A probable reason for this difference is most likely connected to that pure laboratory ice particles below ca 7 nm, have a tendency to stick to the impact surface and evaporate (Tomsic, 2001). On the other hand the NLC/PMSE icy particles, containing a substantial number of embedded MSPs (Hervig et al., 2012; Havnes and Næsheim, 2007) will partly fragment on impact and MSPs which are released will not evaporate but survive to carry away "rubbed off" electrons. With a MSP volume filling factor of 3% in a NLC/PMSE particle (Hervig et al., 2012), even a 7 nm NLC/PMSE icy particle will contain some 10 to 30 MSPs if their sizes are in the range 0.7 to 1 nm.

The secondary production, the number of charged fragments produced by one impacting NLC/PMSE particle of radius r_d, varies with the cross section of the impacting particle as

$$\eta_S(r_d) = \eta_{S,ref}\,(r_d/r_{d,ref})^2 \quad . \qquad (6)$$

Havnes and Næsheim (2007) found that for a reference icy dust particle, of radius $r_{d,ref}$ = 50 nm a number of $\eta_{S,ref}$= 50 to 100 negative unit charges would be released. With 3% MSP volume filling factor (Hervig et al., 2012) this corresponds to that ~1% of the embedded MSPs become charged fragments, if we set the embedded MSP radius to 1 nm.

We can now express the secondary current I_S by a use of Eq. (6) and a knowledge of how large fraction of the grid wires which contribute to the secondary charge production. In the modeling by Havnes and Næsheim (2007) they found that secondary charges are produced on a fraction

$\sigma_{2,sec}$~0.28 of the G2 grid diameter, where the total area of G2 in MXD-1 covers a fraction σ_2 = 0.235 of the total probe cross section $\sigma_P = \pi R_P^2$. The probe radius is R_P = 0.04 m. From this we can express the secondary charge current as

$$I_S = eN_D V_R A_{sec} \eta_S(r_d) \quad . \tag{7}$$

Here $N_D = \Sigma N_Z$, the total dust number density and $A_{sec} = \sigma_{2,sec}\sigma_2\sigma_p$ is the effective area of the probe for secondary charge production. This is only ~ 7% of the total probe cross section σ_p . The observed secondary charge current I_S is also found from Eqs. 1 and 2 as

$$I_S = (1-\sigma_2)I_{G2} - \sigma_2 I_{BP} \quad . \tag{8}$$

Inserting Eq. (6) in Eq. (7) we can solve Eqs. (7) and (8) for the dust radius

$$\left(\frac{r_d}{r_{d,ref}}\right)^2 = \frac{(1-\sigma_2)I_{G2} - \sigma_2 I_{BP}}{A_{sec}\eta_{S,ref} e N_D V_R} \quad . \tag{9}$$

Fixing the values for $\eta_{S,ref}$ and $r_{d,ref}$, the only unknown parameter on the right hand side is the total dust density N_D. If this is also known, we can find the dust radius from Eq. (9). However, the value of N_D is not directly available, but can be found in an iteration process which includes a charging model for the dust.

The charging model computes the equilibrium charge distribution of the ambient dust particles. The electron density n_e (Fig. 9) is measured by various probes on the payload. We require charge neutrality and find the ion density n_i from

$$n_i - n_e + \sum N_Z Z_D = 0 \quad . \tag{10}$$

The plasma temperature is equal to the neutral temperature and we will use a temperature of 150 K. For our equilibrium charging model we require that the rate at which dust particles of charge Z are given the charge number $(Z\text{-}1)$ by an electron colliding with it and sticking to it, is equal to the rate by which dust with charge number $(Z\text{-}1)$ are given charge number Z by ions colliding and sticking to it

$$N_Z J_e(Z) = N_{Z-1} J_i(Z-1) \quad . \tag{11}$$

Here $J_e(Z)$ and $J_i(Z)$ are the rates at which charged particles (electrons or ions) arrive at the surface of a dust particle with charge number Z, and stick to it. We have used the expressions for J_e and J_i from Draine and Sutin (1987) which include the short range polarization forces and refer to that paper for the full expressions.

The iteration procedure to extract values for dust radius r_d , dust total density N_D and also the dust charge distribution N_Z , together with other relevant parameters dependent on r_d and N_D, starts with a guess for the average dust charge number Z_{av}. A good guess is normally Z_{av}= -1. This will give an initial value for the total dust number density $N_D = \sum(N_Z Z_D)/Z_{av}$. Here $\sum(N_Z Z_D)$ is the observed dust charge density found from Eq. (4). From this value of N_D we calculate a value for the dust radius from Eq. (9). These approximations to N_D and r_d are now used in the charging model, together with known values for the plasma parameters, to calculate a new total dust density and a new average dust charge number which is used to find a new value for r_d . This process is repeatedly run through the charging code until it converges to a solution.

3 Measurements by the DUSTY probe on MAXIDUSTY-1, analyzed with the extended method.

We now use the observations by the DUSTY probe on MXD-1 and the new extended method to find the basic dust parameters: radius r_d, total density N_D and average dust charge number Z_{av} throughout the observed NLC/PMSE clouds. The electron data are taken from the results by the on board Faraday instrument (Friedrich and Rapp, 2009). In Fig. 3 we show smoothed raw currents I_{G2} and I_{BP} and the adopted background which will be subtracted from the raw currents to give the net currents . The curves show that the main cloud system extends from

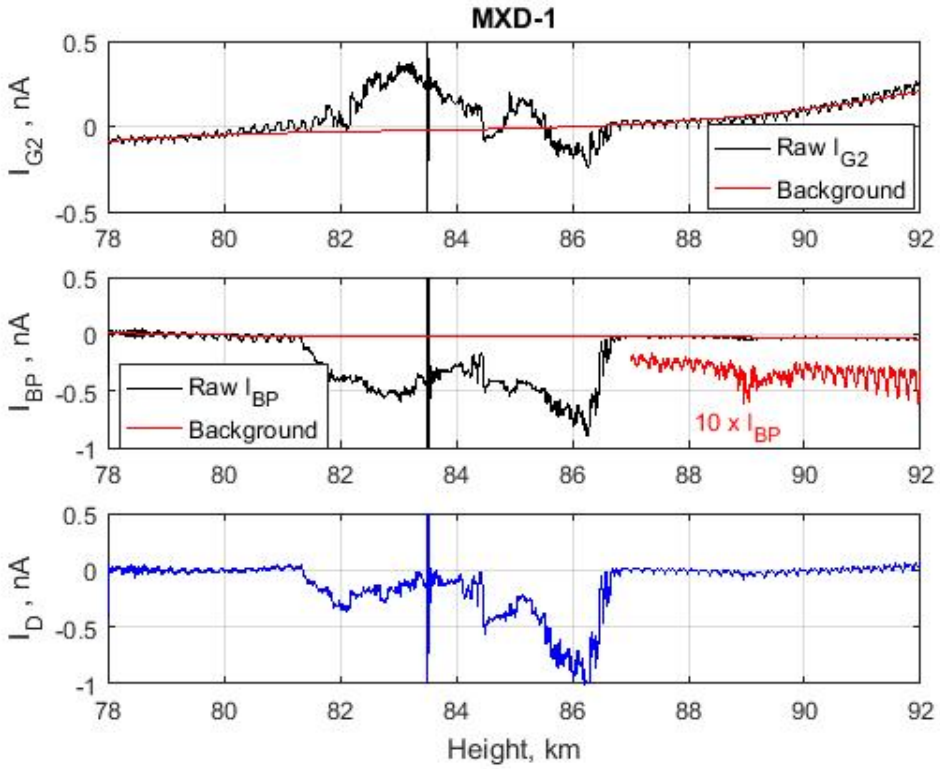

Figure 3. The smoothed currents I_{G2} and I_{BP} and the assumed background currents, are shown in the upper two panels. In the bottom panel we show the I_D current based on the currents I_{G2} and I_{BP}, corrected for background. The "event" at ~83.5 km is due to a squib being fired to open another instrument on the payload. In panel 2 we have also plotted in red a current *10 x* I_{BP} to empasize that there is a clear but weak dust structure at least spanning the altitude region from ~88.5 to ~89.9 km.

~81.3 to ~86.8 km with a clear but weak additional dust cloud structure between ~88.5 to ~89.9 km. We see indications that a weak structure also extends below 81.3 km, possibly down to ~ 80 km. This is apparent mainly in panel 1 where there is a weak I_{G2} in this interval and the payload rotation effect is different above and below 80 km, possibly indicating the presence of small MSP's in the size range up to several nm. They may have been released by melting of the larger icy particles and may be affected by the airstream around the payload and by the payload rotation.

In Fig. 4 we show the inferred values for dust radius r_d and N_D. The large noise signals around ~83.5 km in Figs .2 and 3, which were caused by a squib being fired, have been removed. The other 4 narrow and strong features in the middle of the cloud region (~83.3 to ~84.5 km) indicate the presence of dust layers, or "dust voids" with much larger dust sizes than just outside these

layers. The presence of dust of radius up to and even above 100 nm within the layers is indicated, compared to

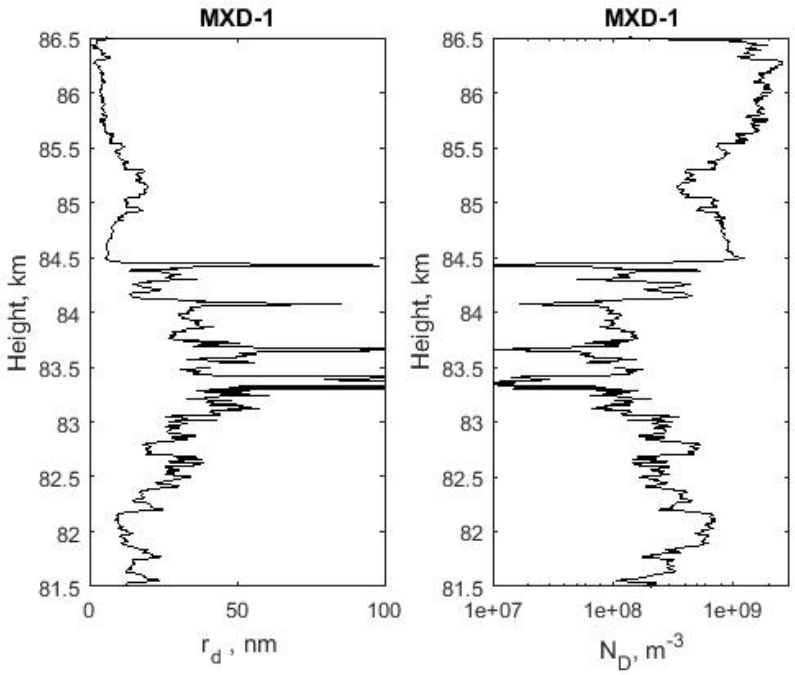

Figure 4. The inferred dust radius r_d and dust density N_D within the main cloud. We have applied a moderate sliding mean smoothing over 100 data points, changing the altitude resolution from 0.1 m in the observed data points, to 10 m. We have also removed the signals in the altitude region 83.5 to 83.55 km which are dominated by the strong noise from the squib firing, shown in Figs. 2 and 3.

dust sizes just outside the layers ranging from ~10 to ~ 40 nm. However, the values for r_d in these 4 narrow layers with large dust, are probably considerably more uncertain than in most other parts of the NLC/PMSE cloud. The reason for this is that these 4 layers (voids) have a very low dust density N_D, much lower than in the regions just outside the layers. We can see this from Figs. 2 and 3 where the current I_D is very low within the 4 layers and therefore the dust density N_D will also be low. This is directly evident from Fig .4, which show both r_d and N_D. The narrow layers with the large increase in dust sizes r_d also have low dust densities, where N_D can be down to ~ 10^7 m^{-3}. At such low values for the dust density, the dust radius r_d computed by Eq. (9), can be much affected by noise fluctuations in the signals, by payload rotational effects and uncertainties in the assumed background currents. This will lead to relatively large uncertainties in N_D and therefore also in r_d when computed with Eq. (9). The

narrow layers or voids in NLC/PMSE clouds will probably still exist (see also Havnes et al., 1996b) and contain large dust particles but their peak values may be questionable.

4 Comparison of the extended DUSTY method results with lidar and photometer results.

As a test on the values of r_d and N_D found by the extended method we compare with corresponding values found from the ALOMAR RMR Lidar observations (von Zahn et al., 2000, Baumgarten et al., 2007) and the on board MISU photometer (Gumbel et al., 2001; Hedin et al., 2008; Megner et al., 2009).

The ALOMAR RMR Lidar is a twin-Lidar system with two power lasers simultaneously emitting at 1064, 532 and 355 nm wavelengths, and with two receiving telescopes each with a 1.8 m primary mirror. The Lidar can be operated all year and under daylight conditions. During the MAXDUSTY-1 launch one beam was pointed along the predicted payload trajectory at 85 km and one in the vertical direction. In Fig. 5 we show the RMR observations close to the payload trajectory where the separation of the lidar and rocket measurements was less than 2 km. The second lidar performed measurements above the lidar station about 18 km separated from MXD-1 measurements. At both locations a double layer was observed and both layers show up and downward motion indicating small scale perturbations of the atmosphere. The size of the particles is calculated from the signal of three wavelengths assuming a distribution of needle and plate like particles of multiple sizes (Baumgarten et al., 2007). The size values given here are radii of a volume equivalent sphere, and give the mode of a Gaussian distribution of particle sizes.

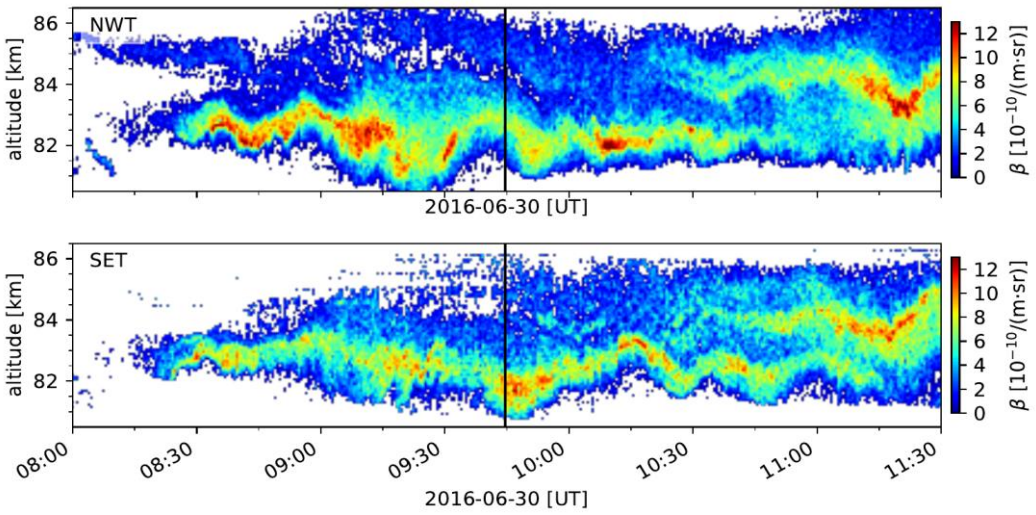

Figure 5. Backscatter coefficient (532 nm) measured by the RMR-Lidar along the payload trajectory of MXD-1 (upper panel) and about 18 km to the south-east of the trajectory (lower panel). The time of the rocket penetrating through the NLC layer is marked by the vertical black line.

The Side-looking MISU NLC photometer on board the payload also detected a two-layer NLC with an altitude profile very similar to the one in Fig. 5 at the time of the rocket measurement. Comparing the angle dependence of the scattering of sunlight on the NLC particles to theoretical Mie scattering phase functions, one can find an effective optical scattering radius, r_{Eff} of the particles in the NLC. This method is biased towards the largest particles due to the very strong dependence of scattering on dust radius. Below the layer, measuring the entire vertical extent of the NLC, the effective radius r_{Eff} = 46 (±4) nm. As we ascend through the NLC, the retrieved particle radius decreases with increasing altitude and the effective optical scattering radius in the top layer is 40 (±8) nm.

The two extended layers in Fig. 5, centered on ~ 83 and ~ 85 km also coincide with two layers at the same altitudes at which layers were detected with DUSTY. For DUSTY each of the two layers are characterized by containing large dust particles of low number density. This demonstrates again the strong dependence of scattering of light on the dust radius, increasing very rapidly with size so layers of low density but containing large dust can dominate the scattering. .

In Fig. 6 we show the DUSTY results, for one set of secondary charging parameters, for dust radius r_d, total dust number density N_D, and average dust charge number Z_{av}. We also show RMR Lidar results for 5 minutes centered on the MXD-1 measurements (09:44:36 UT) as well as the photometer measurements. The average sizes of the lidar measurements through the layer is 22 nm with standard deviation of 5 nm. The average width of the Gaussian size distribution is 8 nm. In the last panel we show the RMR Lidar observations of NLC brightness for 30 seconds around 09:44:36 UT compared with two model Lidar profiles computed for dust parameters inferred from the DUSTY observations and for the assumptions that the particles are pure ice or ice contaminated with 5% FeO which is the upper limit used by Hervig et al. (2012). We calculated the refractive index for mixture with FeO using the effective medium approximation (Garnett, 1904). We have excluded the data in the altitude region ~83.5 to ~83.7 km which were affected by the squib event.

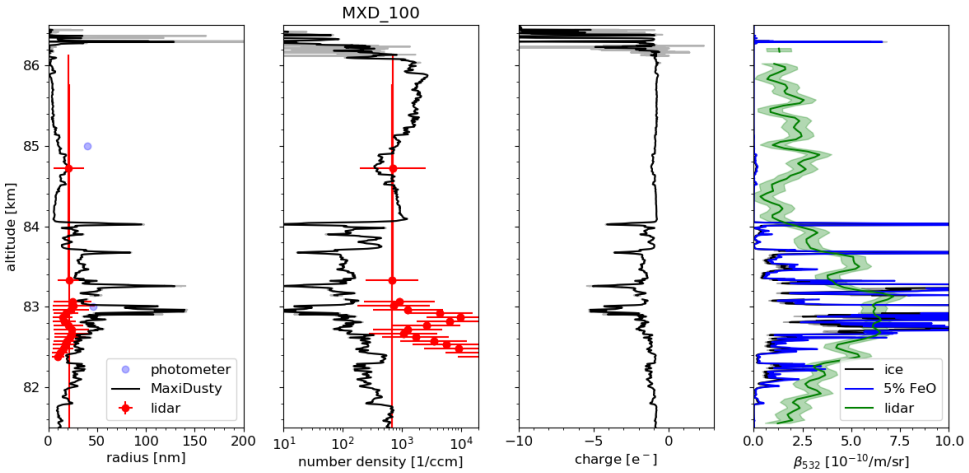

Figure 6 The first three panels show results for r_d , N_D and Z_{av} for an assumed value of $\eta_{S,ref}$ = 100. RMR Lidar results are marked by red dots while the two blue dots at 83 and 85 km are for the MISU photometer. The last panel shows the observed Lidar altitude profile where the black curve shows model results computed based on the MAXIDUSTY data of panel 1 and 2 and the assumption of pure ice particles, and the blue curve shows results based on the assumption that the ice particles contain 5% FeO. The green shaded area indicates the measurement uncertainty.

The variations of the DUSTY results for r_d, N_D and Z_{av} seem qualitatively reasonable. At the top of the cloud we find the smallest dust particles with sizes r_d well below 10 nm. These dust particles have presumably been created recently and now grow by deposition of water vapor which freezes out on their surface and contain embedded MSPs which become attached to them (Havnes and Næsheim, 2007; Hervig et al., 2012). The highest dust number density, close to 2×10^9 m^{-3}, is found in this region. In the middle of the cloud the dust sizes outside the narrow dust voids have increased to a maximum value of around 40 nm and number density is around 10^8 m^{-3}. The dust radius becomes smaller further down into the bottom parts of the cloud with values of around ~ 20 nm and the number density increases to ~ 6×10^8 m^{-3}. The average dust charge number is close to Z_{av} = -1 in the lower and upper parts of the cloud while in the middle part it is around Z_{av} ~ -2 to -3. That the comparatively large grains in the middle part do not have larger negative charge numbers is due to a paucity of electrons which is demonstrated by the electron bite out from ~ 82 to 84 km, shown in Fig. 7. In this figure we also show the dust

charge density $\sum(N_Z Z_D)$ and note that the dust particles are the dominant negative charge carriers in practically the whole extent of the cloud.

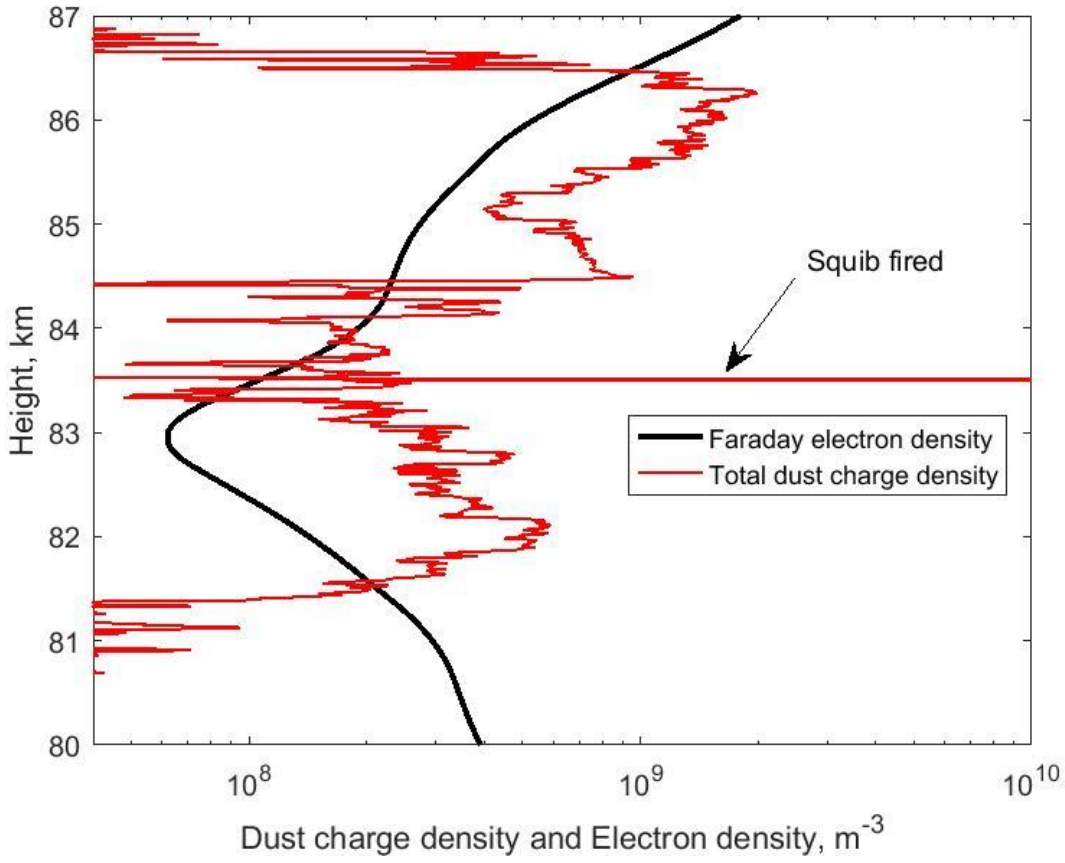

Figure 7. Electron density measured with the Faraday instrument, and the total dust charge density as observed by DUSTY, on MXD-1.

5 Discussion and conclusion. The extended method with its unsurpassed altitude resolution gives, in our opinion, reasonable results which compare well with the RMR Lidar and MISU photometer results (Fig. 6). It is noteworthy that the parameters for the secondary charging model in the present work have been taken from earlier modeling not aimed at finding r_d, N_D and Z_{av} but to demonstrate that secondary charging was essential in reproducing the currents to

400 BP and G2 and their variation with payload rotation (Havnes and Næsheim, 2007; Havnes et
401 al., 2009; Kassa et al., 2012).

402 If we compare the various results in Fig.6, where DUSTY results are based on $\eta_{S,ref} = 100$, there
403 are some significant differences between DUSTY results and the RMR Lidar or MISU
404 photometer results. The first is that the RMR Lidar in the region at and slightly below 83 km,
405 finds particles of half or less the sizes that DUSTY finds. The MISU photometer is closer to
406 the DUSTY values. Also, the Lidar total dust densities in the same altitude region are in general
407 more than a magnitude larger than what DUSTY finds.

408 We should bear in mind that some of the differences may result from the Lidar and DUSTY
409 probe sampling very different volumes. The sounding volumes are separated horizontally by
410 about 2 km and differ in size. With an altitude resolution of 475 m and integration time of 300
411 sec the Lidar samples a volume of about 10^5 m^3 while DUSTY, with some smoothing of the
412 data, samples 0.5 m^3 (5×10^{-4} m^3 with unsmoothed data). These differences may be important
413 taking into account small scale dynamics (Baumgarten and Fritts, 2014; Fritts et al., 2017). The
414 time evolution shown in Fig. 5 indicates that such small scale variations were indeed likely
415 during the time of the measurement.

416

417 For DUSTY we could lower the computed r_d and increase the N_D by increasing the secondary
418 efficiency $\eta_{S,ref}$ in Eq. (9) from its "accepted" values between 50 and 100. This may require
419 that the embedded MSPs occupy an exceptionally large volume of the icy NLC/PMSE particles.
420 However, we see from Fig. 6d that the Lidar profile, computed on the basis of the DUSTY
421 results for a $\eta_{S,ref} = 100$ compares reasonably with the observed Lidar profile while an increase
422 of $\eta_{S,ref}$ to 150 will lead to the computed DUSTY Lidar profile becoming very weak compared
423 the observed one. The best fit of the model DUSTY Lidar profile to the observed results is
424 obtained for a value of $\eta_{S,ref}$ around 70 to 80.

425 The values of r_d, N_D and Z_{av} from the DUSTY data will also be affected by the electron density
426 within the dust cloud. This can be critical if the dust density is large enough to create an electron
427 bite-out with locally large reductions in the electron density. In such cases the dust charges can
428 be reduced significantly compared to those that would occur if no bite-out were present. We
429 see in Fig. 7 a significant electron bite-out with a minimum electron density of 6×10^7 m^{-3} at an
430 altitude of 83 km. At such low electron densities the Faraday method to determine the electron
431 density is quite uncertain, which motivates us to examine the consequences of reducing the true

electron density within the bite-out compared to that in Fig. 7. Reducing it by a factor of 10 will lead to a reduction of r_d by a factor of ~2 and an increase in N_D by a factor of ~3 within the bite-out.

The charge model we have used does not include the photodetachment effect (Havnes and Kassa, 2009; Rapp, 2009) and it does not include any photoelectric effect. Inclusion of a photodetachment effect will have some – but not serious - effect on dust particles less than ~5 nm. It will lead to a moderate increase in dust density and a decrease of the dust radius. In our model, using values of the photodetachment effect taken from Havnes and Kassa (2009), we get a moderate reduction of the dust radius r_d in the altitude region above ~ 85.5 km.

Another uncertainty, caused by the design of the DUSTY probe, is that small dust particles (less than ~ 2 nm at an altitude ~ 85 km), which may be carrying a non-negligible part of the charge density, will be swept away from the probe by the airstream around the payload and its probes (Horányi et al., 1999; Hedin et al., 2007). Observations by the MASS instrument (Robertson et al., 2009, 2014; Knappmiller, 2008) indicate that considerable amounts of small charged dust particles have a tendency to be present in the upper layers of NLC/PMSE clouds, together with larger NLC/PMSE cloud particles. We cannot exclude that this is also the case for the clouds observed by MXD-1. To evaluate the consequences of small charged particles potentially not being registered by DUSTY we will need a charging model with more than one dust size. Such models should also improve the comparison to lidar measurements, as these take the effect of different sizes into account and show that the ensemble of particles often has a width of the size distribution of about half the mode radius (Baumgarten et al., 2010).

We find that the development of the new extended method to analyze the DUSTY measurements, has given this probe a power which is astounding considering its simplicity. It can in principle be used to measure the dust radius, dust total density, dust charge density and dust charge – all with an unsurpassed altitude resolution down to 10 cm or smaller scales. This will also open up for a mapping of the distribution of dust size, dust density and dust charges within small scale dust structures (Havnes et al., 1996b). To achieve the best foundation for the extended method and future use of DUSTY-like probes, we plan to refine the analysis with a more complete charging model and to map the effects of changes in the various parameters involved in the method. A comparison with the RMR lidar and MISU photometer observations during the MXD-1 flight will continue to be essential in refining the method. This may also

lead to a fine-tuning of the construction of the DUSTY probe for which the basic structure should be retained though modifications of G2 might be advantageous. For future campaigns we intend to improve the collocation of the measurement volumes and use the high resolution DUSTY measurements to derive the actual size distribution within the lidar sounding volume.

Author contribution.

OH, AB, TA and TWH extended the theory for analyzing the rocket data. OH and TA analyzed the rocket data. GB collected and analyzed the Lidar data. TA and ÅF tested rocket instruments. MF analyzed the Faraday data and provided the electron density data. JH collected the photometer data and analyzed them. OH prepared the manuscript with contributions from all co-authors.

Acknowledgements and Data

The rocket campaign and the construction of the rocket instrumentation was supported by grants from the Norwegian Space Centre (VIT.04.14.7; VIT.02.14.1; VIT.03.15.7; VIT.03.16.7**)**, the Research Council of Norway (240065) and by the Arctic University of Norway.

Replication data is available through the UiT Open Research Repository at https://doi.org/10.18710/LEMXBU

The authors declare that they have no conflict of interest.

References

Adams, N.G., and Smith,D.: Studies of microparticle impact phenomena leading to the development of a highly sensitive micrometeroid detector. 1971, Planet. Space.Sci, **19,** 195-204, 1971.

Amyx, K., Sternovsky, Z., Knappmiller, S., Robertson, S., Horányi, M., and Gumbel, J.: In-situ measurement of smoke particles in the wintertime polar mesosphere between 80 and 85 km altitude, J. Atmos.Solar-Terrestrial Physics, **70**, 61-70, 2008

Antonsen, T, and Havnes, O.: On the detection of mesospheric meteoric smoke particles embedded in noctilucent cloud particles with rocket-borne dust probes Review of Scientific Instruments, **86**, 033305; doi: 10.1063/1.4914394, 2015.

Antonsen, T., Havnes, O., and Mann, I.: Estimates of the Size Distribution of Meteoric Smoke Particles From Rocket-Borne Impact Probes, J. Geophys.Res, **122**, 12353-12365, DOI: 10.1002/2017JD027220 , 2017.

Asmus, H., Robertson, S., Dickson, S., Friedrich, M., and Megner, L.: Charge balance for the mesosphere with meteoric dust particles, J. Atmos.Solar-Terrestrial Physics., **127**, 137-149,. http://dx.doi.org/10.1016/j.jastp.2014.07.010, 2015.

Backhouse, T.W.: The luminous cirrus cloud of June and July. Meteorological Mag. **20**, 133, 1885.

Baumgarten, G., J. Fiedler, and G. von Cossart.: The size of noctilucent cloud particles above ALOMAR (69N, 16E): Optical modeling and method description, Adv. Space Res., **40**, 772-784, 2007.

Baumgarten G., J. Fiedler, and M. Rapp.: On microphysical processes of noctilucent clouds (NLC): Observations and modeling of mean and width of the particle size-distribution, Atmos. Chem. Phys., 10, 6661-6668, 2010.

Baumgarten G., and Fritts, D.C.: Quantifying Kelvin-Helmholtz instability dynamics observed in Noctilucent Clouds: 1. methods and observations, J. Geophys. Res., 119, 9324-9337, doi:10.1002/2014JD021832, 2014.

Czechowsky, P., Rüster, R., and Schmidt, G.: Variations of mesospheric structures in different seasons, Geophys.Res.Lett., **6**, 459-462, 1979.

DeLand, M. T., Shettle, E. P., Thomas, G. E., and Olivero, J. J.: Latitude-dependent long-term variations in polar mesospheric clouds from SBUV version 3 PMC data, J. Geophys. Res.,**112**, D10315, doi:10.1029/2006JD007857, 2007.

Draine, B.T., and Sutin, B. : Collisional charging of interstellar grains. The Astrophys. Journal. **320**, 803-817, 1987.

Friedrich, M., and Rapp, M.: News from the Lower Ionosphere: A Review of Recent Developments. Surv Geophys **30**, 525–559. DOI 10.1007/s10712-009-9074-2, 2009.

Friichtenicht, J.F.: Micrometeroid simulation using nuclear accelerator techniques. Nucl.Instr.Meth. **28,** 70-78, 1964.

Fritts, D. C., Wang, L., Baumgarten, G., Miller, A.D., Geller, M.A., Jones, G., Limon, M., Chapman, D., Didier, J., Kjellstrand, C.B., Araujo, D., Hillbrand, S., Korotkov, A., Tucker, G., and Vinokurov, J.: High-resolution observations and modeling of turbulence sources, structures, and intensities in the upper mesosphere, J. Atmos. Solar-Terr. Phys., 162, 57-78, doi:10.1016/j.jastp.2016.11.006, 2017.

Gadsden, M., and Schröder, W.: Noctilucent Clouds, Springer-Verlag, New York, 1989.

Garnett, J.C.M.: Colours in metal glasses and in metallic films. Philosophical Transactions of the Royal Society A203, 385–420, 1904.

Gumbel, J., J. Stegman, D. P. Murtagh, and Witt, G.: Scattering phase functions and particle sizes in noctilucent clouds, Geophys. Res. Lett., **28**, 1415-1418, 2001.

Havnes, O., Trøim, J., Blix, T., Mortensen, W., Næsheim, L. I., Thrane, E., and Tønnesen, T.: First detection of charged dust particles in the Earth's mesosphere, J. Geophys. Res., **101,** 10 839-10 847, 1996a.

Havnes,O., Næsheim, L.I.,Hartquist, T.W., Morfill, G.E., Melandsø, F., Schleicher,B., Trøim, J., Blix, T., Thrane, E.: Meter-scale variations of the charge carried by mesospheric dust. Planet. Space Sci., **44(10)**, pp. 1191-1194, 1996b.

Havnes,O., and Næsheim, L.I.: On the secondary charging effects and structure of mesospheric dust particles impacting on rocket probes. Ann.Geophys, **25**, 623-637, 2007.

Havnes, O; Surdal, L.H; and Philbrick, C.R.:., Mesospheric dust and its secondary effects as observed by the ESPRIT payload. Ann. Geophys., **27**, 1–10, 2009

Havnes, O., Gumbel, J., Antonsen,T, Hedin, J., and LaHoz, C.: On the size distribution of collision fragments of NLC dust particles and their relevance to meteoric smokeparticles, J. Atmos. Solar-Terr. Phys.**118**, 190–198 , http://dx.doi.org/10.1016/j.jastp.2014.03.008 , 2014.

Hedin, J., Gumbel, J., and Rapp, M.: On the efficiency of rocket-borne particle detection in the mesosphere, Atmos. Chem. Phys., **7**, 3701-3711, 2007.

Hedin, J. Gumbel, J, Khaplanov, M, Witt, G and Stegman, J.: Optical studies of noctilucent clouds in the extreme ultraviolet, Ann. Geophys., 26, 1–11, 2008.

Hervig, M.E., Gordley, L.L., Deaver, L.E., Siskind, D.E., Stevens, M.H., Russell III, J.M., Bailey, S.M., Megner, L., and Bardeen, C.G.: First satellite observations of meteoric smoke in the middle atmosphere, Geophys. Res. Lett., http://dx.doi. org/10.1029/2009GL039737, 2009.

Hervig,M.E.,Deaver,L.E.,Bardeen,C.G.,Russel III,J.M.,Bailey,S.M.,and Gordley,L.L.: The content and composition of meteoric smoke in mesospheric ice particles from SOFIE observations. J.Atmos.Sol.Terr.Phys.**84–85**, 1–6, 2012.

Hervig, M.E., Bardeen, CG., Siskind, DE., Mills, MJ; and Stockwell, R .: Meteoric smoke and H2SO4 aerosols in the upper stratosphere and mesosphere. Geophys. Res.Lett., **44**, 2, 1150-1157**;** DOI**:** 10.1002/2016GL072049, 2017.

Horányi, M., Gumbel, J., Witt, G., and Robertson, S.: Simulation of rocket-borne particle measurements in the mesosphere, Geophys. Res. Lett. **26**, 1537-1540, 1999.

Hunten, D. M., Turco, R. P., and Toon, O. B.: Smoke and dust particles of meteoric origin in the mesosphere and stratosphere, J. Atmos. Sci., **37**, 1342-1357, 1980.

Höffner, J., and Lautenbach, J.: Daylight measurements of mesopause temperature and vertical wind with the mobile scanning iron lidar, Opt. Lett., 34, 1351–1353, 2009.

Huang W., Chu X., Gardner C. S., Carrillo-Sánchez J. D., Feng W., Plane J. M. C., and Nesvorný D.: Measurements of the vertical fluxes of atomic Fe and Na at the mesopause: Implications for the velocity of cosmic dust entering the atmosphere, Geophys. Res. Lett., **42**, 169–175, doi:10.1002/2014GL062390, 2015.

Jesse, O.: Auffallende Abenderscheinungen am Himmel, Meteorol. Z., **2**, 311–312, 1885.

Kassa, M., Rapp, M., Hartquist, T.W., and Havnes, O.: Secondary charging effects due to icy dust particle impacts on rocket payloads. Ann. Geophys., **30**, 433–439, www.ann-geophys.net/30/433/2012/doi:10.5194/angeo-30-433-2012 , 2012.

Knappmiller, S., Robertson, S., Sternovsky, Z. and Friedrich, M.: A Rocket-Borne Mass Analyzer for Charged Aerosol Particles in the Mesosphere, Rev. Sci. Instr. **79 (10)** doi:104502, 2008.

Latteck, R., and Strelnikova, I.: Extended observations of polar mesospheric winter echoes over Andøya (69^{o}) using MAARSY. J. Geophys.Res. (Atmospheres)., **120**, 8216-8225, doi:10.1002/2015JD023291, 2015.

Megner, L., Khaplanov,M., Baumgarten, G., Gumbel, J., Stegman, J., Strelnikov, B and Robertson, S.: Large mesospheric ice particles at exceptionally high altitudes, Ann. Geophys., **27**, 943-951, 2009.

Ogurtsov, M.G.,and Raspopov,O.M.: Possible impact of interplanetary and interstellardust fluxes on the Earth's climate, Geomag.Aeron.**51**, 275–283, 2011.

Plane, J. M. C.: Cosmic dust in the Earth's atmosphere, Chem. Soc. Rev. **41 (19),** 6507 – 6518, 2012.

Rapp, M.: Charging of mesospheric aerosol particles: the role of photodetachment and photoionization from mesospheric smoke and ice particles. Ann.Geophys., **27**, 2417-2422, 2009.

Rapp, M., and Strelnikova, I.: Measurements of meteor smoke particles during the ECOMA-2006 campaign; 1. Particle detection by active photoionization, J. Atmos. Solar-Terrestrial Phys, **71**, 477-485, 2009.

Rapp, M ., and Thomas, G.E.: Modeling the microphysics of mesospheric ice particles: Assessment of current capabilities and basic sensitivities, J. Atmos. Solar-Terrestrial Phys. **68**, 715-744, 2006.

Reddmann, T., Funke, B., Konopka, P., Stiller, G., Versick, S, and Vogel, B.: In Climate and Weather of the Sun-Earth System (CAWSES), Ed. F.-J. Lübken. 247-273. Springer Atmospheric Sciences. Dordrecht. DOI 10.1007/978-94-007-4348-9_15, 2013.

Robertson, S., Horányi, M., Knappmiller, S., Sternovsky, Z., Holzworth, R., Shimogawa, M., Friedrich, M., Torkar, K., Gumbel, J., Megner, L., Baumgarten, G., Latteck, R., Rapp, M., Hoppe, U.-P., and Hervig, M. E.: Mass analysis of charged aerosol particles in NLC and PMSE during the ECOMA/MASS campaign, Ann. Geophys., **27**, 1213-1232, https://doi.org/10.5194/angeo-27-1213-2009, 2009.

Robertson, S., Dickson, S., Horányi, M., Sternovsky, Z., Friedrich, M., Janches, D., Megner, L., Williams, B.: Detection of meteoric smoke particles in the mesosphere by a rocket-borne mass spectrometer, J. Atmos. Solar-Terr. Phys. **118**, pp. 161–179, 2014.

Rosinski, J., and Snow, R. H.: Secondary particulate matter from meteor vapors, J. Met. **18**, 736-745, 1961.

Symons, G.J. (ed).: The Eruption of Krakatoa and Subsequent Phenomena (Report of the Krakatoa Committee of the Royal Society) London, 1888.

Thomas, G.: Is the polar mesosphere the miner's canary of global change?, Advances in Space Research, 18, 149 – 158, doi:10.1016/0273-1177(95)00855-9, 1996.

649 Tomsic, A.: Collisions between water clusters and surfaces, Ph.D thesis, Gothenburg
650 University, 2001.

651 Turco, R., Toon, O., Whitten, R., Keesee, R., and Hollenbach, D.: Noctilucent clouds:
652 Simulation studies of their genesis, properties and global influences, Planetary and Space
653 Science, 30, 1147 – 1181, doi:10.1016/0032-0633(82)90126-X, 1982.

654 Von Cossart, G., Fiedler, J., and von Zahn, U.: Size distributions of NLC particles as determined
655 from 3-color observations of NLC by ground-based lidar, Geophys. Res. Letter. **26**, 1513-1516,
656 1999.

657 von Zahn, U., von Cossart, G., Fiedler, J., Fricke, K. H., Nelke, G., Baumgarten, G., Rees, D.,
658 Hauchecorne, A., and Adolfsen, K.: The ALOMAR Rayleigh/Mie/Raman lidar: objectives,
659 configuration, and performance, Ann. Geophys., **18**, 815-833, https://doi.org/10.1007/s00585-
660 000-0815-2, 2000.

661 Zeller, O., Zecha, M., Bremer, J., Latteck,R., and Singer, W.: Mean characteristics of
662 mesospheric winter echoes at mid- and high-latitudes, J. Atmos. Sol. Terr. Phys, **68 (10),**
663 1087-1104, doi:10.10.1016/j.jastp.2006.02.015, 2006.

664
665
666
667
668

669

670

PAPER V

Havnes, O., Latteck, R., Hartquist, T. W., and Antonsen, T.: First simultaneous rocket and radar detections of rare low summer mesospheric clouds., Geophysical Research Letters, 45, 5727–5734, doi: 10.1029/2018GL078218, 2018b

Geophysical Research Letters

RESEARCH LETTER
10.1029/2018GL078218

Key Points:
- The first simultaneous radar and rocket observations of weak, low, and rare polar mesospheric summer clouds were obtained
- The majority of the dust particles appear to be neutral but with a net positive dust charge density
- Size sorting of dust must take place

Correspondence to:
O. Havnes,
ove.havnes@uit.no

Citation:
Havnes, O., Latteck, R., Hartquist, T. W., & Antonsen, T. (2018). First simultaneous rocket and radar detections of rare low summer mesospheric clouds. *Geophysical Research Letters*, *45*, 5727–5734. https://doi.org/10.1029/2018GL078218

Received 5 APR 2018
Accepted 24 MAY 2018
Accepted article online 30 MAY 2018
Published online 10 JUN 2018

First Simultaneous Rocket and Radar Detections of Rare Low Summer Mesospheric Clouds

O. Havnes[1], R. Latteck[2], T. W. Hartquist[3], and T. Antonsen[1]

[1]Institute of Physics and Technology, Arctic University of Norway, Tromsø, Norway, [2]Institute of Atmospheric Physics, Kühlungsborn, Germany, [3]School of Physics and Astronomy, University of Leeds, Leeds, UK

Abstract On 30 June 2016 a layer of dust, possibly meteoric smoke particles (MSPs), was observed with a rocket borne probe at 69.29°N, 16.02°E and altitudes of ~74 km where patchy thin cloud layers, detected with the Middle Atmosphere Alomar Radar System, were present. The rocket traversed a layer with a net positive dust charge density of ~10^7 unit charges per cubic meters and a number density of neutral dust particles with sizes ≥4 nm of ~10^8 m^{-3}. The positive charge density may require that elements that lower the photoelectric work function coat MSPs. The presence of this relatively large dust is consistent with smaller MSPs being swept out of the low mesospheric cloud region during the summer, while larger MSPs remain where their fall velocities equals the circulation updraught velocities. Large MSPs initially embedded in icy particles that subsequently sublimate may also fall until their fall velocities match the updraught velocities.

Plain Language Summary A rocket and radar campaign was conducted in the summer of 2016 to investigate the clouds in the Earth's polar middle atmosphere and the role of meteoric smoke particles. They are produced by meteorites entering the atmosphere at high velocities, where they are heated by friction and ablate. We lack knowledge of the cloud transition phases from winter to summer conditions in late May and back in late August. Recent radar observations show that contrary to the belief a few years back, weak and low clouds are not totally absent in the summer season. One of the rockets flew through a very weak and low cloud, which also was observed by radar. The probability for this to happen is very low. Analysis shows that the cloud consists of 4- to 5-nm-sized meteoric smoke particles of number density a few times 10^8 particles m^{-3} with a low positive dust charge density of ~10^7 m^{-3}. Our findings are consistent with size sorting being active and important in the low cloud region especially during the transition phases. The positive charge density apparently requires that the photoelectric properties of the smoke particles are affected by coating with or absorption of gases.

1. Introduction

The various clouds in the Earth's mesosphere have traditionally been classified as either summer clouds or winter clouds. With clouds we mean (mesospheric) dust clouds. The only visually observable clouds are the noctilucent clouds at altitudes of ~80 to ~90 km. They consist of icy particles with sizes up to ~100 nm (Von Cossart et al., 1999). Other clouds that are detected with radars are called polar mesospheric summer echoes (PMSEs; Ecklund & Balsley, 1981) and polar mesospheric winter echoes (PMWEs; Czechowsky et al., 1979). Mesospheric radar echoes, probably formed by turbulence linked to Kelvin-Helmholtz instabilities, are observed at sites close to the equator (Lehmacher et al., 2007).

The NLC/PMSE season starts when the mesopause temperature changes from a winter temperature around 200–220 K to a summer temperature as low as 110–130 K (Lübken, 1999; Von Zahn & Meyer, 1989). The change arises from seasonal variations in the global atmospheric circulation pattern, with the onset of a polar updraught and associated adiabatic cooling. Water vapor then condenses, most likely on meteoric smoke particles (MSPs) (Hervig et al., 2012; Rapp & Thomas, 2006; Rosinski & Snow, 1961).

The PMWEs are much weaker than the PMSEs and occur less frequently. Observed with standard MST radars they disappear in late May and reappear at the beginning of September (Zeller et al., 2006). Since 2011 a new MST radar MAARSY has been in operation at Andøya Rocket Range, Norway. MAARSY has 20 times the power and ~half the beam width of the ALOMAR Wind radar (ALWIN) it replaced (Latteck et al., 2012). The MAARSY observations give significantly different statistics for the PMWEs. One difference is that although the PMWEs become rarer toward the end of the standard PMWE season in May, weak radar scattering layers are occasionally observed with MAARSY during the summer months, at altitudes well below the main NLC/PMSE altitudes (Latteck & Strelnikova, 2015). The temperatures at these lower altitudes are high enough to remove icy particles.

In the following we will call these weak summer echoes rare low summer echoes (RLSEs). This to emphasize that they are different from the much stronger NLC/PMSE, which in summer are nearly always present above the RLSE heights, and further that they differ from the PMWE by being weaker with a much lower occurrence frequency. If dust particles are present in and active in creating the PMWEs, and also the RLSEs, they must be nonvolatile and differ from the icy particles of the NLC/PMSE clouds. MSPs are obvious candidates.

Support for the conjecture that MSPs are involved in creating the PMWEs comes from observations of the radar overshoot effect (Havnes, 2004). The overshoot is produced by the use of artificial periodic RF heating of electrons (Rietveld et al., 1993). The overshoot effect, first observed for NLC/PMSE clouds (Havnes et al., 2003), has also been observed for PMWEs with the European Incoherent Scatter scientific association 224-MHz radar (Belova et al., 2008; Kavanagh et al., 2006; Kero et al., 2008) and the Mobile Radar and Rocket Observatory (MORRO) 56-MHz radar (Havnes et al., 2011; La Hoz & Havnes, 2008). The weak RLSEs that are detected occasionally with MAARSY have not been detected with either of these other radars, which are collocated with the European Incoherent Scatter Heating Facility.

There is no heating facility at the MAARSY site. Consequently, the radar overshoot effect cannot be studied with MAARSY, which has left open several questions about the RLSE clouds. Are they, like the NLC/PMSE and PMWE clouds, controlled by dust particles? If so, are the RLSE particles those remnants of PMWE dust that have not been swept out of the lower mesosphere by the summer updraught? Are they related to the particles in the higher NLC/PMSE clouds? Is it possible that the NLC/PMSE icy particles, when sublimating as they sink to warmer altitudes, release a sufficient number of large MSPs that can overcome the updraught, fall below the NLC/PMSE clouds, and become important charge carriers in RLSE clouds? These are among the many questions requiring answers for an understanding of the transport and role of MSPs, from their creation in the upper mesosphere until they are deposited on the Earth's surface (Plane, 2012), to emerge.

The first step, which can be achieved with rocket borne probes, is to establish whether dust exists in RLSE clouds. However, the rarity of RLSEs presents a challenge.

Below we present, and provide an analysis of data for a RLSE layer that is the first to be detected simultaneously with radar and a rocket borne probe. In section 2 we provide the data. In section 3 we report on the analysis of the data obtained with the probe to find the RLSE dust density and dust charge density, and section 4 contains a discussion and conclusions.

2. The MAXIDUSTY Campaign

During the MXD-1 payload launch on 30 June 2016 at $09^h\,43^m\,18^s$ UT, a weak RLSE layer was detected with a DUSTY probe and the MAARSY radar. Though it is always small, the probability for RLSEs to be detectable with MAARSY is largest at the beginning of the NLC/PMSE season and falls significantly by the end of June (Latteck & Strelnikova, 2015). Usually, hardly any detectable RLSEs would be expected when MXD-1 was launched.

Disturbed magnetospheric conditions increase the electron density and the fraction of negatively charged dust and are normally required for PMWEs to be detectable with standard MST radars (Zeller et al., 2006). However, the sensitivity of MAARSY is 17 dB greater than that of ALWIN, a typical MST radar operated at Andøya until 2008. This enabled the detection of RLSEs during quiet magnetospheric, but sunlit, conditions obtained during the MXD-1 flight.

We focus on the DUSTY and MAARSY measurements in the height region below the NLC/PMSE altitudes. The MXD-1 DUSTY probe (Havnes et al., 1996, 2015) is bucket shaped with three grids and a bottom impact plate (BP). Only the currents I_{G2} to the lowest grid G2 and I_{BP} to BP are used since they, being screened from the ambient plasma, are the grids with significant dust impact currents. Figure 1a shows I_{G2} and Figure 1d I_{BP} for the upward trajectory. The main NLC/PMSE are easily identified at altitudes from approximately 81 to 86 km, but there are no clear indications of any RLSEs below these main clouds. However, zooming in on I_{BP} and I_{G2} in the region from 66 to 78 km, as shown in Figures 1b and 1c, we see small changes in the currents up to ~5 pA. This is less than ~1% of the current changes when the NLC/PMSE clouds were traversed.

Near the time t_{74}, MAARSY detected thin patchy RLSEs in the altitude region around 74 km. Figure 2 shows results for four MAARSY beams at 0°, 4°, 8°, and 12° from the vertical toward the azimuth of the rocket trajectory. All beams contained one relatively strong RLSE layer (which was not traversed by the rocket), which

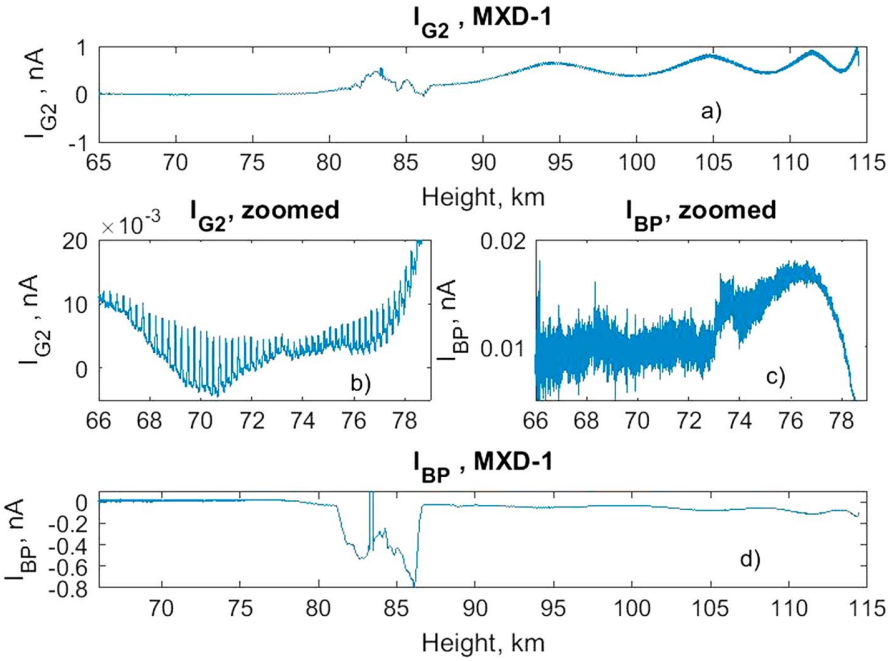

Figure 1. (a and d) The observed current I_{G2} and I_{BP} for altitudes up to apogee. (b and c) Zoom in on the altitude range of the rare low summer echo layer. The disturbance in Figures 1a and 1d at ~83 km is due to the firing of a squib for another instrument.

moved to the north-west and descended. In the MAARSY 12° beam at t_{74}, we see another weaker and more complex RLSE, which was traversed by and detected by rocket instrumentation.

The raw data shown in Figures 1 and 3 contain electronic noise and payload rotation effects. In addition to this we see in the upper heights of Figure 1a, the effect rocket precession with a period ~19.5 s.

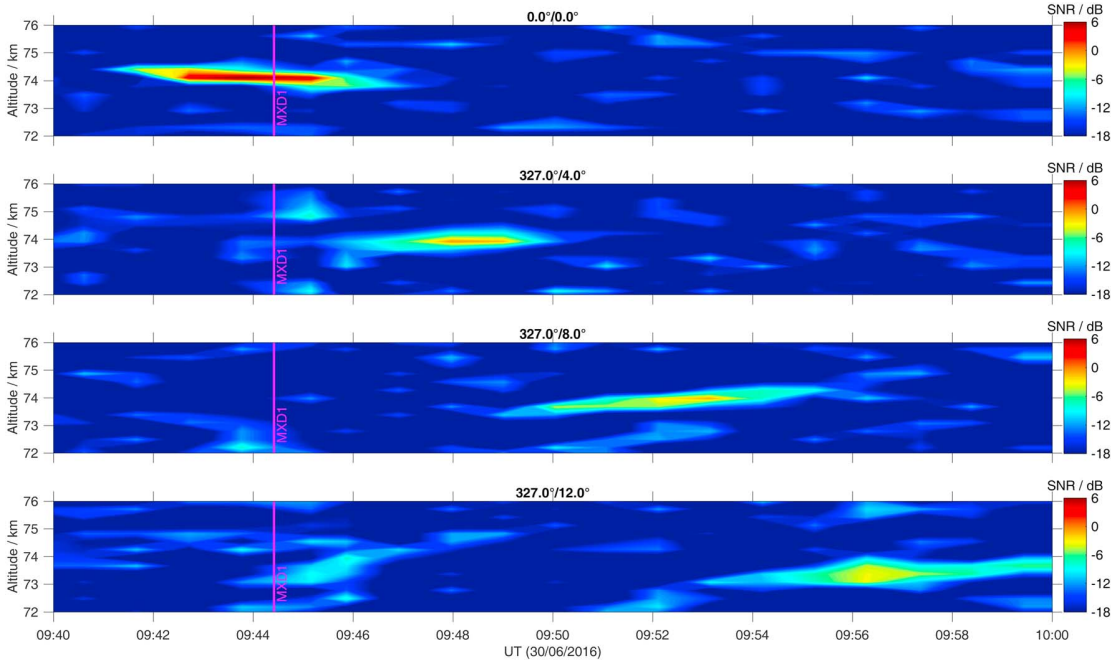

Figure 2. This figure shows results for MAARSY beams in the vertical direction and in directions toward the azimuth of the rocket trajectory at angles of 4°, 8°, and 12° from the vertical. The 12° beam was closest to the rocket trajectory, which passed 74-km height at the time $t_{74} = 09^{h}\ 44^{m}\ 25^{s}$, as indicated by the vertical line. SNR = signal-to-noise ratio.

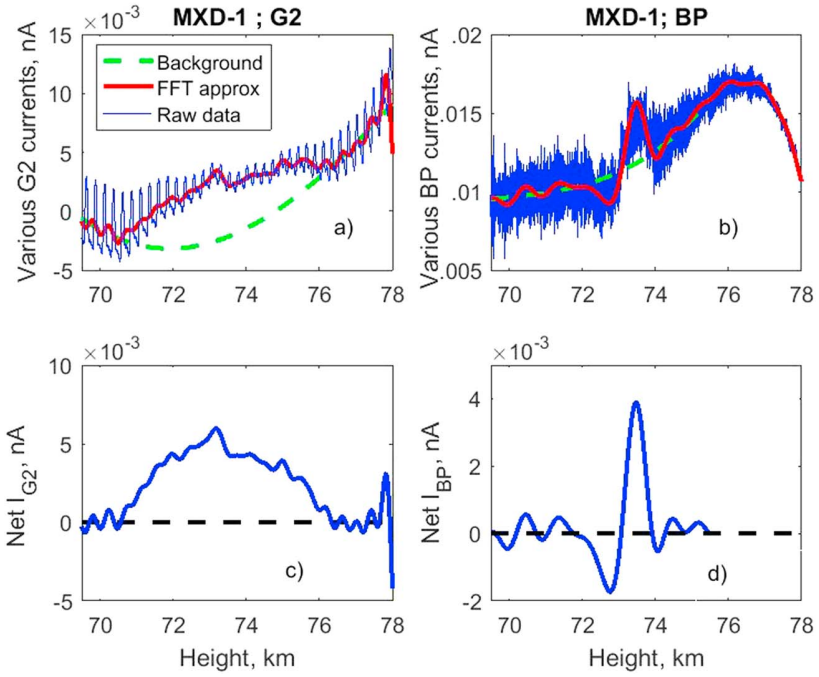

Figure 3. (a and b) The raw current to G2 and bottom impact plate (BP), respectively, the fast Fourier transform (FFT) approximations to the currents and the assumed background currents. (c and d) The net currents to G2 and BP.

Extrapolating this backward in time we find that there should be a minimum effect of the precession at height ~72 km. Without dust we would expect a mean current as shown by the background (green line) in Figure 3a. The actual observations in this height region show that there must have been dust impacts on G2 creating positive currents to it by direct deposition or by rubbing off electrons. To find the net currents to G2 and BP in the RLSE, we used fast Fourier transform (FFT) on the raw currents and an inverse FFT with a cutoff in frequency to remove payload spin effects at ~ 4.5 rps and higher frequency noise. The inverse FFT curves, representing the observations, are shown in Figures 3a and 3b as are the adopted background currents, which we found by interpolating with a third-degree polynomial fitted to altitude regions below (69–70.6 km) and above (76.2–77.5 km) the observed RLSE layer. In Figures 3c and 3d we show the final net currents I_{G2} and I_{BP} where the background has been subtracted.

3. Analysis of the RLSE Observations

The currents I_{BP} and I_{G2} measured with the DUSTY probe are due to impacts of charged and neutral dust particles. We suppose that in RLSEs, as in PMWEs, the particles are probably MSPs with charge number Z distributed between -1, 0, and +1. Photodetachment (Havnes & Kassa, 2009; Rapp, 2009; Weingartner & Draine, 2001) can at sunlit conditions cause the majority of dust particles to be neutral. Though photoionization may produce a significant number of positively charged dust (Asmus et al., 2015; Havnes et al., 1990; Rapp, 2009; Robertson et al., 2009), the number density of neutral dust particles can be much higher than that of the charged dust particles. In such cases the neutral dust particles can play a major role in determining I_{BP} and I_{G2} by rubbing off negative charge when impacting the grid wires of G2 at glancing angles (Havnes & Næsheim, 2007; Tomsic, 2001). The extraction of negative charges from G2 produces a positive current to G2 and a negative current to BP when they impact it.

A distribution of MSPs sizes can extend to sizes below 0.5 nm (Hunten et al., 1980; Rapp & Thomas, 2006). If a full MSP size distribution had been present in the RLSE cloud, DUSTY would have detected only a fraction of the ambient cloud particles because MSPs below a certain size would be swept away from the DUSTY probe by the airstream around the payload. Hedin et al. (2007) calculated the fraction of impacting dust, which were swept away from DUSTY-like probes at various atmospheric conditions. From their results one can conclude that at ~74 km, the fraction γ of particles with radii of 3, 4, and 5 nm that entered DUSTY was 0, 0.4, and 0.7,

respectively. At 74 km the real RLSE particle size distribution will probably differ substantially from the full MSP size distribution because the summer updraught will, within a few weeks after its onset, sweep away the smallest MSPs, while the larger MSPs linger at altitudes at which their fall velocities are comparable to the local updraught velocities (Havnes & Kassa, 2009). MAARSY observations (Latteck & Strelnikova, 2015, Figure 5) showing that RLSEs are found at altitudes from ~60 to ~80 km in the early phases of the NLC/PMSE season but that the lower altitude limit gradually increases with time provide evidence that this is the case. This is consistent with Rapp et al. (2010) not detecting MSPs in the lower RLSE region during the last part of the summer. We attribute this behavior to the lower regions, where fall velocities are smallest, being swept nearly clean of dust first.

Thus, for our analysis we assume that the MSPs can have three different charge states $Z = +1$, 0, and -1 (Asmus et al., 2015). We also assume that at the launch of MXD-1 all of the small particles had been swept out of the RLSE altitude region, while particles with sizes of several nanometers remained present in the upper parts of the RLSE region. Some large MSPs may also have fallen into the upper RLSE regions when sublimating NLC/PMSE particles released their embedded MSPs. In the following we will take the RLSE particle size lower limit to be large enough that the DUSTY probe registered the impact of a major fraction of the charged RLSE particles. Observations for which the dust capture efficiency is lower than 100% would mimic observations with a smaller cross section than that of the real DUSTY.

The flux of positively charged dust in front of G2 is $\Gamma(+)$, that of neutral dust is $\Gamma(0)$, and that of negatively charged dust is $\Gamma(-)$. The current I_{G2} is given by

$$I_{G2} = e\,[\Gamma(+) - \Gamma(-)]\sigma_2 + e\,[\Gamma(+) + \Gamma(0) + \Gamma(-)]\eta\sigma_{2,s} \tag{1}$$

The DUSTY probe is closed to ambient electrons and ions, which do not contribute to I_{G2} or I_{BP}. The first term on the right-hand side of equation (1) is due to positively and negatively charged dust colliding with G2. The second term describes the secondary charging effect due to high impact angle collisions of particles near the edges of the G2 grid wires rubbing off electrons and creating a positive current to G2. The G2 wire thickness and grid density is such that the G2 grid, if projected on to the bottom plate of DUSTY, covers a fraction $\sigma_2 = 0.235$ of it. Glancing impacts that produce secondary charges, occur according to our model (Havnes & Næsheim, 2007) on ~28% of the G2 cross section and $\sigma_{2,s} = 0.28\sigma_2$ is therefore the fraction of the DUSTY cross section that produces secondary charges. The secondary charge production efficiency η, which is proportional to the cross section of the impacting dust particle (see equation (6)), is the average number of unit charges that are rubbed off by dust particles impacting near the G2 wire edges.

The current I_{BP} is given by

$$I_{BP} = e\,[\Gamma(+) - \Gamma(-)](1 - \sigma_2) - e\,[\Gamma(+) + \Gamma(0) + \Gamma(-)]\eta\sigma_{2,s} \tag{2}$$

The first term on the right-hand side is due to the direct dust charge deposition on BP. The second term is caused by electrons that were rubbed off G2 being deposited as a negative current to BP.

The sum of equations (1) and (2) gives the net flux of charged dust in front of G2 as

$$\Gamma\,(\mathrm{Ch}) = \Gamma(+) - \Gamma(-) = (I_{G2} + I_{BP})/e \tag{3}$$

Considering the currents shown in Figures 3c and 3d, we see that Γ (Ch) must be positive. This rules out the ambient electron number density being large compared to the MSP number density since in such circumstances the majority of the MSPs would have $Z = -1$. We ignore this possibility and take the majority of the MSPs to be neutral and moderate fractions of MSPs to have $Z = -1$ and +1. Neglecting $\Gamma(+)$ and $\Gamma(-)$ in comparison with $\Gamma(0)$ in the last term of each of equations (1) and (2) and inserting equation (3) into equation (2) we find that

$$\Gamma(0) = [(1 - \sigma_2)\, I_{G2} - \sigma_2\, I_{BP}]/e\eta\sigma_{2,s} \tag{4}$$

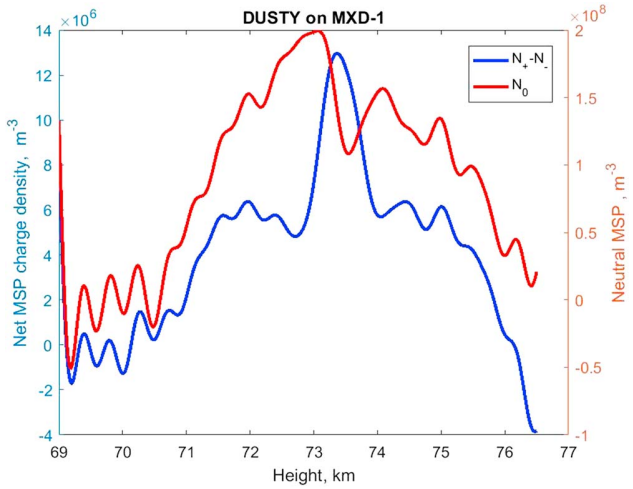

Figure 4. The dust charge density and the total number density $N(0)$ of neutral particles are shown. $N(0)$ is inversely proportional to the secondary charge production factor η. For this figure $\eta = 0.5$. MSP = meteoric smoke particle.

The secondary charge production efficiency is given by

$$\eta = \eta_{\text{ref}} \left(r_D/50\right)^2 \tag{5}$$

Here r_D is the radius of the impacting dust in nanometers. Modeling of rocket observations (Havnes & Næsheim, 2007; Kassa et al., 2012) implies that the reference value η_{ref} is in the range of ~50 to ~100 secondary unit charges produced per impact by a 50-nm-sized NLC/PMSE particle. This is several magnitudes larger than for impacts of pure ice particles (Andersson & Pettersson, 1998; Dubov & Vostrikov, 1991; Tomsic, 2001). This difference can be due to the large number of MSPs embedded in NLC/PMSE particles (Havnes & Næsheim, 2007; Hervig et al., 2012) because when a NLC/PMSE particle collides near the edge of, for example, a grid wire, it fragments and releases embedded MSPs. Pure ice particles smaller than ~7 nm attach to the impact surface and melt (Tomsic, 2001), but nonvolatile MSPs released in the collision do not. Using equation (5) we find that η may be in the range 0.3 to 1 unit charge per impact if we vary η_{ref} from 50 to 100 and the dust radius from 4 to 5 nm.

The ambient number density of the neutral dust $N(0)$ and net ambient dust charge number density, N (Ch) = $N(+) - N(-)$, are

$$N\left(X\right) = \Gamma\left(X\right)/\pi R^2 V_R \left(1-\sigma_1\right)^2 \tag{6}$$

where $X = 0$ or $X =$ Ch and $R = 0.04$ m is the DUSTY probe radius, V_R is the rocket speed (~910 m/s at altitude 74 km) and $\sigma_1 = 0.045$ is the fraction of the DUSTY cross section covered by the two screening grids G1 and G0 at the top of DUSTY. Equation (6) is based on the assumption that none of the RLSE dust particles are deflected away from the probe. Using Γ (Ch) and $\Gamma(0)$ from equations (3) and (4) with $\eta = 0.5$, we find the number densities $N(0)$ and N (Ch) throughout the cloud shown in Figure 4.

We see from a comparison between the radar observations in the 12° beam in Figure 2 and the DUST charge density in Figure 4 that the charged dust layer extends from ~71.5 to 75 km, which is roughly the height range of the radar echo when the payload is at 74-km height. The local maximum in dust charge density at slightly above 73 km also fits well with a local radar echo maximum.

Equations (3) and (4) show that N (Ch) is independent of η and that $N(0)$ is inversely proportional to η. If the effective cross section of DUSTY is smaller than the geometric cross section πR^2 by a factor γ then both N (Ch) and $N(0)$ increase by a factor $1/\gamma$.

4. Discussion and Conclusions

This paper reports the first simultaneous radar and rocket summer observations of the weak and low mesospheric dust clouds (Latteck & Strelnikova, 2015). The observed layer was found to have a net positive dust charge density ~10^7 unit charges per cubic meters and a neutral dust density ~10 times above this. We find that the dust sizes have to be of the order of 4 to 5 nm both to be detectable by the DUSTY probe and to balance the expected updraught. A rough comparison between dust fall velocity (Havnes & Kassa, 2009) and zonal mean upward vertical velocity (Crane et al., 1980) indicates that 4- to 5-nm particles are lifted by the updraught at altitudes below ~70 km but that their fall velocity may balance the updraught velocity at the altitude of the observed RLSE layer. If so, such particles accumulate there. Large MSPs released by sublimating NLC/PMSE icy particles may provide a source of particles in RLSE layers above about 70 km but should not fall much lower.

As mentioned above, the results of Hedin et al. (2007) indicate that at ~74 km all particles with sizes less than ~3 nm would have been deflected away from DUSTY by the airstream around the payload. However, for the particles that updraughts should leave to remain at ~74 km, γ is in the range of 0.4 to 0.7 indicating that the number densities in Figure 4 might be a factor of about 2 too small.

Since many particles in the RLSE layer are charged positively, photodetachment and photoionization must be important. This is consistent with the sunlit conditions during the MXD-1 flight and the finding of Havnes

et al. (2011) that photodetachment was the dominant mechanism returning the dust charges back to equilibrium in PMWE overshoot experiments.

For the photoionization to be effective, the dust work function has to be low. Havnes et al. (1990) suggested that a thin coating of other elements, or trace contaminations on NLC/PMSE dust particles, could lower the work function, as what happens on other substances. For example, Na and NH_3, when codeposited on thin films, result in a work function of only 0.9 eV (Qiu et al., 1989). Small dust particles can also have a much lower work function than the bulk material (Burtscher et al., 1984; Schmidt-Ott et al., 1980). The relevant observational breakthrough is due to Robertson et al. (2014) who, using a new dust mass spectrometer MASS (Knappmiller et al., 2008) launched in October 2011, found coexisting small positive and negative MSPs at altitudes from 60 to 70 km. The possibility that coatings reduce the work function of mesospheric NLC/PMSE particles had previously been discarded with respect to Na contamination because there is not enough contaminating material (Vondrak et al., 2006). However, our RLSE has a total particle surface area per atmospheric volume that is more than 2 orders of magnitude smaller than that in a moderately strong NLC/PMSE cloud, which may lead to a much more complete surface coating and a stronger contamination in the RLSE clouds.

In summary, we find that the following issues are raised by our observations:

1. Size sorting should occur when the updraught starts at the beginning of the summer NLC/PMSE season. How effective is this for MSPs and at what altitudes, as functions of time from the onset of the updraught, are the various particles deposited?
2. The charged particles in the RLSE that we observed are mainly positively charged, which we attribute to a comparatively low electron density and efficient photodetachment and photoionization. In order to gain further insight into RLSE formation, one should aim to launch probes early in the NLC/PMSE season through RLSEs, which are much more common then. We predict that normally a net positive dust charge density will be found in RLSEs when quiet magnetospheric conditions obtain since then the electron density will be low.
3. During high magnetospheric activity the electron density should normally be larger and in such a case we would expect the net dust charge density in a RLSE to be negative.
4. There should be intermediate conditions for which the net dust charge density is small. In such cases we would expect the radar backscatter on RLSEs to be particularly weak. In a plot of RLSE radar strength against magnetospheric activity a local minimum in RLSE strength and occurrence rate may be found between extremely quiet activity and strong activity.

Acknowledgments
The rocket campaign and the construction of the rocket instrumentation was supported by grants from the Norwegian Space Centre (VIT.04.14.7; VIT.02.14.1; VIT.03.15.7; VIT.03.16.7), the Research Council of Norway (240065), and by the Arctic University of Norway. Rocket and radar data for replication of results are available through the UiT Open Research Repository through the DOI https://doi.org/10.18710/PRJW7B.

References

Andersson, P. U., & Pettersson, J. B. (1998). Water cluster collisions with graphite surfaces: Angular-resolved emission of large cluster ions. *The Journal of Physical Chemistry B*, *102*(38), 7428–7433. https://doi.org/10.1021/jp981889x

Asmus, H., Robertson, S., Dickson, S., Friedrich, M., & Megner, L. (2015). Charge balance for the mesosphere with meteoric dust particles. *Journal of Atmospheric and Solar-Terrestrial Physics*, *127*, 137–149. https://doi.org/10.1016/j.jastp.2014.07.010

Belova, E., Smirnova, M., Rietveld, M. T., Isham, B., Kirkwood, S., & Sergienko, T. (2008). First observation of the overshoot effect for polar mesosphere winter echoes during radiowave electron temperature modulation. *Geophysical Research Letters*, *35*, L03110. https://doi.org/10.1029/2007GL032457

Burtscher, H., Schmidt-Ott, A., & Siegmann, H. C. (1984). Photoelectron yield of small silver and gold particles suspended in gas up to a photon energy of 10 eV. *Zeitschrift fur Physik B: Condensed Matter*, *56*(3), 197–199. https://doi.org/10.1007/BF01304172

Crane, A. J., Haigh, J. D., Pyle, J. A., & Rogers, C. F. (1980). Mean meridional circulations of the stratosphere and mesosphere. *Pure and Applied Geophysics*, *118*(1), 307–328. https://doi.org/10.1007/BF01586456

Czechowsky, P., Rüster, R., & Schmidt, G. (1979). Variations of mesospheric structures in different seasons. *Geophysical Research Letters*, *6*(6), 459–462. https://doi.org/10.1029/GL006i006p00459

Dubov, D. Y., & Vostrikov, A. A. (1991). Collision induced electrification of large water clusters. *Journal of Aerosol Science*, *22*, S245–S248. https://doi.org/10.1016/S0021-8502(05)80081-3

Ecklund, W. L., & Balsley, B. B. (1981). Long-term observations of the Arctic mesosphere with the MST radar at poker flat, Alaska. *Journal of Geophysical Research*, *86*(A9), 7775–7780. https://doi.org/10.1029/JA086iA09p07775

Havnes, O. (2004). Polar mesospheric summer echoes (PMSE) overshoot effect due to cycling of artificial electron heating. *Journal of Geophysical Research*, *109*, A02309. https://doi.org/10.1029/2003JA010159

Havnes, O., Antonsen, T., Hartquist, T. W., Fredriksen, Å., & Plane, J. M. C. (2015). The Tromsø programme of in situ and sample return studies of mesospheric nanoparticles. *Journal of Atmospheric and Solar-Terrestrial Physics*, *127*, 129–136. https://doi.org/10.1016/j.jastp.2014.09.010

Havnes, O., de Angelis, U., Bingham, R., Goertz, C. K., Morfill, G. E., & Tsytovich, V. (1990). On the role of dust in the summer mesopause. *Journal of Atmospheric and Terrestrial Physics*, *52*, 637.

Havnes, O., & Kassa, M. (2009). On the sizes and observable effects of dust particles in polar mesospheric winter echoes. *Journal of Geophysical Research*, *114*, D09209. https://doi.org/10.1029/2008JD011276

Havnes, O., La Hoz, C., Næsheim, L. I., & Rietveld, M. T. (2003). First observations of the PMSE overshoot effect and its use for investigating the conditions in the summer mesosphere. *Geophysical Research Letters*, *30*(23), 2229. https://doi.org/10.1029/2003GL018429

Havnes, O., La Hoz, C., Rietveld, M. T., Kassa, M., Baroni, G., & Biebricher, A. (2011). Dust charging and density conditions deduced from observations of PMWE modulated by artificial electron heating. *Journal of Geophysical Research*, *116*, D24203. https://doi.org/10.1029/2011JD016411

Havnes, O., & Næsheim, L. I. (2007). On the secondary charging effects and structure of mesospheric dust particles impacting on rocket probes. *Annales Geophysicae*, *25*, 623–637. https://doi.org/10.5194/angeo-25-623-2007

Havnes, O., Trøim, J., Blix, T., Mortensen, W., Næsheim, L. I., Thrane, E., & Tønnesen, T. (1996). First detection of charged dust particles in the Earth's mesosphere. *Journal of Geophysical Research*, *101*(A5), 10,839–10,847. https://doi.org/10.1029/96JA00003

Hedin, J., Gumbel, J., & Rapp, M. (2007). On the efficiency of rocket-borne particle detection in the mesosphere. *Atmospheric Chemistry and Physics*, *7*(14), 3701–3711. https://doi.org/10.5194/acp-7-3701-2007

Hervig, M. E., Deaver, L. E., Bardeen, C. G., Russell, J. M. III, Bailey, S. M., & Gordley, L. L. (2012). The content and composition of meteoric smoke in mesospheric ice particles from SOFIE observations. *Journal of Atmospheric and Solar-Terrestrial Physics*, *84-85*, 1–6. https://doi.org/10.1016/j.jastp.2012.04.005

Hunten, D. M., Turco, R. P., & Toon, O. B. (1980). Smoke and dust particles of meteoric origin in the mesosphere and stratosphere. *Journal of the Atmospheric Sciences*, *37*(6), 1342–1357. https://doi.org/10.1175/1520-0469(1980)037%3C1342:SADPOM%3E2.0.CO;2

Kassa, M., Rapp, M., Hartquist, T. W., & Havnes, O. (2012, March). Secondary charging effects due to icy dust particle impacts on rocket payloads. *Annales Geophysicae*, *30*(3), 433–439. https://doi.org/10.5194/angeo-30-433-2012

Kavanagh, A. J., Honary, F., Rietveld, M. T., & Senior, A. (2006). First observations of the artificial modulation of polar mesospheric winter echoes. *Geophysical Research Letters*, *33*, L19801. https://doi.org/10.1029/2006GL027565

Kero, A., Enell, C. F., Kavanagh, A. J., Vierinen, J., Virtanen, I., & Turunen, E. (2008). Could negative ion production explain the polar mesosphere winter echo (PMWE) modulation in active HF heating experiments? *Geophysical Research Letters*, *35*, L23102. https://doi.org/10.1029/2008GL035798

Knappmiller, S., Robertson, S., Sternovsky, Z., & Friedrich, M. (2008). A rocket-borne mass analyzer for charged aerosol particles in the mesosphere. *Review of Scientific Instruments*, *79*(10), 104502. https://doi.org/10.1063/1.2999580

La Hoz, C., & Havnes, O. (2008). Artificial modification of polar mesospheric winter echoes with an RF heater: Do charged dust particles play an active role? *Journal of Geophysical Research*, *113*, D19205. https://doi.org/10.1029/2008JD010460

Latteck, R., Singer, W., Rapp, M., Vandepeer, B., Renkwitz, T., Zecha, M., & Stober, G. (2012). MAARSY: The new MST radar on Andøya—System description and first results. *Radio Science*, *47*, RS1006. https://doi.org/10.1029/2011RS004775

Latteck, R., & Strelnikova, I. (2015). Extended observations of polar mesosphere winter echoes over Andøya (69°N) using MAARSY. *Journal of Geophysical Research: Atmospheres*, *120*, 8216–8226. https://doi.org/10.1002/2015JD023291

Lehmacher, G. A., Guo, L., Kudeki, E., Reyes, P. M., Akgiray, A., & Chau, J. L. (2007). High-resolution observations of mesospheric layers with the Jicamarca VHF radar. *Advances in Space Research*, *40*(6), 734–743. https://doi.org/10.1016/j.asr.2007.05.059

Lübken, F. J. (1999). Thermal structure of the Arctic summer mesosphere. *Journal of Geophysical Research*, *104*(D22), 27,803–27,810. https://doi.org/10.1029/1999JD900076

Plane, J. M. C. (2012). Cosmic dust in the Earth's atmosphere. *Chemical Society Reviews*, *41*(19), 6507–6518. https://doi.org/10.1039/C2CS35132C

Qiu, S. L., Lin, C. L., Jiang, L. Q., & Strongin, M. (1989). Photoemission studies of the metal-nonmetal transition of sodium on solid ammonia. *Physical Review B*, *39*(3), 1958–1961. https://doi.org/10.1103/PhysRevB.39.1958

Rapp, M. (2009). Charging of mesospheric aerosol particles: The role of photodetachment and photoionization from meteoric smoke and ice particles. *Annales Geophysicae*, *27*(6), 2417–2422. https://doi.org/10.5194/angeo-27-2417-2009

Rapp, M., Strelnikova, I., Strelnikov, B., Hoffmann, P., Friedrich, M., Gumbel, J., et al. (2010). Rocket-borne in situ measurements of meteor smoke: Charging properties and implications for seasonal variation. *Journal of Geophysical Research*, *115*, D00I16. https://doi.org/10.1029/2009JD012725

Rapp, M., & Thomas, G. E. (2006). Modeling the microphysics of mesospheric ice particles: Assessment of current capabilities and basic sensitivities. *Journal of Atmospheric and Solar-Terrestrial Physics*, *68*(7), 715–744. https://doi.org/10.1016/j.jastp.2005.10.015

Rietveld, M. T., Kohl, H., Kopka, H., & Stubbe, P. (1993). Introduction to ionospheric heating at Tromsø—I. Experimental overview. *Journal of Atmospheric and Terrestrial Physics*, *55*(4–5), 577–599. https://doi.org/10.1016/0021-9169(93)90007-L

Robertson, S., Dickson, S., Horányi, M., Sternovsky, Z., Friedrich, M., Janches, D., et al. (2014). Detection of meteoric smoke particles in the mesosphere by a rocket-borne mass spectrometer. *Journal of Atmospheric and Solar-Terrestrial Physics*, *118*, 161–179.

Robertson, S., Horányi, M., Knappmiller, S., Sternovsky, Z., Holzworth, R., Shimogawa, M., et al. (2009). Mass analysis of charged aerosol particles in NLC and PMSE during the ECOMA/MASS campaign. *Annales Geophysicae*, *27*, 1213–1232. https://doi.org/10.5194/angeo-27-1213-2009

Rosinski, J., & Snow, R. H. (1961). Secondary particulate matter from meteor vapors. *Journal of Meteorology*, *18*(6), 736–745. https://doi.org/10.1175/1520-0469(1961)018%3C0736:SPMFMV%3E2.0.CO;2

Schmidt-Ott, A. P. H. C., Schurtenberger, P., & Siegmann, H. C. (1980). Enormous yield of photoelectrons from small particles. *Physical Review Letters*, *45*(15), 1284. https://doi.org/10.1103/PhysRevLett.45.1284

Tomsic, A. (2001). Collisions between water clusters and surfaces, PhD thesis, Gothenburg University.

Von Cossart, G., Fiedler, J., & Von Zahn, U. (1999). Size distributions of NLC particles as determined from 3-color observations of NLC by ground-based lidar. *Geophysical Research Letters*, *26*(11), 1513–1516. https://doi.org/10.1029/1999GL900226

Von Zahn, U., & Meyer, W. (1989). Mesopause temperatures in polar summer. *Journal of Geophysical Research*, *94*(D12), 14,647–14,651. https://doi.org/10.1029/JD094iD12p14647

Vondrak, T., Plane, J. M. C., & Meech, S. R. (2006). Photoemission from sodium on ice: A mechanism for positive and negative charge coexistence in the mesosphere. *The Journal of Physical Chemistry B*, *110*(9), 3860–3863. https://doi.org/10.1021/jp0571630

Weingartner, J. C., & Draine, B. T. (2001). Electron-ion recombination on grains and polycyclic aromatic hydrocarbons. *The Astrophysical Journal*, *563*(2), 842. https://doi.org/10.1086/324035–852

Zeller, O., Zecha, M., Bremer, J., Latteck, R., & Singer, W. (2006). Mean characteristics of mesosphere winter echoes at mid- and high-latitudes. *Journal of Atmospheric and Solar-Terrestrial Physics*, *68*(10), 1087–1104. https://doi.org/10.1016/j.jastp.2006.02.015

Appendices

Appendix A

Abbreviations

AMU	Atomic Mass Units
CARMA	Community Aerosol and Radiation Model for Atmospheres
DROPPS	Distribution and Role of Particles in the Polar Summer Mesosphere
DUSTY	DUSTY is not an acronym
ECOMA	Existence and Charge state Of Meteoric smoke particles in the middle Atmosphere
ICON	Identification of the COntent of Noctilucent cloud particles
IDP	Interplanetary Dust Particle input
MAARSY	Middle Atmosphere Alomar Radar System
MaCWAVE	Mountain and Convective Waves Ascending Vertically
MESS	Meteoric Smoke Sampler
MIDAS	Middle Atmosphere Dynamics and Structure
mNLP	multi-Needle Langmuir Probe
MSP	Meteoric Smoke Particles
MUDD	MUltiple Dust Detector
MXD	MAXIDUSTY
NLC	Noctilucent Clouds

OML	Orbital Motion Limited
PHOCUS	Particles, Hydrogen and Oxygen Chemistry in the Upper Summer mesosphere
PMSE	Polar Mesospheric Summer Echoes
PMWE	Polar Mesospherivc Winter Echoes
RLSE	Rare Low Summer Echoes
RGA	Residual Gas Analyser
RMR	Raman-Mie-Rayleigh (scattering; as utilized in LIDAR)
SNR	Signal-to-Noise Ratio
SOFIE	Solar Occulatation For Ice
SPID	Smoke Particle Impact Probe
UHF	Ultra High Frequency
UHV	Ultra High Vacuum
VHF	Very High Frequency
WACCM	Whole Atmosphere Comunity Climate Model